Charge control of defect colour centres in hexagonal boron nitride

Doctoral Thesis

Madhava Krishna Prasad

Supervised by Dr. Jonathan D. Mar

Co-supervised by Dr. Jonathan P. Goss

May 2025

School of Mathematics, Statistics and Physics,

Newcastle University, Newcastle upon Tyne, NE1 7RU, UK

Life is a highway,

and I want to ride it ...

- Rascal Flatts

Acknowledgement

This thesis marks the end of a journey that began with me fist pumping in the middle of lockdown in a London apartment when I found out that it was now my turn to start speaking like Brian Cox to others about physics. It was a dream come true to be able to study the topic in physics that prefaced all invited talks during my undergraduate degree.

I am eternally grateful to have been offered such an opportunity by my supervisor, Dr. Jonathan Mar. His guidance and support extended beyond an academic nature and has helped become a well rounded researcher. When deciding to do a PhD, I was told that the supervisor plays a crucial role in a successful thesis. I believe I was most fortunate in that aspect. Jon Mar while motivating me to apply myself was always understanding when I had to take a break during challenging times in my personal life. I would also like to thank the 'other Jon' in my academic life. My secondary supervisor, Prof. Jon Goss, whom through our endless conversations on Thursday evenings always nudged me to be more precise with my scientific arguments, highlighted by his famous question '*Where is an electron?*'. I will also be eternally grateful to the Hofmann group at the University of Cambridge, who welcomed me with open arms and helped me build memories beyond the lab. From three hour group meetings to having Chinese takeaway lunches, my time in Cambridge will always be unforgettable.

If there was one thing that helped me persevere through the past four years, it would be the people who have inspired me so much. Perhaps the real thesis was the friends we made along the way? My colleagues in the Magic room, Patrick Williams and Patrick O'Neill, were the reason I chose not to work from home. Outside of the university bubble, my friends at the chaplaincy were always a source of comfort in the middle of a storm. Leah, Susie, Sabina, Michael and Loretta - thank you for all the times you listened to

me drone on about work, personal life and my negative orgones. The times we shared along this long journey (not just on the Great North Run), are what made Newcastle and Cambridge the homes they are today and the reason moving on to a next adventure elsewhere difficult.

Last but not the least, to make this acknowledgement worthy of being an acceptance speech at the Oscar's, I'd like to thank my family. Their constant support despite the thousands of miles of separation, comforting calls, texts and ever-presence is what has allowed me to come so far in my life. I hope my work in this thesis does justice to the faith they have always put in me through all of the choices I have made in my life.

Abstract

Colour centres in hexagonal boron nitride (hBN) have gained significant interest as they are active at room temperature and embedded in a two-dimensional material. The latter leads to minimal total internal reflection and coupling to photonic devices with nanometre proximity. Colour centres in hBN are particularly interesting as they have applications in quantum information, communications, metrology and LED technology. Current research has largely focused on photoluminescence from these defects. However, the integration of solid-state emitters into electronics necessitates the defects to be electrically driven. It is therefore essential to understand charge control of these defects.

Recently, it was discovered that the charge state of defects in hBN can be controlled by interfacing it with graphene. It was observed that charge transfer between optically active defects in hBN and graphene led to the quenching of photoluminescence from these emitters. Therefore, interfacing hBN with graphene offers a pathway to inject carriers into hBN for the electrical control of defects. This is especially useful as graphene, also being a two-dimensional material, is a suitable gate to apply vertical electric fields across emitters in hBN.

In this thesis, the study of charge transfer between hBN and graphene has been explored both from a theoretical and experimental standpoint. The theoretical approach involves using density functional theory to perform electronic structure calculations of defects in hBN and subsequently deriving defect properties, such as band structure, defect geometry, and formation energies. The results of these calculations allowed the determination of the degree of charge transfer between defects in hBN and graphene. Furthermore, periodic boundary conditions and the choice of methodology for the assignment of charge to different layers had a significant impact on the derived value of charge transfer. A methodology to determine charge transfer that was robust against these effects was developed.

The impact of the thickness of encapsulating hBN and graphene layers on charge transfer and the thermodynamics of the defect was also explored. The energy path for the

reorientation of the defect between two equilibrium structures was studied to determine metastable intermediate states. It was found that the energy ordering of different phases of a defect was sensitive to the encapsulation of the host layer by graphene and hBN. As such, encapsulating layers can impact the spectroscopic properties of the defect.

Experimentally, site control of emitters in hBN was studied. This involved the growth of an aluminium oxide (Al_2O_3) spacer between graphene and hBN to mitigate the quenching of emitters. The Al_2O_3 was then patterned using electron beam lithography and etched to create an array of pillars. hBN was then deposited on top hosting emitters, with the aim of emitters being quenched in regions where there was direct contact with graphene and active in regions where an intermediate Al_2O_3 layer was present. Emitters were found predominantly on the edges of the pillars and quenching occurred in the regions where the pillars were absent. Hence spatial contol over colour centres in hBN was achieved.

Publications

M. K. Prasad, O. A. Al-Ani, J. P. Goss, and J. D. Mar, "Charge transfer due to defects in hexagonal boron nitride/graphene heterostructures: An *ab initio* study," Physical Review Materials, Vol. 7, No. 9, 2023, doi: 10.1103/PhysRevMaterials.7.094003

M. K. Prasad, O. A. Al-Ani, J. P. Goss, and J. D. Mar, "Charge transfer and quantum emitters in two-dimensional heterostructures: An *ab initio* study," in AIP Conference Proceedings, 2023, Vol. 2743, no. 1, doi: 10.1063/5.0131961.

M. K. Prasad, M. P. C. Taverne, C.-C. Huang, J. D. Mar, and Y.-L. D. Ho, "Hexagonal Boron Nitride Based Photonic Quantum Technologies," Materials, 17, 4122 (2024), doi: 10.3390/ma17164122

Contents

1 Background and Motivation **1**

1.1 Colour centres and their applications 1

1.2 Existing sources of solid-state colour centres 2

1.3 Hexagonal boron nitride and its colour centres 4

1.4 Controlling hBN colour centres 7

1.5 Theoretical identification of defects 7

1.6 Charge transfer and electrical control of emitters in hBN 9

1.7 Thesis aims and objectives 13

2 Theoretical Methods **15**

2.1 The Core Principles of DFT 16

2.1.1 The Many-Body Schrödinger Equation 16

2.1.2 The Born-Oppenheimer (BO) approximation 16

2.1.3 Hohenberg-Kohn Theorems 17

2.1.4 Kohn-Sham Equations 19

2.1.5 The Exchange-Correlation Potential 20

2.2 Implementing DFT 21

2.2.1 Periodic Boundary Conditions (PBCs) and Basis Sets 21

2.2.2 Pseudopotentials 23

2.2.3 k-point sampling scheme 23

2.2.4 The Self-Consistency Process 25

2.3 Structural Optimisation 26

2.3.1 Optmising atomic positions 26

2.3.2 Interlayer interactions: van der Waals forces . . . 27
2.4 Computational approach for systems of interest . . . 28
2.4.1 DFT Parameters . . . 28
2.5 Derived properties from DFT . . . 30
2.5.1 Vibrational modes . . . 30
2.5.2 Band structure and density of states (DOS) . . . 31
2.5.3 Partial atomic charges . . . 31
2.5.4 Other methods . . . 32
2.5.5 Calculation of Formation Energies . . . 33
2.5.6 Activation Energies . . . 33
2.6 Summary . . . 37

3 Theoretical Results **38**
3.1 Pristine Structures . . . 38
3.1.1 Isolated hBN . . . 38
3.1.2 Graphene . . . 46
3.1.3 hBN/graphene Heterostructure . . . 48
3.2 Summary . . . 52
3.3 Charge transfer and defects in hBN . . . 54
3.3.1 Boron Vacancy - V_B . . . 55
3.3.2 Nitrogen Vacancy - V_N . . . 61
3.3.3 Nitrogen Antisite - N_B . . . 64
3.3.4 Boron Antisite - B_N . . . 64
3.3.5 Substitutional Carbon Nitrogen Vacancy Complex - C_BV_N . . . 67
3.3.6 Antisite Nitrogen Boron Vacancy Complex - N_BV_N . . . 69
3.3.7 Discussion . . . 71
3.3.8 Conclusion . . . 77
3.4 Potential energy surfaces (PES) of defects . . . 80
3.4.1 Energy paths for the reorientation of C_BV_N . . . 82
3.4.2 Discussion . . . 91
3.4.3 Conclusion . . . 100

4 Experimental Methods **101**

4.1 Nanofabrication techniques . . . 101

4.1.1 Wet transfer . . . 102

4.1.2 Electrochemical delamination . . . 103

4.1.3 Liquid-Phase Exfoliation (LPE) . . . 104

4.1.4 Atomic layer deposition (ALD) . . . 105

4.1.5 Electron beam lithography (EBL) . . . 108

4.2 Spectroscopy techniques . . . 110

4.2.1 Raman spectroscopy . . . 110

4.2.2 Photoluminescence (PL) Spectroscopy . . . 111

4.2.3 Confocal PL mapping . . . 113

4.2.4 Ellipsometry . . . 115

4.3 Microscopy techniques . . . 117

4.3.1 Scanning electron microscopy (SEM) . . . 117

4.3.2 Atomic force microscopy (AFM) . . . 118

4.4 Summary . . . 120

5 Experimental Results **122**

5.1 Tunnel barrier design . . . 123

5.1.1 Variation of charge tunneling rate with barrier thickness . . . 123

5.1.2 Förster resonant energy transfer (FRET) . . . 126

5.1.3 Device schematic . . . 126

5.2 Transfer of hBN . . . 127

5.3 Confocal PL Mapping . . . 132

5.4 PL spectroscopy . . . 135

5.5 ALD of Al_2O_3 . . . 137

5.6 Patterning of Al_2O_3/Gr . . . 141

5.7 Localisation of emitters . . . 144

5.7.1 Quenching in hBN/Graphene heterostructures . . . 146

5.7.2 Localisation of emitters in hBN flakes . . . 149

5.7.3 Localisation of emitters in CVD hBN . . . 155

5.8 Discussion 159
5.8.1 Degree of localisation 160
5.8.2 Fabrication challenges and proposed solutions 162
5.9 Conclusion 165

6 Overview and Future Outlook **166**

List of Figures

1.1 Configuration coordination diagram showing the photoluminescence process. The black arrows represent photoabsorption and relaxation. The dashed arrow shows the zero phonon line transition. The green curly arrows show phonon emission processes during electron relaxation within an electronic state. 3

1.2 (**a**) Schematic of hBN with pink spheres representing boron atoms and blue spheres nitrogen atoms. (**c**) High-resolution TEM (HRTEM) image of hBN of different thicknesses. By measuring the intensity profile across linear path in the image, it is possible to determine the stacking. Fig. 1.2b has been reproduced from Ref. 1. 5

1.3 **(a)** (**Left**) Confocal PL map of colour centres in hBN. (**Right**) Representative spectra of a visible light colour centre in multilayer and monolayer hBN. Emitters have a significantly narrower linewidth when embedded in multilayer hBN. **(b)** (**Left**) Wide range of spectra obtained from different emitters. Due to their similar lineshapes, it is common to divide these spectra into two groups. (**Centre**) shows that both categories of emitters have PSBs a similar distance away from the ZPL. Fig. 1.3 has been reproduced from Ref. 2. Fig. **(b)** has been reproduced from Ref. 3. 6

1.4 (**a**) (**Left**) Negatively charged boron vacancies observed in a confocal scan, created using a focused ion beam of Xe^+ ions, with the fluence of ions increasing with each row and constant across each row. Scale bar 20 µm. (**Right**) Variation of PL intensity with Xe^+ fluence. The inset shows a representative PL spectrum for each fluence. (**b**) (**Top-left**) Image taken using a scanning electron microscope (SEM) of a hBN flake, with the blue rectangle indicating the region irradiated with an electron beam. (**Top-right**) Confocal map of rectangle zone. (**Bottom-left**) and (**bottom-right**) are PL spectra at each exposed site taken at low temperature (5 K) at two different spectral resolutions, showing a reproducible 0.7 nm spectral linewidth. Fig. 1.4a has been reproduced from Ref. 4. Fig. 1.4b has been reproduced from Ref. 5. 8

1.5 (**Left**) Confocal PL intensity maps of strain induced colour centres in hBN. The hBN was directly grown using CVD onto the nanopillars. The pillar diameters are 250, 450, 650, and 950 nm and the scale bar is 10 µm. The unit for the intensity is photon counts/s. (**Right**) Wide-field images of each pillar array with hBN deposited on it. White circles indicate pillars with multiple emitters. The scale bar is 2 µm. The figure has been reproduced from Ref. 6. 9

1.6 hBN with a nitrogen vacancy adjacent to a carbon impurity, C_BV_N. C_BV_N could act as a colour centre. The carbon atom is represented by the gray sphere. The colour scheme for boron and nitrogen atoms follow Fig. 1.2a. . 10

1.7 **(a)** Using a Gr mask and trilayer stack of hBN (with the layer hosting emitters embedded in the middle), lateral and vertical localisation of emitters can be achieved by exploiting quenching due to graphene. **(b)** Charge transfer between defects in hBN and graphene can be controlled by manipulating the Fermi level of graphene. This can then be used to turn emitters on/off. Fig 1.7a was reproduced from Ref. 7. Fig. 1.7b has been reproduced from Ref. 8 11

2.1 The real, also known as the all-electron, wavefunctions and potentials (solid lines) and the pseudo-wavefunctions and pseudopotentials (dashed). Beyond the core radius, r_c, the real wavefunctions and potentials cannot be distinguished from the pseudowavefunctions and pseudopotentials. The figure has been reproduced from Ref. 9 24

2.2 The potential energy curves for Kr-Kr (Kr_2) (left) and benzene (right) molecules calculated using B3LYP, PBE-GGA and coupled cluster singles doubles with peturbative triples CCSD(T), which is considered the most reliable for obtaining electronic properties of molecules as a reference. The curve obtained using PBE-GGA shows some binding, although significantly weaker than the CCSD(T) reference, and the B3LYP derived curve shows repulsive force between the molecules. This shows the necessity for accounting for dispersive forces in DFT calculations of vdW materials. The figure has been reproduced with permission from Ref. 10. 29

2.3 A comparison of CI-NEB and standard NEB. The MEP obtained from both calculations are for the adsorption of CH_4 on an iridium surface Ir (111). The reaction coordination, 0.0, represents the dissociated end products CH_3+H fragments and 1.0 corresponds to a CH_4 molecular 4.0 Å away. It is clear here that standard NEB leads to poor resolution of the barrier and interpolation leads to its underestimate. This is solved by CI-NEB which leads to an image being located accurately on the saddle point. This image is reproduced from Ref. 11. 36

3.1 Optimised structure of a single layer of hBN. The computationally derived in-plane lattice constant is 2.51 Å. The colour schemes for the boron and nitrogen atoms follow Fig. 1.2a 39

3.2 The figures show the displacements of the atoms in different vibrational modes. (a) and (b) show the degenerate E_{2g} modes, which are in-plane and Raman active. (c) is the out-of plane A_{2u} mode which is IR active. The arrows indicate the direction of displacement. 40

3.3 The points of high symmetry in the Brillouin zone of a hexagonal lattice. This is shared by hBN, graphene and their heterostructures. 41

3.4 **(a)** Calculated band structure of hBN in the vicinity of the Fermi energy along high-symmetry branches of the Brillouin zone. Blue and red lines represent nominally occupied and empty bands, respectively, with the underlying shading highlighting the envelopes of the valence and conduction bands. The zero on the energy scale is set at the midpoint of the band gap in pristine hBN to allow a more direct comparison with the band structure in Ref. 12. **(b)** The total DOS of hBN, with the filling of occupied and empty states following that of the band structure. **(c)** The total DOS of hBN as well as the partial density of states for each atomic species in hBN calculated by Ref. 12. 42

3.5 The partial density of states for each atomic species is shown, along with the total density of states for the hBN monolayer (grey line). The N (green hatched filling) and B (red red hatched filling) contributions have been indicated. The zero in the energy scale is set to the mid point of the band gap and the position of the valence edge has been indicated by a dotted grid line labelled 'VBM'. 44

3.6 (a) Shows the pDOS calculated using the Mulliken populations analysis for B atoms. The contribution of the s (red) and p (green) orbitals are shown. (b) Corresponding pDOS for N atoms. The zero in the energy scale is set to the mid point of the band gap. 45

3.7 The contributions of s and p_i, where $i = x, y, z$, obtained from Mulliken analysis is shown by the different hatched shading. The zero in the energy scale is set to the mid point of the band gap. 46

3.8 Optimised structure of a single layer of graphene. The lattice constant is indicated by the dashed arrows. Gray spheres represent carbon atoms. . . 47

3.9 **(a)**The band structure of the primitive unit cell of pristine graphene. **(b)** The DOS of pristine monolayer graphene. Colours and shading follow Fig. 3.4. The zero in the energy scale is set to the Dirac point of graphene. 48

3.10 Plan view (top) of the relaxed structure of the hBN/Gr heterostructure and the side view (bottom) in **(a)** AA stacking and **(b)** AB′ stacking. The colour schemes for atoms follow Fig. 1.2a and Fig. 3.8. 49

3.11 The DOS of the hBN/Gr structure (solid lines with filling), with the DOS of graphene (dotted) and hBN (dashed) monolayers superimposed for comparison. The arrows indicate the respective DOS to aid the reader. The zero point in the energy scale is the Dirac point of isolated graphene. Colours and shading follow Fig. 3.4. 50

3.12 The band structure of the heterostructure **(a)** without and **(b)** with vdW forces. **(c)** and **(d)** show the same band structures as **(a)** and **(b)** respectively, but with the region near the Dirac point magnified to highlight the band gap when vdW forces are included. The zero point in the energy scale is the Dirac point of isolated graphene. Colours and shading follow Fig. 3.4. 51

3.13 **(a)** The band structure of the heterostructure in the AB′ stacking. **(b)** The same band structures with the region near the Dirac point magnified to highlight the band gap when vdW forces are included. The zero point in the energy scale is the Dirac point of isolated graphene. Colours and shading follow Fig. 3.4a. 52

3.14 **(a)** The structure of of V_B. The band structures of **(b)** V_B^0 in isolated hBN. Colours and scales are as in Fig. 3.4a. **(c)** Band structure of V_B in hBN/Gr. The hatched shading in **(c)** indicates the filling of the graphene bands up to the Fermi level, with the underlying shading indicating occupied and empty bands of the corresponding pristine hBN/Gr for comparison. **(d)** the localisation of the electronic states in either hBN or graphene based on Mulliken populations analysis. The red (blue) dots correspond to electronic levels with a greater (lesser) localisation in hBN than graphene. 56

3.15 The figure shows the extrapolation of the formation energies of V_B^q, with $q = (0, -1, -2)$, calculated as a function of cell size. The smallest cell corresponds to the 4×4 case and the larger cells are obtained by uniformly scaling in all dimensions. A cubic polynomial fit is performed to the energies to obtain the formation energies at the infinitely dilute limit. 57

3.16 **(a)** Illustrative DOS of hBN/Gr with a defect in the hBN layer. The purple line represents the DOS almost entirely contributed by graphene and the green line represents the delta peak that corresponds to defect in hBN. The region between μ_E and the Dirac point (or the small band gap induced) is integrated to obtain the degree of charge transfer. **(b)** An illustration of the variation of the charge density averaged over the xy plane as a function of z. The minimum in the average charge density is chosen as the location of the separation plane. 61

3.17 **(a)** Plan-view schematics of V_N^0 (top left) and V_N^{+1} (bottom left) in isolated hBN, V_N^{+1} in monolayer hBN with the in-plane lattice constant of that of the heterostructure (top right), and V_N in hBN/Gr heterostructure (bottom right). **(b)** Band structure of V_N in isolated hBN. **(c)** Band structure of V_N in hBN/Gr. **(d)** Localization of the bands to hBN or graphene based upon Mulliken populations. Colours and scales of the band structures are as in Figs. 3.4a, 3.14c and 3.14d respectively. 62

3.18 **(a)** The structure of N_B in hBN (left) and hBN/Gr (right). Band structure of N_B in **(b)** hBN and **(c)** hBN/Gr. Colours and scales of the band structures are as in Figs. 3.4a and 3.14c respectively. 65

3.19 **(a)** The structure of B_N in isolated hBN. The band structure of B_N in **(b)** isolated hBN and **(c)** hBN/Gr. Colours and scales of the band structures are as in Figs. 3.4a and 3.14c respectively. 66

3.20 The structure of C_BV_N in the singlet state in **(a)** hBN and **(b)** hBN/Gr. (c) Structure of C_BV_N in the triplet state in hBN. The band structure of C_BV_N in the singlet state in **(d)** hBN and **(e)** hBN/Gr. Colours and scales of the band structures are as in Figs. 3.4a and 3.14c respectively. 68

3.21 The structure of the N_BV_N in **(a)** hBN and **(b)** hBN/Gr. The band structure of N_BV_N in **(b)** hBN and **(c)** hBN/Gr. Colours and scales of the band structures are as in Figs. 3.4a and 3.14c respectively. The zero in the energy scale is set to the work function of graphene after alignment to a common vacuum potential. 70

3.22 Charge transition levels of defects studied in this report, calculated using (a) PBE-GGA functional, relative to the calculated work function of graphene, and (b) HSE CTLs, relative to the experimental work function of graphene. HSE [13, 14] and experimental work functions are indistinguishable on this scale 72

3.23 (a) A plot of the total electronic DOS for pristine graphene at the approximately linear region close to the Dirac point. The vertical dotted black line is the $(-/0)$ level of V_B in isolated hBN relative to the Dirac point in pristine graphene. (b) The degree of charge transfer obtained by the integration of the DOS of graphene and the heterostructure (red line and red circles, respectively) and by the charge density distribution with and without van der Waals forces (blue squares and green triangles, respectively). 73

3.24 A plot of μ_B with respect to the cell size for V_B in hBN/Gr. 74

3.25 The variation of the CTLs of defects in hBN with the number of encapsulating hBN layers. The zero of the scale is aligned to the vacuum level. From this, the donor level of C_BV_N in 5 layer hBN is $\sim 0.2\,\text{eV}$ from the Dirac point in graphene. The figure has been reproduced from [15]. 81

3.26 The end-points for the NEB calculation of C_BV_N in hBN of different thicknesses. The end-points correspond to the singlet configuration with the carbon atom perturbed above and below the hBN plane. Each row of images correspond one of the mono-, bi- or trilayer hBN systems. For the trilayer, **(g)-(i)** correspond to the defect located in the layer adjacent to vacuum, and **(j)-(l)** correspond to the defect in the middle hBN layer. . . 83

3.27 Shows the variation in the formation energy with each image of C_BV_N as it traverses the energy path to move to the equilibrium position on the opposite side of the plane. Both singlet and triplet states are shown in the diagram. 84
3.28 The end-points for the NEB calculation of C_BV_N for the hBN/Gr (light blue panel) and Gr/hBN/Gr (light green panel) systems. In each of these systems, the equilibrium positions of the singlet state, with the carbon atom perturbed above and below the host hBN plane are shown. 86
3.29 Similar to the Fig. 3.27, the energy path for the re-orientation of C_BV_N is shown for a hBN/Gr system with a varying number of hBN layers. 87
3.30 **(a)** The energy path obtained for defect re-orientation of C_BV_N . The calculations were performed with the system constrained to the singlet (S=0), doublet (S=$\frac{1}{2}$) and triplet (S=1) states and an unconstrained spin state. **(b)** The energy path with formation energies as a function of the vertical displacement of the carbon atom from the plane. 89
3.31 The band structures of **(a)** $S = 0$ calculation in 2-hBN/Gr ,**(b)** $S = 0$, **(c)** $S = 1$, **(d)** $S = 0.5$ and **(e)** free spin calculations in in Gr/hBN/Gr. Colours and scales of the band structures are as in Figs. 3.4a and 3.14c respectively. The zero in the energy scale is set to the Dirac point of the corresponding pristine structure. 94
3.32 The variation of the CTLs of C_BV_N with cell size for both the singlet (red squares and crosses) and triplet (green circles and triangles). The cubic polynomial fit for each CTL is shown as dotted or dashed lines with a color corresponding to the spin state of the neutral defect. The Fermi level of graphene (Dirac point) has been explicitly labelled by a blue dashed line. The yellow vertical band highlights the data points corresponding to the $6 \times 6 \times 1$ cell. 95

3.33 **(a)** The energy ordering when charge transfer is not favoured in the ground states of both the singlet and triplet configurations. The energy ordering of the $S = 0$ and $S = 0.5$ states are shown **(b)** without and **(c)** with an electric field. 96

3.34 **(a)** Shows the change in intensity of the emission when the electrostatic potential across the hBN is increased. **(b)** The third column shows the V-shaped Stark shift attributed to change in the orientation of the out-of-plane dipole with respect to the host hBN plane. This is attributed to the charging of the defect. Both of these images have been reproduced from Ref. 16 99

4.1 An outline of the steps of wet transfer using APS to remove the Cu substrate. 104

4.2 An outline of the steps of electrochemical delamination process using NaOH as the electrolyte. 105

4.3 A schematic of the self-limiting process in ALD. **(a)** The substrate surface is functionalised or has natural functionalisation to lead to nucleation sites for precursors. **(b)** The organo-metallic precursor A is pulsed and reacts at the nucleation sites. **(c)** The excess precursor is purged by an inert carrier gas. **(d)** The counter-reactant precursor B is pulsed, which reacts with the products of the reaction of precursor A and the functionalised surface. **(e)** The reaction by-products and excess precursor B is then purged by the inert carrier gas. **(f)** To achieve the desired thickness, steps **(b)** to **(e)** are repeated as necessary. The figure has been reproduced from Ref. 17. 106

4.4 The spin curves for **(a)** PMMA 950 A4 and **(b)** Ma-N-2410. Fig **(a)** has been reproduced from Ref. 18 and Fig. **(b)** has been reproduced from Ref. 19. 109

4.5 Variation of the Raman shift of the E_{2g} mode in hBN with thickness. The figure has been reproduced from Ref. [20]. 112

4.6 Schematic of PL and Raman spectroscopy. In PL spectroscopy the absolute emission wavelengths are measured whereas in Raman spectroscopy the difference between the excitation and emission wavelengths are measured. . 113

4.7 Optical path of a laser scanning confocal microscope. The figure has been reproduced from Ref. 21. 115
4.8 Optical pathway of an ellipsometer showing the polarisers and compensators, which combine to produce light polarised between linear to circular polarisation, depending on the orientation of the compensator with respect to the linear polariser, to be incident on the sample, and the analyser which only permits reflected light polarised along its polarisation axis to be transmitted for detection. The figure has been reproduced from Ref. 22. 117
4.9 **(a)** Schematic showing the trajectory of the scattered electrons and the detectors used to detect the various scattered electrons. **(b)** Schematic of region of the sample from which the various scattered electrons and radiation used for imaging arise from. Fig. **a)** and **b)** have been reproduced from Ref. 23. 119
4.10 Shows the oscillation amplitude of the AFM cantilever when away from the sample (top) and in contact with the sample (bottom) in tapping mode. . . 121

5.1 The band structure of the hBN/Al_2O_3/Gr heterostructure. The electrons from the occupied defect states (dashed lines in hBN) tunnel to empty states in graphene (red region of Dirac cone) and electrons from occupied states in graphene tunnel to empty states in hBN. The tunneling directions are indicated by green arrows. The band structure of each individual layer is aligned such that their vacuum levels coincide. 124
5.2 The variation of the tunneling lifetimes with Al_2O_3 barrier thickness for a range of electron energies based on Eqn. 5.2. The inverse fraction of Eqn. 5.2 gives the tunneling lifetime. The zero of the electron energy is the Dirac point in graphene. The dashed line is at 1 ns, which is on the order of the lifetime of hBN emitters. 125

5.3 **a** (Top) shows the schematic of the device used in Ref. 24 and (bottom) shows the variation of the fluorescence intensity with space thickness. **b)** Shows the PL spectrum of the QDs. **c)** Shows the variation of the normalised intensity of the QDs with spacer thickness. The solid line is fit of a theoretical model for FRET intensity variation with QD-graphene distance. The dotted line is located at $R_0 = 18\,\text{nm}$, which was obtained from the fit. **d)** Shows the lifetime measurements for different spacer thicknesses. **e** Shows the variation of the fluorescence lifetime with spacer thickness. The solid line is obtained from a fit. 127

5.4 **(a)** Schematic of hBN flakes on Al_2O_3 pillars on graphene and **(b)** CVD hBN on Al_2O_3 pillars on graphene. 128

5.5 **(a)** Shows an SEM image of multilayer CVD hBN on copper before transfer. **(b)** SEM image of hBN flakes obtained from LPE deposited on SiO_2/Si . . 129

5.6 **(a)** Raman spectra of CVD hBN transferred using wet transfer (black) and electrochemical delamination (red) before oxidation at 500 °C. **(b)** Raman spectra of CVD hBN after oxidation. **(c)** Raman map of CVD hBN. Starting from the left the images shows the variation of the amplitude, peak position and FWHM of the Lorentzian function fitted to the raw Raman data. Example spectra with successful (red circles) and unsuccessful (white circles) fits are shown. **(d)-(i)** Selected Raman spectra from points on the map, with the point number corresponding to the marked region on the map in **(c)**. 130

5.7 SEM image of CVD hBN film transferred using electrochemical delamination. 131

5.8 **(a) - (e)** are optical images of drop casted hBN taken at 5× magnification. Starting from **(a)** the sonication times were no sonication, 5 mins, 10 mins, 30 mins, 60 mins. **(f)** shows a high magnification (100 ×) image of the dispersed flakes after 30 mins of sonication. 133

5.9 Confocal PL intensity map of hBN flakes **(a)** prior to annealing, **(b)** after argon annealing, and **(c)** after argon plasma etching and argon annealing. (d) Emitters in CVD hBN on SiO_2. 135

5.10 **(a)**A PL image of a large region of plasma treated flakes with many emitters showing fluorescence intermittency, **(b)** after argon annealing. **(b)** A close up image of a single emitter exhibiting intermittency in fluorescence. . . . 136

5.11 **(a)** Intensity map obtained by hyperspectral PL measurement of Ar plasma treated and annealed flakes. **(b)-(e)** are representative spectra of PL obtained from the points in the map marked by red circles. The position of the ZPL and PSB is annotated at the top right of each spectrum. The point number in the title of the spectra correspond to the point number in the label of the red circles in **(a)**. 138

5.12 PL spectra of emitters in flakes which were only annealed in Ar **(a)** centered around 615 nm and **(b)** 675 nm. 139

5.13 PL spectra of emitters in CVD hBN which were transferred by electrochemical delamination **(a)** centered around 620 nm and **(b)** 590 nm. 139

5.14 **(a)** SEM image of standard Al_2O_3 ALD on graphene. **(b)** Al_2O_3 on graphene after pretreatment by 10 H_2O pulses in the PM process (PM1). **(c)** Al_2O_3 grown using the SM process. **(d)** PM with ozone pretreatment at 80 °C (PM2). 142

5.15 Growth per cycle of Al_2O_3 on graphene using SM operation. The black circular markers are raw ellipsometry measurements of thickness and the red solid line is a linear fit to the data. The uncertainty in the fitting of the ellipsometry measurements is of the order ± 0.01 nm. There error bars are therefore less than the markersize and are not indicated. 143

5.16 **(a)** and **(b)** Show bright and dark-field images of the exposed resist remaining after development using TMAH, respectively. Dark field images allow high contrast imaging of resist remaining in the exposed regions. **c)** and **d)** Show the bright and dark-field images of the exposed resist remaining after the surrounding Al_2O_3 film was removed in phosphoric acid, respectively. **e)** A bright-field image of the Al_2O_3 pillars after the removal of the resist cap by acetone and IPA. This region was specifically chosen to show the preservation of the graphene layer, as can be seen with the multilayer pyramid below the top row of blue Al_2O_3 pillars. 145

5.17 SEM images of the etched Al_2O_3 layer, which was grown using 100 ALD cycles. **(a)** A low magnification view of the etched pattern. **(b)** A high magnification image of a single pillar obtained using the in-lens detector for SE1 electrons. **(c)**Image obtained using the Everhart-Thornley detector (SE2). SE2 allows better visualisation of surface morphology. 146

5.18 a) AFM image of an etched region and b) AFM height profile along horizontal axis of crosshair (black solid line) and step function fit to the middle pillar (red solid line). The fit height is 15.37±0.23 nm. 147

5.19 **(a)** A pseudo bright-field image of CVD hBN on graphene. **(b)** The same region imaged with 473 nm excitation and a band pass filter as in Sec. 4.2.3. The regions overlapping graphene appear black and weak luminescence is observed in regions without an underlying graphene layer. 148

5.20 **(a)** A pseudo bright-field image of hBN flakes on graphene. **(b)** The same region imaged with 473 nm excitation with a 560-660 nm band pass filter. The PL image shows no active emitters. **(c)** PL image of reflected laser light showing scrolling of graphene due to hBN flakes around Al_2O_3 pillars. 149

5.21 Optical image of region of graphene where 50:50 ethanol:DI water solution dropcasted, dried and heated to 200 °C. Scrolling of graphene in regions of Ethanol:Water residue (appear as colourful droplets and films in the image) can be seen. 150

5.22 Optical image of hBN flakes deposited on Al_2O_3 pillars after an additional 50 ALD cycles in PM operation to grow the passivation film was performed. 150

5.23 (a) Flakes deposited on 300 cycles ($\sim 40\,nm$) of Al_2O_3 grown and patterned into pillars, imaged in the pseudo bright-field mode as in Fig. 5.20a. (b) PL image of the flakes prior to annealing showing luminescence from the edges of the pillars. (c) SEM image of flakes deposited on these pillars. **(d)** A hyperspectral PL map of hBN flakes deposited on pillars formed from 300 ALD cycles performed to grow Al_2O_3. The red circles indicate regions where the spectrums showed a PL signal. 152

5.24 PL spectra at selected points, indicated by the title of the spectrum, in the hyperspectral PL map in Fig. 5.23d. **(a)** The ZPL appears to exist outside the measured spectral range. The PSB can be seen at $\sim 610\,nm$. **(b)** ZPL wavelength at $\sim 580\,nm$. **(c)** ZPL wavelength at $\sim 610\,nm$. **(d)** ZPL wavelength at $\sim$590 nm and PSB at $\sim 635\,nm$. The ubiquitous sharp peaks at 580 nm and 620 nm are the G and $2D$ Raman peaks of the underlying graphene. 153

5.25 A pseudo bright-field image of a region of pillars close to the "coffee-ring" edge of the dropcasted flakes. 155

5.26 **(a)** PL image of the flakes post annealing showing luminescence from the edges of the pillars. This image was obtained by the summation of all the spectral slices over the range of 570-695 nm performed in the spectral scan. **(b)-(f)** Show some of these slices where diffraction limited spots were observed (circled in red). These are representative slices showing the brightest emitters. The yellow circles indicate regions where emission was observed on graphene in a narrow spectral window. The green ellipsoids highlight features that appeared in all windows, indicated a broadband spectrum. The pillars has been outlined by dashed border to aid the identification of their location. The scale bars correspond to 5 µm. 156

5.27 A PL image of a subsection of a region with low flake density, away from the coffee ring edge. The scale bar corresponds to 5 µm. The pillars have been outlined by dashed border to aid the identification of their location. . 157

5.28 **(a)**AFM image of pillars with hBN flakes deposited on top. **(b)** Height profile of the pillars along the horizontal axis of the crosshair showing that the flakes preferentially agglomerate at the pillar edges. The solid line shows a region where the flakes exist on both edges of the pillar. The dotted line is a profile along the same pillar at a region without flakes on the right edge of the left pillar. The fit to the step height of the dotted line is indicated by a red solid line. The measured height is step height 39.1±2.5 nm. 157

5.29 An SEM image of 4.75 µm × 4.75 µm pillars with multilayer CVD hBN transferred on top. The pillars were etched from an Al_2O_3 layer grown using 300 ALD cycles. 158

5.30 **(a)** PL image of the emitters in CVD hBN transferred onto pillars . This image was obtained by the summation of all the spectral slices over the range of 570-695 nm performed in the spectral scan. **(b)-(d)** Show some of these slices where diffraction limited spots which showed spectroscopic character typical to emitters (narrow linewidth emission) observed (circled in red). The blue circles indicate regions where emission was observed on bare graphene in a narrow spectral window. The green oval highlight features that appeared in nearly all windows, indicating a broad spectrum. These are representative slices showing the brightest emitters and are not an exhaustive list. The pillars has been outlined by dashed border to aid the identification of its location. The scale bar in all images corresponds to 5 µm. 159

5.31 **(a)** PL image of the emitters in CVD hBN transferred onto pillars with half the dimension. This image was obtained by the summation of all the spectral slices in the 570-695 nm range performed in the spectral scan. **(b** and **(c)** Show some of these slices where diffraction limited spots which showed spectroscopic character typical to emitters (narrow linewidth emission) observed (circled in red). These are representative slices showing the brightest emitters and are not an exhaustive list. The pillars has been outlined by dashed border to aid the identification of its location. The scale bar in all images corresponds to 2 µm. 160
5.32 An illustration of the draping of the hBN film on an Al_2O_3 pillar 162
5.33 **(a)**AFM image of undercut pillars of Al_2O_3 obtained from a film grown using 500 ALD cycles. **(b)** Height profile along white line indicated in **(a)** showing pyramidal shape. **(c)** Shows an illustration of the undercutting process. 164

List of Tables

3.1 The table shows the 3 vibrational modes of the primitive unit cell calculated using AIMPRO. The 1st mode is IR active, the 2nd and 3rd modes are Raman active. 40

Nomenclature

S_{HR} Huang-Rhys factor

W Debye-Waller factor

2D Two-dimensional

AFM Atomic Force Microscopy

AIMPRO Ab Initio Modelling PROgram

ALD Atomic Layer Deposition

APS Ammonium persulfate

ARPES Angle Resolved Photoemission Spectroscopy

B3LYP Becke 3-parameter Lee-Yang-Parr

BO Born-Oppenheimer

BSIE Basis Set Incompleteness Error

BSSE Basis Set Superposition Error

CBM Conduction Band Minimum

CCSD(T) Coupled Cluster Singles Doubles with peturbative Triples CCSD(T)

CI-NEB Climbing Image - Nudged Elastic Band

CTL Charge Transition Level

CVD Chemical Vapour Deposition

DFT Density Functional Theory

DI Deionised

DIIS direct inversion in the iterative subspace

DOS Density of States

EBL Electron Beam Lithography

FRET Förster resonant energy transfer

FWHM Full-Width at Half Maximum

GGA Generalised Gradient Approximation

GPC Growth Per Cycle

Gr Graphene

hBN hexagonal boron nitride

HRTEM High-Resolution Transmission Electron Microscopy

HSE Heyd-Scuseria-Ernzerhof

IPA Isopropyl Alcohol

KS Kohn-Sham

LDA Local Density Approximation

LPE Liquid Phase Exfoliation

LSDA Local Spin Density Approximation

MBE Molecular Beam Epitaxy

MEP Minimum Energy Path

ML-hBN Multilayer hBN

NEB Nudged Elastic Band

NMP N-Methyl-2-pyrrolidone

PBC Periodic Boundary Conditions

PBE Perdew-Burke-Ernzerhof

pDOS Partial Density of States

PES Potential Energy Surface

PL Photoluminescence

PM Pulsed Mode

PMMA Poly(methyl methacrylate)

PSB Phonon Side Band

PZT Piezoelectric

RIE Reactive Ion Etching

SEM Scanning Electron Microscopy

SM Stopped-flow Mode

SPE Single Photon Emitters

TEM Transmission Electron Microscopy

TMA trimethylaluminium

TMAH tetramethylammonium hydroxide

TMD Transition Metal Dichalcogenide

UV Ultraviolet

VBM Valence Band Maximum

vdW van der Waals

ZPL Zero Phonon Line

Chapter 1

Background and Motivation

In this chapter the background and motivation for the study of charge control of colour centres, also known as F-centres, in hexagonal boron nitride (hBN) are presented. Briefly, a general introduction to colour centres and its applications are provided, followed by an introduction to defects in hBN that are sources of light emission, and existing progress in the control of these F-centres.

1.1 Colour centres and their applications

Colour centres are formed by the introduction of a defect in a crystal [25]. A subset of these defects are point defects, which occur at a single atomic site. Point defects occur due to missing atoms (vacancies), atoms occuring at positions that it does not normally occupy, termed antisites or interstitials depending on whether they occur at a site occupied by an atom of a different species or between crystallographic planes, respectively. A third method by which point defects are created are by impurity atoms, which are of species not intrinsic to the crystal, replacing atoms at lattice points or existing as intersititials. Each of these defect types disrupt the periodicity of the crystal and therefore affect the electronic band structure of the crystal [26]. The defect leads to a local change in charge, and the localised charge behaves like an artificial atom [26]. Electronic transitions between states originating from the defect leads to the emission of light, with the energy of the emitted light depending on the energy difference between the states involved in the transition.

In crystals that possess a band gap, these defects can lead to defect states within the band gap. Optical transitions between states in the band gap have well-defined energies [27] and can be engineered for different applications in optoelectronics. These applications include LEDs [28, 29], quantum photonics [2] and metrology [30]. When F-centres that lead to a two-level system within the band gap occur in isolation, they can act as single-photon emitters (SPEs) [27, 31]. This is because an electronic transition between the two states leads to the emission of a single-photon and the controlled driving of this transition allows individual photons to be emitted on demand.

1.2 Existing sources of solid-state colour centres

Some of the first colour centres that were explored for these applications were large band gap bulk materials such as defects in SiC and Diamond NV centres [31, 32]. However, when coupling colour centres to other photonic devices, it is desirable to have the sources responsible for the emission as close as possible to the devices and to have a high extraction efficiency of photons (e.g low probability of total internal reflection of the photons within the material) [33, 34, 35].

Therefore, optically active defects in two-dimensional (2D) materials are of great interest due to the proximity of the emitters to the surface. Until recently, only 2D materials that exhibited photoluminescence at cryogenic temperatures were known, such as in emitters in Transition Metal Dihalcogenides (TMDs) [36, 37, 38]. A recent breakthrough occurred with the large band gap 2D material hBN, which demonstrated hosting of emitters active at room temperature [2].

Properties of emitters in crystals are usually described by the zero phonon line (ZPL) wavelengths, linewidths of ZPLs, and degree of phonon coupling. In a PL experiment, photons with energy greater than or equal to the energy difference between the ground and excited electronic states are used to drive the electron to an excited state. The electron is excited to a vibrational state in the excited electronic state with the largest overlap with ground vibrational state, according to Franck-Condon principles. The electron then relaxes to the ground vibrational state of the electronic excited state by releasing energy

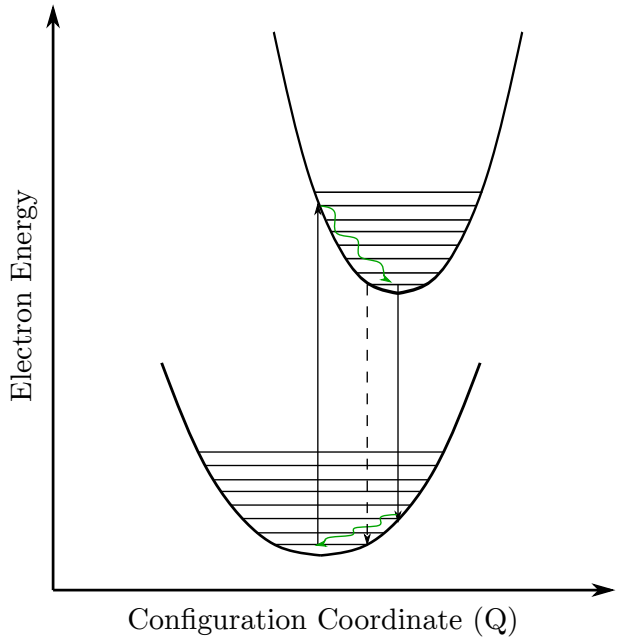

Figure 1.1: Configuration coordination diagram showing the photoluminescence process. The black arrows represent photoabsorption and relaxation. The dashed arrow shows the zero phonon line transition. The green curly arrows show phonon emission processes during electron relaxation within an electronic state.

to the crystal via phonon coupling, a process known as thermalisation. The electron then relaxes to the ground electronic state by the emission of a photon. If a transition occurs between the ground vibrational state of both the excited and ground electronic states, no phonons are emitted and the transition is known as a zero phonon transition. A transition between the ground vibrational state of the electronic excited state and any excited vibrational state of the ground electronic state is followed by the emission of phonons as the electron relaxes to the ground vibrational state of the electronic ground state. The photons emitted will have an energy less than the zero phonon line (ZPL) and will appear as a side band, known as a phonon side band (PSB). The configuration coordinate diagram, Fig. 1.1, explains this process. The ZPL transition corresponds to the optical transition between ground vibrational states of electronic excited state and ground state.

The linewidth corresponding to this transition has an inverse relationship to the brightness of the transition. As bright sources are desirable, emitters with narrow linewidths

are preferred. The degree of phonon coupling is evaluated by the percentage of the total emission intensity that is due to the ZPL transition. This is known as the Debye-Waller factor (W) and is related to the Huang-Rhys factor, S_{HR}, by the relation $W = e^{-S_{\mathrm{HR}}}$.

1.3 Hexagonal boron nitride and its colour centres

hBN has a similar lattice structure to graphene and can be found in a layerered structure like graphite [39, 40, 41]. Monolayer hBN is 2D and has a hexagonal structure with sp^2 orbitals forming bonds between the boron and nitrogen atoms, as shown in Fig. 1.2a [39, 40, 41].

Multilayer hBN is formed by stacking layers of monolayer hBN on top of each other, held together by van der Waals forces. Due to weak interlayer forces, hBN is often used as a lubricant [42]. The lattice constant of hBN is 2.50 Å and the equilibrium interlayer spacing is 3.35 Å [39]. The preferred stacking order was confirmed to be AA′ experimentally by transmission electron microscopy, TEM, (Fig. 1.2b) [1, 43, 44]. This comprises of switching the position of boron and nitrogen atoms in each layer, resulting in a stack where each boron (nitrogen) atom is located in-between a nitrogen (boron) atom in the adjacent layers.

It is a large band gap material, with a band gap of $\sim 6\,\mathrm{eV}$ [45], and can host defect states deep in the band gap, some of which have been found to be quantum emitters [2]. Chemical Vapour Deposition (CVD) has proven to be an inexpensive way of manufacturing large area hBN [46] and has been known to naturally host a large density of defects [47, 48]. This is advantageous as it can result in large number of emitters, and the large film area allows wafer scale production of devices. However, with CVD hBN, the transfer process can lead to polymer residue contaminating the sample [49]. Colour centres in multilayer hBN also show a ZPL with significantly smaller linewidth, Fig. 1.3a, possibly due to shielding from environmental effects that leading to broadening [2]. Furthemore, majority of the emission intensity is in the ZPL transition, leading to a high W factor of 80%.

hBN obtained from mechanical exfoliation methods is cleaner and has greater crys-

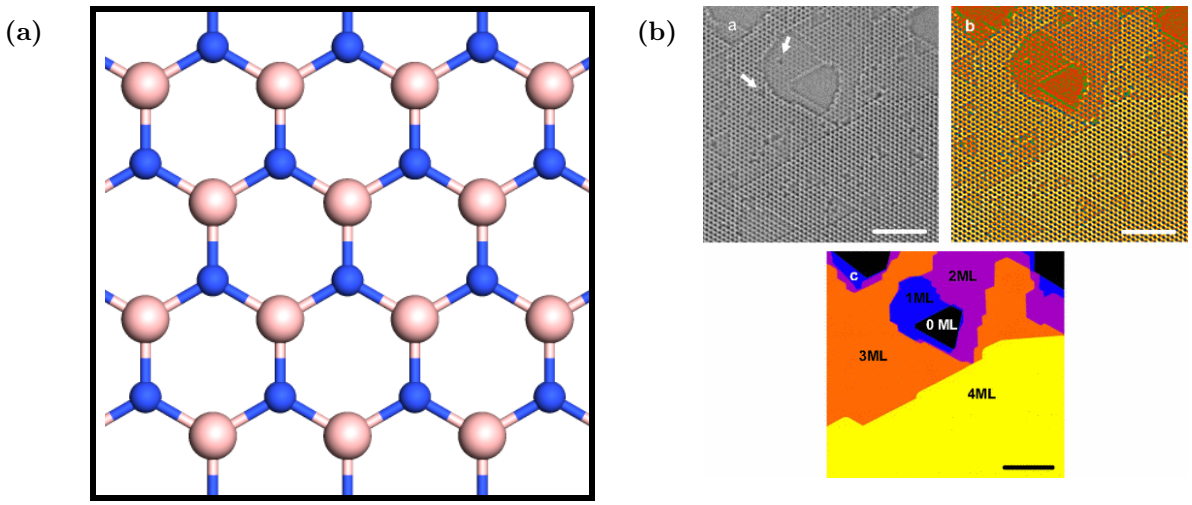

Figure 1.2: (**a**) Schematic of hBN with pink spheres representing boron atoms and blue spheres nitrogen atoms. (**c**) High-resolution TEM (HRTEM) image of hBN of different thicknesses. By measuring the intensity profile across linear path in the image, it is possible to determine the stacking. Fig. 1.2b has been reproduced from Ref. 1.

tallinity [50, 51]. However, this leads to a low density of naturally occuring colour centres. Therefore techniques that increase emitter density, such as annealing in Ar at high temperature need to be performed [2, 3]. Colour centres have been observed in hBN grown using CVD, Molecular Beam Epitaxy (MBE) , and mechanical exfoliation methods [52, 53, 54]. Each of these methods allow the production of hBN layers with different defect densities and emitters with different emission wavelengths, Fig. 1.3b, thus the source of hBN samples will depend on the application. From the spectra, it can also be seen that there is a side band due to electronic transitions to excited vibrational states in the ground electronic state of the defect. This is known as the phonon side band (PSB) and is known to commonly occur at ∼160 meV from the ZPL [3].

As hBN can be made to be atomically thin, it can be easily incorporated into integrated circuits and coupled to photonic devices with nanometer separations. Defects in hBN can be thought of as artificial atoms that have energy levels deep within the band gap of the host material [55]. The defect states lying deep in the large band gap of hBN are less vulnerable to carrier recombination due to thermal excitations than in small band gap semicondutors such as TMDs and so are active at room temperature. It was found that emitters in hBN are one of the brightest in the visible range with intensities on the order

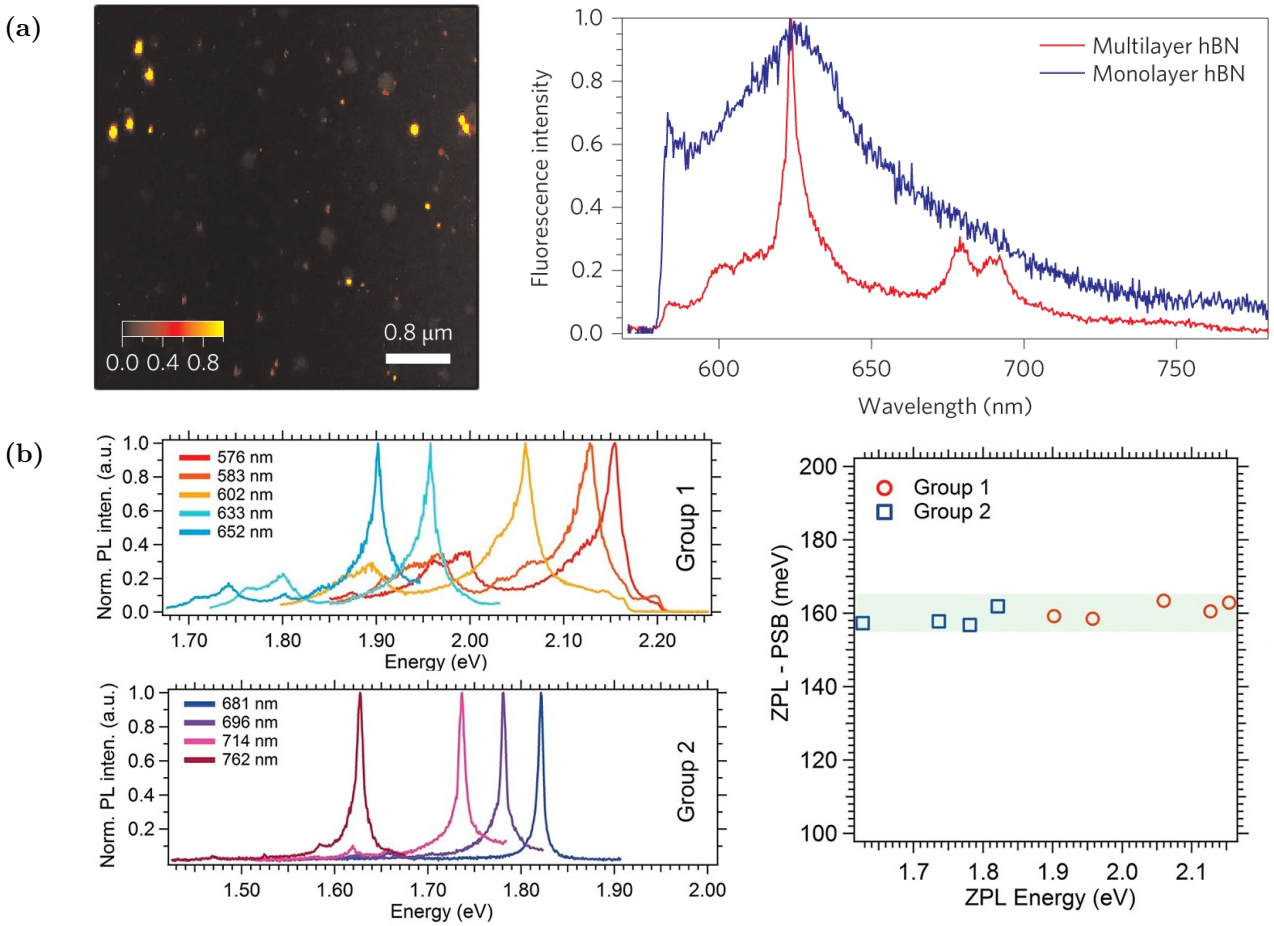

Figure 1.3: **(a)** (**Left**) Confocal PL map of colour centres in hBN. (**Right**) Representative spectra of a visible light colour centre in multilayer and monolayer hBN. Emitters have a significantly narrower linewidth when embedded in multilayer hBN. **(b)** (**Left**) Wide range of spectra obtained from different emitters. Due to their similar lineshapes, it is common to divide these spectra into two groups. (**Centre**) shows that both categories of emitters have PSBs a similar distance away from the ZPL. Fig. 1.3 has been reproduced from Ref. 2. Fig. **(b)** has been reproduced from Ref. 3.

of 10^6 counts per second being observed at saturation[2, 56]. Furthermore, defects in hBN have a wide spectral range of emission, with optical transitions occurring at visible and UV wavelengths [2, 3, 57, 58, 59]. These features make defects in hBN exciting prospects for use as scalable single-photon sources and defect based LEDs.

1.4 Controlling hBN colour centres

As a wide range of defects, each with its own unique photophysical property, are randomly distributed throughout the material during growth, it is challenging to perform high throughput fabrication of devices. Particularly for applications in scalable quantum technologies, it is important to exercise precise control over the spatial location and spectral properties of the defects.

Existing explorations in literature aiming to achieve site-controlled creation of emitters have exploited strain and irradiation techniques[4, 6, 60, 61]. These techniques have yielded SPEs on demand with varying degrees of success. Irradiation techniques resulted in low probabilities of single emitters, with most irradiated regions hosting clusters of emitters, [62], Fig. 1.4. Strain activated emission has shown greater promise for localisation [6]. In this study, SiO_2 nanopillars of various diameters were etched and hBN was grown directly on these nanopillars using CVD (Figure 1.5), and it was found that when the pillars were 250 nm and 650 nm high, there was an 80% yield of SPEs at the pillar site [6]. Therefore, research into the deterministic creation of desired defects is still in its infancy.

1.5 Theoretical identification of defects

It is useful to be able to theoretically model the photophysical properties of defects responsible for emission as this can allow a deeper understanding of the defect properties, which eventually allows us to manipulate the optoelectronic properties for various applications. A method to model the electronic properties of these defects, from which other experimentally observable properties can be derived, is by density functional theory (DFT) . Using DFT, researchers have been able to shed light on the defect geometries, allowed optical transitions, ZPL energies and phonon coupling of different defects making it a very useful tool [63, 64, 65]. DFT calculations revealed that defects such as the antisite nitrogen-vacancy complex N_BV_N has an allowed transition with a theoretical ZPL energy similar to the experimentally observed energy, making it a candidate defect [2]. Other studies focusing on the PSB of the emission spectra suggest that C_BV_N has a predicted

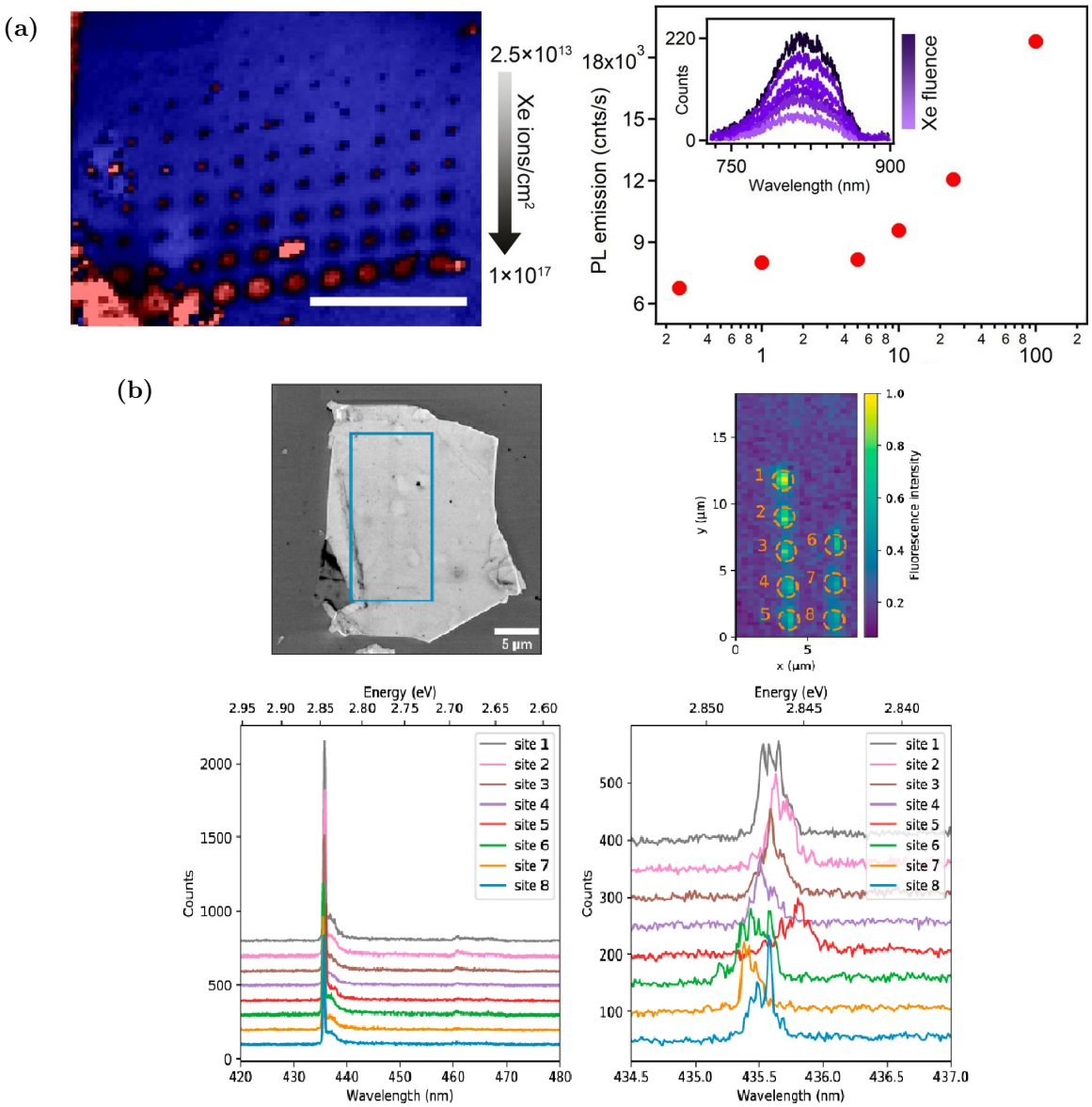

Figure 1.4: (**a**) (**Left**) Negatively charged boron vacancies observed in a confocal scan, created using a focused ion beam of Xe^+ ions, with the fluence of ions increasing with each row and constant across each row. Scale bar 20 µm. (**Right**) Variation of PL intensity with Xe^+ fluence. The inset shows a representative PL spectrum for each fluence. (**b**) (**Top-left**) Image taken using a scanning electron microscope (SEM) of a hBN flake, with the blue rectangle indicating the region irradiated with an electron beam. (**Top-right**) Confocal map of rectangle zone. (**Bottom-left**) and (**bottom-right**) are PL spectra at each exposed site taken at low temperature (5 K) at two different spectral resolutions, showing a reproducible 0.7 nm spectral linewidth. Fig. 1.4a has been reproduced from Ref. 4. Fig. 1.4b has been reproduced from Ref. 5.

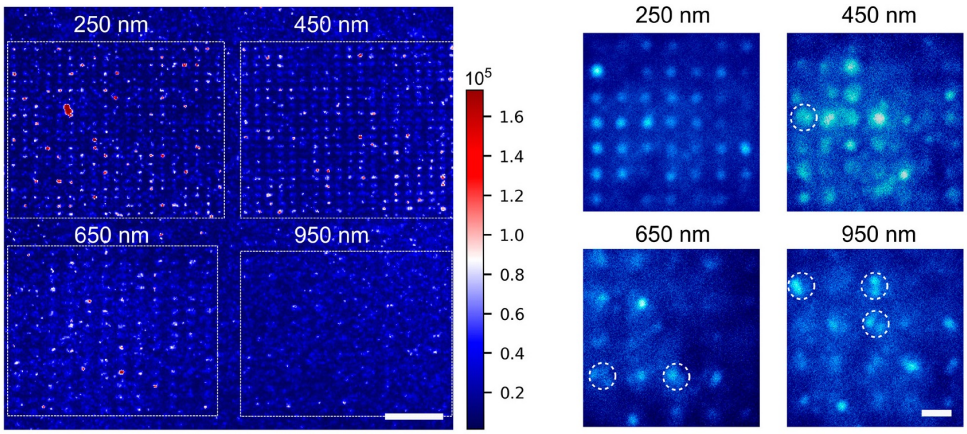

Figure 1.5: (**Left**) Confocal PL intensity maps of strain induced colour centres in hBN. The hBN was directly grown using CVD onto the nanopillars. The pillar diameters are 250, 450, 650, and 950 nm and the scale bar is 10 µm. The unit for the intensity is photon counts/s. (**Right**) Wide-field images of each pillar array with hBN deposited on it. White circles indicate pillars with multiple emitters. The scale bar is 2 µm. The figure has been reproduced from Ref. 6.

photoluminescence spectrum that is consistent with experimental observations [65, 66]. The impact of the charged state of the defect on its spectral properties has also gained significant interest [56, 67].

1.6 Charge transfer and electrical control of emitters in hBN

The fabrication of electrically driven emitters is key in the scaling up of hBN based optoelectronic technologies. On demand charge control is necessary for the operation of these devices. Recently, it was found that when hBN was deposited on graphene, majority of F-centres did not emit light, possibly due to a combination of charge and energy transfer, known as quenching [67]. However, when the graphene layer was functionalised with N-Methyl-2-pyrrolidone (NMP), to increase its Fermi level, these emitters remained active. This provided strong evidence for charge and energy transfer processes between the two layers.

Quenching of emitters due to graphene was also used to spatially localise emitters in

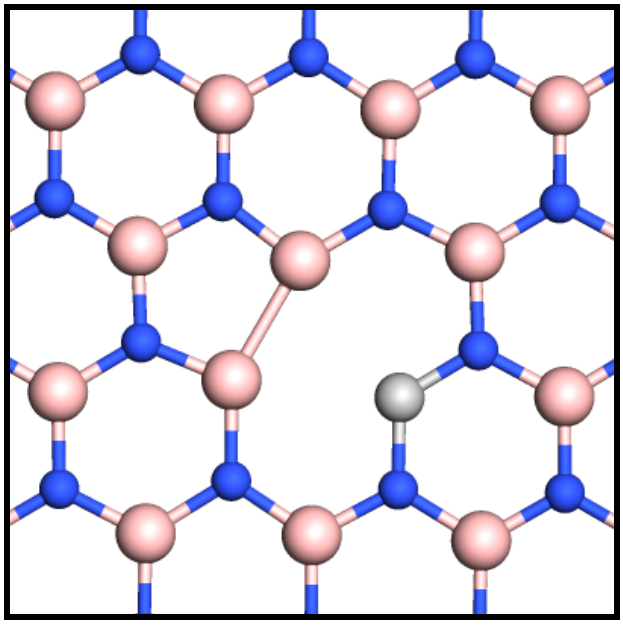

Figure 1.6: hBN with a nitrogen vacancy adjacent to a carbon impurity, C_BV_N. C_BV_N could act as a colour centre. The carbon atom is represented by the gray sphere. The colour scheme for boron and nitrogen atoms follow Fig. 1.2a.

hBN [7]. A host hBN layer with emitters activated by Ar annealing was embedded in a trilayer hBN stack, with the encapsulating hBN layers being oxidised to remove emitters and serving the role of protecting the host layer from the environment. By activating only the emitters in a host layer in the stack, vertical localisation was achieved. The trilayer stack was then placed on top of a Gr layer with windows patterned using electron beam lithography, EBL, (Fig. 1.7a). Quenching occurred only in areas where the Gr was in contact with hBN, leaving windows with emitters remaining active.

Therefore, interfacing hBN with graphene is a possible scheme to exploit charge control of emitters. This was exploited in a study that showed that changing the Fermi level of the graphene layer adjacent to hBN can lead to charging and discharging of the defect (Fig. 1.7b) leading to the defect turning on/off [8, 68]. Although the defects in these studies were optically excited and not electrically pumped, they represent initial steps towards achieving electrical pumping of hBN colour centres.

Early-stage studies on the tunability of these emitters show that the saturation intensity of the emitters can be greatly increased by strain control [69]. Tuning of the

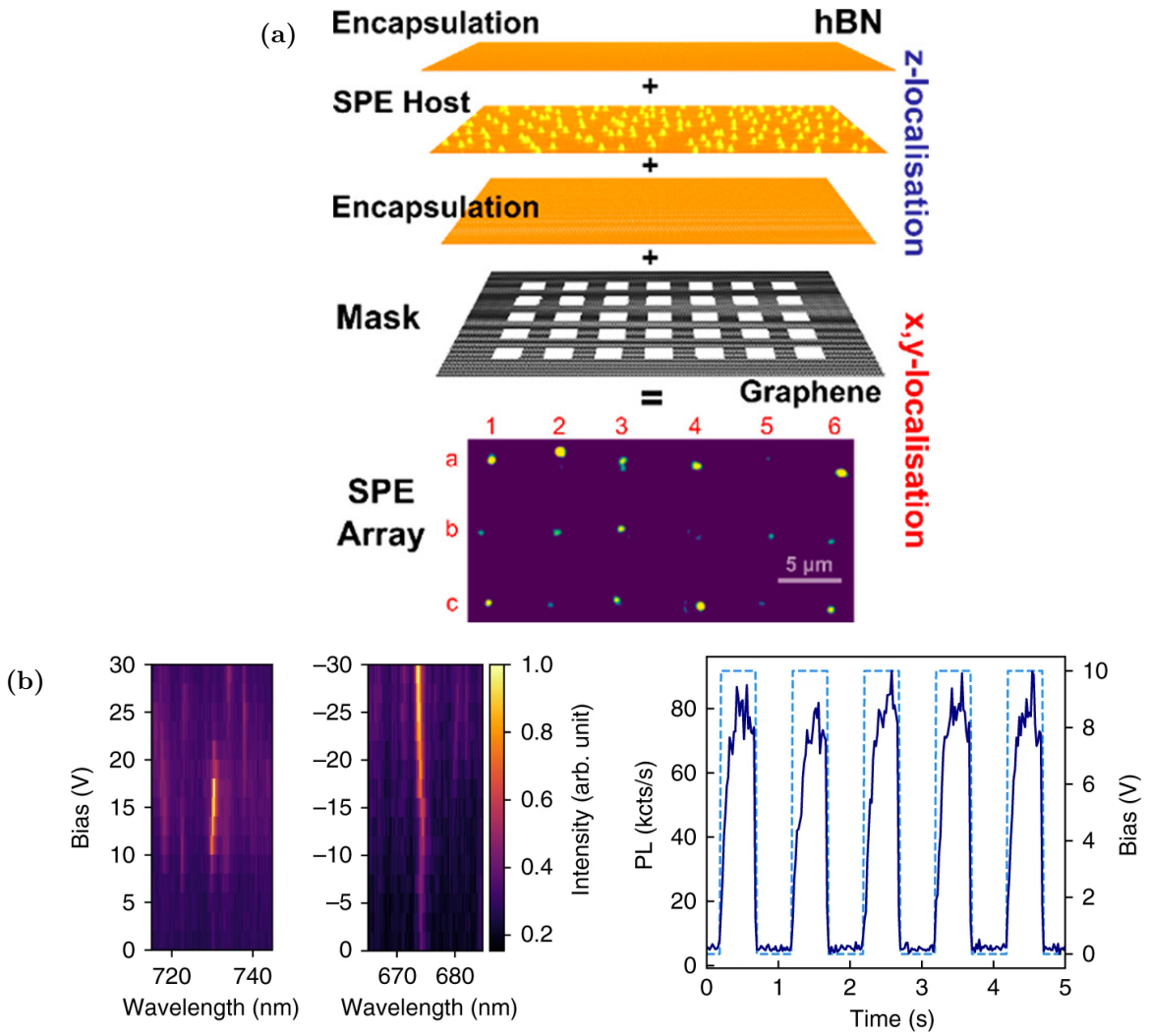

Figure 1.7: **(a)** Using a Gr mask and trilayer stack of hBN (with the layer hosting emitters embedded in the middle), lateral and vertical localisation of emitters can be achieved by exploiting quenching due to graphene. **(b)** Charge transfer between defects in hBN and graphene can be controlled by manipulating the Fermi level of graphene. This can then be used to turn emitters on/off. Fig 1.7a was reproduced from Ref. 7. Fig. 1.7b has been reproduced from Ref. 8

single-photon energies with electric fields has also been demonstrated both at cryogenic and room temperature [16, 70]. In these devices, graphene was used as a gate layer to apply an electric field across the device. This has the additional advantage that graphene, being a 2D and transparent material allows the heterostructure to still be only a few nanometers thick, allowing high photon extraction efficiency, and coupling to other photonic devices with nanometre proximity. The application of graphene both as a gate and

mask to localise emitters has earned it a lot of interest in the engineering of scalable SPE devices using hBN.

In this thesis, charge and site control of emitters has been studied in great detail using both theoretical and experimental methods. Theoretically, charge transfer processes between defects in hBN and graphene were studied using DFT. Experimentally, an alternative approach to the design in Ref. 7 was explored, where windows were replaced by Al_2O_3 pillars, which act as barriers to quenching to control regions of active emitters. Such a device can then be optimised to allow controlled charge injection into defects in hBN and apply electric fields while simultaneously allowing site control.

1.7 Thesis aims and objectives

In this section, the aims of the PhD project have been outlined, along with a summary of the chapters.

The aim of the thesis was to develop on existing methods of charge control of emitters in hBN to address issues regarding site control of emitters. The problem has been approached both theoretically and experimentally.

The theoretical approach involves computational modelling of defects in isolated monolayer and multilayer hBN, hBN/Gr and Gr/hBN/Gr heterostructures. These structures were studied sequentially to gain an understanding of how properties of defects in hBN are affected by the introduction of an increasing number encapsulating graphene layers. The goal was to identify defects that participated in charge transfer with graphene, to quantify the degree of charge transfer and understand the impact of encapsulating layers on the thermodynamics of structural reorganisation of the defect.

The experimental work develops on the study performed in Ref. 7, where windows of etched graphene hosted emitters in hBN. A drawback of this approach was the lack of graphene, which crucially plays the role of a voltage gate to apply electric fields and inject carriers into hBN, below the emitters. In this thesis, the problem is approached by growing a spacer layer of alumina (Al_2O_3) to act as a barrier to quenching. This layer was then patterned to form grids before hBN was transferred, with the intention of allowing quenching of emission where hBN made direct contact with graphene and emission where the Al_2O_3 barrier was present. A significant advantage of this design is that in a single step, the Al_2O_3 barrier thicknesses can be controlled based on the requirements of the device. For example, charge injection would require thinner spacers than compared to field control of emitters.

The following is a summary of the chapters in this thesis starting from Chapter 2:

- Chapter 2: The theoretical methodology is explained, such as the principles of DFT and its approximations. A brief summary of derived properties from DFT, such as the band structure and activation energies, are also provided.

- Chapter 3: Following an overview of the computationally derived properties of pris-

tine structure, outcomes from the theoretical work exploring charge transfer between defects in hBN and graphene and activation energies for defect reorientation are discussed. Emphasis is given to quantification of charge transfer, band structures reflecting changes to the occupancy of electronic levels and geometric changes to the defect.

- Chapter 4: Experimental methodologies used for nanofabrication and device characterisation are discussed. Some of these techniques include deposition techniques for the thin Al_2O_3 film, the transfer process of hBN, microscopy and spectroscopy processes to identify emitters.

- Chapter 5: Results from the experimental exploration on site control via quenching is presented. Images of the device showing the degree of localisation of the emitters to patterned Al_2O_3 regions is shown, supported by spectra to confirm the nature of the source of emission.

- Chapter 6: Future prospects and outlook of the research conducted in this thesis is discussed.

Chapter 2

Theoretical Methods

Theoretical modelling of hBN and defects allows the derivation of its electronic and structural properties. These properties can then be compared with experiment to understand the nature of the defects responsible for luminescence. Calculation of the electronic properties involves solving the full Schrödinger equation describing the electronic and ionic kinetic energies, inter-electronic interactions, electron-ion interactions and ion-ion interactions. This is a problem with a high computational complexity as the system being studied has a large number of atoms. DFT is a quantum mechanical theory that allows the calculation of the electronic structure of a many-electron system. It is implemented computationally to investigate the electronic structure of the system in its ground state. The benefit of this methodology compared to traditonal methods such as Hartree-Fock theory is that the computational cost of doing these calculations scales orders of magnitude more slowly with system size. In this section, the core principles of DFT are outlined.

2.1 The Core Principles of DFT

2.1.1 The Many-Body Schrödinger Equation

The general time-independent Schrödinger equation for a system with a total number of N electrons and K nuclei with charges Z_n can be written as [71],

$$H = -\frac{1}{2}\sum_{n=1}^{N}\nabla_n^2 - \frac{1}{2}\sum_{i=1}^{K}\frac{\nabla_i^2}{M_i} + \frac{1}{2}\sum_{n,n'=1;n\neq n'}^{N}\frac{e^2}{|\mathbf{r}_n - \mathbf{r}_{n'}|} - \sum_{n=1}^{N}\sum_{i=1}^{K}\frac{Z_i e^2}{|\mathbf{r}_n - \mathbf{R}_i|} + \frac{1}{2}\sum_{i,j=1;i\neq j}^{K}\frac{Z_i Z_j e^2}{|\mathbf{R}_i - \mathbf{R}_j|}. \tag{2.1}$$

The equation is given in atomic units, where the physical constants are set to equal one to ease calculation. The first two terms correspond to the kinetic energies of the electrons and nuclei respectively, where M_i is the mass of nucleus i. The third to fifth terms correspond to Coulomb interactions, namely the electron-electron repulsion, electron-nuclear attraction and internuclear repulsion terms in that order. The position of the n^{th} electron is given by $\mathbf{r}_n$ and that of the i^{th} nucleus is $\mathbf{R}_i$.

As the computational cost of solving the exact Schrödinger equation for the many-body system in Eqn. 2.1 makes it unsolvable with the largest and fastest computers available for any system with more than a few atoms, approximations are made to make the calculations feasible.

2.1.2 The Born-Oppenheimer (BO) approximation

The BO approximation results in the separation of the terms connected to the motion of the nuclei (the kinetic energy of the nuclei and the internuclear repulsion terms) from those of the electron. This is justified by the significantly heavier nuclei (protons and neutrons are approximately 1835 times heavier than electrons) moving much more slowly than the electrons, allowing the electrons to adapt to each nuclear configuration. The separated electronic Schrödinger equation describes the motion of the electrons in the field generated by a static configuration of the nuclei. The nuclear motion is then dictated by the potential due to the electronic energies and is described by a separate Schrödinger equation. The decoupling of the electronic and nuclear contributions to the Hamiltonian reduces the degrees of freedom that need to be solved for each equation, reducing computational cost.

After the BO approximation, the Hamiltonian for the electrons takes the form,

$$H = -\frac{1}{2}\sum_{n=1}^{N}\nabla_n^2 + \frac{1}{2}\sum_{n,n'=1;n\neq n'}^{N}\frac{e^2}{|\mathbf{r}_n - \mathbf{r}_{n'}|} - \sum_{n=1}^{N}\sum_{i=1}^{K}\frac{Z_i e^2}{|\mathbf{r}_n - \mathbf{R}_i|}. \tag{2.2}$$

This could be further reduced in complexity by approximating that the motion of the nuclei is neglected and only the energy due to the Coulomb interactions of the nuclei with each other is added to the electron energy to obtain the total energy. Thus, the ground state configuration of the nuclei is determined by the minimum in their potential.

However, the complexity of the Eqn. 2.2 with static nuclear configurations is still intractable by computers for large systems due to the large number of electronic degrees of freedom. The next step to reduce this complexity is to employ an independent particle Hamiltonian where each electron only 'feels' the averaged potential of the other electrons and is uncoupled from the other electronic wavefunctions. The independent particle Hamiltonian takes the form,

$$H = \sum_{n}^{N}\Big[-\frac{1}{2}\nabla_n^2 + V(\mathbf{r}_n)\Big]. \tag{2.3}$$

In Eqn. 2.3, $V(\mathbf{r})$ stems from the positions $\mathbf{R}_n$ of the nuclei and its form depends on the electronic wavefunction, ψ, the independent particle Hamiltonian is acting on. Furthermore, the value of $V\psi$ at position $\mathbf{r}$ is determined by the value of ψ at positions $\mathbf{r}' \neq \mathbf{r}$, which is why it is known as a nonlocal operator.

2.1.3 Hohenberg-Kohn Theorems

In traditional methods, such as Hartree-Fock, the averaged potential in Eqn. 2.3 depends explicitly on the wavefunctions and the process of solving for a set of N antisymmetrised eigenfunctions for the Hamiltonian does not scale favourably with system size. DFT addresses this issue by making the potential dependent on the charge density, $n = |\psi|^2 d\mathbf{r}$, instead. This is a significantly more computationally accessible means to compute the potential and allows energies of systems of thousands of electrons to be calculated in reasonable times. In DFT, the many-body Schrödinger equation that is solved to calculate the total energy is given by [71],

$$\left[-\frac{1}{2}\nabla^2 - \sum_n \frac{Z_n}{|\mathbf{r}-\mathbf{R_n}|} + \int d^3r' n(\mathbf{r}') \frac{1}{|\mathbf{r}-\mathbf{r}'|} + V_{\mathrm{xc}}[n](\mathbf{r}) \right] \psi_k(\mathbf{r}) = \varepsilon_k \psi_k(\mathbf{r}). \tag{2.4}$$

On the left hand side of Eqn. 2.4, the first term refers to the kinetic energy, the second is the electrostatic interaction between the electrons and the nuclei, and the final two terms refer to the many-body effects. The first of these two is the Coulomb interaction term and the second is referred to as the 'exchange-correlation potential', V_{xc}. The other terms in Eqn. 2.4 are, $n(\mathbf{r})$, which represents the charge density at position $\mathbf{r}$, $\mathbf{R_n}$, the position of nucleus, Z_n, the atomic number of the atomic species, and $\varepsilon_{\mathbf{k}}$, are the energy eigenvalues. Finally, $\psi_k(\mathbf{r})$ corresponds to electron wavefunction with wavevector k at $\mathbf{r}$. This takes the form of a functional and depends on the charge density alone and hence, this form of the independent particle Hamiltonian has a potential term determined solely by the charge density and not the explicit form of the wavefunctions. A functional takes a function as an input, in this case $n(\mathbf{r})$, and returns a scalar, which is V_{xc}.

The first Hohenberg-Kohn theorem states that [72]:

"The ground-state energy and all other ground-state electronic properties are uniquely determined by the electron density."

The general idea is that there exists an exchange-correlation potential that depends only on $n(\mathbf{r})$ that yields the exact ground state energy and density. The computational problem is that the form of the exchange-correlation contribution is not known. However, there are several approximations for it.

The second Hohenberg-Kohn theorem states that [72]:

"For a trial density function $n(\mathbf{r}')$, the energy functional $E_0[n']$ cannot be less than the true ground-state energy of the molecule."

This allows the usage of variational methods, starting with a trial density, $n(\mathbf{r}')$, which is positive in all space and integrates to the total number of electrons in the system, N_c, and corresponds to an external potential $V[n](\mathbf{r}')$ and Hamiltonian H', which is then

self consistently varied with $n(\mathbf{r}')$ to arrive at the final ground state energy and electron density. This constrained minimisation procedure corresponds to solving the following,

$$\delta\left\{E[n] - \mu \int n(\mathbf{r}) d\mathbf{r}\right\} = 0, \tag{2.5}$$

where the Lagrange multiplier, μ, constrains the integral of the charge density to equal the total number of electrons. The ground state energy then satisfies,

$$\mu = V_{\text{ext}}(\mathbf{r}) + \frac{\delta E_{\text{HK}}[n]}{\delta n(\mathbf{r})} \qquad E_{\text{HK}}[n] = T[n] + V_{ee}[n]. \tag{2.6}$$

$V_{\text{ext}}(\mathbf{r})$ is the external potential, $T[n]$ is the total kinetic energy functional, and V_{ee} in Eqn. 2.6 refers to all the different electron-electron interactions.

2.1.4 Kohn-Sham Equations

The search for the ground state energy of a system is done through the variational process in two steps. The first step is to minimise the energy with respect to the wavefunctions for a fixed electron density, the second step is to minimise the energy with respect to the density.

The set of wavefunctions consistent with a fixed density that minimises the energy is found by developing a hypothetical reference system with N_c non-interacting electrons moving in an effective potential, $V_{\text{eff}}(\mathbf{r})$, such that the reference electron density, $n_{\text{ref}}(\mathbf{r})$, is the same as the true electron density, $n(\mathbf{r})$. The set of equations that allows the calculation of these wavefunctions are known as the Kohn-Sham (KS) equations. This can be written as Ref. 72,

$$h_{\text{ref}} = \sum_{i=1}^{N_c} h_i^{\text{KS}} \qquad h_i^{\text{KS}} \psi_m^{\text{KS}}(\mathbf{r_i}) = \varepsilon_m^{\text{KS}} \psi_m^{\text{KS}}(\mathbf{r_i}), \tag{2.7}$$

where the Kohn-Sham orbitals, ψ_k^{KS}, are solutions to the one-electron Kohn-Sham Hamiltonians, h_{KS}. The one-electron Kohn-Sham Hamiltonian is given by,

$$\left(-\nabla_i^2 + V_{\text{eff}}\right)\psi_k^{\text{KS}}(\mathbf{r}) = \varepsilon_k^{\text{KS}} \psi_k^{\text{KS}}(\mathbf{r}), \tag{2.8}$$

where the first term is the kinetic energy term of the i^{th} electron of the one-electron Hamiltonian, $\varepsilon_m^{\text{KS}}$ is the energy eigenvalue, and V_{eff} is given by,

$$V_{\text{eff}} = V_{\text{ext}}(\mathbf{r}) + \frac{\delta J[n]}{\delta n(\mathbf{r})} + \frac{\delta E_{\text{xc}}[n]}{\delta n(\mathbf{r})}. \tag{2.9}$$

$J[n]$ in Eqn. 2.9, is the Hartree energy of the reference system, which is the same of the real system, and E_{xc} is the exchange-correlation energy. The last term, which is the functional derivative of E_{xc} is aforementioned V_{xc},

$$V_{\mathrm{xc}}(\mathbf{r}) = \frac{\delta E_{\mathrm{xc}}[n]}{\delta n(r)}. \tag{2.10}$$

$J[n]$ and E_{xc} are defined as:

$$\frac{\delta J[n]}{\delta n(\mathbf{r})} = j_0 \int \frac{n(\mathbf{r})}{|\mathbf{r}-\mathbf{r}'|} d\mathbf{r}' \qquad j_0 = \frac{e^2}{4\pi\epsilon_0} \tag{2.11}$$

$$E_{\mathrm{xc}} = (T[n] + V_{ee}[n] - T_{\mathrm{ref}}[n_{\mathrm{ref}}] - J_{\mathrm{ref}}[n_{\mathrm{ref}}]). \tag{2.12}$$

E_{xc} accounts for many-body electron-electron interactions that have not been captured by the reduction of the many-body system to an effective one-electron system. The effective potential is therefore:

$$V_{\mathrm{eff}} = V_{\mathrm{ext}}(\mathbf{r}) + j_0 \int \frac{n(\mathbf{r})}{|\mathbf{r}-\mathbf{r}'|} d\mathbf{r}' + V_{\mathrm{xc}}(\mathbf{r}). \tag{2.13}$$

2.1.5 The Exchange-Correlation Potential

DFT allows the calculation of the exact ground state energy, if the correct exchange-correlation functional is known. The main challenge of DFT is to find E_{xc} and there are numerous approximations for it. Mathematically, the exchange correlation potential, V_{xc} is the functional derivative of the exchange correlation energy with respect to the local charge density, Eqn. 2.10. The simplest approximation is that the local density, the charge density at an infinitesimal volume located at $\mathbf{r}$, is homogeneous. This is called the local density approximation (LDA) , and the V_{xc} is dependent only on the local charge density [71]. The expression for the exchange-correlation potential in the LDA scheme is [71, 73],

$$E_{\mathrm{xc}} = \int \mathrm{d}^3 r \, \varepsilon_{\mathrm{xc}}[n(\mathbf{r})] n(\mathbf{r}), \tag{2.14}$$

where $\varepsilon_{\mathrm{xc}}$[n] is the exchange-correlation energy for one particle in a homogeneous electron gas. The exchange-correlation energy is usually broken down to an exchange and correlation term, $E_{\mathrm{xc}} = E_{\mathrm{x}} + E_{\mathrm{c}}$. The exchange effects, E_{x}, are obtained based on quantum Monte Carlo simulations to be [71],

$$E_{\mathrm{x}} = -\frac{3}{4}\left(\frac{3}{\pi}\right)^{\frac{1}{3}} n^{\frac{1}{3}}(\mathbf{r}). \tag{2.15}$$

In open-shell systems, distinct densities for the spin-up and spin-down electrons are taken to be independent in the exchange-correlation energy. The exchange energy in the local density approximation (now the local spin density approximation - LSDA) takes the form of,

$$E_{\mathrm{x}}[n_+, n_-] = -\frac{3}{2}\left(\frac{3}{4\pi}\right)^{\frac{1}{3}} \int \mathrm{d}^3 r \, [n_+^{\frac{4}{3}}(\mathbf{r}) + n_-^{\frac{4}{3}}(\mathbf{r})]. \tag{2.16}$$

The LDA functional can be extended so that it not only depends on the electron density at that point but also its gradient at that position. This is the basis of the Generalized-Gradient Approximation (GGA) . The exchange-correlation energy then takes the form:

$$E_{\mathrm{xc}}[n] = \int f(n(\mathbf{r}), \nabla n(\mathbf{r})) d\mathbf{r}. \tag{2.17}$$

It is important to highlight the impact of the choice of exchange-correlation functional on the calculated values. The LDA functional is known to lead to an over-binding of electrons and an underestimation of lattice constants, whereas the GGA functional slightly overestimates the lattice constant and under-binds the atoms [71]. Therefore, the choice of functional can be made based on the computational cost and the accuracy gains in the calculated properties of the system. Although GGA and LDA calculations have comparable computational costs, GGA functionals account for the variation in the electron density around the vicinity of $\mathbf{r}$ and it provides a more accurate description of the many-body electron system than the LDA.

2.2 Implementing DFT

2.2.1 Periodic Boundary Conditions (PBCs) and Basis Sets

When calculating the electronic properties of crystals, as is the case in this thesis, it is useful to exploit the periodicity of crystals. A crystal can be thought of as being made from an infinite repetition of the unit cell in the direction of each lattice vector [26]. Solutions to the Schrödinger equation, or its reformulation in DFT, Eqn. 2.4, then only need to be calculated for the unit cell. This reduces the computational load when compared to the same calculation on a cluster of atoms of sufficient size to represent the crystallinity of

the solid [71]. It must be noted that PBCs are only employed when terminations, such as edges, are not of interest.

From Bloch's theorem it is known that electronic wavefunctions in systems with periodic boundary conditions can be expanded using a discrete set of plane-waves, and these plane-waves can now be used as a basis set to represent the Kohn-Sham orbitals in Eqn. 2.7. The main advantages of using a plane-wave basis set is that it naturally reflects the periodicity of crystals, forms an orthogonal basis set and are independent of atomic positions (unbiased basis set) [26, 71]. Furthermore, the possibility of solving the problem in Fourier space, allows the computational time to be reduced significantly [9].

However, there are some significant disadvantages. Atoms have a cusp in the charge density at core regions near the nuclei and the charge density decreases rapidly into the vacuum regions. These regions also have a rapid variation in the electronic wavefunction. To capture these effects accurately, a large plane-wave basis set is required, increasing the computational load [71]. These deficiencies can be addressed by the use of pseudopotentials.

Alternatively, Gaussian basis sets localised at the positions of the nuclei can be used [74]. These localised orbitals better represent the properties of the charge density close to the core, thereby reducing the size of the basis sets needed for the calculations, although pseudopotentials may still be required. Solving eqn. 2.4 and 2.8 also involves calculating complicated integrals, but with the use of Gaussian orbitals, the integrals have known analytical solutions, simplifying the calculations. However, Gaussian basis sets possess some disadvantages of their own. A basis set that is too small can lead to an inaccurate description of electronic states (Basis Set Incompleteness Error - BSIE) or atoms in close proximity to each other "borrow" wavefunctions localised at a different sites, leading to an artificial reduction in energy and bond lengths (Basis Set Superposition Error - BSSE) [74]. For plane-waves, the size of the basis set can be controlled easily by changing the 'cut-off' energy corresponding to the highest energy wavevector in the plane-wave basis set [9]. For Gaussian basis sets, this is a more complicated procedure that requires optimising a set of orbitals for a given system [75].

2.2.2 Pseudopotentials

To overcome the computational challenge of a large plane-wave set needed to capture the rapid oscillations near the core regions of the valence electron wavefunctions [9], pseudopotentials are used. This process works by replacing core electrons and the strong ionic potential by a weaker pseudopotential that acts on a set of pseudo-wavefunctions and the valence electron states rather than the true valence wavefunctions [9, 76]. Since core electron wavefunctions are highly localized and weakly participate in chemical bonding, it justifies the use of pseudopotentials [76].

The set of pseudopotentials and pseudo-wavefunctions should be constructed to reproduce the valence charge density, which is outside a cut-off radius r_c from the nucleus (called the core radius), associated with chemical bonds obtained from all-electron calculations. For such pseudopotentials the integrals of the squared amplitudes of the all-electron and pseudo-wavefunctions beyond r_c are identical, Fig. 2.1, which amounts to one electron per pseudo-wavefunction [77]. These pseuodpotentials are therefore known as norm-conserving [9, 77].

A pseudopotential can be further classified as either being 'hard', [78], or 'soft', [79], if the number of Fourier components of the wavefunction that are needed to represent the core electron-ion Coulomb interaction are large or small respectively. The softer the pseudopotential, the larger the r_c and the lower the computational cost as a smaller basis set is needed to represent the variation of the charge density near the core [79].

A major benefit of the pseudopotential technique is the transferrability across several systems [9]. The construction of pseudopotentials is performed on isolated atoms or ions of fixed electronic configurations. Therefore, they possess the correct scattering properties over a wide energy range and can be used in various solid-state environments, such as in crystals of various phases.

2.2.3 k-point sampling scheme

The boundary conditions of a system impose restrictions on the allowed k-points at which electronic states can exist [26]. Using Bloch's theorem due to the PBCs in the crystal system, the problem of computing the electronic levels is reduced to the k-points within

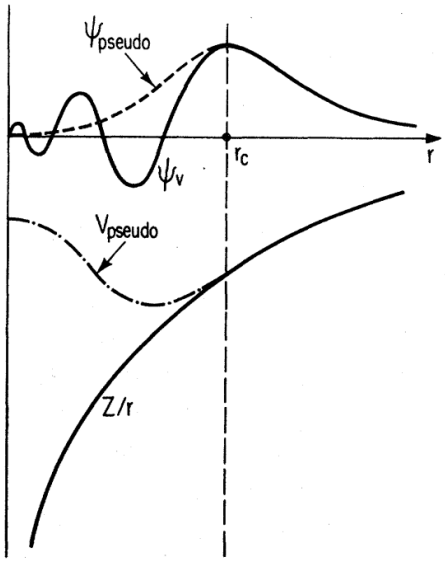

Figure 2.1: The real, also known as the all-electron, wavefunctions and potentials (solid lines) and the pseudo-wavefunctions and pseudopotentials (dashed). Beyond the core radius, r_c, the real wavefunctions and potentials cannot be distinguished from the pseudowavefunctions and pseudopotentials. The figure has been reproduced from Ref. 9

the primitive unit cell in the reciprocal space, which is known as the Brillouin zone [26]. In the case of an infinitely repeating unit cell in the crystal system, there are infinitely many k-points in the Brillouin zone and each occupied state contributes to the potential in Eqn. 2.9, leading to a computational challenge. However, as the electronic wavefunctions at k-points close together have nearly identical wavefunctions, only a finite subset of the infinite number of k-points need to be sampled to accurately calculate the potential in system [9]. The scheme implemented in this study follows, Ref. [80], where k-points along each reciprocal lattice vector is generated by uniformly dividing the basis vector by a user defined number of points. The number of k-points used will depend on the sensitivity of the derived properties of interest of the system to the sampling density. For example, metallic systems, such as the graphene layer studied in this thesis, have a complex Fermi surface that requires a high density of k-points to accurately describe the electronic potential [9, 81]. As such, the sampling density used should correspond to the degree to which the relevant property, such as interatomic distances or electron chemical potentials, need to be converged.

2.2.4 The Self-Consistency Process

Having determined the approximations and general theory for the determination of electronic energies, the algorithm for determining the ground state energy of a system is now discussed.

The process of starting with an *ansatz* charge density and a basis set of wavefunctions corresponding to the charge density, minimising the energy with respect to the wavefunctions with a fixed charge density, then minimising with respect to the charge density and the repeating then process until the change in charge density and total energy is below a tolerance is known as a self-consistent field method.

Computationally, the following method is implemented to achieve self-consistency:

1. Generate a starting input density:

$$n(\mathbf{r}) = \sum_{atoms,a} n_a(\mathbf{r}) \tag{2.18}$$

2. Calculate the effective Kohn-Sham potential, Eqn. 2.13

3. Solve the non-interacting problem, Eqn. 2.8, to generate a set of wavefunctions that minimise the energy corresponding to the starting density.

4. The charge density corresponding to the new set of wavefunctions is computed

$$n(\mathbf{r}) = \sum_{i} |\psi_m^{\mathrm{KS}}(\mathbf{r})|^2 \tag{2.19}$$

5. A new charge density is constructed using a weighted combination of the output and the input charge density.

The above procedure is repeated until the change in the total energy and electron densities between successive calculations are less than a threshold. This threshold to the change in these values is determined by the precision to which the desired properties of a system, such as the lattice constant, need to be known. As will be discussed in Sec. 2.3.1, the nuclei "move" in a potential determined by the electron density, and hence the accuracy of the electronic energies obtained from the self-consistency process will

impact other properties of the system. Once the changes in charge density and total energies satisfy the threshold criteria, the values are considered to be "converged" within the self-consistency cycle and process is completed.

The algorithm used in this project for generating the new input charge density at each self-consistency cycle is a variation of the 'direct inversion in the iterative subspace' or DIIS method [82, 83]. Briefly, the algorithm is as follows. A historical record of input charge densities are maintained as the self-consistency process is followed, and the new input charge density is calculated from a weighted contribution of each historical charge density. The weights are determined so as to minimise the difference between the output charge density of the previous self-consistency cycle and the next input charge density. Hence, the input charge density is always a mixture of contributions from charge densities in previous iterations. The size of the historical record of charge densities and pre-conditioning to determine the extent to which mixing occurs with previous guesses can be controlled to obtain rapid convergence to the ground state charge density [83].

2.3 Structural Optimisation

Using DFT, one can obtain the electronic properties of the system under the Born-Oppenheimer (BO) approximation. In the BO approximation, the electronic and nuclear contributions to the total Hamiltonian is separated and the nuclei move in the electrostatic potential of the electrons [72, 26]. Therefore, an additional step needs to be included in the computational procedure to relax the interatomic distances so that the system is in its electronic and structural ground state. This is necessary as it is of interest to calculate structural properties such as lattice constants and interatomic distances. In this section, the methods used to determine these properties are briefly overviewed.

2.3.1 Optmising atomic positions

The process of structural optimisation involves minimising the forces acting on the atoms in the solid. The nuclei of the atoms can be thought of as moving in the electrostatic potential due to the electronic wavefunction in the BO approximation. Therefore the

force acting on a nucleus is the derivative of the electronic energy obtained from the SCF procedure for a fixed nuclear position. From the Hellman-Feynman theorem, Eqn. 2.20, it is known that the variation of the total energy with respect to a parameter, P, in this case the internuclear distances, is equal to the expectation value of the derivative of the Hamiltonian of the system with respect to that parameter [72]. This allows the forces to be calculated analytically and the search direction for the minimisation of the forces is computed using the conjugate gradient method [76]. The structural relaxation process is necessary to perform, as according to the second law of thermodynamics, the system will be found in its lowest energy configuration at equilibrium.

$$\frac{dE}{d\mathbf{P}} = \left\langle \frac{\partial H}{\partial P} \right\rangle \tag{2.20}$$

2.3.2 Interlayer interactions: van der Waals forces

In many systems, such as large non-polar molecules and, as in the case of this thesis, 2D materials, have long-range interactions due to induced dipoles. At short electron-electron distances, the correlation is modelled well by standard density functionals, as they have a deep relation to the corresponding electron density change, however, such correlation is absent in several local or semi-local exchange-correlation functionals [10]. For example, in Fig. 2.2 , while the PBE (a GGA type functional) functional at least qualitatively mimics the attractive force between atoms/molecules, the Becke 3-parameter Lee-Yang-Parr (B3LYP) hybrid functional predicts a repulsive force [10]. Therefore, there is a need to explicitly incorporate dispersion forces, especially in layered materials as van der Waals (vdW) forces are the primary attractive force leading to binding between different layers. As will be discussed in Sec. 3.3, the accurate modelling of interlayer separation is necessary for the determination of the degree of charge transfer.

The dispersion correction to the total energy used in this thesis is the Grimme DFT-D3 correction [84]. This correction is added separately to the Kohn-Sham DFT total energy, $E_{\text{KS-DFT}}$ in Eqn. 2.22, and therefore only directly affects the optimisation of the nuclear positions. All DFT-D approaches have the same general form of the dispersion correction

i.e [10],

$$E_{\text{disp}}^{\text{DFT-D}} = \sum_{AB} \sum_{n=6,8,10} s_n \frac{c_n^{AB}}{R_{AB}^n} f_{\text{damp}}(R_{AB}), \tag{2.21}$$

$$E_{\text{DFT-D3}} = E_{\text{KS-DFT}} - E_{\text{disp}}^{\text{DFT-D}} \tag{2.22}$$

where the sum is over all atom pairs, AB, in the system and the corrected energies take the form of Eqn. 2.22. In Eqn. 2.21, the c_n^{AB} term denotes the averaged n^{th} order dispersion coefficient (orders $n = 6$, 8, 10, ...) for the atom pair AB, and the internuclear distance of this pair is given by R_{AB}. The global parameters, s_n, are used to modify the correction to suit the behaviour of the chosen density functional. f_{damp} is a damping function and is included to avoid singularities at small R_{AB} and double-counting at intermediate internuclear separations. Hence, f_{damp} determines the range of the dispersion correction. The DFT-D3 scheme can be easily incorporated into standard density functionals, allows the efficient calculation of energy gradients during structural relaxation and finally, interpretation of the dispersion energy is straightforward as it can be assigned to contributions from individual atom pairs, parts of a molecule, or for a particular internuclear separation.

2.4 Computational approach for systems of interest

2.4.1 DFT Parameters

Now that the general DFT theory and its approximations have been discussed, the parameters used in the computation of properties of the defects studied in this thesis are ellaborated.

The DFT calculations were performed using the Ab Initio Modelling PROgram[76] (AIMPRO) with PBC and the PBE-GGA exchange-correlation functional [85]. Atoms are modelled using norm-conserving separable pseudopotentials [86], with 1s-states of B, C and N part of the core. Kohn-Sham eigenfunctions are represented with a basis of sets of independent s- and p-Gaussian orbitals with four different exponents centred on atomic sites [87], with the addition of one (two) sets of d-Gaussian functions for C (B and N) atoms to account for polarization. This amounts to 18 independent Gaussian functions per C atom in the basis, and 28 per B and N atom. Additional sets of functions

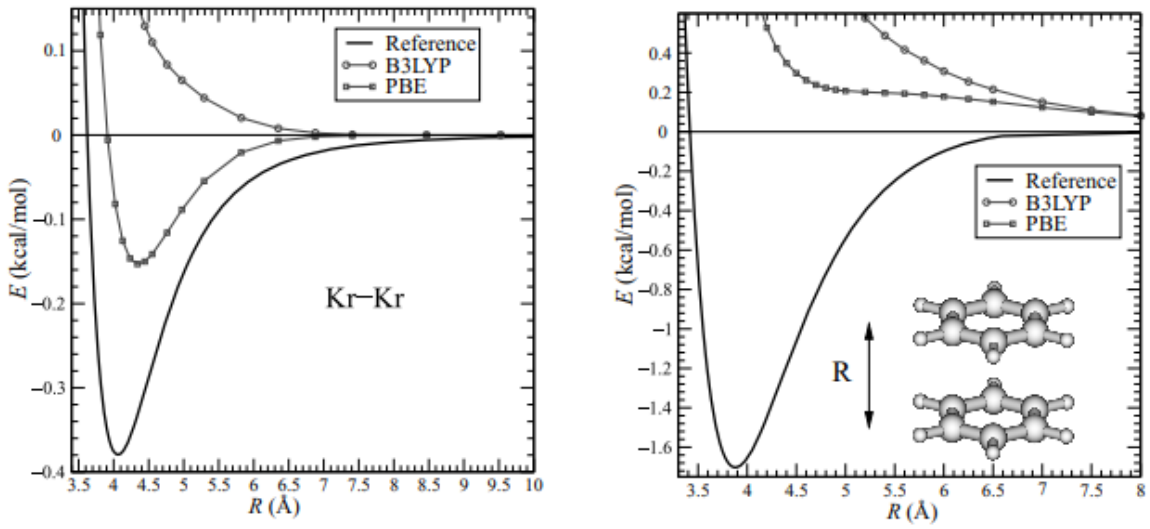

Figure 2.2: The potential energy curves for Kr-Kr (Kr_2) (left) and benzene (right) molecules calculated using B3LYP, PBE-GGA and coupled cluster singles doubles with peturbative triples CCSD(T), which is considered the most reliable for obtaining electronic properties of molecules as a reference. The curve obtained using PBE-GGA shows some binding, although significantly weaker than the CCSD(T) reference, and the B3LYP derived curve shows repulsive force between the molecules. This shows the necessity for accounting for dispersive forces in DFT calculations of vdW materials. The figure has been reproduced with permission from Ref. 10.

are located in the vacuum regions to ensure accurate representation of the evanescence of the electron wavefunctions into the vacuum. The charge density is Fourier transformed using plane-waves with an energy cutoff of 300 Ha, leading to energies converged to better than 1 meV with respect to this parameter. The Brillouin zone of the primitive structures were sampled using a $16 \times 16 \times 1$ k-point grid and the Monkhorst-Pack scheme [80]. Non-primitive cells are modeled using grids with a comparable or denser reciprocal space density. Structures were optimized by the conjugate-gradient method until the total energy changed by less than 10^{-5} Ha, and which corresponded to forces less than 10^{-4} a.u. From these parameters, the error in the total energies is within the "chemical accuracy" of 50 meV [88].

Although screened-exchange functionals, such as the Heyd-Scuseria-Ernzerhof (HSE) functional, produce electronic properties, such as band gaps, significantly closer to experimental results when compared to GGA functionals, they come with significantly greater

computational cost and is also not available as an option in AIMPRO. However, GGA functionals accurately reproduce bond lengths and the band structures qualitatively resemble those derived using HSE, while being computationally efficient. As many modern DFT analyses of hBN use GGA functionals, GGA functionals were used in the calculations as well [12, 89, 90, 91, 65]. Using a scheme proposed by Ref. 92, the calculated PBE values are translated into HSE values to validate the conclusions derived using PBE.

When exploring multilayer hBN and hBN/Gr heterostructures, dispersion forces between adjacent layers were explicitly included to reproduce experimental interlayer spacings. The interlayer vdW interactions were represented using the Grimme-D3 scheme [10]. The impact of the inclusion of vdW interactions is discussed in Sec. 3.3.7.

2.5 Derived properties from DFT

2.5.1 Vibrational modes

After relaxing the nuclear positions of the supercell, the vibrational modes can be calculated. This is done by first displacing atom, a, along the axis direction l (with x, y and z spatial components) by an infinitesimal value ϵ, usually around 0.025 a.u and calculating the new self-consistent charge density [76]. This new charge density will be different from that of the relaxed structure and will be arranged in such a way as to oppose the change, and a second atom, b, will experience a force, $f^{+}_{mb}(l,a)$, along direction m opposing such a change. This is now repeated by displacing atom a in the opposite direction. The new forces, $f^{-}_{mb}(l,a)$, are calculated and the second derivatives to the energy, up to second order in ϵ are calculated as,

$$\nabla^2_{la,mb} = \frac{(f^{+}_{mb}(l,a) - f^{-}_{mb}(l,a))}{2\epsilon}. \tag{2.23}$$

The above only forms part of the dynamical matrix and needs to be repeated for all the atoms in the supercell. The matrix is then diagonalised to find the eigenmodes and values, they are then normalised by the square of the atomic masses of the species involved to determine the vibrational/phonon modes of the system.

2.5.2 Band structure and density of states (DOS)

The band structure shows the variation of the electronic energy levels with k [26]. This calculation is necessary to determine the energies of the occupied and unoccupied states, which subsequently allow the estimation of the energies of the photons involved in the absorption and emission due to an electronic transition in hBN. In DFT, there is no strict physical interpretation of the Kohn-Sham eigenstates and eigenvalues, ψ_k^{KS} and $\varepsilon_k^{\mathrm{KS}}$, apart from the highest eigenvalue, which can be shown to be the negative of the exact many-body ionisation potential [93, 94]. However, the variation of $\varepsilon^{\mathrm{KS}}$ with k provides a reasonable estimate of the variation of the electron energy with k and is interpreted as the band structure of a solid.

The DOS per unit energy, $g(\varepsilon^{\mathrm{KS}})$ is the number of electronic states within an infinitesimal energy range, $\Delta\epsilon^{\mathrm{KS}}$. In the implementation of DFT in this thesis, the electron density is represented by plane-waves of the form $e^{i\mathbf{k}\cdot\mathbf{r}}$, and the plane-waves have the energy $E = \frac{\hbar^2 k^2}{2m_e}$. Therefore, the integration of the charge density within a specfic energy range gives the number of electrons, and hence states, within an energy range $\Delta\epsilon^{\mathrm{KS}}$ [81].

2.5.3 Partial atomic charges

Partial atomic charges show the degree of localisation of a charge around a particular atom.

2.5.3.1 Mulliken populations analysis

The Mulliken populations analysis is a scheme used to calculate partial atomic charges of different electronic states in a system [95]. This can reveal the contribution of different atomic species to states of specific energies in the DOS. Such a projection of the DOS onto different species is known as the partial density of states, pDOS . This is implemented in AIMPRO by expanding the Kohn-Sham orbital of a band n at wavevector λ, $\psi_{n\lambda}(\boldsymbol{r}, s)$,

by a set of localised atomic orbitals, $\phi_{ni}(\boldsymbol{r}-\boldsymbol{R})$, and spin-functions, $\chi_\alpha(s)$ [76],

$$\psi_{n\lambda}(\boldsymbol{r},s)=\chi_\alpha(s)\sum_i c_{ni}^{\lambda}\phi_i(\boldsymbol{r}-\boldsymbol{R}) \tag{2.24}$$

$$M(i,n,\lambda)=\sum_s\int\psi_\lambda^2(\boldsymbol{r},s)d\boldsymbol{r}=\sum_{ij}c_{ni}^{\lambda}c_{nj}^{\lambda}S_{ij\lambda}=\sum_i m_{ni}^{\lambda}, \tag{2.25}$$

where,

$$S_{ij\lambda}=\int\phi_i(\boldsymbol{r}-\boldsymbol{R_i})\phi_j(\boldsymbol{r}-\boldsymbol{R_j})d\boldsymbol{r} \tag{2.26}$$

where, $S_{nij\lambda}$ is the overlap integral between atomic orbitals, i represents the i^{th} atomic species, n is the band index, λ is the wavevector. By collecting orbitals of specific angular momenta, l, the contribution of atomic orbitals with these angular momenta can be projected.

The pDOS is calculated as,

$$p(l,i,E)=\sum_{n\lambda}w_\lambda M(l,i,n,\lambda)\delta(E-E_{n\lambda}). \tag{2.27}$$

The weighting factor, w_λ, is associated with the k-point sampling scheme used after symmetry reduction. The delta function is replaced by a Gaussian broadening function to allow for a smoother pDOS.

2.5.4 Other methods

For the sake of completeness, other methods of calculating atomic charges are discussed briefly. Hirshfeld charge analysis works by proportionately distributing the charge densities among the constituent atoms according to their density at corresponding distances in the free-atom case. The differences in the local charge density in the free-atom and the molecular environments define the partial charges and allow the calculation of multipole moments [96]. Bader charge analysis is a different method that separates two species based on the location of the minimum in the charge density. The points in the volume corresponding to minima in charge density form a surface that separates the two regions [97]. The drawbacks of methods that allocate charge based on their spatial distributions, particularly for the case of hBN/graphene heterostructures discussed in this thesis, are described in detail in Sec. 3.3.7.

2.5.5 Calculation of Formation Energies

The formation energy of a defect in a specific charged state is defined as the following,

$$E_f(q) = E_{\text{tot}}(q) - E_{\text{host}} - \sum_i \Delta n_i \mu_i + q(\varepsilon_{\text{VBM}} + \mu_e). \tag{2.28}$$

Here $E_{tot}(q)$ is the total energy of the defective layer of hBN in a specific charged state, q. E_{host} is the total energy of pristine monolayer hBN. Δn_i is the change in the number of atoms of specific species and μ_i is the chemical potential of the species i. The formation energies were calculated in the N-rich condition specified by,

$$\mu_N + \mu_B = \mu_{hBN}, \tag{2.29}$$

where μ_N was half the total energy of an N_2 molecule. ϵ_{VBM} and μ_e are the energy of the valence band maximum (VBM) of the host and the electron chemical potential respectively. $E(q, q')$ will be used to refer to the (q, q') charge transition level (CTL) with respect to the valence band maximum. When calculating formation energies of charged defects in PBC, a fictitious interaction between the charged defects and their images in the repeated unit cells occur. This interaction has a contribution to the total energy and leads to incorrect formation energies and CTLs. The scheme used to overcome errors due to this interaction are discussed in Sec. 3.3.1.1.

2.5.6 Activation Energies

Some of the defects studied in this paper have multiple stable geometries, some of which are related by symmetry. For example, in monolayer hBN, a defect with an out-of-plane perturbation can be displaced above or below the basal plane. The defect can transition between these two sites, and this requires the defect to traverse across a potential energy surface (PES) . The path followed during the traversal is defined by an energy path. A tool used to determine this energy is the nudged elastic band (NEB) method [98]. The methodology established by Ref. [98], is briefly outlined below.

In the NEB methodology, the energy path is found by optimising a number of images between the initial and final configurations. The energy barrier for the transition between the initial and final points is known as the saddle point. The lowest energy configuration

of each image is found while maintaining an equal spacing along the reaction coordinate with neighbouring images. Naturally during the energy minimisation of each image, the images will tend to 'slide down' the potential curve towards the minimum. Therefore a spring force is added between the images to prevent sliding down.

A chain of $N+1$ images $[\mathbf{R_0}, \mathbf{R_1}, ..., \mathbf{R_N}]$ is created, with $\mathbf{R_i}$ representing the position of the i^{th} image. Throughout the optimisation, the endpoints R_0 and R_N are fixed and only the $N-1$ intermediate images are adjusted by the algorithm. There are two forces used in the optimisation process, the true force due to the potential surface and the spring force artificially added to prevent the images from sliding down. The tangential component of the force due to the energy surface being traversed and the spring force is calculated and subsequently, the component of the spring force that is parallel to the path and the perpendicular component of the true force due to the potential is projected out. Only the parallel component of the spring force is used to maintain an equal spacing between images and the perpendicular components of the true force is minimised, leading to the trajectory converging to the energy path with the lowest barrier to transition. This is known as the minimum energy path (MEP) . Thus, the spring forces do not influence the convergence of the trajectory.

The tangent at image i is determined as,

$$\tau_i = \begin{cases} \tau_i^+ \text{ if } V_{i+1} > V_i > V_{i-1} \\ \tau_i^- \text{ if } V_{i+1} < V_i < V_{i-1}, \end{cases} \tag{2.30}$$

where,

$$\tau_i^+ = R_{i+1} - R_i \text{ and } \tau_i^- = R_i - R_{i-1}. \tag{2.31}$$

Here V_i is the energy of image i. If both neighbouring images possess a greater energy or lower energy than i, a weighted average of the vectors to the adjacent images is used as the tangent, and hence is an extrema along the MEP. Energy of the neighbouring images is used to determine the weight.

If the image is at a minimum or maximum, i.e $V_{i-1} > V_i < Vi+1$ or $V_{i-1} < V_i > V_{i+1}$,

the tangent is calculated as,

$$\tau_i = \begin{cases} \tau_i^+ \Delta V_i^{\max} + \tau_i^- \Delta V_i^{\min} \text{ if } V_{i+1} > V_{i-1} \\ \tau_i^+ \Delta V_i^{\min} + \tau_i^- \Delta V_i^{\max} \text{ if } V_{i+1} < V_{i-1}, \end{cases} \tag{2.32}$$

where,

$$\Delta V_i^{max} = \max(|V_{i+1} - V_i|, |V_{i-1} - V_i|) \tag{2.33}$$

$$\Delta V_i^{min} = \min(|V_{i+1} - V_i|, |V_{i-1} - V_i|). \tag{2.34}$$

The tangent vector is then normalised. The spring force is calculated as,

$$F_i^s|_{\parallel} = k(|R_{i+1} - R_i| - |R_{i+1} - R_i|) \cdot \hat{\tau}_i. \tag{2.35}$$

The true force is given by,

$$\nabla V(\mathbf{R_i})|_{\perp} = \nabla V(\mathbf{R_i}) - \nabla V(\mathbf{R_i}) \cdot \hat{\tau}_i, \tag{2.36}$$

The position of each image is optimised at every iteration. At each iteration, the energy of each image is minimised and moved in the direction of the force towards the minimum of the PES, and the spring force acts to prevent the coalescing of the images. After the changes in the positions of the images is below a threshold, the optimisation is stopped and the positions of the images outline the trajectory of the MEP. In traditional NEB, the saddle point is found by interpolating between the highest energy images (the number of images used will depend on the order of the polynomial used for interpolation).

While interpolation works well for wide saddle points, it does not provide an accurate depiction of narrow energy barriers unless a large number of images are used, leading to an increase in computational cost. This is because few images land in the neighbourhood of the saddle point, affecting the accuracy of the inpterpolation, Fig. 2.3. Climbing image nudged elastic band (CI-NEB) is a small modification to the NEB algorithm allows a rigorous convergence to the true saddle point energy and has no additional computational cost to standard NEB [11].

In CI-NEB, the highest energy image, $i_{\max}$ is identified after a user-defined number of iterations. The force only on this image is defined as [11],

$$F_{i_{\max}} = -\nabla V(\mathbf{R_{i_{\max}}}) + 2\nabla V(\mathbf{R_{i_{\max}}})|_{\parallel} \tag{2.37}$$

$$= -\nabla V(\mathbf{R_{i_{\max}}}) + 2\nabla V(\mathbf{R_{i_{\max}}}) \cdot \hat{\tau}_{i_{\max}} \hat{\tau}_{i_{\max}} \tag{2.38}$$

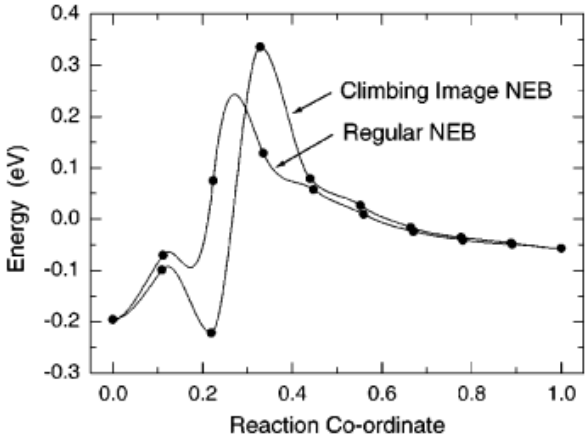

Figure 2.3: A comparison of CI-NEB and standard NEB. The MEP obtained from both calculations are for the adsorption of CH_4 on an iridium surface Ir (111). The reaction coordination, 0.0, represents the dissociated end products CH_3+H fragments and 1.0 corresponds to a CH_4 molecular 4.0 Å away. It is clear here that standard NEB leads to poor resolution of the barrier and interpolation leads to its underestimate. This is solved by CI-NEB which leads to an image being located accurately on the saddle point. This image is reproduced from Ref. 11.

From this modification, the full true force component along the elastic band due to the potential is inverted, and so the maximum energy image moves up the slope of the potential energy surface along the elastic band and also towards the MEP in the direction perpendicular to the band. Therefore the maximum energy image is unaffected by the spring force, and the remaining images define the only degree of freedom for which the maximisation of the energy is carried out.

In CI-NEB, the spacing of the images will be different on either side of the climbing image. This is because as the image moves up to the saddle point, images one side of the climbing will be squeezed together and on the other side will stretched out. However, the spacing between images within each section divided by the climbing will be constant. In this thesis, 11 images were found to be sufficient for convergence to the MEP and the climbing image was identified after 3 iterations.

2.6 Summary

In this chapter the general principles of DFT and its approximations have been discussed. The specific implementation of DFT and parameter choice were then discussed. These choices for implementation were made to allow the calculation of derived properties, such as the band structure, atomic positions, vibrational modes and activation energies. These properties will allow the determination of estimates of the ZPL energy of emitters in hBN, the defect geometry of emitters, and finally the degree of charge transfer with graphene encapsulation layers. In the next section, the results of the calculations of pristine and defective hBN and hBN/Gr heterostructures are discussed.

Chapter 3

Theoretical Results

In this chapter the results from the exploration of the pristine structures of hBN, graphene and their heterostructures are discussed. This is followed by the results of the study on charge transfer between hBN and graphene in hBN/graphene heterostructures, and finally the impact of the dielectric environment on the barrier for defect reorientation is discussed.

3.1 Pristine Structures

3.1.1 Isolated hBN

3.1.1.1 Structural Optimisation

As mentioned in Sec. 2.4, the first step that needs to be performed is structural relaxation of the system to represent an unstrained system. The experimentally obtained lattice constants are good initial guesses but may not be representative of the true equilibrium lattice constants as the system might not have been in its ground state when the measurements were made. Furthermore, the atomic positions need to be relaxed to be consistent with the particular exchange-correlation functional used in the calculations, as this can signficantly affect the bond strength, as discussed in Sec. 2.1.5.

The optimised in-plane lattice constant of hBN was calculated to be 2.514 Å, which is consistent with existing theoretical values calculated using GGA functionals [12, 89, 90, 91] and is in agreement with the experimental value of 2.504 Å at room temperature [99]. The

interlayer spacing was set to 15.89 Å (30 a.u.), which is nearly five times the experimental interlayer spacing of 3.33 Å of bulk hBN in order to effectively simulate monolayer hBN [39]. The optimised hBN structure is shown in Fig. 3.1, with the lattice constants labelled.

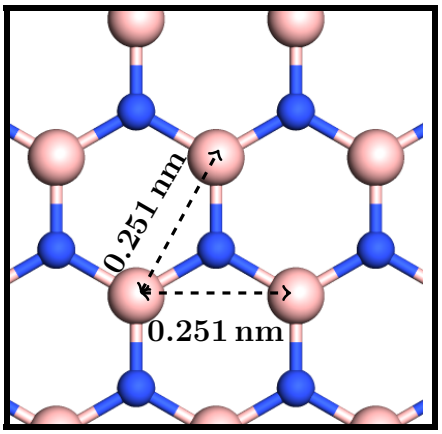

Figure 3.1: Optimised structure of a single layer of hBN. The computationally derived in-plane lattice constant is 2.51 Å. The colour schemes for the boron and nitrogen atoms follow Fig. 1.2a

3.1.1.2 Vibrational Modes

After structural relaxation, the vibrational modes were calculated according to Sec. 2.5.1. The energies of the vibrational modes have been listed in Table 3.1. hBN exibits a degenerate pair of Raman active E_{2g} modes and a non-degenerate infrared (IR) active A_{2u} mode [100, 101]. The IR mode for hBN occurs at 783 cm^{-1} and the Raman mode for bulk hBN has been experimentally observed at 1366 cm^{-1} (1370 cm^{-1} for monolayer) [20]. The intensity of the Raman peak increases in discrete jumps with the number of layers and the peak position is usually red shifted by $\sim 4\,cm^{-1}$ (as shown in Fig. 4.5) [20]. This can be used to estimate the thickness of a hBN film.

The displacement vectors for each of these modes can give us information about the nature of the vibrational mode, i.e. in-plane or out-of-plane.

From the theoretical calculations, it was found that the IR mode at 793 cm^{-1} corresponds to the out-of-plane A_{2u} motion of the atoms, Fig. 3.2c, and the last 2 modes are Raman active degenerate bending modes, Fig. 3.2a and 3.2b, which have E_{2g} symmetry. The IR mode is experimentally observed at 783 cm^{-1} and the degenerate modes are usually observed at 1366 cm^{-1} [100, 101]. The Raman modes obtained using PBE-GGA

No.	Energy (cm^{-1})	Mode
1	793	A_{2u}
2	1337	E_{2g}
3	1337	

Table 3.1: The table shows the 3 vibrational modes of the primitive unit cell calculated using AIMPRO. The 1st mode is IR active, the 2nd and 3rd modes are Raman active.

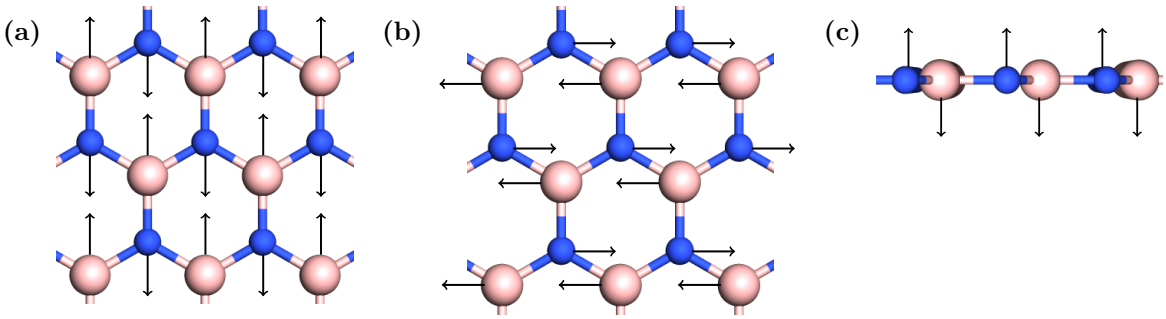

Figure 3.2: The figures show the displacements of the atoms in different vibrational modes. (a) and (b) show the degenerate E_{2g} modes, which are in-plane and Raman active. (c) is the out-of plane A_{2u} mode which is IR active. The arrows indicate the direction of displacement.

functionals have a 20–30 cm^{-1} error, [102, 103], and so the experimentally obtained values are within the uncertainty of the computed values.

3.1.1.3 Band Structure

The band structure of pristine hBN is shown in Fig. 3.4a. It has been plotted along the k-points in paths of high symmetry. hBN, graphene and its heterostructures studied in this thesis have the same type of Brillouin zone (hexagonal) and points of high symmetry, Γ, K and M. The Brillouin zone and the points of high-symmetry have been indicated in Fig. 3.3. For monolayer hBN, the conduction band minimum (CBM) lies directly above the VBM at the K point [45, 104]. The calculated band gap of 4.70 eV is significantly lower than the experimental value of $\approx$ 5.9 eV [51], but agrees within 50 meV of other theoretical calculations of the band gap using GGA functionals [12, 39, 41].

In the primitive unit cell, there are a total of 4 filled valence bands, as the total number of valence electrons is 8 and each band can host 2 electrons. The accuracy of

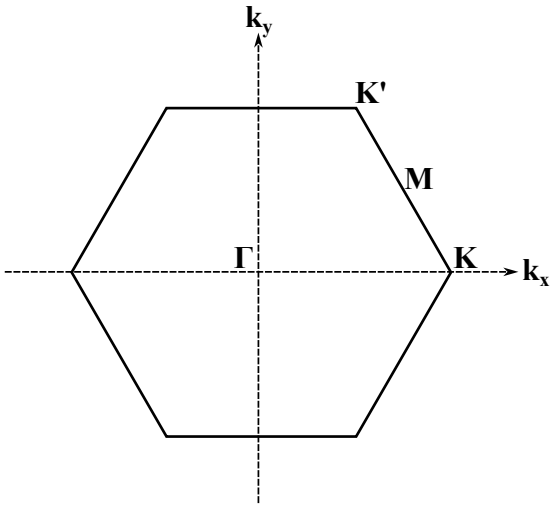

Figure 3.3: The points of high symmetry in the Brillouin zone of a hexagonal lattice. This is shared by hBN, graphene and their heterostructures.

the band structure calculation is confirmed by qualitative agreement with angle resolved photoemission spectroscopy (ARPES) measurements of the valence band structure [105].

In addition to the band structure calculations, the ionisation energy of hBN is determined to be 5.95 eV, which agrees with other work using PBE-GGA functionals [92] but is an underestimate from the HSE ionisation energy by ~ 1 eV [104].

3.1.1.4 Density of States (DOS)

The DOS complements the band structure and is useful in identifying defect states, which presents as small peaks in the band distribution. It is especially useful when distinguishing states contributed by different layers in a heterostructure, as will be discussed in a later section on the calculation of charge transfer, Sec. 3.3.1.2, between hBN and graphene. A k-point sampling density of $50\times50\times1$ and a broadening of 0.2 eV was used to obtain the DOS in Fig. 3.4b. The zero in the DOS has been aligned to the VBM. The sampling density and broadening determine the oscillatory pattern seen. A larger sampling density and an appropriate broadening can eliminate peaks arising due to oscillations.

Up to the valence band (the blue regime in Fig. 3.4b), the shape of the DOS calculated using AIMPRO agrees well with literature, Fig. 3.4c, [12, 106, 107]. The key features of the DOS, such as the $\sim$ 10 eV bandwidth of the upper valence bands, and $\sim$5 eV

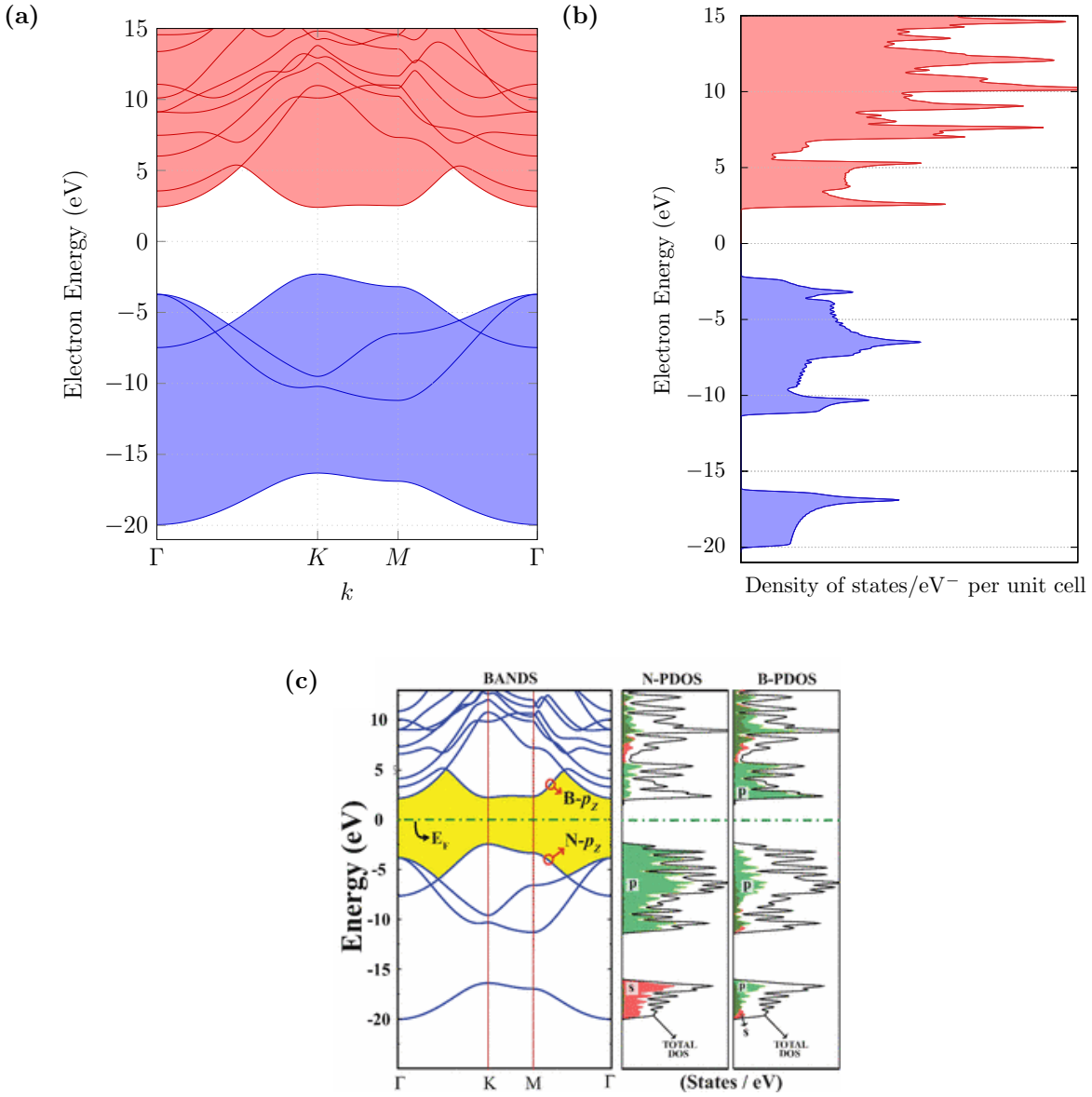

Figure 3.4: **(a)** Calculated band structure of hBN in the vicinity of the Fermi energy along high-symmetry branches of the Brillouin zone. Blue and red lines represent nominally occupied and empty bands, respectively, with the underlying shading highlighting the envelopes of the valence and conduction bands. The zero on the energy scale is set at the midpoint of the band gap in pristine hBN to allow a more direct comparison with the band structure in Ref. 12. **(b)** The total DOS of hBN, with the filling of occupied and empty states following that of the band structure. **(c)** The total DOS of hBN as well as the partial density of states for each atomic species in hBN calculated by Ref. 12.

bandwidth of the lower valence bands, agree with the literature [12, 107, 108]. The sharp and narrow valence bands in hBN are characteristic of two dimensional materials with strong intralayer bonding [108].

The oscillatory pattern seen in the DOS calculation by Ref. [12], Fig. 3.4c, is attributed to a differences in the sampling density. The difference in DOS at energies high in the conduction band DOS calculated using AIMPRO and the literature is due to the augmentation of the basis in vacuum in the AIMPRO to model the evanescent decay of the charge density present into the vacuum above the hBN sheet to be modelled with greater accuracy, which is not required in the calculations of Ref. 107 and [108] where plane-wave basis sets were used.

3.1.1.5 Partial Density of States (pDOS) using Mulliken Populations Analysis

The covalently bonded hBN crystal has electronic states that show different degrees of localisaton around B and N atoms. While there is no principled method of allocating charge to an atomic species in a crystal system, it is useful to understand the spatial distribution of electronic states around specific species. This allows the determination of the contribution of each atomic species to an electronic state of interest. This is highlighted in the results chapter in Sec. 3.3, where the contribution of hBN and graphene to defect states in the heterostructure is evaluated. Another application is in the understanding of the nature of the band edges of the pristine material.

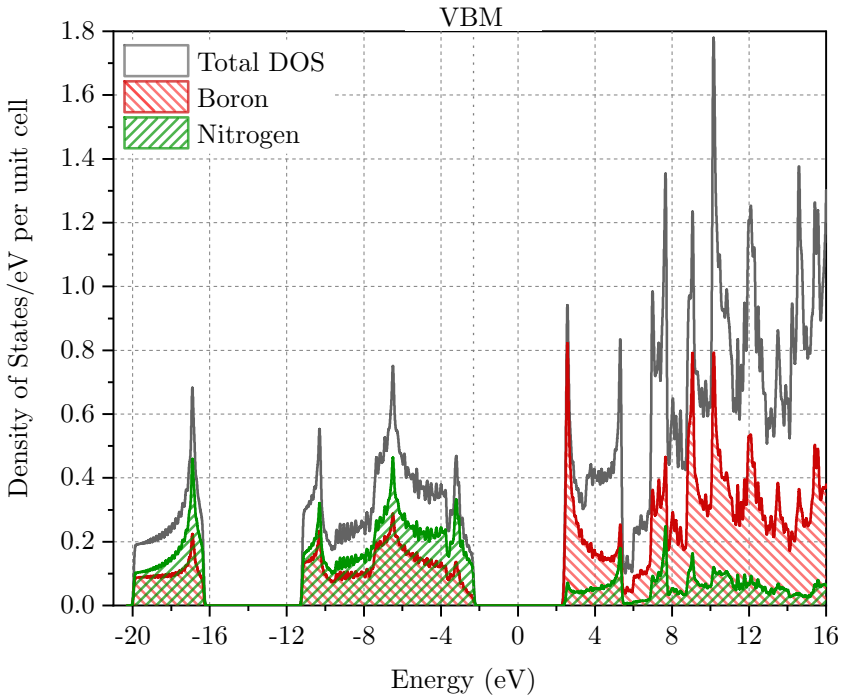

Figure 3.5: The partial density of states for each atomic species is shown, along with the total density of states for the hBN monolayer (grey line). The N (green hatched filling) and B (red red hatched filling) contributions have been indicated. The zero in the energy scale is set to the mid point of the band gap and the position of the valence edge has been indicated by a dotted grid line labelled 'VBM'.

The calculated partial density of states, with a k-point sampling grid of $50 \times 50 \times 1$, and broadening of 0.1 eV is shown in Fig. 3.5.

Based on Fig. 3.6, it can be seen that the electronic states in the VBM have a greater contribution by N than B and the states in the CBM have a greater localisation at the B atom than the N atom, in agreement with existing literature [12, 104]. It is important to note this interpretation is basis set dependent. For example, Mulliken analysis on a DFT calculation performed with an entirely N centered basis set leads to all the states appearing to be localised at the N atom, which would not be the case. The localisation of the electron can also be interpreted in terms of the lifetime of the electron in a specific state. If the majority of states in an energy range is localised around a particular atomic species, it can be interpreted as the electron spending a greater amount of time at the location of these species compared to the vicinity of the other species.

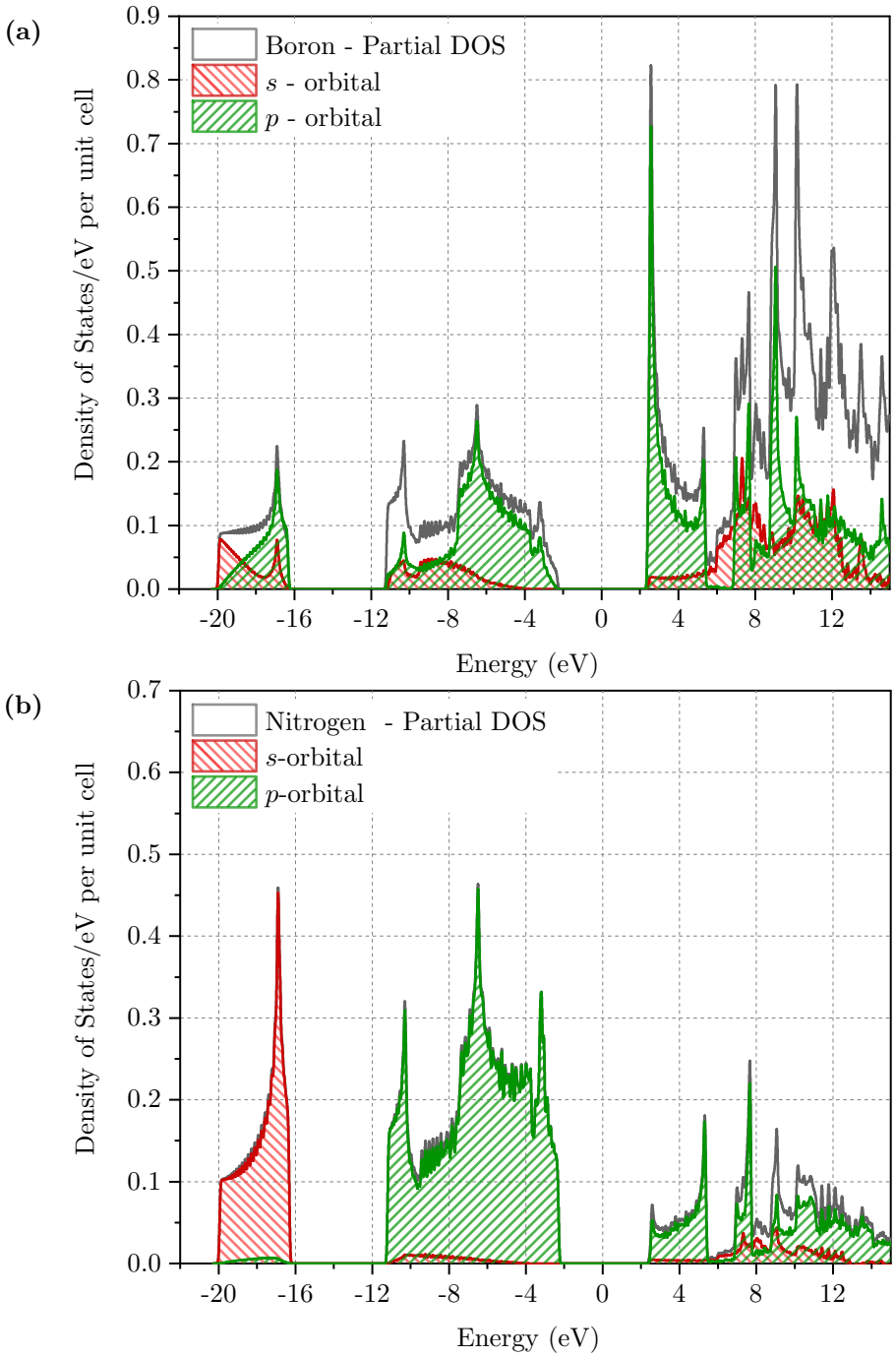

Figure 3.6: (a) Shows the pDOS calculated using the Mulliken populations analysis for B atoms. The contribution of the s (red) and p (green) orbitals are shown. (b) Corresponding pDOS for N atoms. The zero in the energy scale is set to the mid point of the band gap.

Comparing Fig. 3.6a and 3.6b with Fig. 3.4c shows that the angular momentum projections agree well with literature. The strongly bound orbitals deep in the valence band

are dominated by s orbitals localised at N. The states higher up in the valence band are dominated by p orbitals from B. The small peak in the s and p orbital contributions at low energies, seen more clearly in the pDOS for B, indicate sp_2 hybridisation of orbitals. The observation in Fig. 3.7 of the valence band edge states being mostly contributed by the p_z orbitals centered around N atoms and the conduction band edge states being mostly contributed by p_z orbitals centered around B atoms are supported by literature [12, 104]. This reveals that the electron in the p_z orbital of N gets transferred to the p_z state of B [107] when excited across the band gap.

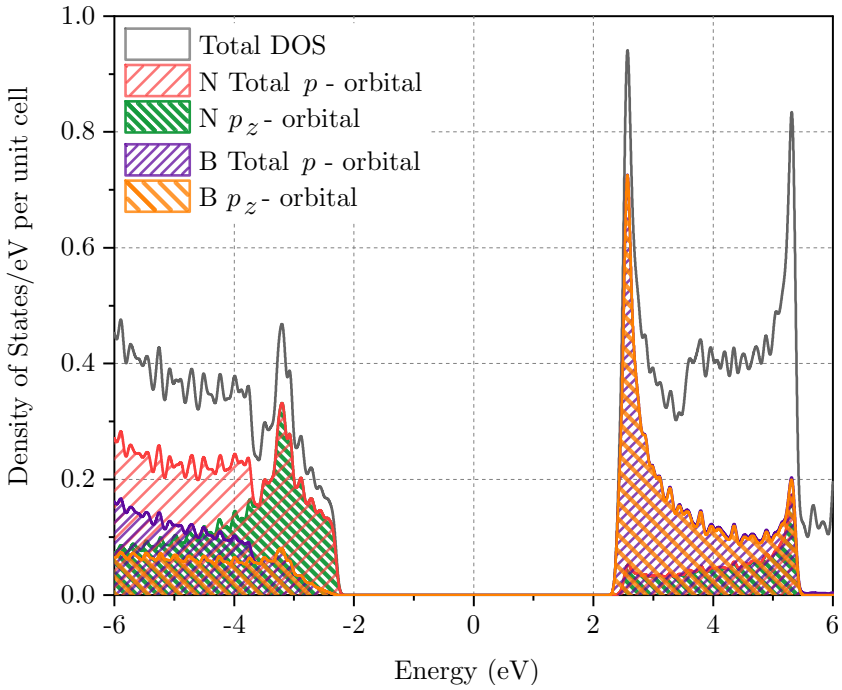

Figure 3.7: The contributions of s and p_i, where $i = x, y, z$, obtained from Mulliken analysis is shown by the different hatched shading. The zero in the energy scale is set to the mid point of the band gap.

3.1.2 Graphene

As hBN/Gr heterostructures are studied in this thesis, it is important to identify the correct parameters needed to model the graphene layer. Experimental measurements indicate that graphene has an in-plane lattice constant of 2.46 Å [39]. It is a semimetal and the conduction band and valence band meet at the Dirac point at the K point [109].

3.1.2.1 Structural Optimisation

The equilibrium lattice constant of monolayer graphene was calculated to be 2.47 Å in agreement with the experimental value of 2.46 Å [39]. The slightly larger lattice constant is due to the underbinding of GGA functionals, as was the case with hBN. The structure of graphene is shown in Fig. 3.8. As with hBN, a large interlayer spacing was set (15.89 Å) to simulate a monolayer. As the lattice constants differ by only ∼2% and the crystal type is the same, the strain induced on either layer in a heterostructure is expected to be small.

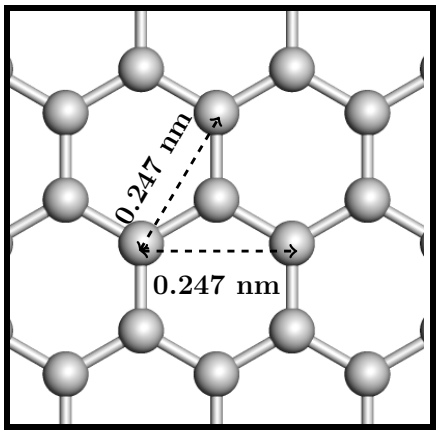

Figure 3.8: Optimised structure of a single layer of graphene. The lattice constant is indicated by the dashed arrows. Gray spheres represent carbon atoms.

3.1.2.2 Band Structure and Density of States

The band structure calculations reproduced the well known Dirac point at the K point, Fig. 3.9a. The DOS, Fig. 3.9b, for graphene was obtained using a denser sampling grid of $75 \times 75 \times 1$ and the same broadening of 0.1 eV. This was done to ellucidate the linear dispersion at the Dirac point, which would be more difficult to observe with a lower sampling density that results in oscillations in the DOS. At the Dirac point there are no states available for the electron to occupy and is reflected with the DOS being zero at this point. Existing literature using DFT, tightbinding and other techniques are in agreement with our calculations [110, 111, 112, 113]. The DOS calculations is linear near the Dirac point and increases with an increase in energy difference from the Dirac point.

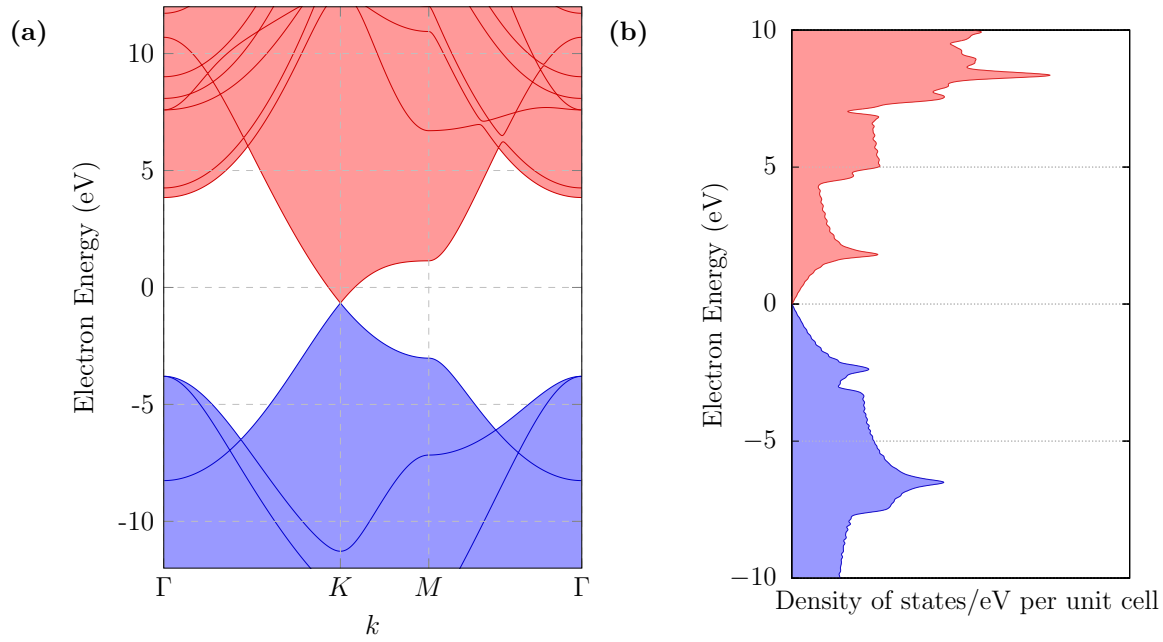

Figure 3.9: **(a)**The band structure of the primitive unit cell of pristine graphene. **(b)** The DOS of pristine monolayer graphene. Colours and shading follow Fig. 3.4. The zero in the energy scale is set to the Dirac point of graphene.

3.1.3 hBN/graphene Heterostructure

The AA-stacking and AB-stackings have been used in this project. In the AA stacking the boron and nitrogen atoms lie directly above the carbon atoms in graphene, Fig. 3.10a. As monolayer hBN and graphene have different in-plane lattice constants, a decision regarding the treatment of the lattice-constants for heterostructures needed to be made. The approach of using a fixed value obtained from the optimisation of the in-plane lattice constant for the combined system was adopted as this lead to a compromise in the degree of strain induced in each layer. Without vdW interactions, Sec. 2.3.2, the in-plane lattice constant was determined to be 2.49 Å for each layer and the interlayer distance is 4.2 Å. The introduction of vdW forces does not affect the in-plane lattice constant, but reduces the interlayer distance to 3.34 Å, Fig. 3.10a. This is a 21% reduction in the interlayer space of the non-dispersion corrected calculation and it is therefore necessary to explicitly include this interaction in the DFT calculations of multilayered structures. The value of 2.49 Å represents a 1% compressive and tensile strain for hBN and graphene, respectively.

From Fig. 3.12 and Fig. 3.11, it can be seen that the band structure and DOS (obtained

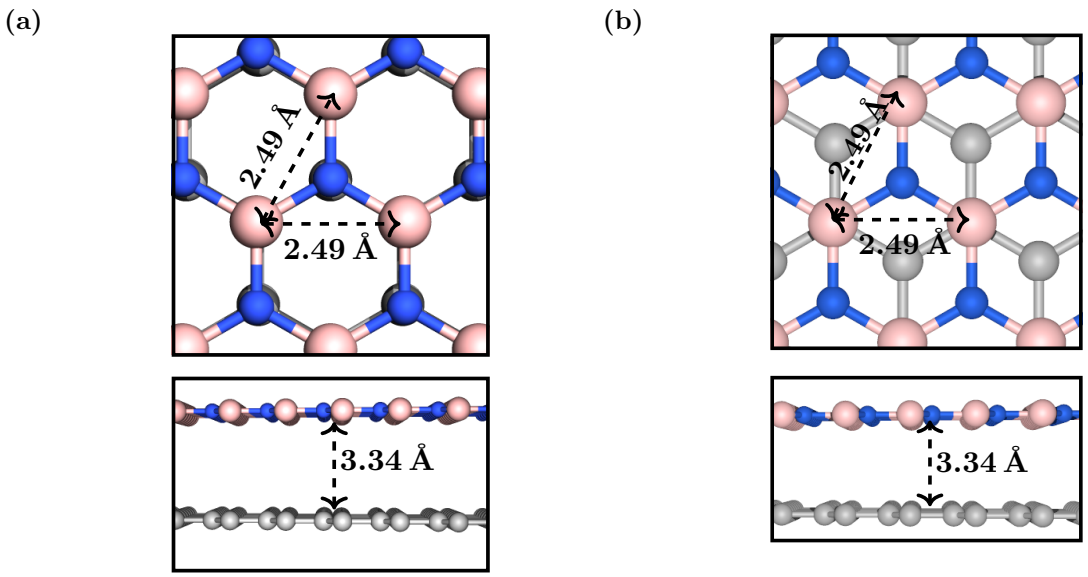

Figure 3.10: Plan view (top) of the relaxed structure of the hBN/Gr heterostructure and the side view (bottom) in **(a)** AA stacking and **(b)** AB′ stacking. The colour schemes for atoms follow Fig. 1.2a and Fig. 3.8.

using a sampling density of $50 \times 50 \times 1$ and a broadening of 0.1 eV) of the heterostructure is similar to a superposition of the band structures and DOS of the individual layers. At the Dirac point, the DOS of hBN/Gr (solid lines) is almost entirely contributed by Gr (dotted lines), and a mixture of hBN (dashed) and graphene contributions occur beyond the linear regime of the graphene DOS. This forms the motivation for the DOS method of determining charge transfer in Sec. 3.3.1.2. The misalignment of peaks in the DOS of isolated hBN and Gr, deep in the conduction band with respect hBN/Gr can be attributed to the weak electric field that exists in the heterostructure due to a lack of a horizontal mirror plane. This affects the evanescent decay of the conduction band states, leading to the misalignment.

The inclusion of vdW forces on the band structure is shown in Fig. 3.12. The band structures are largely similar, except for the opening of the band gap at the K point present in Fig. 3.12b is not present in Fig. 3.12a. The band structure near the Dirac point is magnified in Fig. 3.12c and 3.12d to clearly highlight the opening of a band gap of

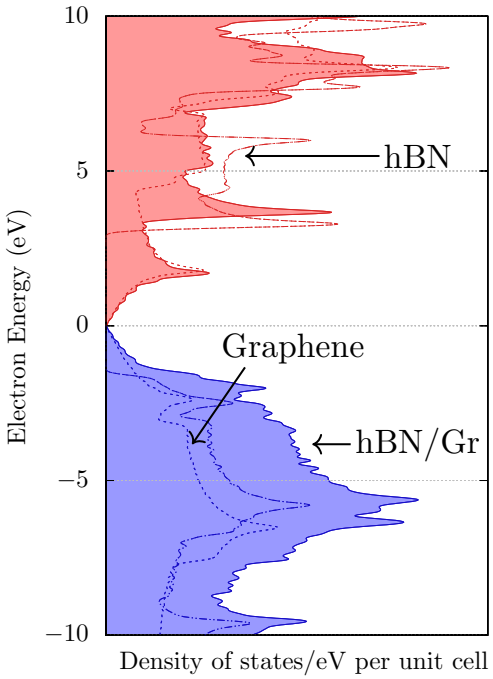

Figure 3.11: The DOS of the hBN/Gr structure (solid lines with filling), with the DOS of graphene (dotted) and hBN (dashed) monolayers superimposed for comparison. The arrows indicate the respective DOS to aid the reader. The zero point in the energy scale is the Dirac point of isolated graphene. Colours and shading follow Fig. 3.4.

0.1 eV, which is on the same order of other first-principles of band gaps in monolayer hBN/Gr heterostructures [111, 114]. It has been speculated in literature that the opening of the band gap is due to a decrease in the overlap of the π bonds in graphene due to Pauli repulsion [114]. The large interlayer spacing when vdW forces are excluded lead to a significantly smaller electronic wavefunction overlap than when vdW interactions are included, leading to a negligible band gap.

In the AB′ stacking, boron atom superimposes a carbon atom and the nitrogen atom exists at the centre of the carbon ring in the underlying graphene, Fig. 3.10b. There is no change in the lattice constant between the AA and AB′ stackings and the interlayer spacing remains the same as well. The band structure for AB′ stacking, Fig. 3.13, largely resembles that of the AA stacking, Fig. 3.12. The band gap in AB′ stacking is ∼0.04 eV, within the range of existng first-principles calculations of hBN/Gr band structures [111, 114]. Although the band gap in hBN/Gr is sensitive to the stacking, its impact

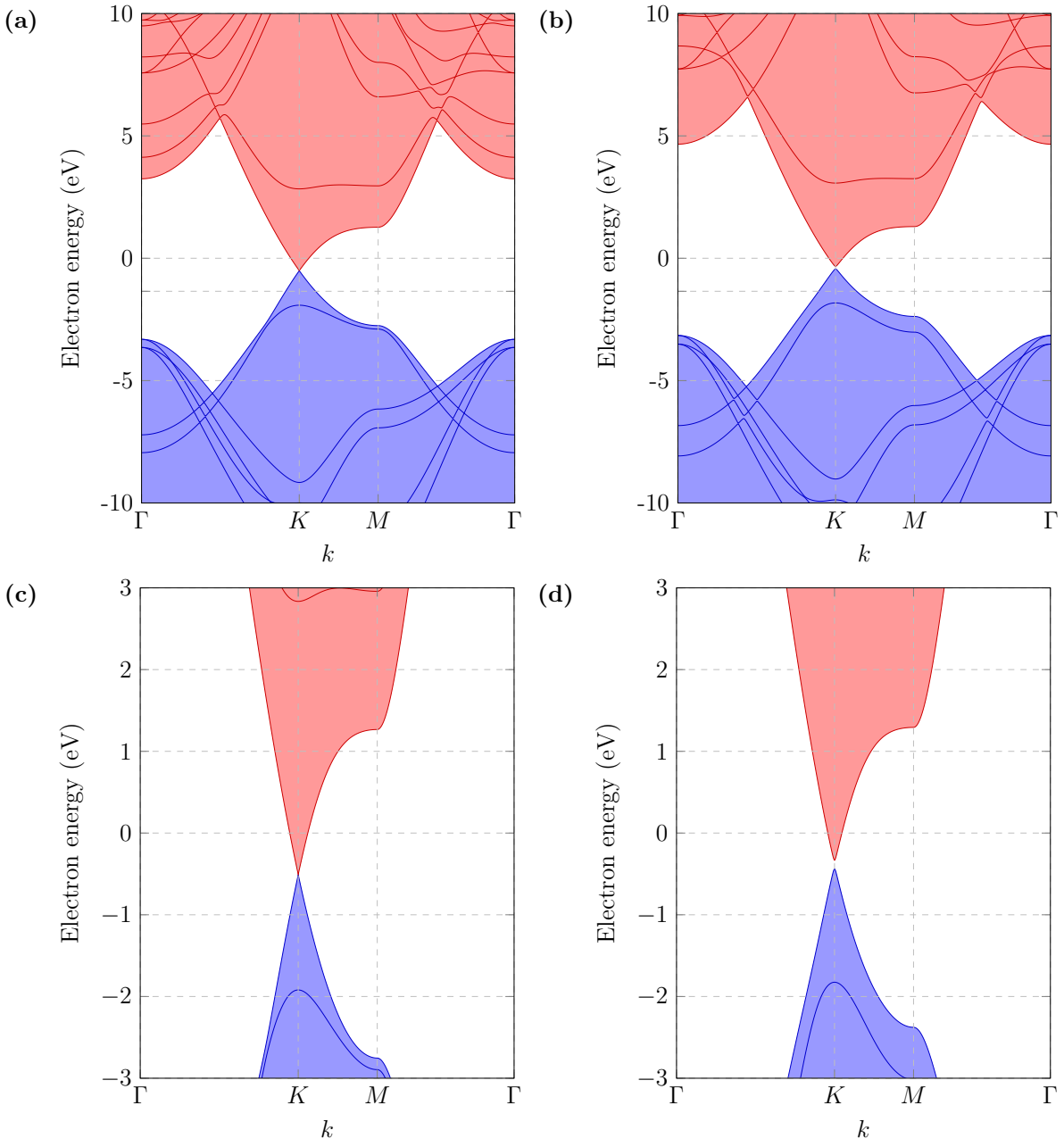

Figure 3.12: The band structure of the heterostructure **(a)** without and **(b)** with vdW forces. **(c)** and **(d)** show the same band structures as **(a)** and **(b)** respectively, but with the region near the Dirac point magnified to highlight the band gap when vdW forces are included. The zero point in the energy scale is the Dirac point of isolated graphene. Colours and shading follow Fig. 3.4.

is not significant when compared to the effects studied in this thesis. In experiment, the mismatch in the lattice constant of hBN and graphene results in a Moiré period and

there is spatial variation in the stacking of the two layers [115]. Therefore, both forms of stacking can exist in the material.

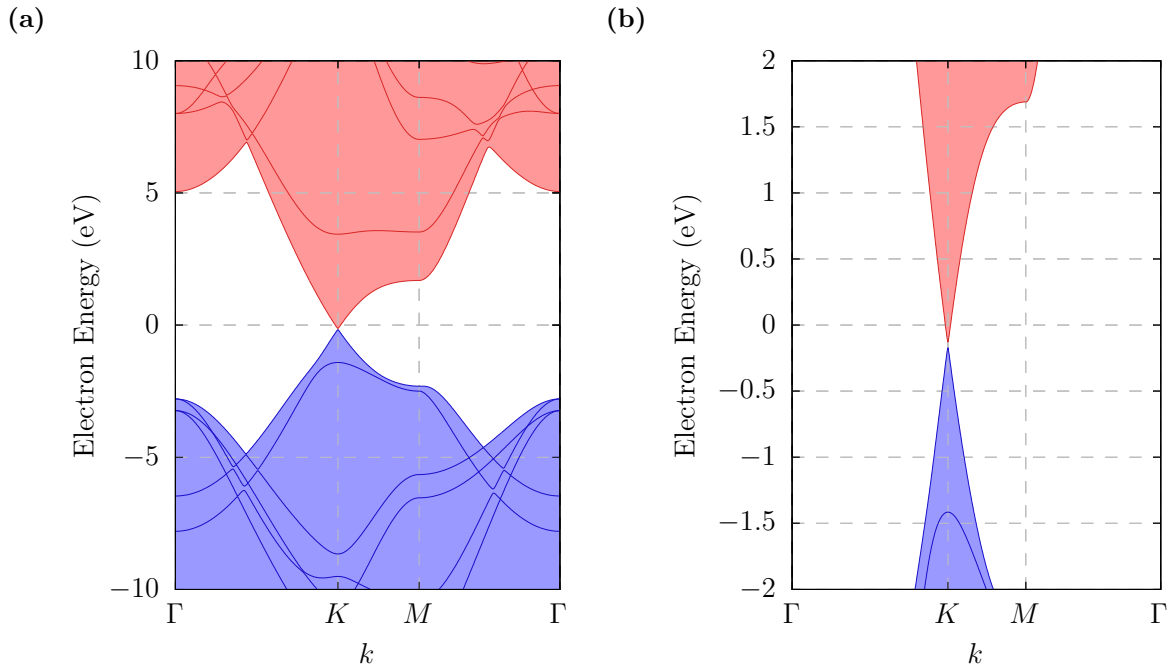

Figure 3.13: **(a)** The band structure of the heterostructure in the AB′ stacking. **(b)** The same band structures with the region near the Dirac point magnified to highlight the band gap when vdW forces are included. The zero point in the energy scale is the Dirac point of isolated graphene. Colours and shading follow Fig. 3.4a.

3.2 Summary

In this section, an overview of the properties of pristine monolayer hBN, graphene and hBN/Gr have been discussed. The properties that have been explored include structural properties such as lattice constants, vibrational modes and interlayer spacings in heterostructures. It has also been shown that the hBN/Gr structure has a graphene layer under tensile strain and a hBN layer under compressive strain of 1% each. The importance of the inclusion of dispersion forces to obtain an accurate interlayer spacing has also been discussed. Furthermore, the electronic structures of hBN, graphene and hBN/Gr have been illustrated through band structure and DOS calculations. It has been shown

that the individual layers of the composite structure remain largely similar to their isolated cases in terms of electronic structure apart from the opening of 0.1 eV band gap at the Dirac point. It is now possible to study the defective cases with reference to these properties and use these systems as building blocks when exploring complex few layer hBN and graphene heterostructures.

3.3 Charge transfer and defects in hBN

Having studied the properties of pristine monolayer hBN, graphene and their heterostructures in Sec. 3.1 as a reference point, the properties of hBN and hBN/Gr heterostructures hosting defects can now be explored. The introduction of a defect leads to a change in the band structure, and depending on the type of defect, the electronic energy levels associated with the defect can lie within the band gap of hBN or the bulk bands. Although the scope of this project is on the general control of colour centres in hBN, in this section particular emphasis is given to defects that can act as sources of single-photon emission. This is not only because of the large interest in the application of colour centres in hBN to quantum photonic technologies, but also because the study of single emitters that lead to at least one occupied and one empty band within the band gap of hBN, can be a building block for the study of complex defect structures and ensembles.

A range of defect properties were calculated. Electronic structure calculations were performed to get an estimate of the ZPL energy, which can be used to screen candidate emitters by comparing them to observed ZPL energies in hBN. The ground state defect arrangement, such as the point group symmetry of the defect, and spin state allow the determination of allowed transitions of the defect and if the defect is a paramagnetic centre. Properties such as the formation energies of the defects were calculated, as they correspond to concentration of the defect in hBN under equilibrium conditions. The greater the formation energy, the lower the defect concentration under equilibrium conditions. The CTLs were also determined from the formation energies, allowing prediction of the preferred charge state of the defect as a function of the chemical potential of electrons in the environment. In this chapter, the defect properties are explored in the context of isolated monolayer hBN, multilayer hBN, and hBN/graphene (hBN/Gr) heterostructures. The work in this chapter expands on the work conducted by the author of the thesis in the journal article and conference proceeding published in Refs. 116 and 117, respectively.

3.3.1 Boron Vacancy - V_B

V_B is created by the removal of a single boron atom, leaving behind a vacancy in its place. In agreement with previous studies, the optimised ground-state structure for V_B^0 has C_{2v} symmetry, arising from a Jahn-Teller distortion [118, 119]. This occurs as two of the nitrogen atoms surrounding the vacancy move further apart and the third nitrogen moves along the prinicple axis towards the two opposite nitrogen atoms.

Two non-degenerate defect levels in the vicinity of the band gap in each spin channel in the neutral charge case was found, Fig. 3.14b, which agrees with previous modelling [118]. For the majority spin, the lower, occupied band is resonant with the top of the valence band and an unoccupied band is within the band gap. The corresponding spin-minority bands are both unoccupied and within the band gap. In the negative charge state, the higher symmetry leads to a doubly degenerate unoccupied spin-down band deep in the band-gap, and an occupied degenerate state close to $\varepsilon_{\mathrm{VBM}}$ that mixes with the valence band states, resulting in a multitude of defect related bands around this energy.

V_B acts as an acceptor [120] with the -1 charge state found to be a spin-triplet with D_{3h} symmetry, whereas the neutral and -2 charge states are doublets with C_{2v} symmetry, in agreement with literature [118, 120, 121]. The formation energies of the defect and its CTLs were also calculated, using Eqn. 2.28, as shown in Fig. 3.15.

3.3.1.1 Correction of Formation Energies Of Charged Defects

To determine the CTLs of a defect, the formation energies of charged defects need to be calculated. However, DFT calculations exploiting periodic boundary conditions suffer from interaction between charged defects and their periodic images and divergence in total energy due to systems with a net charge. The latter is solved by the addition of a neutralising background charge. However, the Coulomb interaction between the defect and its periodic images still exists and contributes to the total energy. As the strength of Coulomb interaction depends on the separation of the defects and degree of screening between the defects, the contribution to the total energy has a cell size dependence. Traditional correction techniques involve calculating the formation energies at different cell sizes and extrapolating the formation energy to the infinitely dilute limit [122, 123].

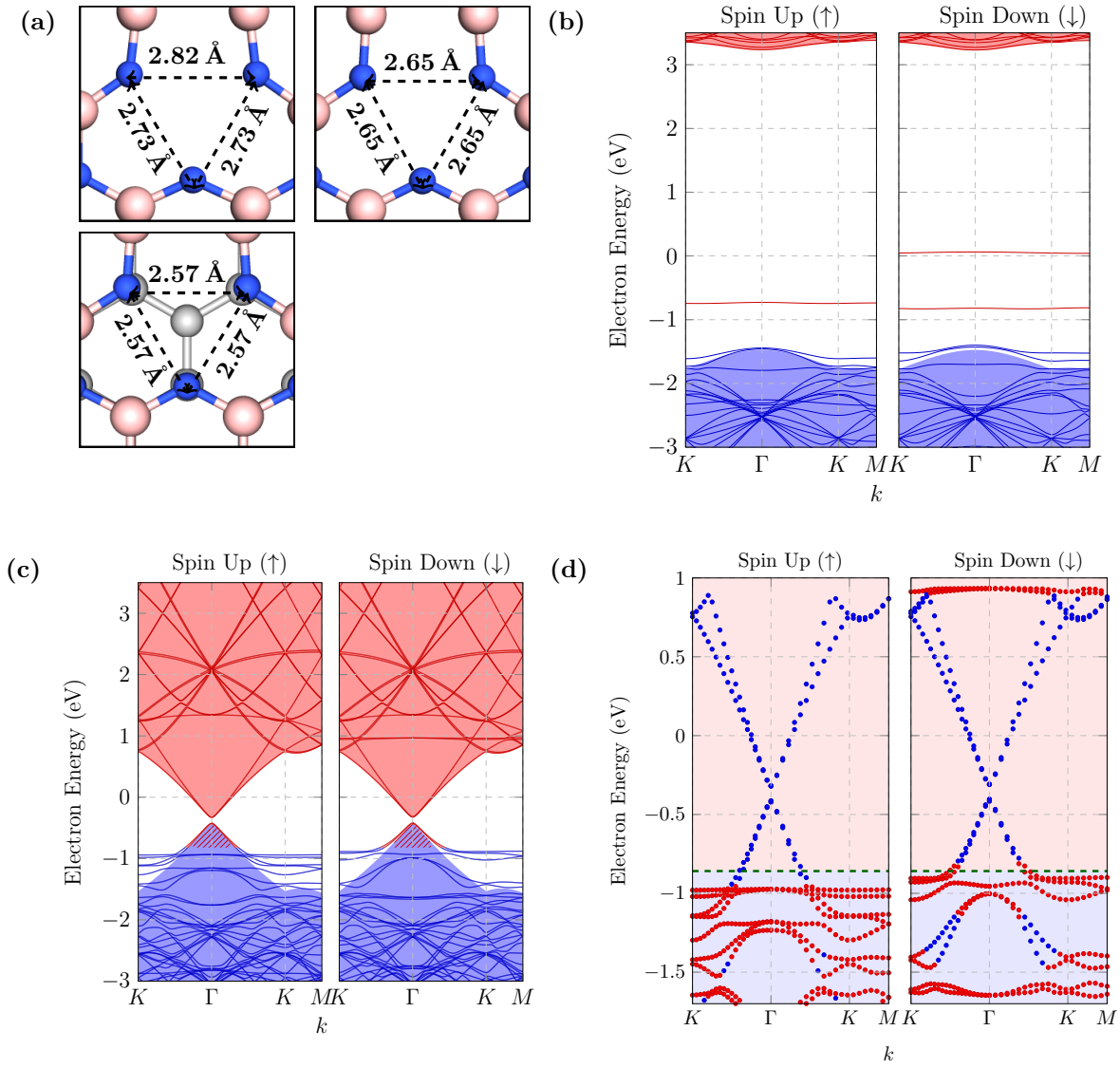

Figure 3.14: **(a)** The structure of of V_B. The band structures of **(b)** V_B^0 in isolated hBN. Colours and scales are as in Fig. 3.4a. **(c)** Band structure of V_B in hBN/Gr. The hatched shading in **(c)** indicates the filling of the graphene bands up to the Fermi level, with the underlying shading indicating occupied and empty bands of the corresponding pristine hBN/Gr for comparison. **(d)** the localisation of the electronic states in either hBN or graphene based on Mulliken populations analysis. The red (blue) dots correspond to electronic levels with a greater (lesser) localisation in hBN than graphene.

While the scaling scheme for cell sizes has minimal impact on isotropic bulk materials, charged defects in anisotropic materials, like monolayer hBN, are screened in-plane and unscreened across vacuum and so care needs to be taken when varying the supercell

dimensions to calculate the energies used for extrapolation [124, 125].

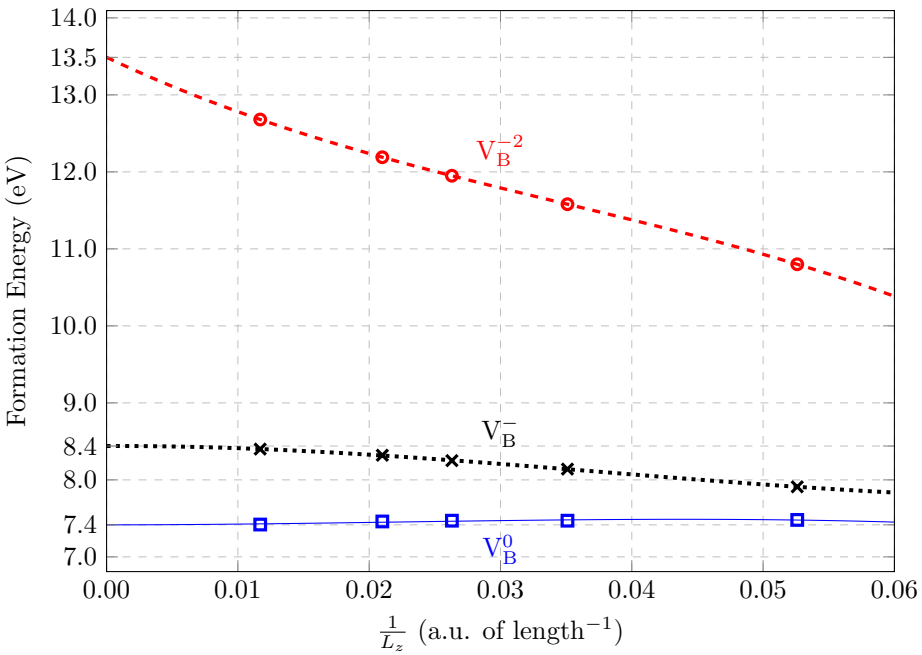

Figure 3.15: The figure shows the extrapolation of the formation energies of V_B^q, with $q = (0, -1, -2)$, calculated as a function of cell size. The smallest cell corresponds to the 4×4 case and the larger cells are obtained by uniformly scaling in all dimensions. A cubic polynomial fit is performed to the energies to obtain the formation energies at the infinitely dilute limit.

It was found that a reliable extrapolated formation energy could be obtained by a uniform scaling procedure [125, 126]. This involves setting the in-plane lattice constant equal to the inter-planar distance during the scaling process. The reliability of the correction scheme is demonstrated by comparing the extrapolated formation energies of different charge states of the boron vacancy, Fig. 3.15, with existing literature which have employed different correction schemes. The range of cell sizes used for extrapolation are, $4a \times 4a, 6a \times 6a, 8a \times 8a, 10a \times 10a$ and $18a \times 18a$. The cell sizes used in the extrapolation of the formation energies are consistent across all defects in this study. The extrapolation was performed with a cubic polynomial function, and the error in the formation energies is of the order of 0.1 eV [126]. As only defects with low charged states considered, the maximum charge being $|2e|$, it was found that the uncertainty in the valence band position due to the artificial electrostatic field from the charged defect was negligible.

An extrapolated value of $E_f(\mathrm{V_B}, 0) = 7.4\,\mathrm{eV}$ was obtained, which agrees with the literature value of 7.4 eV [118].

Previous studies (Ref. 120) indicate $\mathrm{V_B}$ is a triple acceptor. The values obtained for the single and double acceptor levels at 1.0 eV (4.9 eV below vacuum) and 5 eV agree with literature [92, 120]. The triple acceptor level is known to be very close to the conduction band and so is unlikely to participate in charge transfer with graphene, hence it was not included in the current calculation. As the calculated $(-/0)$ level of $\mathrm{V_B}$ in pristine hBN is below the work function of graphene, it may be expected to be thermodynamically favourable for an electron to be transferred from graphene to hBN.

3.3.1.2 Determination of charge transfer

Figure 3.14c shows the band structure of $\mathrm{V_B}$ in the heterostructure. The localisation of bands (Fig. 3.14d) obtained by Mulliken analysis of partial atomic charges supports the association of the relevant bands to hBN. The equilibrium geometry of $\mathrm{V_B}$ in hBN/Gr changes from C_{2v} to D_{3h}, which is the symmetry of $\mathrm{V_B^{-1}}$ in monolayer hBN. This change of geometry is consistent with charge transfer having taken place and the difference in the interatomic distances is attributed to the reduction of the lattice constant of the hBN layer when interfaced with graphene.

It was of interest to determine the quantity of charge that was transferred between graphene and hBN, as this can illuminate whether a covalent bond has been formed between graphene and hBN or if there was a whole electron transfer similar to an ionic interaction.

Quantification of charge transfer was approached in two ways. The first was by integrating the DOS of the heterostructure from the electron chemical potential, μ_e, to the small band gap induced by the formation of the heterostructure. Fig. 3.16a shows how this allows the determination of charge transfer. When the defect level corresponding to the empty acceptor level is below the Dirac point, electrons are transferred from the filled states near the Dirac point to the empty level. The μ_e of the system is then determined by the location of the empty defect level. As such the integral of the DOS depleted from the band gap to the μ_e above the Dirac point corresponds to the charge transferred to

the hBN acceptor level. The integral of the DOS, which determines the amount of charge transferred from graphene to hBN, n_h, is calculated using Eqn. 3.1,

$$n_h = 2\int_0^\infty g(E) f_h(E) dE, \tag{3.1}$$

where $g(E)$ is the density of states per unit energy for an energy E and $f_h(E)$ is the Fermi-Dirac distribution for hole occupancy and is given by,

$$f_h(E) = 1 - f_e(E) \tag{3.2}$$

$$f_e(E) = \left(1 + \exp\left(-\frac{E - \mu_e}{k_B T}\right)\right)^{-1}, \tag{3.3}$$

where $f_e(E)$ is the Fermi-Dirac distribution for electron occupancy. In the implementation of AIMPRO, this reduces to counting the number of k-points in the Brillouin zone corresponding to the empty states, weighted by their multiplicity (the number of k-points equivalent by symmetry). This is given by,

$$n_h = 2\sum_j^{n_E} \sum_i^{n_k(E_j)} \Omega_i f_h(E_j), \tag{3.4}$$

where Ω_i is multiplicity of each k point with the electronic energy, E_j. The sums are carried over the total number of bands pre-defined in the calculation, n_E, and total number k-points sampled for each energy, $n_k(E_j)$.

For the case of donor defects in hBN, charge is transferred from hBN to the empty states above the band gap in graphene. To determine the degree of charge transfer, the difference between the integral of all electronic states up to μ_e and the integral of all states up the band gap energy is calculated. This difference reflects the number of electrons transferred to the graphene layer. Then,

$$n_e = 2\left(\sum_j^{n_E} \sum_i^{n_k(E_j)} \Omega_i f_e(E_j) - \sum_j^{n_{\mu_E}} \sum_i^{n_k(E_j)} \Omega_i f_e(E_j)\right) \tag{3.5}$$

where n_{μ_E} is the total number of energy levels up to μ_e.

The second method involves spatially allocating charge density obtained from the DFT calculation to hBN and graphene. This was done by dividing the space between the two materials according to the location of the minimum in the average charge density in each

plane, as shown in Fig. 3.16b. The charge density was calculated at points determined by a uniform mesh in the volume of the supercell. The minimum was found by fitting a cubic polynomial to the three nearest neighbours to the minimum data point. A uniform mesh density which was sufficient to converge the total charge in the supercell to $10^{-2}e$ was used. The total charge in each half of the system is the difference between the integrated electron density and the ion charges of each half. The degree of charge transfer is the difference between the total charge of each layer in the heterostructure and the isolated case of the same layers.

For both methods, the degree of charge transfer is also compared with the favoured direction of charge transfer predicted by position of the CTLs relative to the work-function of graphene.

As will be discussed in greater detail in Sec. 3.3.7, charge transfer calculated by the DOS method was chosen to be the preferred value. Briefly, the method involving the spatial allocation of charge leads to an underestimate and the degree of charge transfer calculated using the DOS and the magnetic moment of the system converged at the same rate with cell size, unlike charge transfer calculated from the integration of charge density. This is due to the misallocation of the tails of charge density arising from the evanescent decay of states away from hBN (graphene), past the separation plane into the volume of the cell attributed to the graphene layer. Henceforth, the stated value of charge transfer corresponds to the value obtained using the DOS method.

For V_B , calculation of the total charge for each layer using the DOS method confirms the transfer of a whole electron and the magnetic moment of the defect was found to be $2\mu_B$. This value was significantly larger than the degree of charge transfer and magnetic moment reported in Ref. 127, where a spatial discrimination of charge density was used to calculate the degree of charge transfer.

While V_B has not been attributed to be a source of single-photon emission, it has gained significant interest as an optically addressable spin qubit in its negatively charged state [4]. Hence, graphene can act as a suitable substrate to favour defect to exist in its negative charged state.

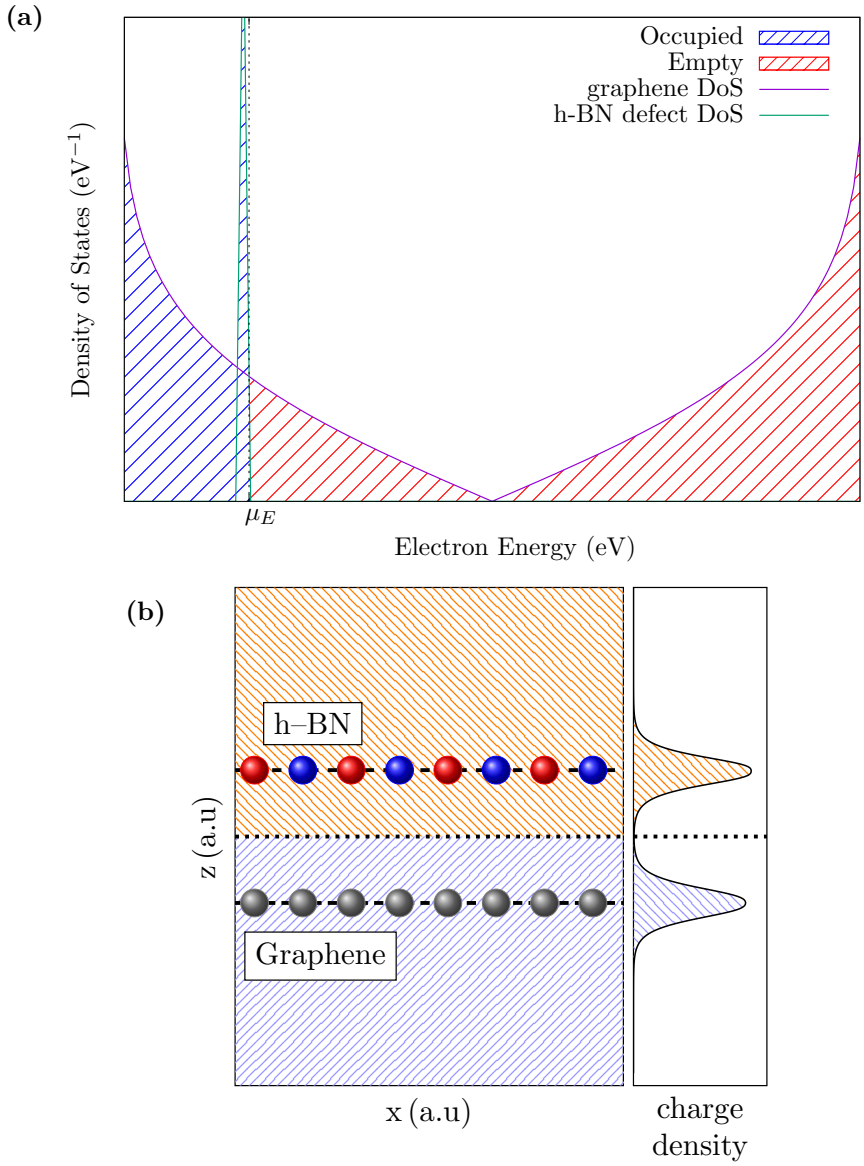

Figure 3.16: **(a)** Illustrative DOS of hBN/Gr with a defect in the hBN layer. The purple line represents the DOS almost entirely contributed by graphene and the green line represents the delta peak that corresponds to defect in hBN. The region between μ_E and the Dirac point (or the small band gap induced) is integrated to obtain the degree of charge transfer. **(b)** An illustration of the variation of the charge density averaged over the xy plane as a function of z. The minimum in the average charge density is chosen as the location of the separation plane.

3.3.2 Nitrogen Vacancy - V_N

The removal of a single nitrogen atom results in a nitrogen vacancy. It was found that V_N^{+1}, V_N^{-1} and V_N^0 all possess D_{3h} symmetry and favour low spin states, which is in agreement

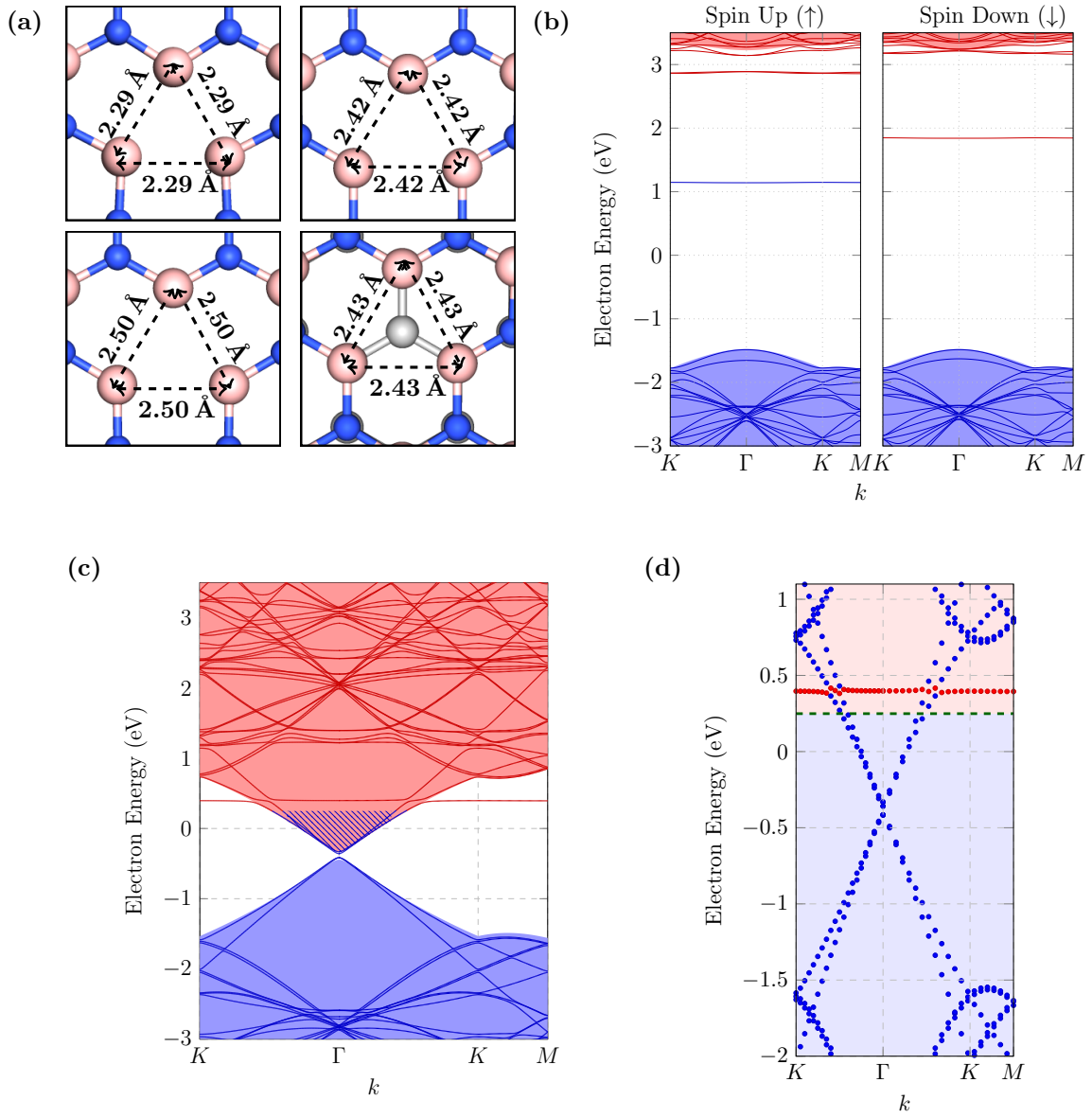

Figure 3.17: **(a)** Plan-view schematics of V_N^0 (top left) and V_N^{+1} (bottom left) in isolated hBN, V_N^{+1} in monolayer hBN with the in-plane lattice constant of that of the heterostructure (top right), and V_N in hBN/Gr heterostructure (bottom right). **(b)** Band structure of V_N in isolated hBN. **(c)** Band structure of V_N in hBN/Gr. **(d)** Localization of the bands to hBN or graphene based upon Mulliken populations. Colours and scales of the band structures are as in Figs. 3.4a, 3.14c and 3.14d respectively.

with literature [118, 120, 128]. The defect in the neutral charge state is a spin doublet and is a singlet in its singly charged states. The removal of the nitrogen atom leads to three states in the band gap of each spin channel, also in agreement with literature [118]. In

the spin-up channel, there is a degenerate unoccupied state close to the conduction band and a singly-occupied non-degenerate level ∼2.5 eV above $\varepsilon_{\mathrm{VBM}}$. In the heterostructure, the corresponding gap-level is depopulated.

Although a transition between the unoccupied defect states and the occupied defect state in the spin up channel has an energy of ∼ 2.1 eV which lies within the spectral range of emitters in hBN, earlier studies of the defect have discovered that the transition is forbidden by symmetry [2]. This makes it an unlikely candidate for single-photon emission.

The heterostructure system favours a singlet state, corresponding to $\mathrm{V_N^+}1$ and a non-magnetic configuration of a partially occupied Dirac cone (Fig. 3.17c). To further illustrate the association of the bands near the Fermi energy with the defect, Fig. 3.17d shows the same band structure where each state is denoted as hBN or graphene based upon Mulliken populations: red circles indicate bands more localised in the hBN layer and blue circles indicate bands more localised in the graphene layer. Therefore, it is clear that the defect level is localised in hBN. The impact of charge transfer is seen in the increase of the interatomic distances between the boron atoms surrounding the vacancy, Fig. 3.17a. The bottom left image shows the interatomic distances of the positively charged $\mathrm{V_N}$ in isolated hBN, and the top right image shows the interatomic distances of $\mathrm{V_N^+}1$ also in isolated hBN but with the lattice constant set to that of the heterostructure. This results in the interatomic distances resembling that of the defect in the heterostructure (bottom right image), showing that the difference in interatomic distances is predominantly due to the impact of strain in the heterostructure.

The calculated (0/+) level is 1.9 eV, placing it 4.0 eV below vacuum. (−/0) lies at 3.9 eV, which is 2.0 eV below vacuum. Both levels lie above the work-function of graphene, and are in good agreement with previous calculations [92, 129].

Energetically, the location of the (0/+) level suggests electron transfer to the graphene layer should occur, consistent with the band structure and spin state. Furthermore, the calculated net charge of the defective hBN is $+e$ in the heterostructure, indicating that a whole electron was transferred to the graphene layer. The structure of the defect in the heterostructure is similar to $\mathrm{V_N^{+1}}$ in isolated hBN (Fig. 3.17a), consistent with charge

transfer.

3.3.3 Nitrogen Antisite - N_B

The replacement of a boron atom by a nitrogen atom results in the nitrogen antisite, N_B. In monolayer hBN this centre favours a spin-doublet in its uncharged state and a singlet in the positive charge state. Neutral N_B possesses an occupied non-degenerate level deep within the band gap, Fig. 3.18b (left). The antisite nitrogen atom moves out-of-plane resulting in C_{3v} symmetry, Fig. 3.18a. As this does not happen for the positively charged case (the defect remains co-planar with the hBN, yielding D_{3h} symmetry), a change in geometry is expected if charge transfer involving donation of an electron were to take place. The single defect level in the band gap makes N_B unable to act as a two-level system and contribute to single-photon emission in hBN. Emission involving delocalised energy levels, such as those in band edges, lead to emission spectra with a large linewidth. This is not found in experiment suggesting that the emission is between two localised levels in the band gap.

In hBN/Gr the band structure (Fig. 3.18c) shows the occupied defect band to lie in the band gap, and the antisite nitrogen atom moves out of the hBN plane. This is consistent with the electrical levels determined for the antisite: the (0/+) level of N_B is calculated at 0.9 eV, which is 5.0 eV below the vacuum, in agreement with literature [92], and hence the ionisation energy of the defect exceeds the work function of graphene. Thus it is energetically unfavourable for this defect to donate any charge to the neighbouring graphene. Indeed, no change in the total charge was calculated in each layer and the geometry closely resembles the C_{3v} neutral charge state. It is therefore concluded that under equilibrium conditions N_B does not donate or accept charge with graphene.

3.3.4 Boron Antisite - B_N

The results for the boron antisite, B_N are discussed. Like its nitrogen counterpart, it exists in a spin singlet ground state in its neutral charge state and as a spin doublet in its ionised state. The introduction of the defect into hBN leads to three states in the band gap. A doubly-degenerate band occupied band lies close to $\varepsilon_{\mathrm{VBM}}$, and a non-degenerate

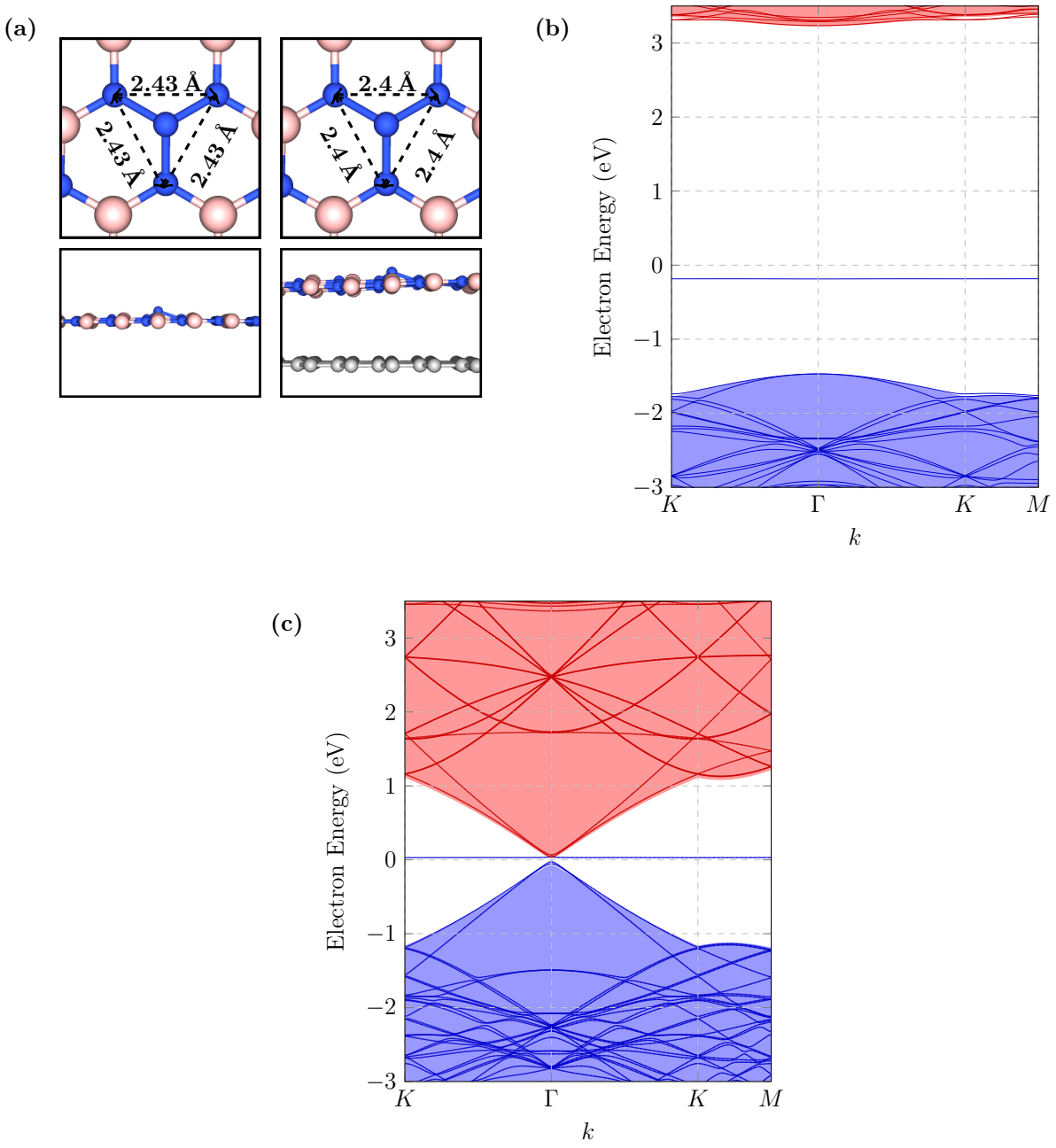

Figure 3.18: **(a)** The structure of N_B in hBN (left) and hBN/Gr (right). Band structure of N_B in **(b)** hBN and **(c)** hBN/Gr. Colours and scales of the band structures are as in Figs. 3.4a and 3.14c respectively.

unoccupied band lies mid-gap (Fig. 3.19b). The defect possesses C_{3v} symmetry. This is due to the boron atom moving out-of-plane whilst the interatomic distances between the nearest neighbour nitrogen atoms remain equal. The boron atom also causes the surrounding atoms to slightly move out-of-plane leading to curvature in the structure

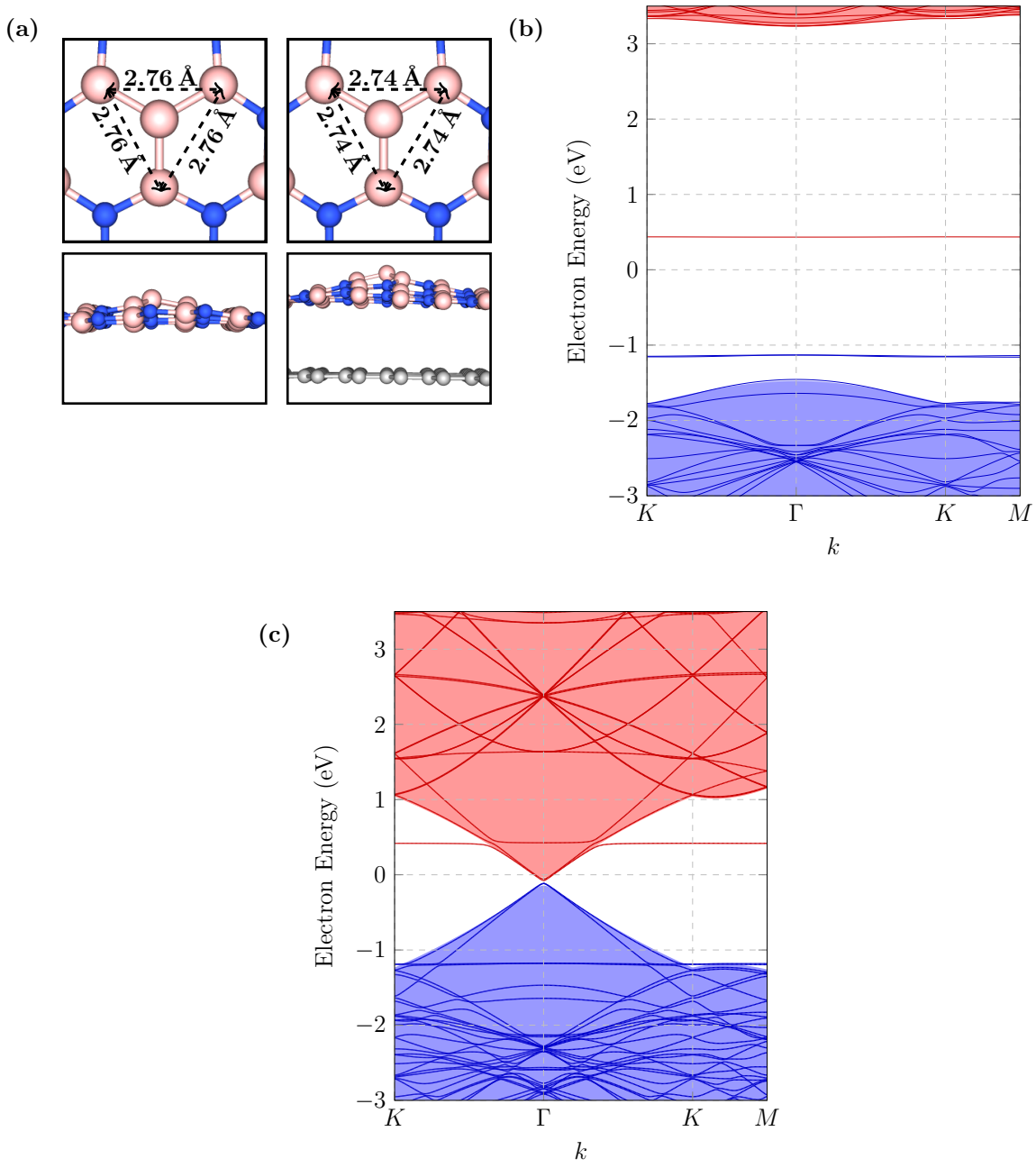

Figure 3.19: **(a)** The structure of B_N in isolated hBN. The band structure of B_N in **(b)** isolated hBN and **(c)** hBN/Gr. Colours and scales of the band structures are as in Figs. 3.4a and 3.14c respectively.

around the vicinity of the antisite, as indicated in Fig. 3.19a.

In hBN/Gr the occupied states corresponding to B_N lie below the small induced band gap at the Dirac point (Fig. 3.19c, right) and the empty state lies above it, so the band structure indicates charge transfer to be unlikely. This is supported by the calculation

of the CTLs of the defect. The $(-/0)$ level for B_N is calculated to be 2.8 eV, i.e. 3.1 eV below vacuum, placing the acceptor level well above the work function of graphene. These values of CTLs are consistent with literature [92, 120], and the lack of charge transfer is confirmed by the integrated DOS showing negligible change in total charges on the two layers.

An electronic transition between the occupied and unoccupied defect states would have an energy of ∼1.6 eV. Although this lies in the observed spectra of ZPLs, the high formation energy of the boron antisite (9.2 eV), makes it unlikley to exist in significant concentrations in hBN, rendering it less likely to be a candidate single-photon emitter when compared to the other defects explored in this study.

3.3.5 Substitutional Carbon Nitrogen Vacancy Complex - C_BV_N

C_BV_N is formed when a carbon atom substitutes for a boron atom adjacent to a nitrogen vacancy. The ground state structure of the defect is a spin singlet, with C_s symmetry due to the out-of-plane movement of the carbon atom, Fig.3.20a. A mirror plane perpendicular to the hBN plane exists, which passes through the carbon atom and bisects the reconstructed bond between the two boron atoms neighbouring the vacancy.

The introduction of this defect leads to three non-degenerate defect levels in the band gap, Fig. 3.20d, with only the lowest non-degenerate level occupied. C_BV_N has gained significant interest in the research community for being a likely source of visible single-photon emission. From the band structure it can be estimated that the ZPL transition energy is $\sim$ 2 eV, which lies in the experimentally observed range of zero phonon lines. Although the ground state is a spin singlet, studies have found that a subset of the experimentally observed spectra resemble that of a spin triplet state more closely. The triplet state of C_BV_N is approximately 0.6 eV higher in energy, has a planar structure with C_{2v} [130], Fig. 3.20c, and ZPL transition energy of 1.5 eV. Hence, intersystem crossing following an electronic excitation process, such as photoexcitation, could lead to the defect being in the triplet state [65, 128, 130]. Furthermore, as many defects in hBN show Stark shifts in response to vertical electric fields across the hBN plane [65, 131], they must possess a component of the electric dipole that is out-of-plane. This observation suggests

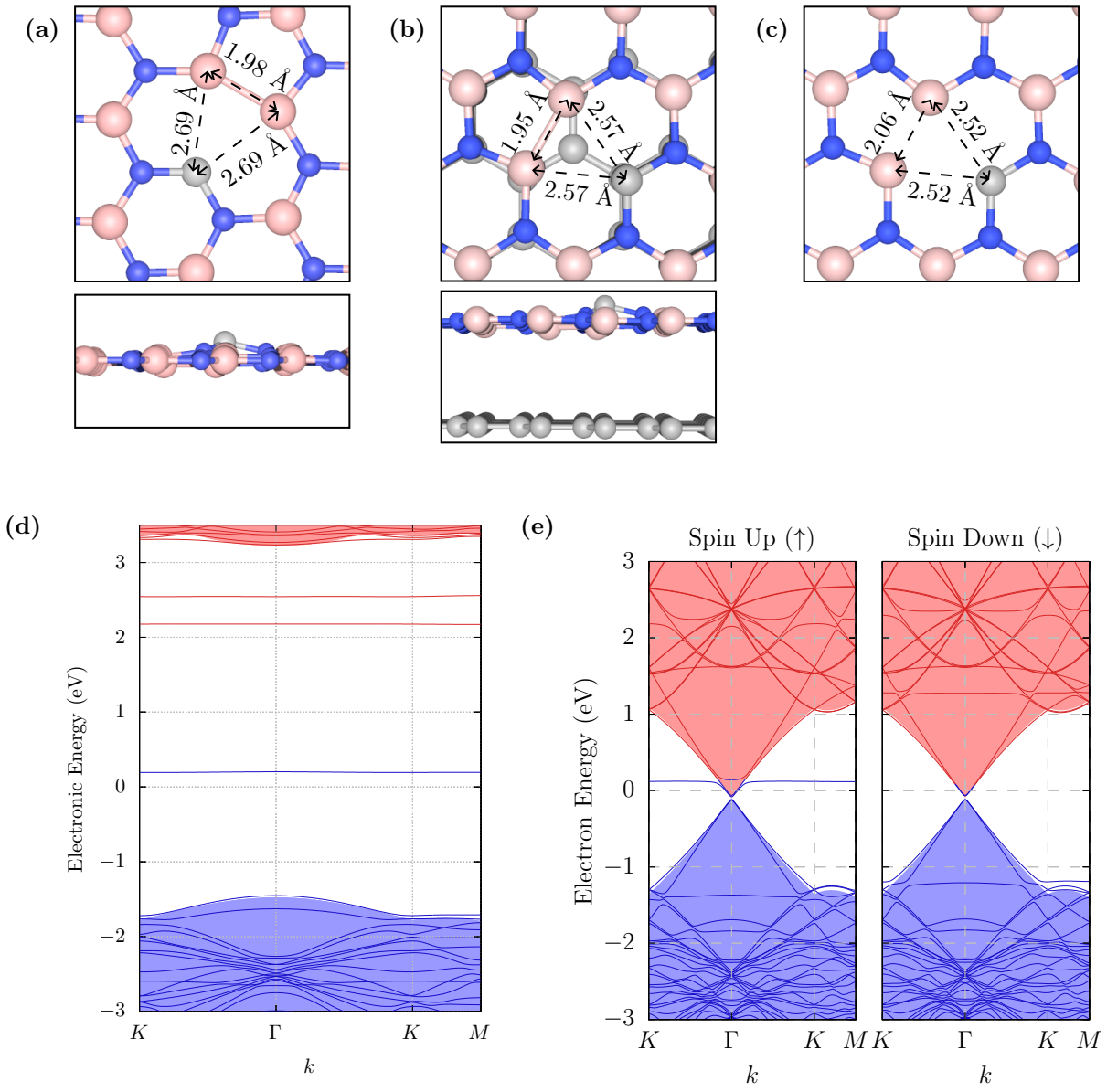

Figure 3.20: The structure of C_BV_N in the singlet state in **(a)** hBN and **(b)** hBN/Gr. (c) Structure of C_BV_N in the triplet state in hBN. The band structure of C_BV_N in the singlet state in **(d)** hBN and **(e)** hBN/Gr. Colours and scales of the band structures are as in Figs. 3.4a and 3.14c respectively.

that despite the large Huang-Rhys factor of the singlet state, it cannot be ruled out as a candidate SPE.

The defect in its positively charged form is a spin doublet with C_{2v} symmetry and in its negatively charged state is a doublet with C_s symmetry. The formation energies of the $C_BV_N^0$ (C_s), $C_BV_N^+$ (C_{2v}) and $C_BV_N^-$ (C_s) are 7.3 eV, 6.5 eV and 11.9 eV respec-

tively. Hence, the donor level of C_BV_N is 0.8 eV and the acceptor level is 4.6 eV from the valence band edge of hBN. This places the donor (acceptor) level below (above) the Dirac point in hBN, which lies 1.6 eV above the valence band edge when aligned to a common vacuum potential. The band structure is shown in Fig. 3.20e, where the electronic level corresponding to that introduced by the defect is located in the band gap of the heterostructure. However, as the band gap of hBN/Gr is on the order of 10 meV, which is below the uncertainty of electronic energy calculations of DFT, it is not possible to predict if charge transfer will occur from the band structure alone. Explicit calculations of degree of charge transfer using the DOS show that there is no change in the charge state of either the hBN or graphene layer. Comparing the structure of the defect with, Fig. 3.20b and without the graphene layer, Fig. 3.20a, the symmetry of the defect remains the same and the reduction in C−B distances can be attributed to the reduction in the in-plane lattice constant of hBN in hBN/Gr. Explicit calculations of the degree of charge transfer, defect structure and the location of the donor level relative to the Dirac point suggests that charge transfer is not expected in this system with graphene.

3.3.6 Antisite Nitrogen Boron Vacancy Complex - N_BV_N

N_BV_N is formed when a nitrogen atom substitutes a boron atom with a neighbouring nitrogen vacancy. It was found that N_BV_N has C_s symmetry in the ground state and possesses the same symmetry operations as C_BV_N (Fig. 3.21a), in a spin doublet state agreeing with recent DFT calculations, [16]. Early calculations predicted a planar structure, [65, 132]. In this study, it was found that this was indeed higher in energy than the planar structure by 60 meV in the dilute limit. In Fig. 3.21c, three in-gap defect levels in both spin channels can be observed. In the spin up channel, there are two occupied and an empty state and vice versa in the spin down channel. The electronic energy levels are non-degenerate by symmetry and the ZPL can be estimated to be ∼2 eV. This is within the range of emission wavelengths found in experiment and so N_BV_N can be a candidate emitter.

Majority of the literature on this defect have focused on the planar form the defect [65, 133]. Although the energy separation of ∼ 2 eV between the highest occupied and

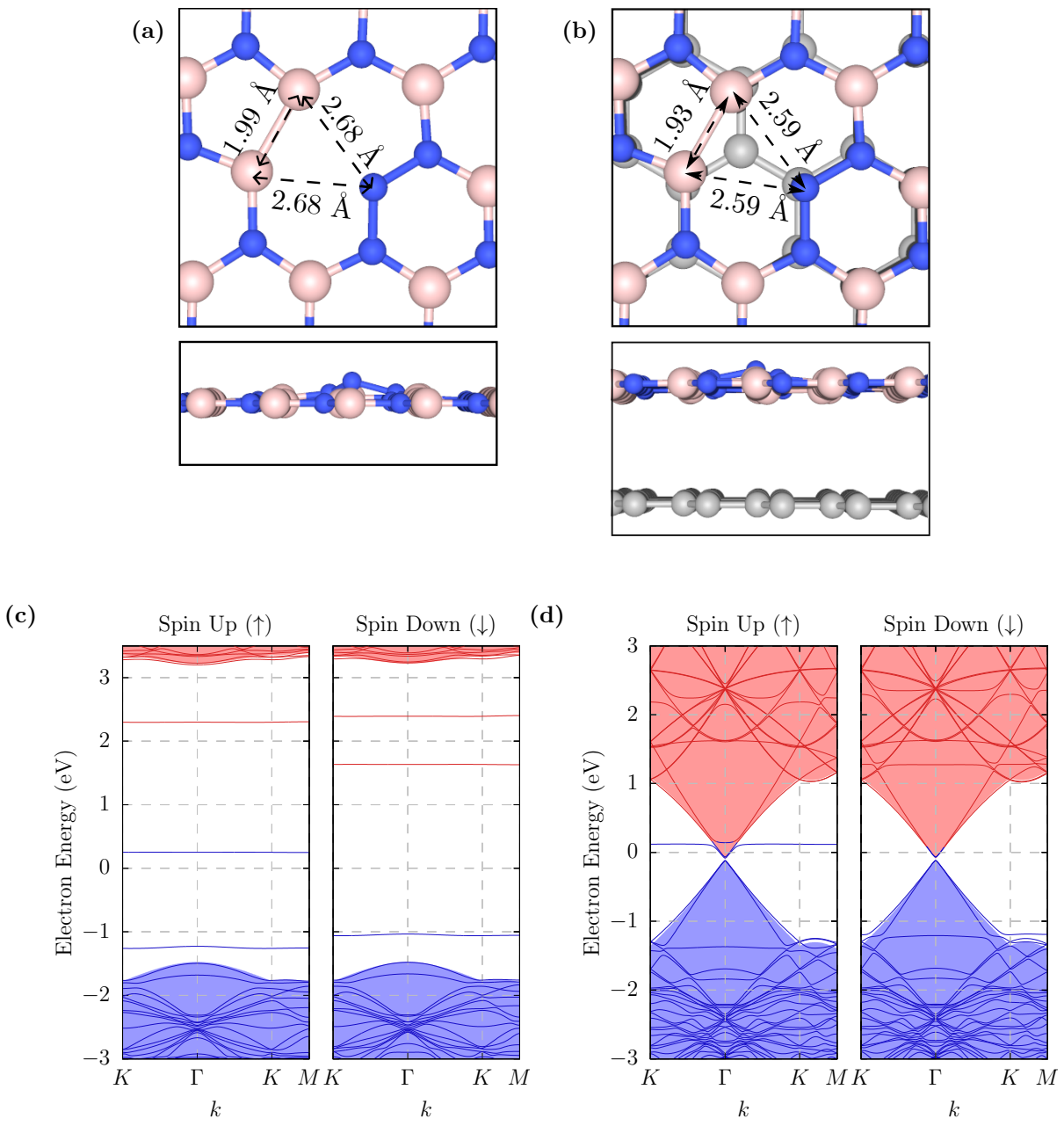

Figure 3.21: The structure of the N_BV_N in **(a)** hBN and **(b)** hBN/Gr. The band structure of N_BV_N in **(b)** hBN and **(c)** hBN/Gr. Colours and scales of the band structures are as in Figs. 3.4a and 3.14c respectively. The zero in the energy scale is set to the work function of graphene after alignment to a common vacuum potential.

lowest unoccupied defect levels of the planar configuration is in the range of experimentally observed ZPLs and hence has been suggested in existing studies to be a candidate single-photon emitter [2], other theoretical studies on the degree of phonon coupling of the defect

reveal that it has a S_{HR} not observed in experiment [130]. Spectroscopic studies on the defect where the nitrogen atom is perturbed out-of-plane does not seem to exist in current literature and is worth exploring as defects with a permanent dipole perpendicular to the hBN plane can be controlled with a vertical electric field via Stark effect.

Calculations of CTLs suggests the donor level of $\mathrm{N_B V_N}$ is 0.7 eV above the hBN VBM, which places it well below the Dirac point in the dilute limit. Explorations in literature show that the acceptor level is close to the conduction band edge of hBN and is therefore unlikely to accept charge from graphene [130, 133]. As such, no charge transfer is expected. Calculations of band structure show that the highest occupied defect level in the spin up channel, Fig. 3.21d, is slightly above the Dirac point. This is leads to $0.15\,e^-$ being transferred to graphene, based on explicit calculations of charge transfer. This appears to have a negligible impact on the defect geometry, with it largely resembling the geometry of the neutral charge state in isolated hBN. The small amount of charge being transferred could be due to the effect of finite cell size, as the donor level of a smaller cell may be closer to the conduction band edge than in the infinitely dilute limit. Therefore, by considering the location of the CTLs in the dilute limit, the negligible amount of charge being transferred to graphene, the proximity of the defect state to the band gap and the negligible change to the defect geometry, it is concluded that charge transfer to graphene is not expected for this defect.

3.3.7 Discussion

In this section the impact of different DFT parameters on the degree of charge transfer is elaborated upon and the interpretation of the position of the CTLs relative to the work-function of graphene is discussed alongside charge transfer quantification to gain a deeper understanding of the process.

It is informative to compare charge transfer across the defects studied. The CTLs of the defect in isolated hBN with respect to the Dirac point of graphene is a good predictor of the propensity for charge transfer. The CTLs of the antisites are such that there is an energy cost for charge transfer to occur, whereas for vacancies it is thermodynamically favorable for charge transfer to occur as the donor (acceptor) state lies above (below) the

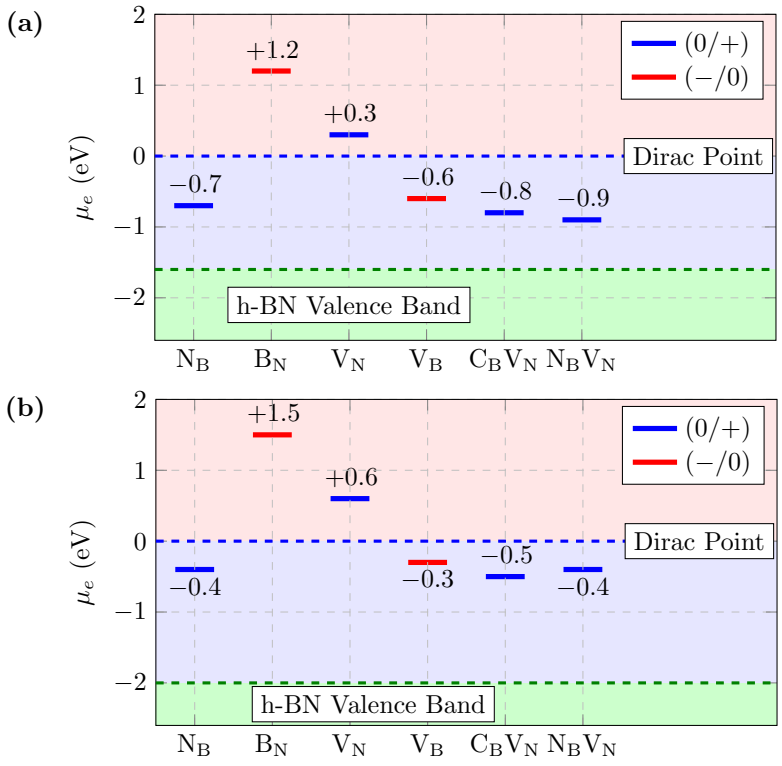

Figure 3.22: Charge transition levels of defects studied in this report, calculated using (a) PBE-GGA functional, relative to the calculated work function of graphene, and (b) HSE CTLs, relative to the experimental work function of graphene. HSE [13, 14] and experimental work functions are indistinguishable on this scale .

Dirac point in graphene (Fig. 3.22). For the vacancy complexes, C_BV_N and N_BV_N, charge transfer would be expected to be unfavourable thermodynamically as both their donor levels lie below the Dirac point.

3.3.7.1 Impact of choice of Exchange-Correlation Functional on CTLs:

It is also instructive to reflect upon potential impact of the choice of exchange-correlation functional. Using techniques in literature, Ref. 92, CTLs of the defects in hBN obtained using screened-exchange methods (HSE) can be estimated from PBE-GGA values. In Fig. 3.22 PBE-based CTLs calculated in this report and the HSE-based CTLs obtained from Ref. 92 are plotted, where the values are stated relative to the work function of graphene. Note that the HSE values in Ref. 92 have only been quoted for individual intrinsic defects, i.e the antisites and vacancies alone. The HSE values for C_BV_N and

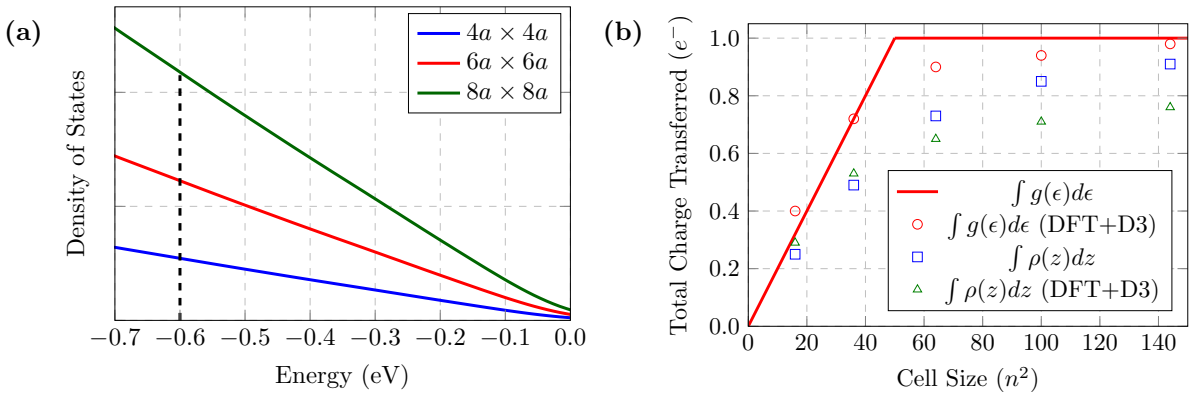

Figure 3.23: (a) A plot of the total electronic DOS for pristine graphene at the approximately linear region close to the Dirac point. The vertical dotted black line is the $(-/0)$ level of V_B in isolated hBN relative to the Dirac point in pristine graphene. (b) The degree of charge transfer obtained by the integration of the DOS of graphene and the heterostructure (red line and red circles, respectively) and by the charge density distribution with and without van der Waals forces (blue squares and green triangles, respectively).

N_BV_N have been obtained using the same translation technique as the other defects. Despite an increase of ∼0.4 eV in the energy difference between the hBN VBM and the Dirac point going from PBE to HSE, the differences in the location of CTLs between PBE-GGA and HSE estimates have been shown to be largely systematic [92] and whether donor and acceptor levels lie above or below the Dirac-point is independent of approach for the cases examined. Hence, computation of the propensity for charge transfer between defects in hBN and graphene can be performed with PBE-GGA functionals to take advantage of the relatively lower computational cost.

3.3.7.2 Impact of method of charge allocation and supercell size effects:

The key impact of simulation cell-size and method of allocation of charge to the two layers on the calculated degree of charge transfer is now discussed. For this V_B is used as an illustrative example.

Firstly, the data resulting from the integration of the charge density when dividing the volume into two halves based on the plane containing the minimum of the average charge density (the methodology is described in 3.3.1.2) are analysed. Fig. 3.23b shows

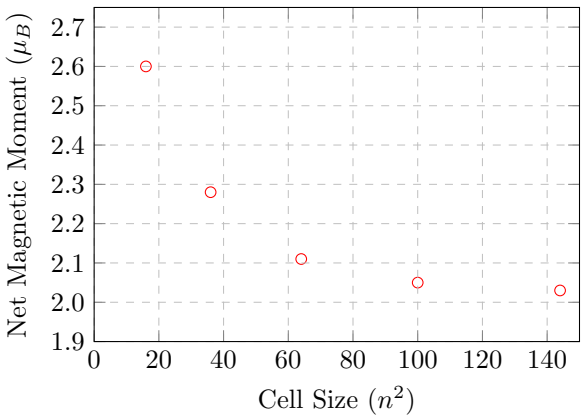

Figure 3.24: A plot of μ_B with respect to the cell size for V_B in hBN/Gr.

the degree of charge transfer for two cases. In the absence of the van der Waals correction (blue squares), the inter-plane separation is larger (4.2 Å) than with the correction (green triangles), where the interlayer separation is 3.3 Å, and for these data the average charge density between the graphene and hBN drops to a very low value. When the van der Waals correction is included, the overlap in the charge density coming from the two materials is much greater, and the minimum value of the charge density between the layers is much greater.

In the absence of the van der Waals correction, the integration of the charge density suggests that the transfer of a whole electron would be expected, with the trend in the data suggesting the integrated charge asymptotically approaches one, whereas for the corrected case the convergence is to a much smaller quantity.

From a fundamental physics point of view, there is no principled way to spatially allocate electron charge to a specific atom, and in this case to either hBN or graphene. For the cases with different inter-plane distances there is a difference in the evanescent decay of charge density into vacuum, and charge density allocated using proximity to a specific layer suggests that the degree of charge transfer is strongly dependent upon the inter-planar distance.

Evaluation of charge transfer based upon the integration of the electronic DOS is now done. The use of the electronic DOS is distinct from integration of charge density, as it takes into account the separation in energy of bands associated with graphene and hBN.

As the CTLs of the point defects examined in this report lie within a linear regime of

the graphene DOS, $g(\epsilon)$, The graphene DOS is approximated as $g(\epsilon) = n^2\lambda\epsilon$, where n is the number of lattice constants in the supercell and λ is the gradient of the primitive pristine graphene DOS, found to be $0.055\,\mathrm{eV}^{-2}$ from DFT calculations. Then, to estimate the cell size required to observe a charge transfer of N electrons, a fixed value of the location of the defect CTL is taken and require the graphene DOS between this level and the Dirac-point to account for one charge carrier. The integrated DOS is determined as

$$2\int_0^{\mu_{\mathrm{CTL}}} n^2\lambda\epsilon d\epsilon = N \quad \Rightarrow \quad n = \frac{1}{\mu_{\mathrm{CTL}}}\sqrt{\frac{N}{\lambda}}. \tag{3.6}$$

Here the Dirac-point is taken to be zero on the electron energy scale and the factor of two accounts for spin degeneracy. Then, for single electron or hole transfer

$$n = \left|\frac{1}{\mu_{\mathrm{CTL}}\sqrt{\lambda}}\right|. \tag{3.7}$$

For $\mathrm{V_B}$ and for μ_{CTL} located 0.6 eV from the Dirac point, the minimum cell size needed to observe a whole electron transfer would be approximately 50 times larger than the primitive. Fig. 3.23a shows the scaling of the density of states near the Dirac point for different cell sizes, illustrating that the integrated DOS between the CTL and the Dirac-point increases with cell size. It also shows that there is a minimum cell for which the area under the graphene DOS is sufficient to allow for a whole electron transfer.

While the model in Eq. 3.7 does not take into account shifts in the Fermi level occurring due to dispersion in the defect level with supercell size, it remains useful to identify the approximately minimum cell size where the charge transfer obtained by the integration of the DOS will be close to a whole electron. Fig. 3.23b shows that the estimate for the minimum size in Eq. 3.7 is significantly smaller than that implied by the calculated charge transfer from the integrated charge density. However, charge transfer calculated by the integration of the DOS is $\sim 0.9\,e^-$ at the minimum cell size predicted by the model.

The DOS model can be developed further by using the electron energy spectra from the heterostructures. For the combined systems there is a defect band associated with the point defect that exhibits relatively small amounts of dispersion, and for $\mathrm{V_B}$ this lies below the Dirac-point of the neighboring graphene. As with the more elementary model DOS approach, as the simulation system size increases the underlying graphene DOS increases and the dispersion in the defect band decreases.

Once the underlying graphene DOS in the vicinity of the localised V_B band is sufficiently large, the integrated DOS above the defect band exceeds one electron. Once this happens a whole electron is transferred, filling the localized defect band. Further increases in the simulation system size does not increase the integrated DOS between the Fermi energy and the band gap, as the defect band is filled and there is no empty DOS associated with the hBN or defect to populate from the graphene DOS in the vicinity of the Dirac point. Indeed, using the DOS estimate it was found that a cell size greater than $12a \times 12a$ showed a whole electron transfer within computational uncertainty (Fig. 3.23b), and even cells as small as $12a \times 12a$ estimate the transfer to be as much as 98% of an electron.

Given that the two approaches, integration of DOS and spatial allocation of charge, yield such significant differences in the estimate of the charge transfer, it is important to resolve which approach, if either, produces the more reliable estimate. To answer this question, some properties of the system that are independent of any attempt to separate the charge allocation to graphene or hBN are addressed.

First, if the degree of charge transfer varies with cell size and converges to less than one carrier, as predicted by examination of the spatial variation in the charge density, the total effective electronic spin of these systems would be expected to follow a comparable pattern. Comparing the calculated effective electronic spin plotted in Fig. 3.24 with the charge transfer estimates in Fig. 3.23, it can be seen that the degree of charge transfer converges with respect to the cell size at the same rate as the DOS calculations. The effective spin of V_B converges rapidly to $S = 2$, corresponding to the spin-state of the negatively charged vacancy in isolated hBN and is consistent with a whole electron transfer from the graphene.

Secondly, band structure and analysis of the electronic orbitals of V_B in hBN/Gr are consistent with it being in the negative charge state. For example, V_B experiences a Jahn-Teller distortion from D_{3h} to C_{2v} in the neutral charge state in isolated hBN, whereas the negatively charged spin-triplet case retains the D_{3h} symmetry. In our calculations, the cell-size converged result shows a geometry indistinguishable from the D_{3h} symmetry case in isolated hBN. All the available data, other than the integrated charge density, points

to the defect being fully ionized and not to a situation with a partial charge transfer. This casts some light on the result previously published for charge transfer between graphene and hBN [127], which predicted 50% of an electron transfer and a total effective spin of $S = 3/2$. This result was obtained using a simulation cell which has been shown in this report to not yield a converged effective spin. Furthermore, the method adopted to estimate the charge transfer was based upon the charge density rather than the band structure.

3.3.8 Conclusion

In this section, it has been shown that routinely employed methods of determining charge transfer based on spatially allocating charge density results in the misallocation of charge. This becomes especially important in the case of 2D material heterostructures because charge is distributed in the delocalized π-states where the distinction between bands associated with dissimilar materials is primarily in terms of their energy rather than their spatial distribution. Therefore, the adoption of an alternative method based on the integration of the electronic DOS has been done, where for the present application the error of assigning charge in a spatial location to a plane of atoms by integrating the states which have been depleted (filled) from (in) the donor (acceptor) species is avoided. In complete support of this approach, it was found that the degree of charge transfer with respect to cell size obtained from the integration of DOS follows closely the convergence of the effective electronic spin in the system – the magnitude of which is closely related to the population of the localised defect states. The magnetic properties are inconsistent with the estimate of the charge transfer from charge-density integration.

Conclusions in the context of the specific material system that has been analyzed have been drawn. It has been shown that the position of charge transition levels of defects in hBN with respect to the work function of graphene can be used to predict the propensity for charge transfer. From calculations of the CTLs, band structure and quantity of charge transfer, it can be concluded that N_B, B_N, C_BV_N and N_BV_N do not undergo charge transfer, whereas V_N and V_B exchange a whole electron with graphene.

The conclusions are supported by a combination of band structure, integrated charge

density and geometric changes associated with ionized forms of the vacancies.

Critically, there is a clear dependence of charge transfer with supercell dimensions and there is a need to perform calculations of charge transfer quantification in a sufficiently large cell size to achieve convergence. This is in part a consequence of the localised nature of the states involved in the defects in hBN, as well as the delocalised states in the graphene. It can also be understood in terms of the graphene density of states in the vicinity of the donor or acceptor band of the defect in the heterostructure. For V_B, it was found that 12×12 unit cells were sufficiently large to approximate the dilute limit and it is predicted that this should be the case for defects where the defect bands have a similar degree of localisation and an acceptor/donor level with a similar energy difference from the Dirac point.

Finally, the defects studied in this report serve as prototypes to illustrate the susceptibility of different defects to charge transfer. The choices of these defects have also been motivated by the interest they have gained as sources of quantum emission in hBN. As the principles presented here apply quite generally in hBN/Gr heterostructures and the likelihood for charge transfer to take place can be gauged from a knowledge of the location of the donor or acceptor levels relative to the graphene Dirac-point, it can be extended to a wider range of defects. For example, carbon substituting for boron has a donor level 2.2 eV above the hBN VBM[15], placing it 0.6 eV above the Dirac point; therefore, it can be expected that charge transfer will take place in this case. Additionally, the CTL of this defect shifts away from the Dirac point by 0.5 eV in hBN, so one would expect a layer-number dependence for the propensity and degree of charge transfer [15]. The impact of encapsulating hBN and graphene layers is explored in the next section Sec. 3.4.

In this section, it has been shown that great care is required in the quantitative prediction of charge transfer. This is especially important in the next stage of experimental work when designing devices to study quenching of emitters in hBN. The work in this chapter forms the basis for the device design in Sec. 5.1, where the final device structure uses graphene as a means to quench unwanted emission by charge and energy transfer.

It is important to note that the focus has been on the thermodynamics of charge transfer. The calculations show that the Fermi level of graphene and the CTLs of defects

in hBN can be used to predict the degree of charge transfer and it usually involves the transfer of a whole electron. The defects that undergo charge transfer will be in a charged state under equilibrium conditions when interfaced with graphene. However, it does not give any information regarding the rate of the charge transfer. This requires the modelling of time-dependent processes to explore the dynamics of charge transfer, such as the tunnelling rates, Sec. 5.1, and excited state lifetimes. The calculation of donor and acceptor levels is also crucial when electrically driving emission, as gate voltages will need to be sufficient to pump electrons to the appropriate defect states. Therefore, this exploration contributes to the development of charge control of emitters in hBN. Furthermore, beyond quantum technologies, theoretical modelling of charge transfer aids the design of also spin valves using magnetic defect states for spin-dependent tunnelling, quantum LEDs and highly sensitive devices for biosensing applications [8, 68, 134, 135].

3.4 Potential energy surfaces (PES) of defects

In the Sec. 3.3, it wasdiscussed that a defect can possess different geometries corresponding to different spin and charge states. It is important to know the lowest energy arrangement as this will be the form that will be most abundant in nature under equilibrium conditions and will form the basis for subsequent calculations for predicting spectra for comparison with experiment. While many simulations focus on defects in monolayer hBN, defects in hBN are often embedded in multilayer stacks and heterostructures. An experimental study on the impact of strain on the ZPL of the defects showed that the emission wavelengths can shift by 20.8 nm (65 meV) upon the application of 5.55% strain [136], and other studies also show noticeable shifts in ZPL wavelengths due to strain [137, 138]. Therefore, large ZPL shifts can occur due to the strain induced by a substrate with significant lattice constant mismatch with hBN. Furthermore, the inclusion of a substrate and/or additional encapsulating layers of hBN leads to a change in the dielectric environment and hence the localised charge at the defect experiences a different degree of screening when compared to the isolated case. This is reflected in the shift in the CTLs of defects when embedded in multilayer hBN and/or interfaced with a substrate [15, 139], Fig. 3.25. The influence of the environment on the nature of the defect, such as ground state geometry, also has implications on the interaction of the defect with external fields. A study on the response of a defect to a vertical electric field showed that many defects in hBN displayed a Stark effect, indicating a dipole moment orientated in the out-of-plane direction [16, 131]. It was suggested that a defect, such as C_BV_N in its singlet state could be a candidate emitter, due to its out-of-plane dipole moment. Theoretical explorations of the impact of stacking on the electronic and optical properties of C_BV_N showed that large tunings, on the order of 100 meV, of the ZPL can be achieved by controlling the orientation of one layer with respect to another [140, 141]. Additionally, recent observations of a reduction in the PSB intensity from emitters in few layer to bulk hBN has suggested that the degree of structural distortion due to electronic excitation is affected by the number of layers encapsulating the defect [142].

The evidence for the high sensitivity of defects to the dielectric environment motivates the capture of the design of experimental device structures in computational models.

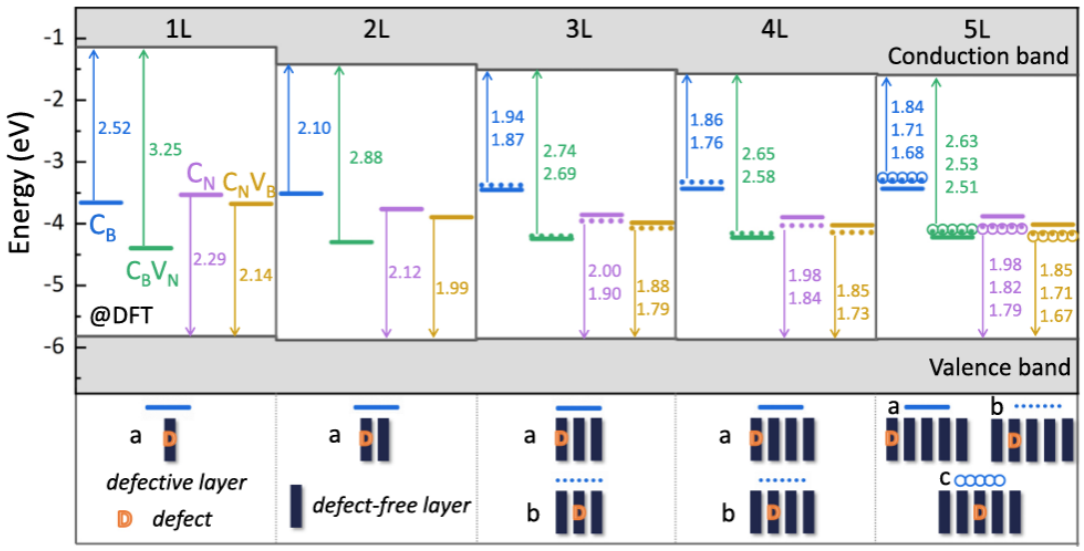

Figure 3.25: The variation of the CTLs of defects in hBN with the number of encapsulating hBN layers. The zero of the scale is aligned to the vacuum level. From this, the donor level of C_BV_N in 5 layer hBN is $\sim 0.2\,eV$ from the Dirac point in graphene. The figure has been reproduced from [15].

Using C_BV_N as an illustrative example due to its out-of-plane dipole moment allowing Stark tuning with a vertical electric field, the impact of surrounding layers, whether hBN or graphene, on the preferred geometry and spin state of the defect is studied and the effect of the shift in CTLs due to the dielectric environment on charge transfer to graphene is also explored. Furthermore, as the broader scope of the research explored in this thesis is in the charge control and electrical field control of SPEs in hBN, it is of interest to study Gr/hBN/Gr stacks as this is the simplest device structure that can be used to apply external electric fields and inject carriers for electroluminescence.

In principle two effects are focused upon: (1) due to the structural differences between the singlet and triplet ground states of C_BV_N , it is of interest to know if the two configurations interact differently with the encapsulating layers and if such interactions lead to a change in the energy ordering of these configurations and (2) if the shift in CTLs due to the inclusion of additional hBN layers, as shown in Refs. 15, 139, leads to change in the degree of charge transfer between C_BV_N and graphene with the thickness of hBN. This is performed using the NEB methodology, outlined in Sec. 2.5.6, to obtain the energy

path for structural distortions of C_BV_N in different environments, allowing us to identify any metastable intermediate states caused by the dielectric environment. In cases where the initial and final configurations are equilibrium defect arrangements, the energy path traversed during reorientation is the MEP, as defined in Sec. 2.5.6. All of the following calculations have been performed in a $6 \times 6 \times 1$ cell, unless explicitly stated, with spacing between supercells across vacuum being fixed at ~ 13 Å to ensure that the electric field induced across the vacuum between systems with different number of hBN and/or graphene layers would be comparable. The number of images between the initial and final states that was found to sufficiently resolve the energy surface was 11. The energy paths are visualised by plotting the formation energy of the structure at each image with respect to the image number and the vertical displacement of the carbon atom with respect to the hBN plane. The reference state, E_{host} in Eqn. 2.28, for the formation energy is taken to be the pristine form of the system. In terms of nomenclature, in multilayer hBN systems (trilayer hBN and bilayer hBN on graphene), the inner hBN layers is denoted as L1 and the outer layer adjacent to vacuum hosting C_BV_N as L2.

3.4.1 Energy paths for the reorientation of C_BV_N

3.4.1.1 Mono-, bi- and trilayer hBN

The lowest energy configuration of C_BV_N in monolayer hBN is the spin singlet state with a corresponding vertical displacement of the carbon atom, resulting in a C_s symmetry. From Figs. 3.26a–3.26c, the distortion can either lead to the carbon atom being located above or below the basal plane and due to the mirror symmetry between these two structures, they possess the same total energy. The MEP for the traversal between these two configurations is shown in Fig. 3.27 with a red solid line, with the red circles indicating the formation energies of the images. The shape of this potential is a double well with a saddle point when carbon lies in the hBN plane.

The other possible state, and one that existing literature attributes to be a source of single-photon emission, is its triplet state with a planar geometry. The defect in this configuration possesses C_{2v} symmetry, with an additional mirror plane in the hBN layer. In Fig. 3.27, it can be seen that an out-of plane displacement of the carbon atom, for

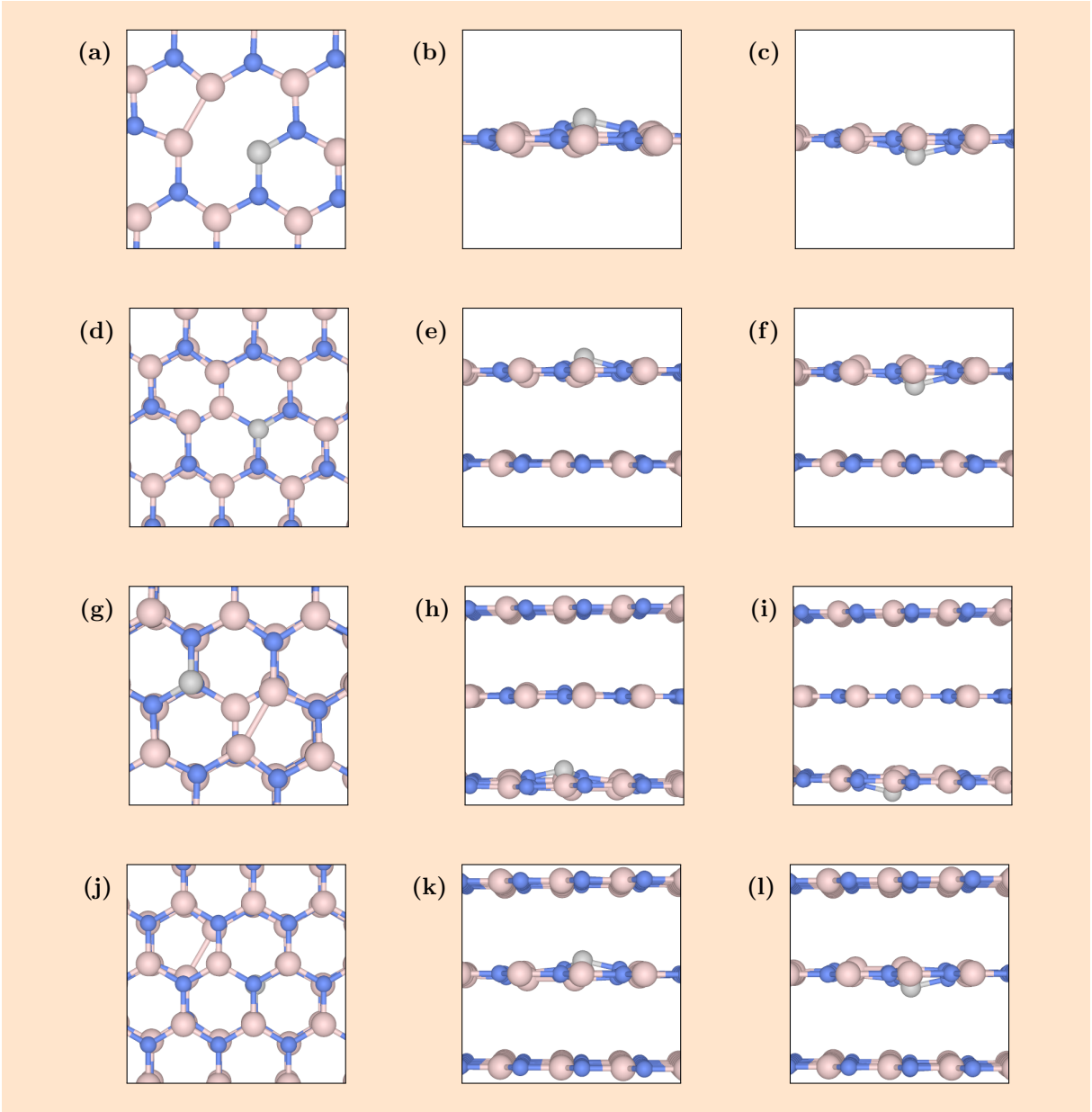

Figure 3.26: The end-points for the NEB calculation of C_BV_N in hBN of different thicknesses. The end-points correspond to the singlet configuration with the carbon atom perturbed above and below the hBN plane. Each row of images correspond one of the mono-, bi- or trilayer hBN systems. For the trilayer, **(g)-(i)** correspond to the defect located in the layer adjacent to vacuum, and **(j)-(l)** correspond to the defect in the middle hBN layer.

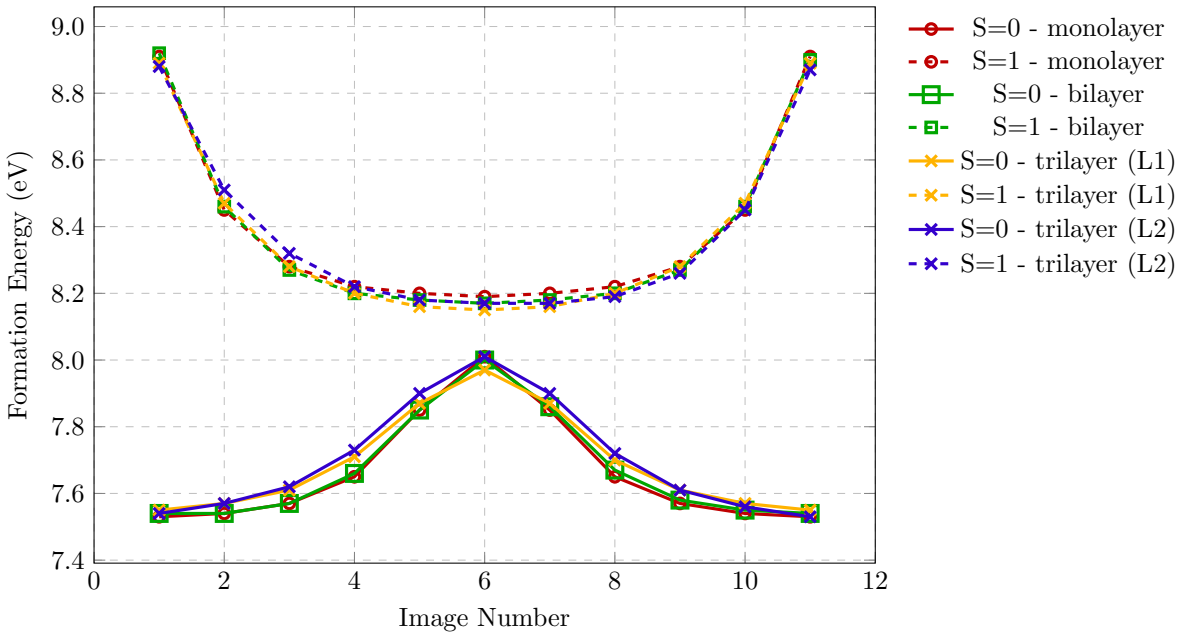

Figure 3.27: Shows the variation in the formation energy with each image of C_BV_N as it traverses the energy path to move to the equilibrium position on the opposite side of the plane. Both singlet and triplet states are shown in the diagram.

the triplet state, leads to an increase in the total energy, reducing its stability. As no equilibrium arrangement exists for the triplet state where the carbon is displaced vertical to the plane, the end-points for the NEB calculation were set to the arrangement of the singlet state. In Fig. 3.27, the red dashed line shows the energy surface for the triplet state as it traverses between the two end-points. The shape is that of a parabola with a minimum when the carbon atom is in the hBN plane.

From these energy paths in the monolayer, a 177 meV, energy difference between the saddle point of the singlet and the minimum of the triplet states is observed, which is denoted as $\Delta E_{\text{s-t}}$. This is in agreement with other calculations of this defect in monolayer hBN, which found a 0.2 eV difference between the planar configuration of the singlet state and triplet state [130]. Therefore, in free-standing monolayer hBN, C_BV_N will exist in the singlet state with an distortion out-of-the plane at equilibrium conditions. The barrier to the transition between the two sites for the singlet set, ΔE_B, is 0.5 eV for the monolayer case. This is a large barrier to be overcome for the reorientation via a thermal process at room temperature (which is on the order of $k_BT = 0.02$ eV), which is the temperature at

which hBN colour centre based devices are intended to be operated at. However, it can be overcome by the application of external electric fields and photoexcitation processes.

The impact of the inclusion of additional hBN layers on the defect is now studied in comparison with the isolated monolayers. The defect is embedded in bilayer and trilayer systems, with the hBN layers organised in AA′ stacking order. This involves the boron (nitrogen) atoms overlapped by nitrogen (boron) atoms in adjacent layers, as shown in Figs. 3.26a, 3.26d and 3.26g. The AA′ stacking is the lowest energy stacking in multilayer hBN [1, 39], and was therefore chosen.

In the bilayer system, the placement of C_BV_N in either layer is equivalent by symmetry, Figs. 3.26d–3.26f. There is an asymmetry in the potential curve due to the establishment of an electric dipole between the two layers due to the inequivalence of the two layers. In the trilayer case, Figs. 3.26g–3.26i, the defect could be located in either L1 or L2. Similar to the bilayer stack, the inclusion of the defect in the outer layer removes the mirror symmetry in the stack, and hence leads to an induced electric field.

$\Delta E_{\text{s-t}}$ ranges from 160-180 meV for all thicknesses of hBN studied in this report. As the spread in the energy difference is below the accuracy of the calculations, no trend showing a reduction or increase in the gap between the triplet and singlet states is found. While no metastable state is observed in the hBN only system, the $\Delta E_{\text{s-t}}$ is sufficiently small for substrate induced effects. For example strain induced effects can cause spectral shifts of 0.22 eV [143]. These shifts can lead to the triplet state to lie below the planar singlet state in energy, leading to a metastable state. ΔE_{B} on the other hand shows a greater response to encapsulation by hBN layers. ΔE_{B} reduces by 0.1 eV from the monolayer case when the defect is embedded in L1 (yellow solid line) in Fig. 3.27. This motivates the study of the impact of graphene on the thermodynamics of the defect.

3.4.1.2 1-hBN/Gr and 2-hBN/Gr

The next step in complexity is introduced by replacing a hBN layer with graphene. Three different hBN/Gr systems were studied, a single hBN layer on graphene, which is called 1-hBN/Gr, and bilayer hBN on graphene (2-hBN/Gr). For the 2-hBN/Gr system, the defect can be located in either hBN layer, resulting in two distinct configurations. The stacking

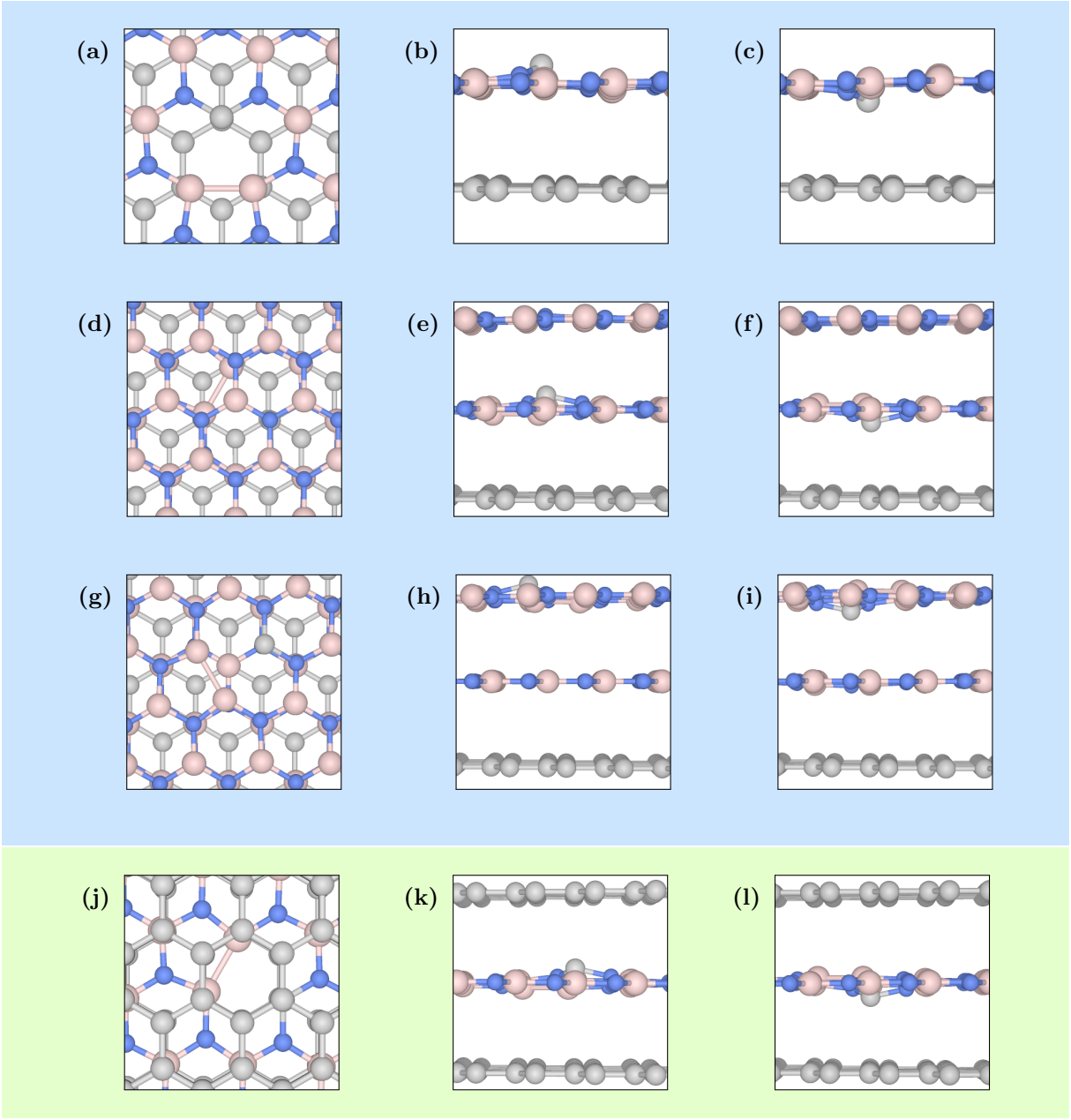

Figure 3.28: The end-points for the NEB calculation of C_BV_N for the hBN/Gr (light blue panel) and Gr/hBN/Gr (light green panel) systems. In each of these systems, the equilibrium positions of the singlet state, with the carbon atom perturbed above and below the host hBN plane are shown.

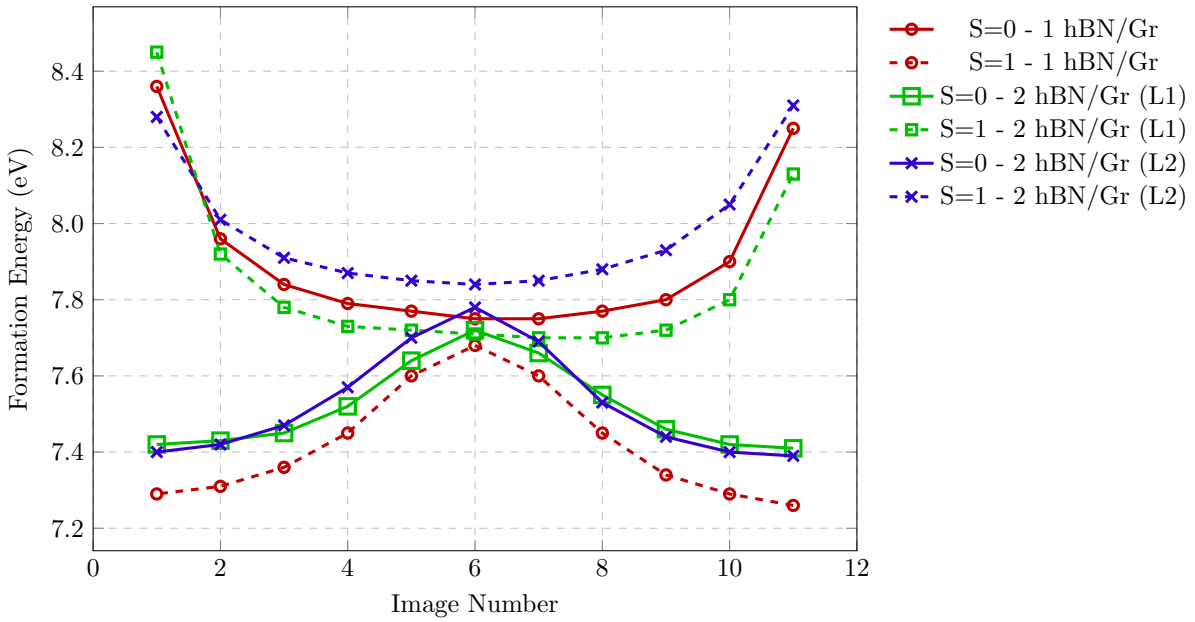

Figure 3.29: Similar to the Fig. 3.27, the energy path for the re-orientation of C_BV_N is shown for a hBN/Gr system with a varying number of hBN layers.

between hBN and graphene was chosen to be AB′ as it is the energetically favoured stacking [39]. All stacks do not have a horizontal mirror plane due to the presence of graphene and polarisation is induced in the supercells in the vertical direction. Such a field will lead to asymmetry in the potential curves generated as in the case of bilayer hBN and trilayer hBN with the defect located in the outer layer. In Fig. 3.28, the equilibrium positions above and below the host hBN plane for C_BV_N in the singlet state is shown. As with the hBN only case, these have been used as end-points for the NEB calculations for both the singlet and triplet configurations.

The potential curves for the three possible locations of the defect is shown in Fig. 3.29 and for each of these configurations, two spin states are considered – singlet (solid lines) and triplet (dashed lines). Comparing all the energy paths in Fig. 3.27 to thosein Fig. 3.29, a greater sensitivity of $\Delta E_{\text{s-t}}$ to the layer location of C_BV_N is observed when graphene is introduced. $\Delta E_{\text{s-t}}$ has values ~~of~~ from 70 meV in the monolayer case, 60 meV when the defect is located in L2 of 2-hBN/Gr and −20 meV in L1 of 2-hBN/Gr. The case of L1 in 2-hBN/Gr shows that the formation energy of the triplet configuration falls below the saddle point of the singlet configuration. This is a signal of substrate modification

of defect energetics such that it leads to a metastable intermediate state during defect reorientation.

There is a net reduction of formation energies due to the inclusion of graphene. It is interesting to note that unlike in the hBN only case, the additon of a hBN layer to 1-hBN/Gr leads to a 160 meV increase in the formation energy of the singlet state, regardless of the layer location of C_BV_N . However, for the triplet case, the formation energy reduces by 50 meV when placed in L1 and increases by 90 meV when placed in L2. The differences in the direction of change in the formation energy of the triplet state is attributed to the reduction in screening as C_BV_N is brought closer to vacuum from L1 to L2.

In terms of the energy barrier for the transition of C_BV_N in $S = 0$ between the two sites, $\Delta E_B = 0.4\,\text{eV}$ for 1-hBN/Gr, which is comparable to the hBN only barrier energies. For the 2-hBN/Gr cases, the barrier further reduces to 0.3 eV when C_BV_N is in L1, but returns to 0.4 eV in L2. As such, an average reduction 0.1 eV is found when compared to the pure hBN cases. This would lead to an increased rate of transition between the two sites, however the barrier is still large when compared to the thermal energy at room temperature.

3.4.1.3 Gr/hBN/Gr

Since the inclusion of a single graphene layer had an observable impact on the defect energetics when compared to the hBN only case, it was of interest to study the inclusion of a second graphene layer on the system. The top hBN layer in the 2-hBN/Gr system was replaced by a graphene layer. The AB′ stacking sequence was maintained between both graphene layers and hBN. This restored mirror symmetry to the pristine heterostructure, with the mirror plane located in the hBN layer (without the defect). Although the pristine system has no net field, a defect displaced out-of-the plane can lead to an induced polarisation and hence a weak electric field.

The energy paths look qualitatively different when compared to the case with a single graphene layer, as shown in Fig. 3.30a. The triplet state energy path, black line, is below the saddle point of the singlet state, path indicated by green line, by 0.2 eV. This is a significant reduction of $\Delta E_{\text{s-t}}$ when compared to 2-hBN/Gr with C_BV_N in L1. This

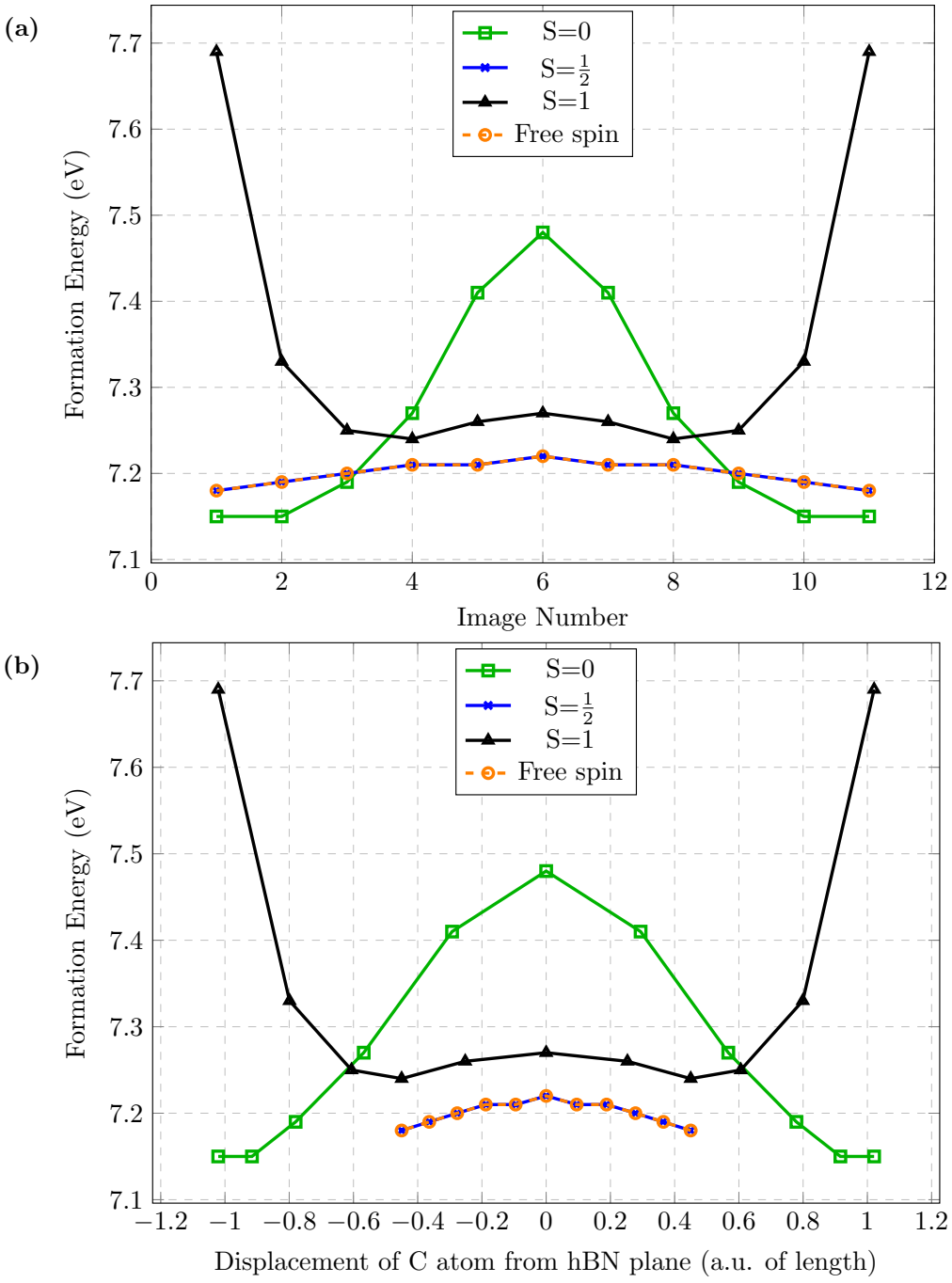

Figure 3.30: **(a)** The energy path obtained for defect re-orientation of C_BV_N . The calculations were performed with the system constrained to the singlet (S=0), doublet (S=$\frac{1}{2}$) and triplet (S=1) states and an unconstrained spin state. **(b)** The energy path with formation energies as a function of the vertical displacement of the carbon atom from the plane.

suggests that the triplet configuration is a metastable state in the path taken during the traversal of C_BV_N between the two singlet equilibrium arrangements.

The formation energies of the equilibrium configuration of the singlet state also reduces by 0.1-0.2 eV and the triplet state reduces by 0.4-0.5 eV when compared to the hBN/Gr cases. This suggests that the additional graphene layer dramatically stabilises C_BV_N and can lead to it being present in greater abundance.

To confirm that the triplet state would indeed be the preferred spin configuration if the defect was confined to the hBN plane, a calculation was performed where the spin of the system was allowed to be a free parameter. However, this calculation resulted in the defect being in a doublet state, which was 0.1 eV lower in energy than the triplet state. The system would possess this magnetic moment only if charge transfer had occurred. This is in contrast to the prediction in Sec. 3.3, where the donor level of C_BV_N was found to be below the Dirac point of graphene, making charge transfer not feasible from a thermodynamic standpoint.

When structural optimisation with free spin was performed, a small out-of-plane distortion was found. This is reflected in the NEB calculation of the MEP for the transition of the defect between the two equilibrium arrangements (with the carbon atom above or below the hBN plane), yellow dashed line in Fig. 3.30a. A second NEB calculation was performed with the spin being fixed to the doublet state, blue line in Fig. 3.30a. In Fig. 3.30a, MEPs for both the fixed spin and free spin calculations are identical, reinforcing the conclusion that charge transfer has occurred. To show that the structure corresponding the free spin state at each image is identical to that of the doublet, in Fig. 3.30b the variation of the formation energies with displacement of the carbon atom from the plane is plotted. The formation energies of the fixed spin, $S = \frac{1}{2}$, and the free spin calculations are identical at every image. Additionally, from this plot, it can be seen that the equilibrium positions for the doublet state lies within the barrier of the MEP of the singlet state. Therefore, true ΔE_B for the traversal of the defect between the two equilibrium arrangements of the $S = 0$ state is dramatically reduced, from 0.3 eV (which is comparable to when C_BV_N was located in L1 of 2-hBN/Gr) to less than 0.1 eV. While this is still significantly higher than the thermal energy at room temperature, moderate

electric fields and photon energies can drive the carbon atom between the two sites. The doublet state also acts as a true metastable state during this traversal and can increase the transition time if the defect is trapped in the equilibrium configuration of the doublet state.

3.4.2 Discussion

The impact of additional hBN and/or graphene layers on the energetics and charge state of the defect is now discussed. The modification of $E_{\Delta\text{s-t}}$ and ΔE_{B} with the addition of graphene shows that the defect interacts strongly with its environment.

This interaction could be due to mixing between states in hBN and graphene leading to stabilisation of the defect. Studies on the band gap of hBN and its variation with the thickness of hBN showed that it transitions from a direct to an indirect band gap material from monolayer to bulk phases [104]. It was found that states at the M point in the conduction band of hBN would interact with surrounding layers and hence lead to the lowering of the conduction band edge. A change in the location of the band edges would lead to a shift in the location of the CTLs with respect to vacuum, especially if the states arising from the defect have significant contribution from the bulk material.

Furthermore, there is screening of charged defects across the vacuum due to additional encapsulating layers. In Ref. 15, this shift in ionisation energies and lowering of conduction band edges (with a relatively unchanged valence band edge) with respect to the vacuum level resulted in shallower donor and acceptor levels. If the donor levels shift above the Dirac point due to the effect of screening and mixing with states contributed by graphene, charge transfer would be feasible in the heterostructure, in contrast to the prediction from the study of CTLs in isolated monolayer hBN.

While the above explains the differences between systems that appear as rigid shifts in energies across all configurations, it is still unknown why the triplet state formation energies are more sensitive to the presence of graphene than the singlet states

To gain a deeper understanding of the states involved in charge transfer in the heterostructures, band structure calculations were performed for the different configurations that were studied. In Fig. 3.31, the band structures of the $S = 0$ in 2-hBN/Gr, $S = 0$,

$S = \frac{1}{2}$, $S = 1$ and free-spin in Gr/hBN/Gr are shown. The electronic levels have been filled up to the Fermi level, μ_e, in each spin channel, with the filled states indicated in blue and the empty states in red. The reason behind the stabilisation is now revealed as the band structures clearly show charge transfer in each of the scenarios. Even in the singlet state, Fig. 3.31a and 3.31b, partial charge transfer is observed as the defect level is slightly above the Dirac point, and due to the finite electronic temperature ($k_BT = 0.02\,\text{eV}$) the empty graphene states above μ_e of the system, which lies approximately at the defect level, also get filled according to the Fermi-Dirac statistics. The small degree of charge transfer leads to a reduction in μ_e, and in the case of 2-hBN/Gr the additional interaction of the partially charged defect with the electric field, and subsequently this reduces the formation energy of the defect.

The greater stabilisation of the triplet state follows this observation as from the band structure, Fig. 3.31c, it is apparent that there is a whole electron transfer into the spin-up channel of graphene, leading to spin-polarised graphene layers. This unphysical effect leads to the triplet state appearing as a metastable state in Gr/hBN/Gr and in 2-hBN/Gr where the defect is located in the layer adjacent to graphene. Therefore, there is the counter-intuitive observation of the charged defect despite the donor level of C_BV_N being well below the Fermi level of graphene. However, upon closer inspection of the CTLs of C_BV_N at each cell size (Fig. 3.32), it can be seen that the donor level at the $6 \times 6 \times 1$ cell, the CTL point lying in the yellow vertical band in Fig. 3.32, is well above the Dirac point for the planar triplet configuration (green dashed line). Although the the donor level for the singlet out-of-plane configuration (red dashed line) is 130 meV below the Dirac point, the highest occupied electronic level is situated above the Dirac point as seen in the band structure, Fig. 3.31b. This is vastly different from the CTLs in the dilute limit and hence a different effect is observed at high concentrations of the defect.

Therefore, the free spin calculation led to a whole electron shared over spin channels of graphene. This has a lower energy than the triplet state as charge is transferred to both spin channels of graphene, unlike in the spin constrained calculation of the triplet state where charge was constrained to the majority spin channel, leading to higher electronic energy levels being occupied, as seen in the filling of Fig. 3.31e and 3.31c.

In addition to the explicitly calculated degree of charge transfer, the band structure of the system with spin constrained to the doublet state and the free spin calculation are identical (Fig. 3.31d and 3.31e), providing additional support that a whole electron transfer was preferred when the system is initialised with the defect in-plane.

While it is a helpful aid to refer to the donor level of the triplet state to highlight the cause of charge transfer in smaller systems, it does not have a physical interpretation in the heterostructures as the charge is not constrained to the defect, and the CTLs are interpreted in reference to the uncharged defect.

Following the above arguments for the change in $\Delta E_{\text{s-t}}$, the reduction in ΔE_{B} due to the incorporation of graphene in the system can also be explained. As the carbon atom in the $S = 0$ configuration of C_BV_N moves towards the hBN plane, the degree of charge transfer increases. This leads to a lower μ_e than what would exist if charge was constrained to defect and lowers the total energy of the system at all images. This artificial effect has the appearance of a lower energy barrier. As the incorporation of each graphene layer reduced the barrier height by 0.1 eV, the reduction of E_{B} from hBN/Gr to Gr/hBN/Gr can be attributed to their being twice as many graphene states available to be filled.

3.4.2.1 Arguments for existence of modified CTLs

While an argument has been made that the barrier reduction due to charge transfer is an artefact of finite cell size in PBCs, there is support for these effects to be present in the dilute limit and hence a real system. Firstly, the extrapolated CTLs were obtained by simulating the charged defect in an isolated monolayer hBN system. The results seen here, where charge transfer is being observed due to the donor levels lying higher for smaller super cells, can still exist in the dilute limit if there is a substrate induced modification of the CTLs. The substrate induced process include but are not limited to strain, electrostatic effects and mixing with band edge states.

The cell size variation of the formation energies of the charged defect in Gr/hBN/Gr could be different to that in isolated hBN as the electric field across the vacuum is negligible due to the symmetry of the Gr/hBN/Gr system. Therefore, the interaction between

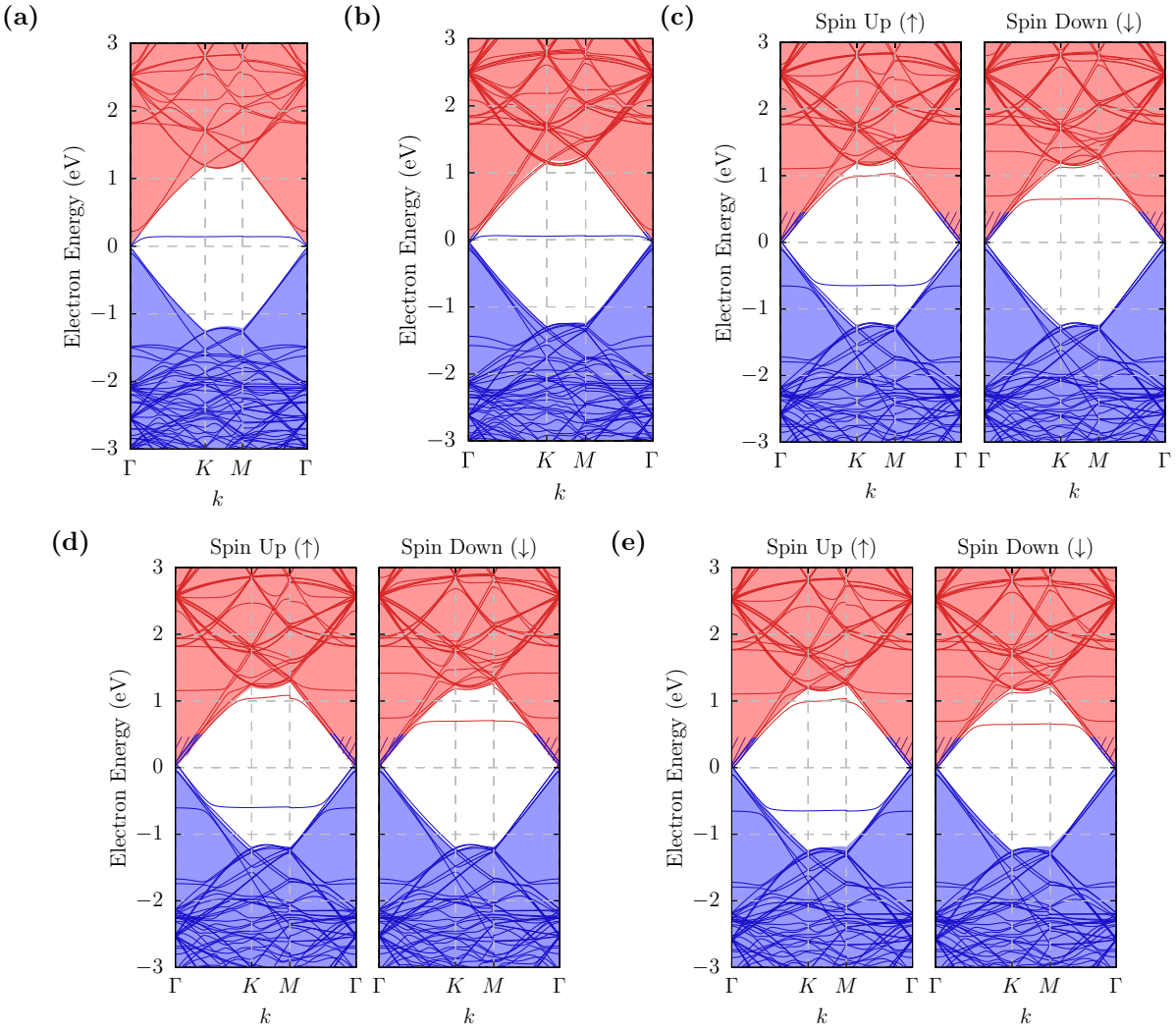

Figure 3.31: The band structures of **(a)** $S = 0$ calculation in 2-hBN/Gr ,**(b)** $S = 0$, **(c)** $S = 1$, **(d)** $S = 0.5$ and **(e)** free spin calculations in in Gr/hBN/Gr. Colours and scales of the band structures are as in Figs. 3.4a and 3.14c respectively. The zero in the energy scale is set to the Dirac point of the corresponding pristine structure.

the defect and its images would be dominated by the in-plane electric fields. However, unlike a field across the vacuum, the Coulomb potentials in the plane are screened by the bulk hBN atoms. Hence, it is possible that the properties of C_BV_N in Gr/hBN/Gr in the dilute limit is captured well in small cell sizes.

Secondly, the work by Ref. [15, 139], show that when a planar configuration of C_BV_N is embedded in the middle layer of a 5-layer hBN system, the donor level lies between 1.7-1.8 eV from the valence band maximum of hBN, Fig. 3.25, with the general trend

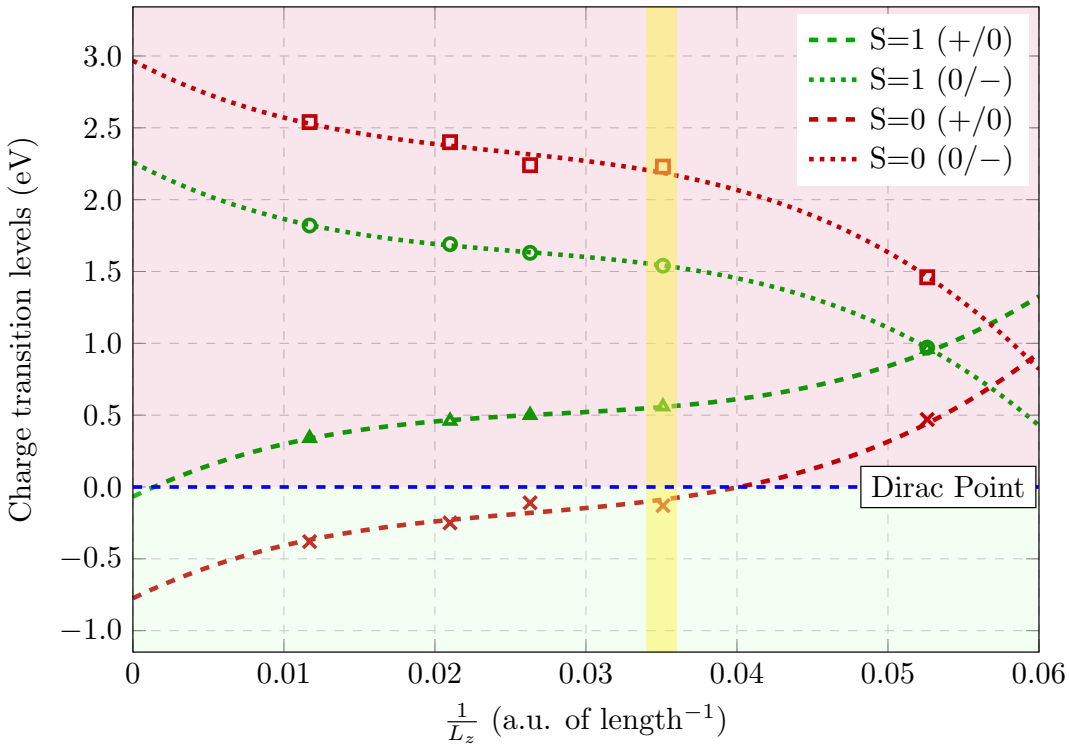

Figure 3.32: The variation of the CTLs of C_BV_N with cell size for both the singlet (red squares and crosses) and triplet (green circles and triangles). The cubic polynomial fit for each CTL is shown as dotted or dashed lines with a color corresponding to the spin state of the neutral defect. The Fermi level of graphene (Dirac point) has been explicitly labelled by a blue dashed line. The yellow vertical band highlights the data points corresponding to the $6 \times 6 \times 1$ cell.

being the shifting of the donor level towards to the vacuum. This places the donor level 0.1-0.2 eV from the Dirac point in 5 layer hBN, depending on the layer location of the defect. Hence, it is feasible for charge transfer to take place between C_BV_N in multilayer hBN and graphene even in the dilute limit. In such a system, the intermediate spin doublet metastable state reduces the barrier height for the traversal of C_BV_N across the hBN plane.

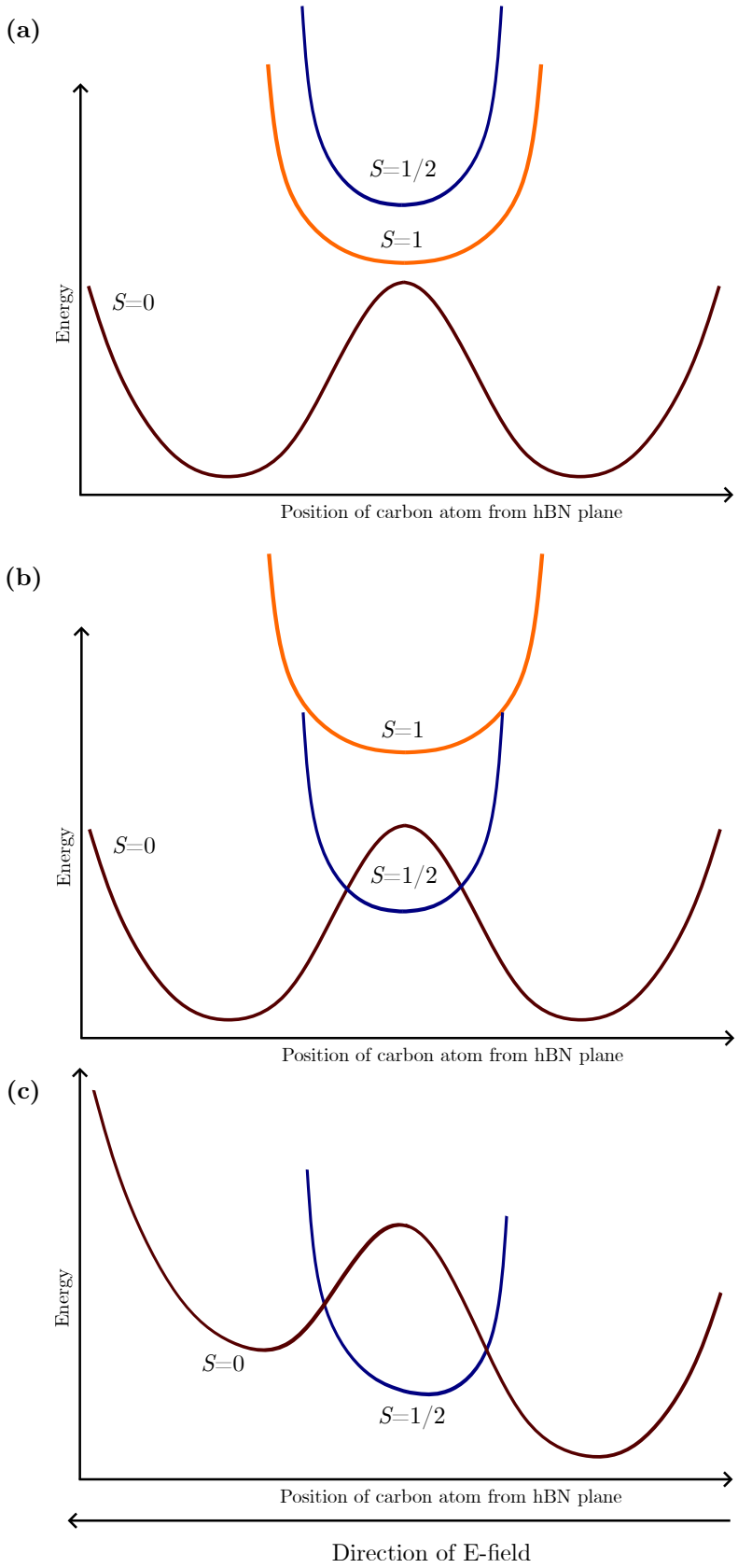

Figure 3.33: **(a)** The energy ordering when charge transfer is not favoured in the ground states of both the singlet and triplet configurations. The energy ordering of the $S = 0$ and $S = 0.5$ states are shown **(b)** without and **(c)** with an electric field.

3.4.2.2 Summary and future outlook

The impact of a metastable state on the electrical control of defects and observable spectroscopic properties are now discussed. In Fig. 3.33, the energy diagram of the transition of the carbon atom between the two minima of the $S = 0$ with an intermediate $S = 1$ state is illustrated. In scenario one, Fig. 3.33a, the defect would rest either above or below the plane unless a process transferring a large quantum of energy aids the carbon to overcome the barrier height for transition, such as a photoexcitation process. When the defect is in an excited state, charge transfer can occur, however, as the charged state is higher in energy than the singlet state (or even the triplet state), in equilibrium the defect returns to the ground singlet state. It is only in this scenario that a triplet state can exist physically, as charge transfer does not lead to a magnetic graphene layer and the triplet state is encountered upon recapture of an electron when the defect is in the plane. In such a system, there is a competition between the radiative relaxation process back to the singlet state or charge transfer from excited singlet or triplet states into graphene and this reduces the intensity of emission as non-radiative relaxation rates are increased.

In the second case, the reduction in barrier height due to the minima of energy curve of the doublet being below the barrier in the singlet energy curve, Fig. 3.33b, leads to a significant enhancement of the rate of transition of the carbon atom between the two equivalent sites. Even when substrates do not change the energy order of the spin states, it can reduce the barrier height for defect reorientation within the same spin state, as is the case with the inclusion of additional hBN and graphene layers in this study.

In Fig. 3.30a, the energy difference between the doublet and singlet states is on the order of 10 meV, which is an energy that can be overcome at room temperature and small electric fields. In Fig. 3.33, it can be seen that the application of a field leads to a gradient in the potential curves and the two minima in the singlet state are no longer equivalent, Fig. 3.33c. If one of the minima in $S = 0$ is shifted to an energy higher than the doublet state, it leads to charge transfer and a change in the spin state of the defect. If the defect is trapped in the metastable state for a duration of time, it causes spectral diffusion in the measured PL lineshapes. These are jumps in the ZPL energy with time.

A shift of the carbon atom from above to below the plane also leads to the inversion

of the out-of-plane component of the electric dipole moment of the defect. In Stark shift measurements, this appears as a 'V-shaped' shift, Fig. 3.34b, in the ZPL with the direction of the applied field. Both changes in emitter intensity and V-shaped Stark effects have been observed in experiment 16, providing further evidence to the theory of barrier reduction. Furthermore, in Ref. 16, the structure of the device was Gr/b-hBN/Gr, where b-hBN refers to bulk hBN. This structure resembles that simulated in this study and from Ref. 15, C_BV_N in b-hBN should posses a donor level closer in energy to the conduction band edge than in monolayer hBN [15], enhancing the rate of charge transfer to graphene.

Finally, in this chapter, the importance of the correct initialisation of structures has been demonstrated. As can be seen, the lack of confinement of the charge to C_BV_N prevents the accurate simulation of the potential curve of the triplet and singlet states due to charge transfer. This led to the false conclusion that the triplet state is stabilised with the inclusion of graphene. It has also been shown that only in the case that the corrected/extrapolated CTLs favours charge transfer can smaller cell sizes qualitatively produce the same band structures as that observed in the dilute limit. This was true in the previous in Sec. 3.3, where a range of defects in monolayer hBN/Gr was simulated.

From Fig. 3.30a, it can be seen that care needs to be taken when breaking the symmetry of the system during self-consistency calculations. For example, to obtain the $S = 0$ configuration in a free spin calculation, it is not sufficient to remove the mirror symmetry constraint by a shallow out-of-plane perturbation of the carbon atom, as the carbon atom may still be trapped in the minimum of the doublet state, which exists within the barrier for transition of the singlet state. Hence, a free spin calculation converges to the singlet only when a sufficiently a large shift is performed on the initial position of the carbon atom.

Therefore, in the broader context of electric field control of emitters using Stark shift, C_BV_N may not be a suitable candidate due to the low barrier for charge transfer and flipping of dipole orientation. Stark effect is one of the most common ways of tuning emission wavelengths of SPEs to achieve indistinguishability of photons, which is key for creating entangled pairs for QKD and quantum computation. However, the low barrier to charge injection also makes it an ideal candidate for electroluminescence. It is therefore

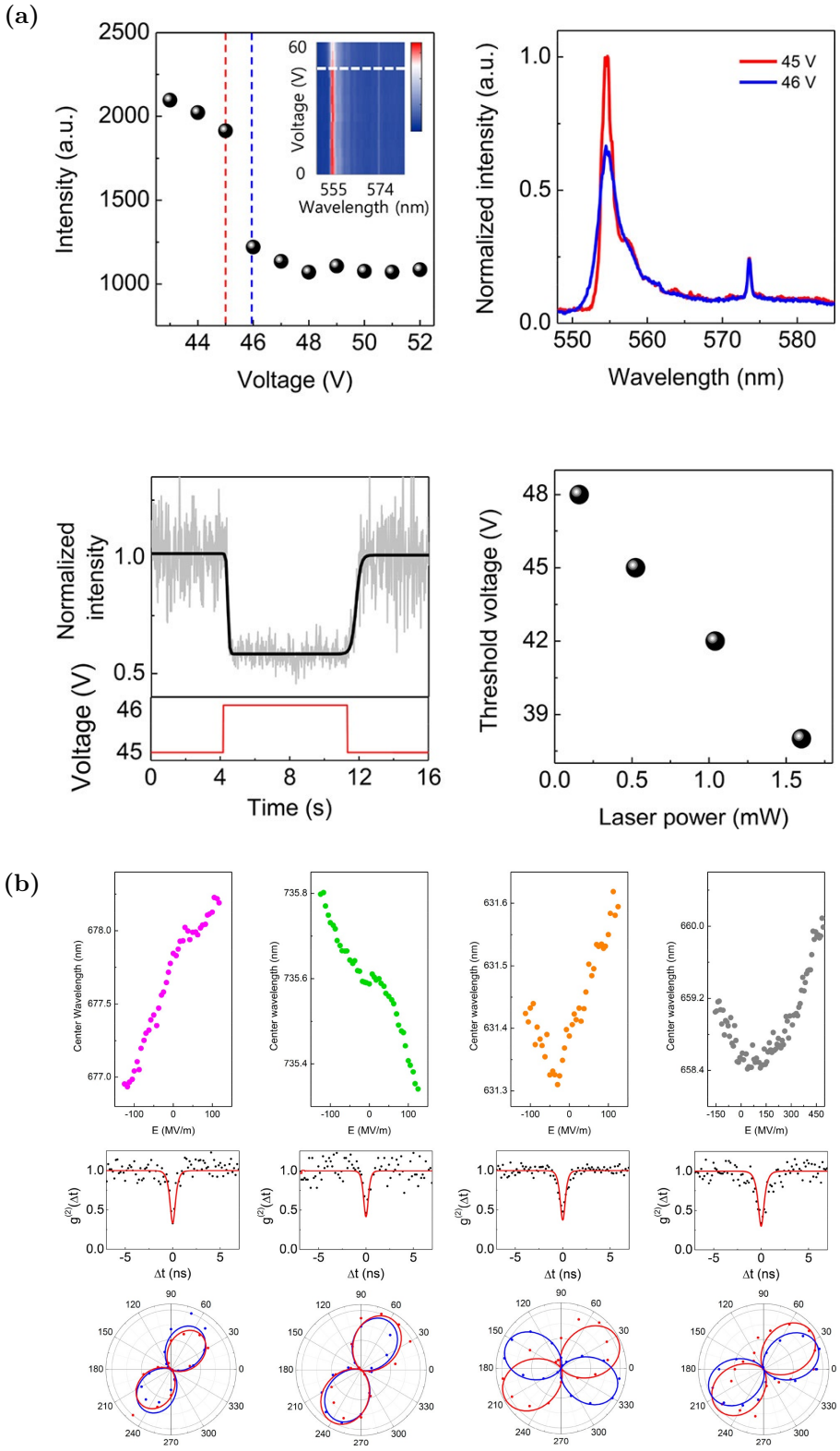

Figure 3.34: **(a)** Shows the change in intensity of the emission when the electrostatic potential across the hBN is increased. **(b)** The third column shows the V-shaped Stark shift attributed to change in the orientation of the out-of-plane dipole with respect to the host hBN plane. This is attributed to the charging of the defect. Both of these images have been reproduced from Ref. 16

crucial to engineer the properties of the substrate to ensure the required properties of the defect are present.

3.4.3 Conclusion

In this section, the energy paths for the transition of the carbon atom in the C_BV_N between equilibrium arrangements on opposite sides of the host hBN plane has been discussed. It was shown that it is difficult to isolate substrate induced modifications to the CTLs from artificial effects due to PBCs. To confirm the existence of the doublet state within the barrier width for the transition of the $S = 0$ C_BV_N , effects of strain and PBCs need to be verified by simulating the structures with different lattice constants and cell sizes. Exploration of effects, such as the impact of strain on the defect structure and the position of the CTLs with respect to the Dirac point, will allow the determination of whether charge transfer was an artefact of finite cell size in PBCs or a real physical effect. The importance of the correct initialisation of the structure in an energy surface with multiple minima was also discussed. This work has significant implications on the electrical and charge control of defects in hBN. Furthermore, the tuning of defects with an out-of-plane electric fields has significant interest in applications in quantum technology. If the barrier to transition to a metastable intermediate state with a different electric dipole orientation is low, then these defects will not be suitable for applications in quantum technology that require control of defects with perpendicular electric fields.

Chapter 4

Experimental Methods

This section describes the experimental techniques that were used in this project. The techniques can be broadly categorised into nanofabrication and characterisation techniques.

4.1 Nanofabrication techniques

In this project the two sources of hBN used were nominally 13 nm thick, multilayer hBN (ML-hBN) grown using CVD on 20 µm thick copper foil (product code: CVD-2X1-BN-ML) and flakes grown at high pressure and temperature using and subsequently immersed in a 50:50 solution of ethanol and water, obtained from Graphene Supermarket. The bottom monolayer graphene on silicon dioxide (SiO_2) on which alumina was grown was obtained from the commercial supplier, Grolltex. This was done as the supplier has a methodology for polymer free transfer of graphene on SiO_2 and polymer residues on graphene from transfer would lead to non-uniform graphene coverage.

To work with hBN, it needed to be transferred to the desired substrate. Several transfer processes, each with their own advantages and disadvantages have been reported in literature. The two most common methods of transfer are wet transfer and electrochemical delamination and both methods were tested in the project [144, 145]. The transfer process discussed here is quite general for 2D materials grown on a metal catalyst.

4.1.1 Wet transfer

The process for wet transfer involves spin coating a polymer layer, in our case poly(methyl methacrylate) (PMMA) , with a molecular weight of 950k, on the top side of commercial ML-hBN sample on Cu. The ML-hBN sample has multilayer on both sides of the Cu foil, a side effect of the CVD process as the precursors contact the underside of the Cu foil. However, as the underside has poorer quality of material, only the top side is transferred. The spin coating was performed at 1000 rpm spin speed and 1500 rpm/s spin acceleration for 60 s. It is then gently baked at 60 °C for 120 s to remove the solvent. This should lead to a 400 nm thick film according to the spin curve of PMMA, which is sufficient to support the hBN film. The underside of the PMMA/hBN/Cu/hBN sheet was then exposed to oxygen plasma in a reactive ion etching (RIE) chamber at 10 W, with a flow rate of 80 sccm for 150 s. This step was necessary to remove islands of hBN that could potentially protect the Cu layer from the etchant solution, leading to incomplete etching of Cu. The etchant solution was 0.1 M ammonium persulfate solution (APS) . This concentration was chosen as it was sufficient to completely etch 20 µm thick Cu films, and a low concentration would lead to a slower etch rate and lead to less damage to the films and ionic contamination. The PMMA/hBN/Cu sheets were then carefully cut into smaller 1 cm×1 cm pieces. The pieces are then floated on top of the etchant solution, with the Cu side exposed to the APS solution. It is imperative that minimal folding occurs at this time, as wrinkles induced during the handling of the pieces can break the surface tension of the solution and cause it to sink. This results in the PMMA/hBN to become difficult to 'fish out' and can also cause incomplete etching. The etching is performed over night in order to ensure complete dissolution of the Cu layer. After dissolving the Cu layer, the PMMA/hBN films remained afloat on the surface of the solution and was subsequently transferred to a bath of deionised water using a glass slide. The deionised (DI) water rinses removed ionic contaminants from the APS solution. The films were floated in the DI water baths for a duration of 10 minutes and repeated 2 times. The films were then extracted onto the desired substrate and were allowed to dry overnight at room temperature. This ensures a slow rate of evaporation of trapped water molecules without bubbling, which can cause tearing of the hBN film. Before the PMMA layer is

removed, the PMMA/hBN/substrate is heated from 50 °C to 130 °C in 20°C steps, with the device being held at each temperature for 10 mins, with the final step being performed for 20 mins. The gentle heating is an additional step to ensure no bubbling of trapped water that was not removed during drying occured. Heating the sample to 130 °C allows the PMMA to transition into its glass phase, and thereby push against the hBN to cause stronger adhesion to the substrate. This also flattens rolling striations imprinted on the PMMA layer due to the surface morphology of the Cu substrate. The device was then immersed in acetone overnight to remove the PMMA layer, after which the sample was rinsed in IPA (Isopropyl alcohol) and dried under N_2 flow. Fig. 4.1 shows a summary of the wet transfer process.

4.1.2 Electrochemical delamination

The process of electrochemical delamination is similar in many ways to the wet process, such as with the usage of a protective PMMA layer during the transfer. Before spin coating however, the hBN/Cu/hBN sheet is soaked in a 50:50 solution of ethanol and water overnight to cause Cu to oxidise, which is known to cause delamination of hBN at lower voltages.

After oxidising the copper, spin coating is performed using the same parameters used in wet transfer. A solution of 1 M sodium hydroxide (NaOH) is prepared to be used as an electrolyte. The PMMA/hBN/Cu is held using a metal tweezer and connected to the negative terminal of a direct current voltage source. A gold wire is connected to the positive terminal to form the anode and is immersed in the electrolyte. The PMMA/hBN/Cu sheet is then gently lowered into the electrolyte using the metal tweezers. Electrochemical delamination occurs due to the formation of H_2 bubbles at the interface between hBN and copper catalyst and due to the decomposition of the intercalated electrolyte. The H_2 bubbles push the PMMA/hBN layer away from the copper substrate and once fully delaminated, the PMMA/hBN film floats on top of the electrolyte. The rest of procedure is identical to wet transfer, from the deionised water baths to PMMA removal.

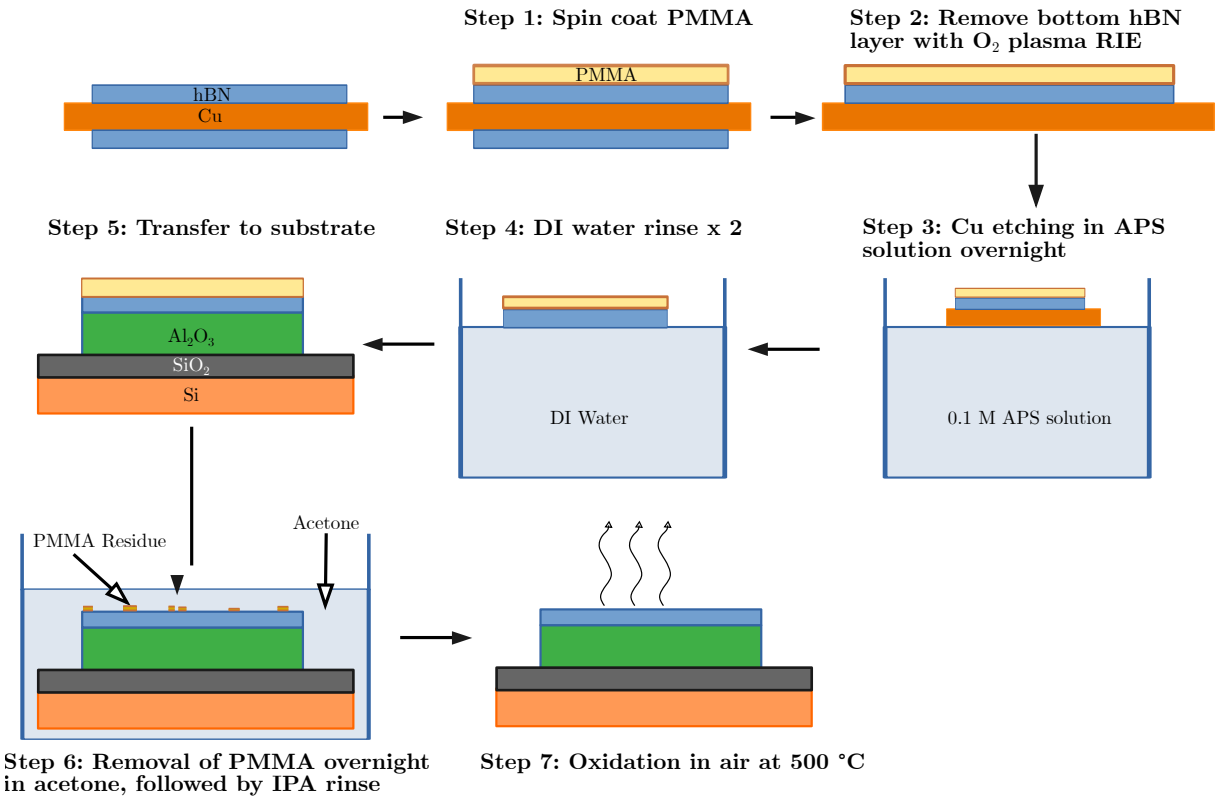

Figure 4.1: An outline of the steps of wet transfer using APS to remove the Cu substrate.

4.1.3 Liquid-Phase Exfoliation (LPE)

hBN flakes in solution (50:50 ethanol:water) were sonicated before being dropcast on the substrate. Sonication disperses the flakes in solution and exfoliates thicker flakes into thinner sheets. This occurs as ethanol and water are polar solvents and can induce stronger attractive forces on the hBN flakes. During sonication, the attractive force between the solvent molecules and the hBN sheets and collision between the intercalated solvent molecules and hBN lead to layers peeling off. Sonication is crucial to obtain a uniform density of flakes on the substrate. A pipette dropper is then used to drop cast the flakes onto the substrate. The LPE flakes had a thickness of 1-5 monolayers and a lateral dimension of 10-50 nm.

The benefit of using flakes obtained by LPE is that lack of polymer residue due to transfer, which can be a source of broad background luminescence in CVD films transferred from growth catalysts using the above methods. However, the lack of uniformity of flakes sizes and thicknesses and incomplete coverage of the substrate by the flakes is a

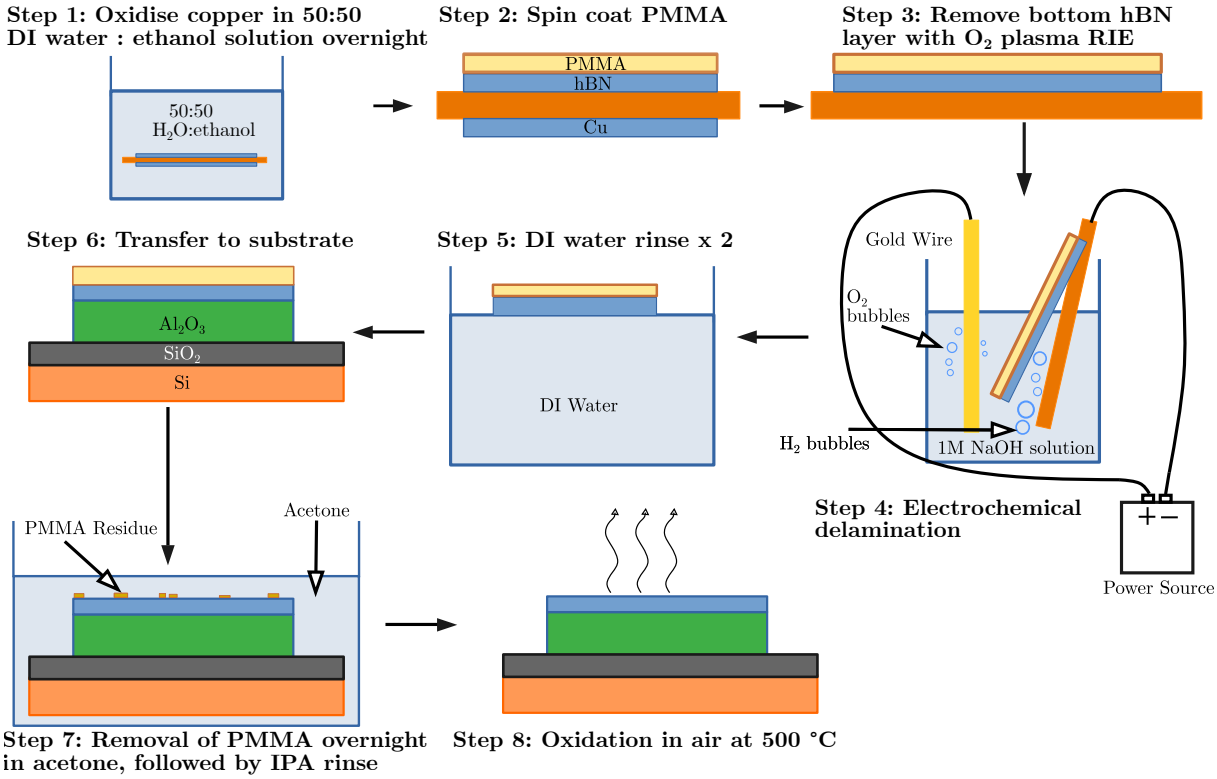

Figure 4.2: An outline of the steps of electrochemical delamination process using NaOH as the electrolyte.

major drawback when compared to CVD hBN films.

4.1.4 Atomic layer deposition (ALD)

ALD is used to deposit various thin films on substrates from vapour phase and has the benefit that it allows Angstrom level control over film thicknesses during growth. The principle feature of ALD that allows this is the self-saturating nature of each growth cycle [146]. In this project, various thickness of aluminium oxide (Al_2O_3) films were grown on graphene.

The general ALD process for metal oxides is shown in Fig. 4.3. Unlike CVD, in ALD the chemical precursors, A and B, are introduced in alternate pulses and react with the substrate and each individual gas-reaction are known as 'half-reactions'. For metal oxide growth, the first precursor, A, is an organometallic species and B is a counter-reactant or oxidant precursor, such as H_2O or Ozone. For the growth of Al_2O_3, trimethylaluminium

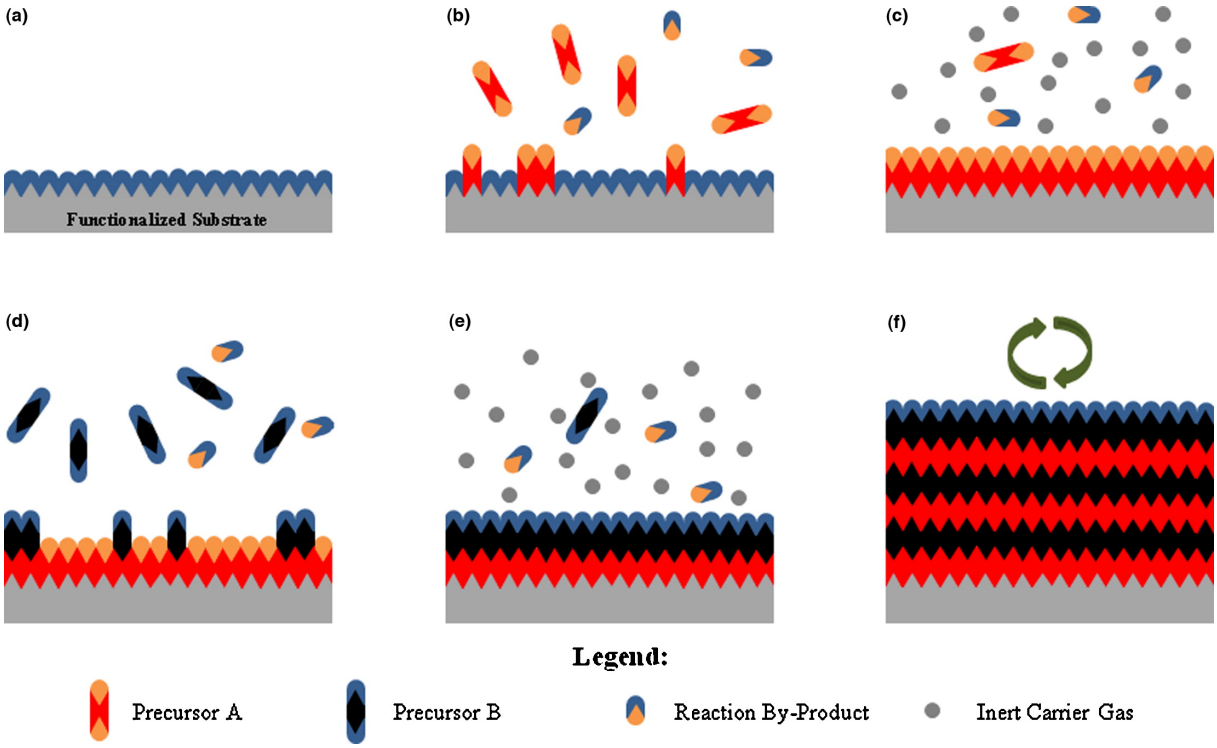

Figure 4.3: A schematic of the self-limiting process in ALD. **(a)** The substrate surface is functionalised or has natural functionalisation to lead to nucleation sites for precursors. **(b)** The organo-metallic precursor A is pulsed and reacts at the nucleation sites. **(c)** The excess precursor is purged by an inert carrier gas. **(d)** The counter-reactant precursor B is pulsed, which reacts with the products of the reaction of precursor A and the functionalised surface. **(e)** The reaction by-products and excess precursor B is then purged by the inert carrier gas. **(f)** To achieve the desired thickness, steps **(b)** to **(e)** are repeated as necessary. The figure has been reproduced from Ref. 17.

(TMA) was used as precursor A and H_2O as precursor B. The two half-reactions and the full equation is,

$$x\,(-\mathrm{OH}) + \mathrm{Al(CH_3)_3} \longrightarrow \mathrm{O}_x\!-\!\mathrm{Al(CH_3)_{3-}}_x + x\,\mathrm{CH_4} \tag{R1}$$

$$\mathrm{O}_x\!-\!\mathrm{Al(CH_3)_{3-}}_x + \frac{3}{2}\,\mathrm{H_2O} \longrightarrow \mathrm{O_{3/2}\!-\!Al\!-\!(OH)}_x + 3\!-\!x\,\mathrm{CH_4} \tag{R2}$$

$$\mathrm{Al(CH_3)_3} + \frac{3}{2}\,\mathrm{H_2O} \longrightarrow \frac{1}{2}\,\mathrm{Al_2O_3} + 3\,\mathrm{CH_4} \tag{R3}$$

For the first half-reaction, Eqn. R1, precursor A is pulsed into the reaction chamber which is under vacuum, usually on the order of 0.1 Torr, and pulse times are set such that there is sufficient time for the precursor to fully react with all the nucleation sites,

which are usually existing hydroxyl groups ($-(OH)$) on the surface of the substrate. A product of this reaction is $O_x-Al(CH_3)_{3-x}$ at the nucleation site. After the pulsing of A, the chamber is evacuated by purging the precursor by an inert carrier gas, usually Ar or N_2. Precursor B is then pulsed and reacts with the $O_x-Al(CH_3)_{3-x}$ sites to form $O_{3/2}-Al-(OH)$, which is equivalent to the growing alumina lattice $\frac{1}{2}Al_2O_3 + x-(OH)$, Eqn. R2. Precursor B and the reaction by-products (CH_4) are then purged before the process is repeated again. The $-(OH)$ groups act as nucleation sites for the next cycle. This leads to layer-by-layer growth of the oxide and ideally should lead to conformal and uniform growth of the oxide film. As the growth per cycle in ALD is well-defined, the desired thickness of the film can be achieved by repeating the process the appropriate number of times.

The quality of the ALD film is influenced by many factors, such as deposition temperature, residence time of each precursor, purge times and availability of nucleation sites [146]. At low deposition temperatures, there may not be sufficient energy for the surface reactions to reach completion and a very high temperature leads to desorption of the reactive species at the nucleation sites [147]. The former leads to a poor quality film and the latter leads to a porous film with a very slow growth rate. Therefore, there is a window in which the ALD process occurs efficiently. A longer residence time for each precursor aids the saturation of all available nucleation sites, however also increases the process time as each cycle will be significantly longer. A short purge time can lead to insufficient removal of each precursor before the next is pulsed in, and this can lead to gas-phase CVD like reactions in the chamber, resulting in powder like deposition on the substrate rather than continuous films. A long purge time avoids CVD like reactions but has the same effect as increasing the temperature as this leads to higher probability of desorption of the reactive species at the nucleation sites. Finally, the substrate itself may be inert and possess a low density of nucleation sites, which may lead to islands of the oxide forming, and several cycles may be required before the islands coalesce to form a continuous film.

4.1.5 Electron beam lithography (EBL)

The uniform Al_2O_3 layer, once grown on graphene needed to be patterned to ensure quenching of emitters in hBN in all regions except those with an intermediate oxide layer. EBL was used to pattern the oxide layer. EBL is a direct writing technique in which an electron beam (e-beam) is scanned across a surface, leading to a modification in the chemical properties, such as its solubility. By controlling the position of the electron beam, custom designs of structures can be written directly onto surfaces. This allows a digital image of the pattern to be transferred onto the substrate [148]. EBL has a higher resolution than standard optical lithography using ultraviolet (UV) light (not deep or extreme UV), due to the shorter wavelength of the electrons associated with its higher energy (10-100 keV). The pattern is written onto an e-beam resist and depending on the type of resist, its solubility in developers changes differently. By immersing the device with the exposed resist in the developer, the unexposed regions/exposed regions are specifically removed, leaving behind a patterned developer.

Two types of resists have been used in this project. A positive tone resist, PMMA, to allow the deposition of registration markers and a negative tone resist, Ma-N-2410, for the patterning of the Al_2O_3 layer. Positive tone resists become soluble in the developer when exposed to the electron beam, due to the backbone of the chain being broken by the beam, whereas for negative tone resists cross-linking of the polymer chains upon exposure to the e-beam leads to its insolubility in the developer [148].

The procedure for lithography using PMMA involved spin coating at 1800 rpm, with a spin acceleration of 1500 rpm/s for 60s, leading to 300 nm thick resist layers according to the spin curve, Fig. 4.4a. This was then baked at 80 °C for 75 s. After e-beam exposure, the resist was developed using a 15:5:1 IPA:MIBK:MEK (Isopropyl Alcohol: Methyl isobutyl ketone: Methyl Ethyl Ketone). The sample with the exposed resist was immersed in this solution for 10 s and then removed and dried under nitrogen (N_2) flow for 10 s. A 5 nm thick adhesive layer of Cr, followed by 100 nm of Au was then deposited via thermal evaporation on the developed regions to form registration marks. The device was then soaked in acetone overnight and the Cr/Au layer was then lifted off by flowing acetone with the help of a syringe to remove the PMMA layer, leaving behind registration marks.

(a)

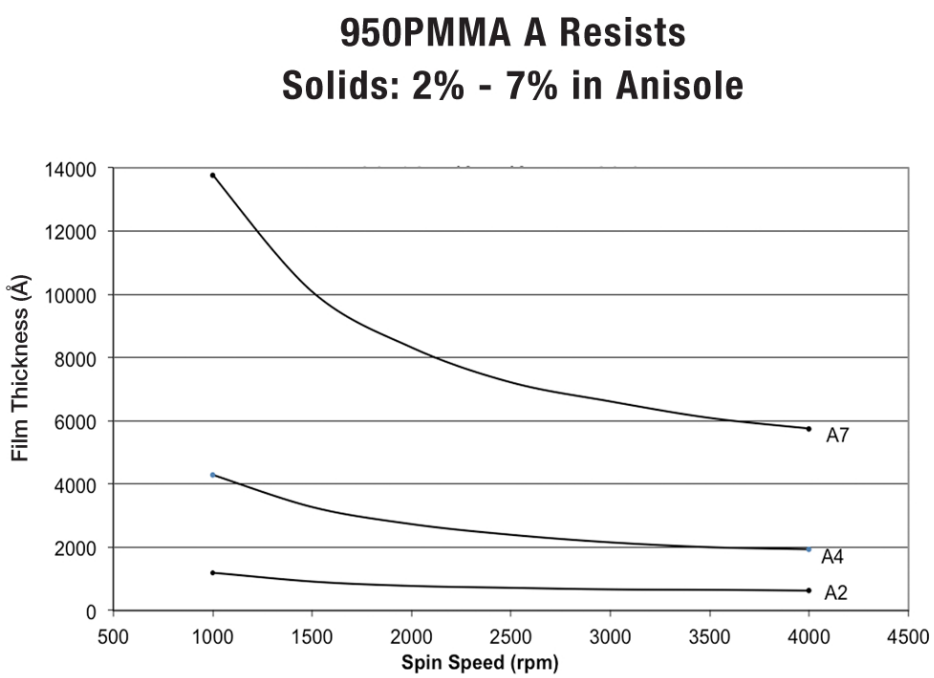

Figure 8

(b)

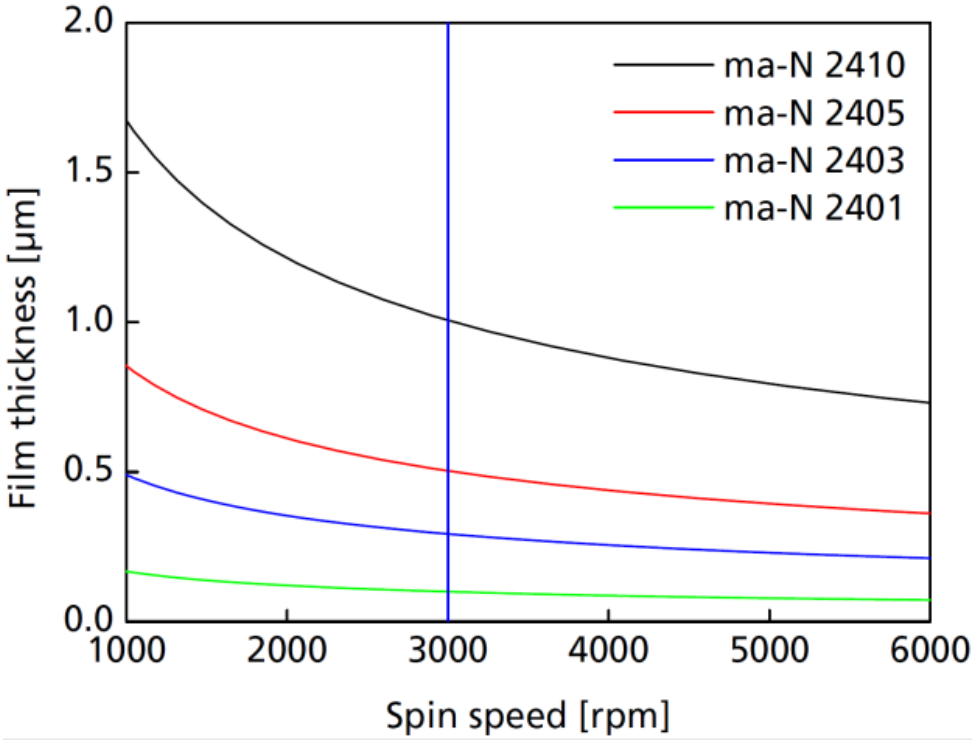

Figure 4.4: The spin curves for **(a)** PMMA 950 A4 and **(b)** Ma-N-2410. Fig **(a)** has been reproduced from Ref. 18 and Fig. **(b)** has been reproduced from Ref. 19.

For Ma-N-2410, the spin coating was performed at 6000 rpm, 1500 rpm/s spin acceleration for 60 s, which would have lead to a 700 nm thick resist layer according to the spin curve, Fig. 4.4b. The wafer was baked at 90 °C for 150 s. After e-beam exposure, it was developed with ma-D-525, a 2.5 % tetramethylammonium hydroxide (TMAH) solution, for 6 mins. Care was taken to avoid UV light exposure as Ma-N is photosensitive to UV light. The Al_2O_3 layer was then etched in a 3:1 85 % phosphoric acid (H_3PO_4):deionised water at 80 °C for 210 s, which was sufficient to etch 30 nm of Al_2O_3. The wafer was subsequently rinsed in DI water and IPA and the exposed Ma-N-2410 was fully removed using acetone and IPA.

The sample preparation of this step, development of resist and etching of Al_2O_3 was done by the thesis author. The lithography process was supported by the Henry Royce Institute for advanced materials through the Equipment Access Scheme enabling access to the Electron-beam Lithography Facility at Cambridge; Cambridge Royce facilities grant EP/P024947/1 and Sir Henry Royce Institute - recurrent grant EP/R00661X/1). Ermanno Miele and Jon Griffiths are acknowledged for their support for the lithography step.

4.2 Spectroscopy techniques

4.2.1 Raman spectroscopy

The principle behind Raman spectroscopy is the process of Raman scattering. This is an inelastic scattering process that occurs when an incident photon interacts with a crystal or molecules, causing a modification of its vibrational state [149].

During Raman scattering, an electron is excited to a virtual state. This state is a coupled state of the electron and photon. When the electron relaxes, it can either relax into a higher, lower energy or the same vibrational state as it was in before excitation. A change in vibrational state leads to a photon with a different energy being emitted, where the shift corresponds to the energy difference between the initial and final vibrational states. The scattered light is detected and the shift in energy, usually given in units of wavenumbers, cm^{-1}, is determined. The scattered photon either has a greater (anti-

Stokes) or lesser (Stokes) energy than the incident photon [149], and the shift in frequency is described by:

$$\omega_{\mathrm{i}} = \omega_{\mathrm{s}} + \omega_{\mathrm{p}} \tag{4.1}$$

ω_{i} is the incident photon frequency, ω_{s} is the scattered photon frequency and ω_{p} is the energy of final vibrational phonon mode of the crystal. Raman spectroscopy reveals the vibrational modes of the material that lead to a change in its polarisabilty. The vibrational modes are a unique property of the material, related to a materials crystallinity, lattice structure and the atoms comprising it. Therefore it is a very powerful tool when characterising the quality of transferred hBN films.

A schematic of the setup for Raman spectroscopy is depicted in Fig. 4.6. For hBN, the defining feature is a peak at a Raman shift of 1366 cm^{-1} [2]. In terms of vibrational modes, hBN exibits a degenerate Raman active E_{2g}, Figs. 3.2a and 3.2b, mode at 1366 cm^{-1} for bulk hBN (1370 cm^{-1} for monolayer) [20, 100, 101]. The intensity of the Raman peak increases with the number of layers and the peak position is usually red shifted by $\sim$4 cm^{-1} (as shown in Figure 4.5) [20]. From the inset in Figure 4.5, it can be seen that the intensity increases linearly with thickness, in discrete increments, and therefore by comparing the intensity of a hBN sample with known thickness and another with unknown thickness, the thickness of the sample can be determined. The linewidth is also a good indicator of defect density, a larger linewidth corresponds to higher defect densities. The Raman measurements were performed using the Renishaw Invia Microscope, with a 532 nm excitation laser and 100$\times$ objective.

4.2.2 Photoluminescence (PL) Spectroscopy

The setup for PL spectroscopy is identical to the Raman setup Fig. 4.6. Here, instead of calculating the shift, the absolute wavelength is detected and measured. The PL spectrum is related to the electronic transitions between the relevant defect states. Colour centres in hBN have been known to emit majority of its emission in the ZPL, and therefore has a sharp ZPL, that can be fit with a Lorentzian lineshape. The linewidth of the Lorentzian is used as a measure of the excited state lifetime. The percentage of the total intensity of PL emission that is present in the ZPL, W, and defects in hBN are characterised by

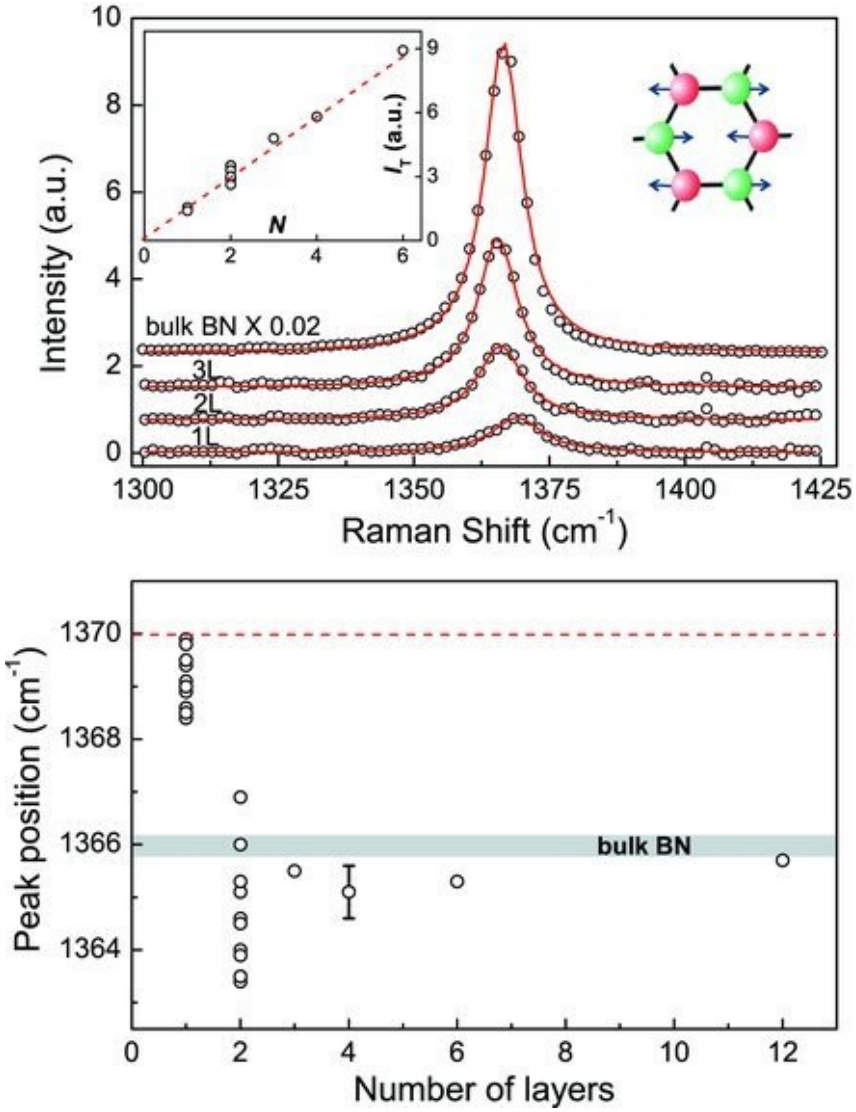

Figure 4.5: Variation of the Raman shift of the E_{2g} mode in hBN with thickness. The figure has been reproduced from Ref. [20].

their large W of approximately 82 % [3].

Depending on the method of fabrication of hBN, the types of defects that can occur vary significantly [3, 55]. The electronic states involved in the transition can vary based on the nature of the defect, resulting in a large variation in the ZPL wavelengths. hBN grown using MBE and CVD have emitters that emit light at around 600nm, [47, 52], whereas hBN flakes obtained from exfoliation, possess emitters that emit a range of wavelengths from 300 nm to 850 nm [55]. Therefore PL spectroscopy allows the probing of the nature of the defect which is a source of single-photon emission. In this thesis, visible light

emitters with ZPL wavelengths at 570 nm and beyond were studied.

The spectroscopy measurements were performed using the same setup as the Raman measurements, but in PL mode. To prevent bleaching, a laser transmissivity of 10% was used, compensated with a long dwell time of 2 s per pixel to obtain a spectrum with sufficient signal to noise ratio. The excitation wavelength was a 532 nm continuous wave laser and the spectrum was obtained with 1200 g/mm diffraction grating, allowing a spectral resolution of 0.1 nm. This allowed the spectrum to be collected over a spectral bandwidth of $\sim$ 90 nm.

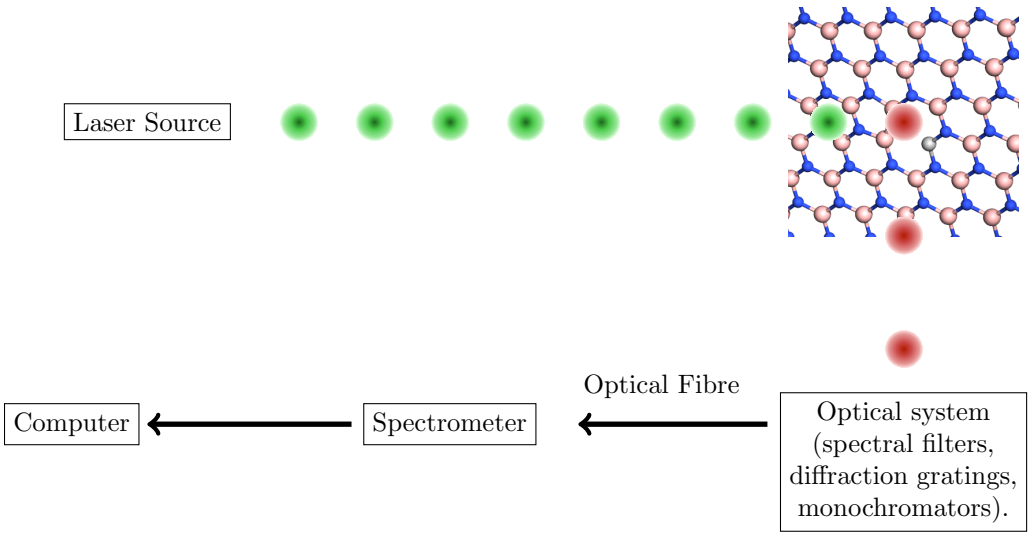

Figure 4.6: Schematic of PL and Raman spectroscopy. In PL spectroscopy the absolute emission wavelengths are measured whereas in Raman spectroscopy the difference between the excitation and emission wavelengths are measured.

4.2.3 Confocal PL mapping

All the optical measurements performed have utilised a confocal setup. Confocal imaging differs from widefield methods through the usage of a pinhole that rejects light with a source located in an out-of-focus plane, Fig. 4.7. This results in a higher resolution than widefield microscopes. In a laser scanning confocal setup, a mirror guides the laser spot across the sample and the scattered light intensity at each step of scan is recorded as a pixel.

As this project was performed over two locations, the University of Cambridge and Newcastle University, two different confocal setups were used at each site. At the University of Cambridge, the confocal PL map was performed using the Olympus FluoView FV1200 Confocal Inverted Microscope. Measurements were recorded using a 60× oil immersion lens with a 1.35 numerical aperture (NA). The excitation source was with a 15 mW 473 nm continuous wave laser, and the detectors were metal-alkali photomultiplier tubes. The system has a variable confocal aperture up to 800 µm. A 560-620 nm band pass filter was also applied to filter out the excitation wavelength and focus on the emission wavelengths most commonly reported in literature. A dwell time of 200 µs per pixel was found to be sufficient to obtain sufficient signal from emitters. At Newcastle University, the Zeiss LSM 880 Airyscan confocal microscope was used. The parameters for mapping were similar to that used in Cambridge, apart from the excitation being a 561 nm diode laser and GaAsP detectors were used. This is not expected to significantly affect the number of observed emitters as majority of the emitters are known to have ZPLs at wavelengths at or beyond 580 nm. The LSM 880 also has spectral scanning capabilities, with a maximum resolution of 3 nm. As this is less than the linewidth of ZPLs in hBN it was possible to simultaneously obtain spectroscopic information while imaging an emitter.

The confocal PL map was able to be performed much faster than the hyperspectral PL map due to the lower shot noise and read-out noise of the detectors used. The charge-coupled detector (CCD) used in the Raman microscope has a higher dynamic range but a lower sensitivity than PMTs, and therefore each pixel acquired in a map required orders of magnitude longer exposure time per pixel. A long exposure time could lead to emitter bleaching and affecting the intensity measured at each point. The high signal-to-noise ratio of PMTs facilitated a significantly shorter exposure time per pixel and allowed the use of lower laser excitation power, reducing the risk of photobleaching of emitters. However, the lack of spectroscopic capabilities, and hence the source of emission, which could be background emission from hBN or colour centres, cannot be confirmed using this setup alone. Therefore a methodology was adopted where quick intensity maps were performed to identify regions of bright emission, followed by hyperspectral maps of the regions of interest to obtain the spectra of emitters to provide evidence of their source as

defects in hBN.

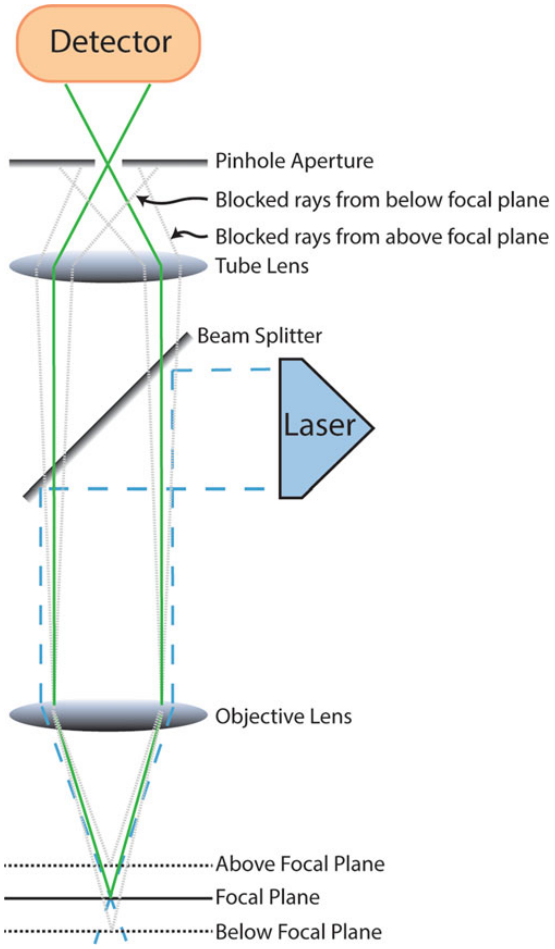

Figure 4.7: Optical path of a laser scanning confocal microscope. The figure has been reproduced from Ref. 21.

4.2.4 Ellipsometry

Ellipsometry is an optical method of determining the thickness of films. The principle behind ellipsometry has been outlined as follows, a detailed description is available on Ref. 150. Light waves can be *s*-polarised (polarised perpendicular to the plane of incidence) or *p*-polarised (parallel to the plane of incidence). Spectroscopic ellipsometry is highly sensitive to the film thickness. When light with s and p components is incident on the sample, the polarisation components of the reflected light incur a change in their intensities and phases. These shifts are determined by the thickness of the film and di-

electric constants. In spectroscopic ellipsometry, the variations in the intensity of the polarisation components of the reflected light and phase delay between the polarisation components are measured for a range of incident light polarisations and wavelengths. The two parameters (Ψ, Δ) that are used to describe the polarisation state of the reflected light are,

$$\rho = \tan\Psi \exp i\Delta \equiv \frac{r_\mathrm{p}}{r_\mathrm{s}}, \tag{4.2}$$

or in the case of transmitted light,

$$\rho = \tan\Psi \exp i\Delta \equiv \frac{t_\mathrm{p}}{t_\mathrm{s}}, \tag{4.3}$$

where r_p and t_p are the amplitudes of the p-polarised reflected or transmitted light, respectively. r_s and t_s are the s-polarised reflected and transmitted light amplitudes. $\Delta = \delta_\mathrm{rs} - \delta_\mathrm{rp}$ or $\Delta = \delta_\mathrm{ts} - \delta_\mathrm{tp}$ is the phase difference between the s- and p-polarised components of the reflected light or transmitted light. $\tan\Psi = \frac{|r_\mathrm{s}|}{|r_\mathrm{p}|}$, is the ratio of the amplitude of the reflected s- and p- polarised light.

After the collection of ψ and Δ values for various wavelengths, a model of ρ is constructed based on the known optical constants of the composite layers of the sample under study,

$$\rho = f(N_0, N_1, ..., N_n, d_0, d_1, ..., d_N, \theta_0) \tag{4.4}$$

where N_x and d_x with $(x = 0, 1, ..., N)$, represent the complex refractive indices and thickness of each component layer and θ_0 is the angle of incidence of light on the sample. This model is then fit to the measured values using d_x as a free parameter to determine the thickness of each layer.

In this study, ellipsometry was used to determine the thickness of Al_2O_3 films grown using ALD on graphene for varying number of cycles. This allowed the determination of the growth per cycle, which was used in subsequent fabrication steps to grow the desired thickness of oxide layer.

Ellipsometry measurements were performed with an EP4 SIE (Park Systems Gmbh, Göttingen), with a spectral range between 400 to 900 nm and a 5 nm output bandwidth. The reflected light is collected through compensator and an analyzer and a 20× or 50× objective to a 1392×1040 pixel CCD camera, allowing for a lateral resolution down

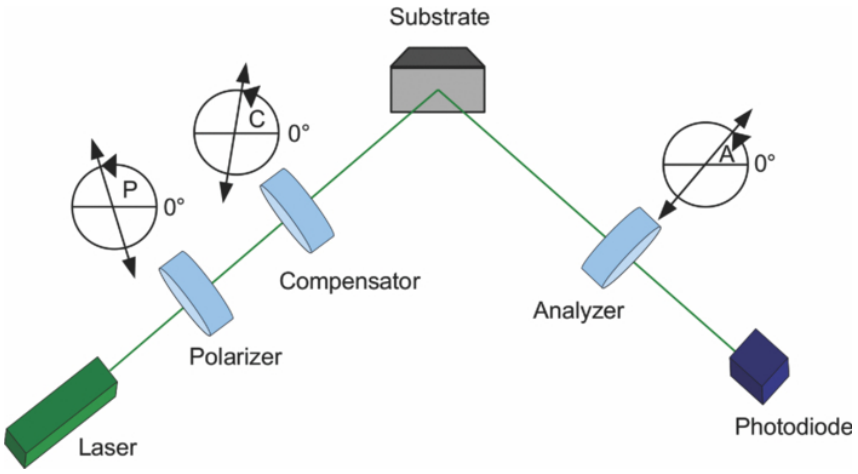

Figure 4.8: Optical pathway of an ellipsometer showing the polarisers and compensators, which combine to produce light polarised between linear to circular polarisation, depending on the orientation of the compensator with respect to the linear polariser, to be incident on the sample, and the analyser which only permits reflected light polarised along its polarisation axis to be transmitted for detection. The figure has been reproduced from Ref. 22.

to 1 µm. The spectra used for fitting the thicknesses are recorded as a signal average over an approx. 10 µm × 10 µm homogeneous region of interest (ROI) via the single-point measurement mode at 51 equidistant λ points along the 400 to 900 nm range. The ellipsometry measurements were performed in the nulling mode. Figure 4.8, shows a schematic of the optical path of the ellipsometer for this mode of operation.

4.3 Microscopy techniques

4.3.1 Scanning electron microscopy (SEM)

The resolution of a microscope can be determined by the Abbe limit:

$$d = \frac{0.612\lambda}{n \sin\theta} \tag{4.5}$$

where d is the minimum resolvable distance between two points, λ is wavelength of the excitation source (laser or electron beam), and $n \sin\theta$ is the numerical aperture (NA), where n is the refractive index of the medium in which sample is immersed. Typically for optical microscopes, this is ~ 200 nm. Hence, the resolution of optical microscopes is well

above the diameters of the liquid exfoliated flakes and pinholes in the growth of Al_2O_3 films. Furthermore, transparent samples, such as CVD grown hBN films have low optical contrast and effects due to thin film interference is the main resource when optically identifying the films on the substrate. SEM allows the imaging of these nanometer sized features of interest and transparent films. This is because of the higher energy of the electron beam when compared to visible light, which leads to the electrons possessing a significantly shorter de Broglie wavelength. From Eqn. 4.5, as the resolution d is proportional to the wavelength, smaller features can be observed. This allows the visualisation of surface morphologies of thin films and detailed analysis of their coverage.

SEM works by scanning an electron beam across the sample and detecting scattered electrons. The electron beams are scattered by both elastic and inelastic scattering processes, and generate back-scattered electrons (BSE) and secondary electrons (SE), Fig. 4.9a. The secondary electrons are generated by inelastic scattering of the primary electron beam (SE1) and back-scattered electrons (SE2) [23]. The in-lens detector placed directly above the sample is used to detect SE1 and the Everhart-Thornley (ET) detector is used to detect SE2, Fig. 4.9b. The SE arise from the surface of the sample and are used when studying thin films. The SEM images were obtained using the ZEISS Gemini 300 SEM. The imaging parameters used were 5 kV primary beam voltage, 30 µm aperture size, and a working distance of 4.5–5 mm.

4.3.2 Atomic force microscopy (AFM)

Atomic force microscopy is a complementary technique to ellipsometry when measuring thicknesses of films. An AFM consists of a cantilever probe with a sharp tip mounted to a piezoelectric (PZT) actuator and a photodetector that is sensitive to displacement to detect a laser beam reflected off of the end-point of the cantilever to determine the state of the cantilever [151]. During operation, the tip is scanned over the sample surface while maintaining a constant force or height above the surface. As the tip scans over the surface, it moves up or down along with the contours and variations in the deflected laser light intensities at the photodetectors are measured.

There are three main modes of operation of an AFM, i.e non-contact, contact and

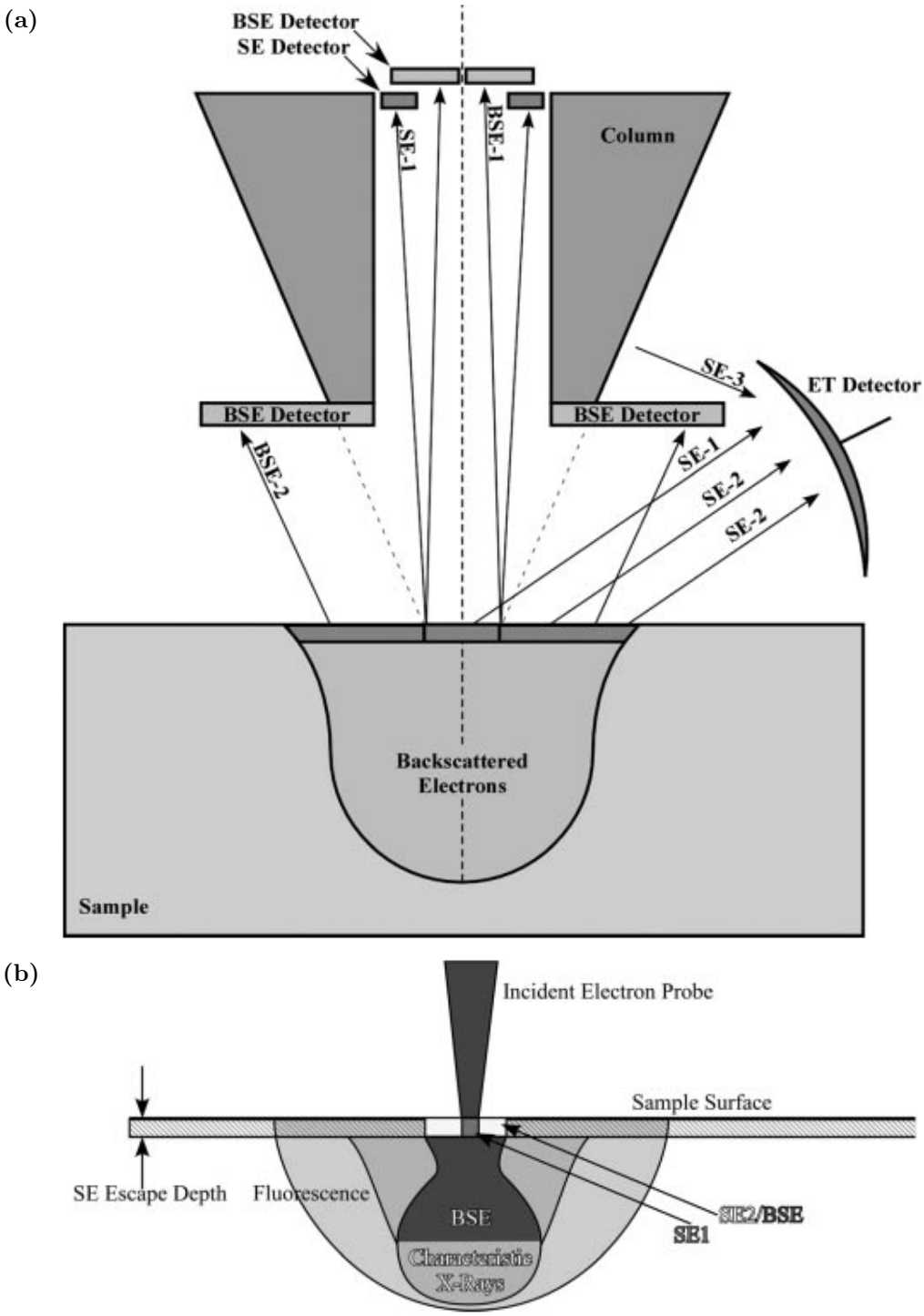

Figure 4.9: **(a)** Schematic showing the trajectory of the scattered electrons and the detectors used to detect the various scattered electrons. **(b)** Schematic of region of the sample from which the various scattered electrons and radiation used for imaging arise from. Fig. **a)** and **b)** have been reproduced from Ref. 23.

tapping modes. In this thesis, the AFM was operated in the tapping mode and its working principle is briefly outlined as follows. Fig. 4.10 shows the tapping moder of operation of the AFM. In this mode, the cantilever is driven to oscillate at its resonant frequency or near resonant frequency. The PZT actuator applies a force at the base of the cantilever to cause it to oscillate between 20-100 nm when away from the sample surface [151]. The tip is lowered to gently make contact with the sample surface and as it oscillates, it taps the surface. As the tip is scanned across the surface, the oscillation amplitude is kept constant in a feedback loop. As the tip encounters steps or depressions, it experiences a shift in the vibration amplitude and the optical system measures this change and it is fed back to the controller which uses a reference value to generate an error signal. The PZT actuator is then activated in response to the error signal to maintain a constant oscillation amplitude. This error signal is plotted as function of the lateral position of the cantilever, allowing the mapping of surface irregularites.

As the lateral dimensions of some of the features in the final device structure are below the resolution limit of the ellipsometer 1 µm, it was not suitable for measuring the step heights of these features. AFM acts as an alternative to ellipsometry to determine the dimensions of these features.

AFM measurements were taken in the tapping mode by Asylum Research AFM. Resonant frequency of the tip is 300kHz, and the initial set-point and gain settings were 700 mV and 8.1 V, respectively. The AFM image was analysed by the software Gwyddion. Then the height contrast between different layers were measured by drawing the cross-axis profiles.

4.4 Summary

In this chapter the experimental methods used in this thesis were introduced. These include a range of nanofabrication techniques, such as 2D material transfer, ALD and EBL. Characterisation techniques to determine the quality of the fabricated device and the presence of hBN colour centres include confocal PL image and spectroscopy, Raman spectroscopy, ellipsometry, SEM and AFM. In the next chapter, these experimental tech-

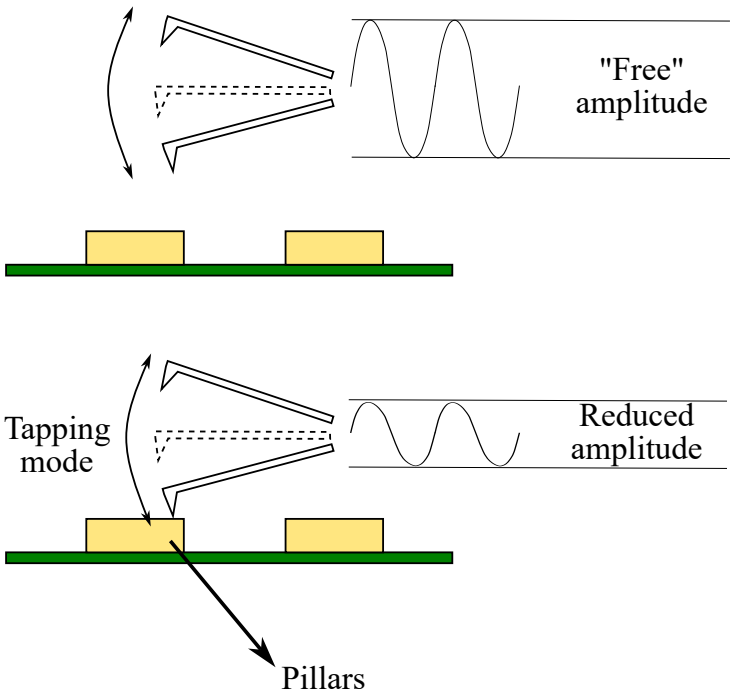

Figure 4.10: Shows the oscillation amplitude of the AFM cantilever when away from the sample (top) and in contact with the sample (bottom) in tapping mode.

niques will be used to fabricate devices that exploit charge control to localise emission to particular regions of the device.

Chapter 5

Experimental Results

In this chapter the results from the experimental device fabrication is discussed. The aim of the experimental work was to fabricate a device that exploited charge and energy transfer to restrict emission from defects to specific sites. The design of the device built on the work done in Ref. 7 where a patterned graphene layer was used to localise emission from a top hBN layer. In Ref. 7, holes were patterned in the underlying graphene layer and trilayer hBN hosting SPEs were transferred on top. Due to charge and energy transfer between defects in hBN and graphene, as explored in the theoretical sections, quenching of emission occured in regions where graphene was present, leading to localisation of emission. However, graphene is a key material when fabricating vertical heterostructures to apply electric fields across hBN and inject carriers.

In this thesis, an Al_2O_3 layer grown using ALD on graphene acts as a barrier to quenching between hBN and graphene. The alumina layer is patterned into grids to expose specific regions of hBN to graphene, with the aim of allowing quenching in all regions except those where Al_2O_3 is present.

Author contribution

The author of this thesis has performed all the work discussed in this section. An exception to this is in the Ar annealing of samples to activate emitters, which was aided by Dr. Vitaly Babenko at the University of Cambridge.

5.1 Tunnel barrier design

Before growing the tunnel barrier, the minimum thickness of alumina needed to prevent quenching needs to be determined. Here two processes that can lead to quenching are considered: charge transfer due to tunneling of charge carriers between hBN and graphene and Förster resonance energy transfer.

5.1.1 Variation of charge tunneling rate with barrier thickness

Studies have shown that Al_2O_3 can be a suitable tunnel barrier for light emitting diodes (LEDs) based on hBN [29]. Hence, it was chosen as the material to act as a tunnel barrier in this study.

According to Bardeen's tunneling theory, the tunneling rate is given by Fermi's golden rule where the initial and final states correspond to the source and drain of the heterostructure [152]. The tunneling operator is then given by $H' = i\hbar J$, where J is the probability current operator [152]. From Fermi's golden rule, the tunneling rate W can be expressed as,

$$W = \frac{1}{\tau} = \frac{2\pi}{\hbar}|\langle f|H'|i\rangle|^2 \rho_{\mathrm{gra}} f_{\mathrm{gra}}(1 - f_{\mathrm{hBN}}). \tag{5.1}$$

Here τ is the tunneling lifetime, $|i\rangle$ and $|f\rangle$ are the initial and final states respectively, ρ_{gra} is the graphene DOS, and f_{gra} and f_{hBN} are the occupancy of the initial (final) states in graphene (hBN). The final defect state into which the transition will occur is considered to be empty, so the final term in the product reduces to unity. From the band diagram, it can be assumed that the tunneling rates are symmetric in both directions, and only the rate in one direction needs to be calculated. Following the derivation in Ref. 152, the tunneling matrix element for a rectangular barrier can be expressed as,

$$M_{if} = |\langle f|H'|i\rangle|^2 = \frac{16\hbar^4\kappa^2k^2}{m^2(\kappa^2 + k^2)^2} e^{(-2\kappa d)}. \tag{5.2}$$

Here, k is the wavevector of the incident electron in graphene, κ is the wavevector corresponding to the exponential decay in the barrier, d is the Al_2O_3 barrier thickness,

and m is the free electron mass. As the incident wave is modelled as a free particle, $\psi_i = Ae^{(ikx)}$, the form of κ and k are given by,

$$k = \sqrt{\frac{2m}{\hbar^2}E}, \qquad \kappa = \sqrt{\frac{2m}{\hbar^2}(\phi_0 - E)} \tag{5.3}$$

where E is the energy of the electron from the Dirac point of graphene and ϕ_0 is the barrier height from the Dirac point.

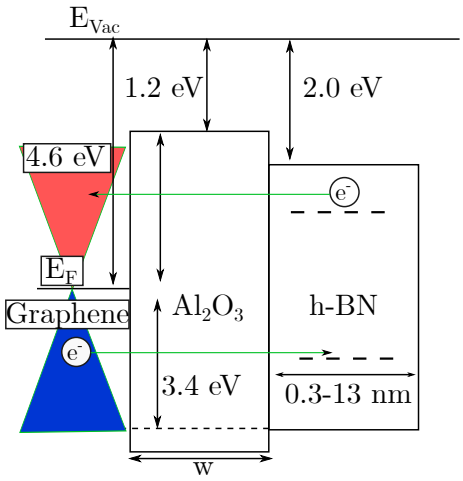

Figure 5.1: The band structure of the hBN/Al_2O_3/Gr heterostructure. The electrons from the occupied defect states (dashed lines in hBN) tunnel to empty states in graphene (red region of Dirac cone) and electrons from occupied states in graphene tunnel to empty states in hBN. The tunneling directions are indicated by green arrows. The band structure of each individual layer is aligned such that their vacuum levels coincide.

Fig. 5.1 shows the band structure of the device. The band alignment has been performed based on work function and electron affinity values in literature. Al_2O_3 layer has an electron affinity of 1.2 eV [153], the electron affinity of hBN is ∼2 eV [154] and the work-function of graphene is 4.6 eV. The thickness of the oxide barrier has to be such that the tunneling lifetime is longer than the radiative recombination lifetime between defect states in hBN. In Fig. 5.2, the variation of tunneling rates for increasing barrier thicknesses have been plotted for different electron energies. The zero of the electron energies is referenced to the Dirac point in graphene. For negative electron energy, E, the electron is tunneling from an occupied state in graphene to an empty acceptor state in hBN and vice versa for positive E. The dashed line is located at 1 ns, which is on the

order of the lifetime of hBN emitters [2]. From this, it can be seen that a minimum barrier thickness of $\sim 2.3\,\text{nm}$ is needed to increase the tunneling lifetime to above the radiative lifetime of defect states in hBN for shallow donors in hBN, which are close in energy to the conduction band of hBN. For states deep in the band gap of hBN, electron tunneling lifetimes are greater than the radiative lifetimes of the emitters for barriers nearly half as thick.

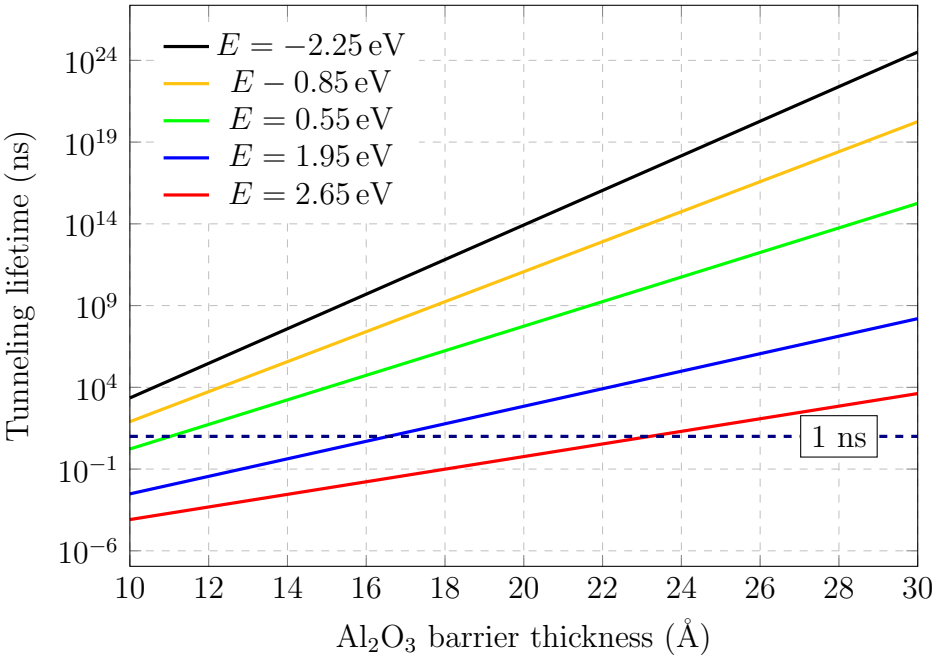

Figure 5.2: The variation of the tunneling lifetimes with Al_2O_3 barrier thickness for a range of electron energies based on Eqn. 5.2. The inverse fraction of Eqn. 5.2 gives the tunneling lifetime. The zero of the electron energy is the Dirac point in graphene. The dashed line is at 1 ns, which is on the order of the lifetime of hBN emitters.

In this model the defect is embedded in monolayer hBN and in the device fabrication process multilayer hBN has been used. Thus, the defect can be located in a layer further away from the interface Al_2O_3, leading to an additional barrier. While this is true, the minimum barrier thickness to prevent quenching with monolayer hBN will also prevent quenching in multilayer hBN. However, it must be noted oxide films grown using ALD are polycrystalline and will possess a large number of defects which can act as sites for trap-assisted tunneling [29]. This leads to an increased tunneling rate and a thicker barrier may be required.

5.1.2 Förster resonant energy transfer (FRET)

In addition to quenching due to charge transfer, energy transfer processes can also lead to a non-radiative process. FRET is an energy transfer process that can lead to quenching over long ranges. The principle behind FRET is as follows. FRET requires the excitation of a donor, which in this case is the emitter in hBN, and the subsequent energy transfer via dipolar coupling to the acceptor (graphene) [155]. As graphene is a semi-metal, there is a continuum of electronic states available for the electron to non-radiatively relax to. Hence, the process can proceed without photon emission and quenching is observed.

The FRET efficiency (E_{FRET})usually increases with the sixth power of the inverse of the separation between the donor and acceptor dipole sources [155]:

$$E_{\mathrm{FRET}} = \frac{R_0^6}{R_0^6 + R^6} \tag{5.4}$$

where R_0 is the Förster critical distance, at which E_{FRET} is 50% and R is the separation between the donor and acceptor. While Eqn. 5.4 is true for molecules, existing literature suggests that E_{FRET} varies as R^{-4} between point dipoles and graphene. As such, this leads to a much longer R_0 when compared to that between two molecules. In Ref. 24, it was found that an approximately 50 nm Si_3N_4 spacer layer between graphene and CdSe/ZnS QDs to recover the approximately 100% emission intensity. As Al_2O_3 and Si_3N_4 have comparable dielectric constants, and hence can lead to similar screening between the emission dipole in hBN and graphene, it was determined that approximately 40-50 nm of Al_2O_3 would be sufficient to recover full bright emission intensity from defects in hBN. Furthermore, as the thickness of the Al_2O_3 film required to suppress FRET mediated quenching is an order of magnitude greater than that necessary to suppress tunneling, the minimum thickness required for the barrier is dictated by FRET efficiency.

5.1.3 Device schematic

The schematic of the final device structure is shown in Fig. 5.4. It consists of a patterned Al_2O_3 layer, where the grids of pillars have different lateral dimensions but fixed vertical dimension. The purpose of varying the lateral dimensions was to have a range of surface

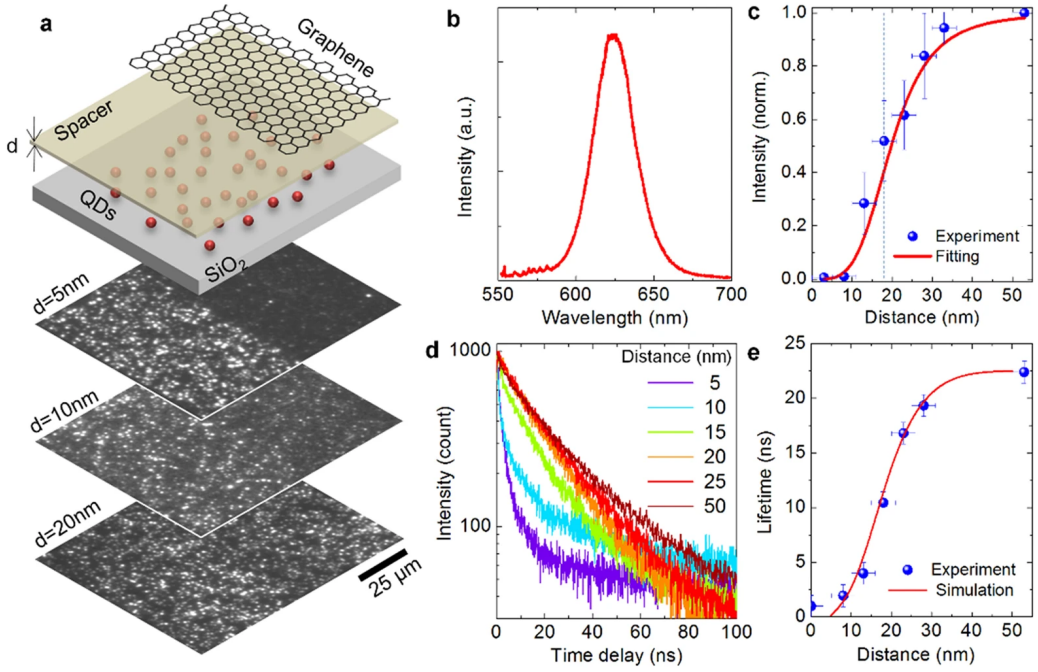

Figure 5.3: **a** (Top) shows the schematic of the device used in Ref. 24 and (bottom) shows the variation of the fluorescence intensity with space thickness. **b)** Shows the PL spectrum of the QDs. **c)** Shows the variation of the normalised intensity of the QDs with spacer thickness. The solid line is fit of a theoretical model for FRET intensity variation with QD-graphene distance. The dotted line is located at $R_0 = 18\,\text{nm}$, which was obtained from the fit. **d)** Shows the lifetime measurements for different spacer thicknesses. **e** Shows the variation of the fluorescence lifetime with spacer thickness. The solid line is obtained from a fit.

areas, and subsequently, a range of number of flakes or area of CVD hBN film protected from quenching. If a uniform emitter density is achieved, then the number of active emitters per pillar can be controlled by the pillar's surface area, leading to a method for localisation of emitters. The devices were fabricated with both hBN flakes, Fig. 5.4a, and CVD hBN transferred onto the pillars, Fig. 5.4b.

5.2 Transfer of hBN

The hBN grown on Cu by a CVD process, Fig. 5.5a, was transferred to the desired substrate by the methodology outlined in Sec. 4.1.1 and 4.1.2. Both wet transfer and electrochemical bubbling were effective ways of transferring large sheets of hBN.

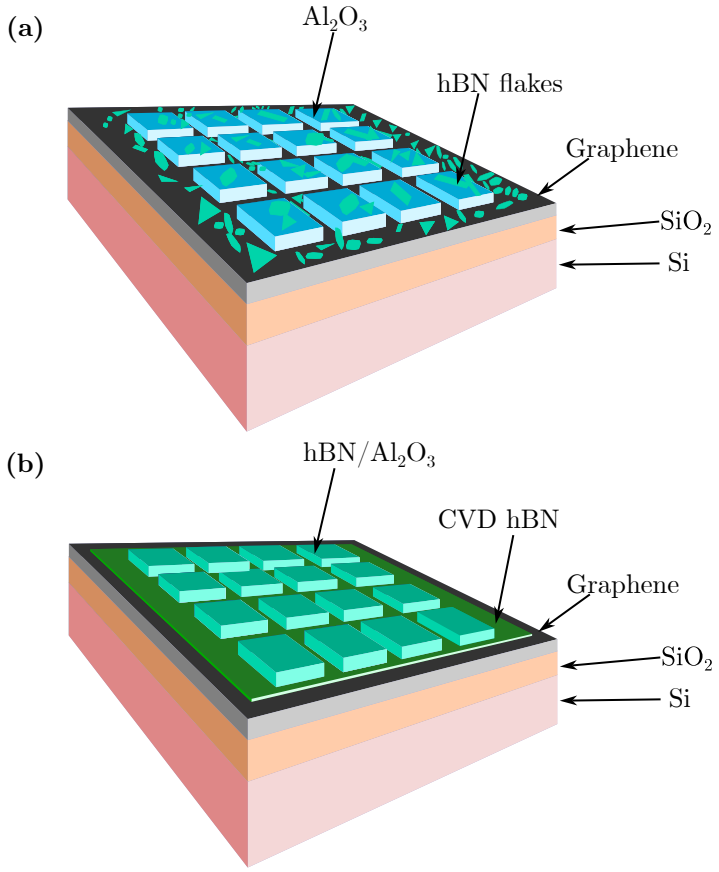

Figure 5.4: **(a)** Schematic of hBN flakes on Al_2O_3 pillars on graphene and **(b)** CVD hBN on Al_2O_3 pillars on graphene.

The films were at first transferred by both methods to a Si/SiO_2 substrate to determine the efficiency of the transfer process. The quality of transferred films was characterised by Raman spectroscopy. As shown in Fig. 5.6a, there is no discernable hBN Raman peak at 1367 cm^{-1} and a strong continuous background signal can be seen. The presence of the background in films transferred using electrochemical delamination and wet transfer eliminates incomplete etching of the copper substrate as a cause of the background signal. This then leaves polymer residue from the supporting PMMA layer as the principal cause.

In Ref. 7 and 49, it was found that heating the transferred material at a temperature beyond the combustion temperature of the polymer in oxygen was an effective way of removing polymer residue. The thermal stability of hBN up to 850 °C allows it to be heated in air at the combustion temperature of PMMA for long periods without damage to the crystal structure. To perform this, the samples were oxidised in air at 500 °C,

which converts the polymer residue to volatile carbon compounds that evaporate from the surface, on an high temperature hot-plate for 6-8 hours. The Raman signal was subsequently measured. Fig. 5.6b shows the Raman measurement after oxidation in air for a sheet of hBN transferred by electrochemical delamination (bubbling transfer) and bare SiO_2/Si. Here, the recovery of the hBN peak at $\sim 1370\,\mathrm{cm}^{-1}$ is highlighted.

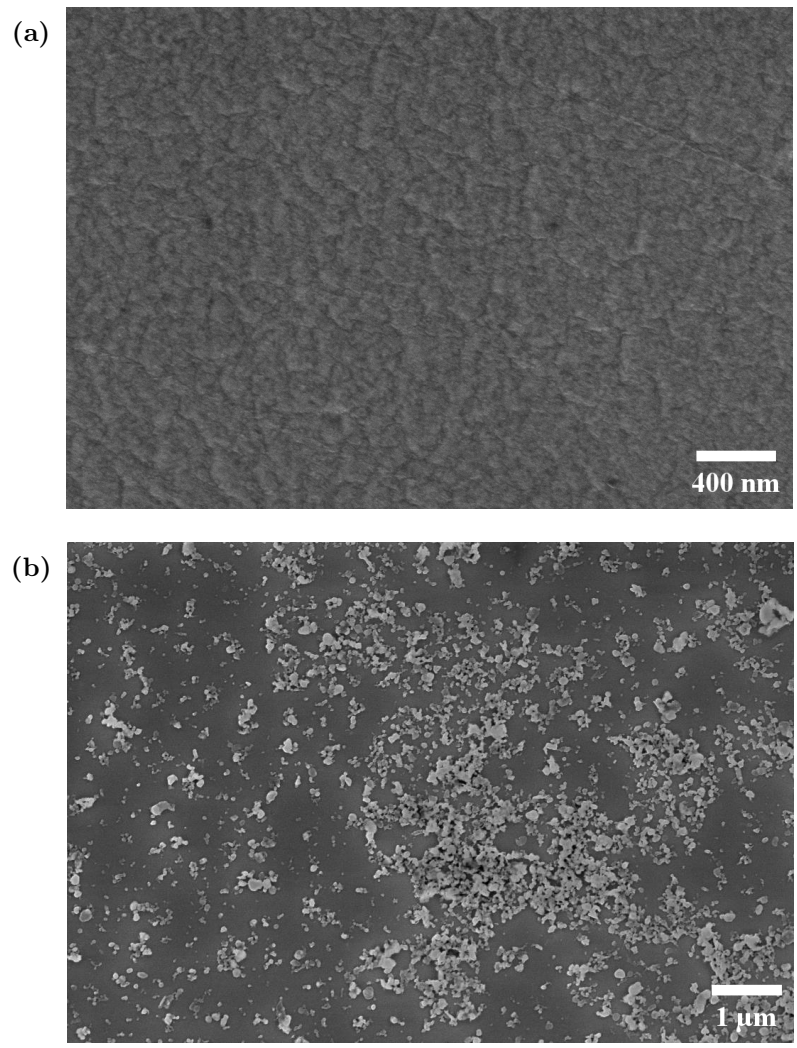

Figure 5.5: **(a)** Shows an SEM image of multilayer CVD hBN on copper before transfer. **(b)** SEM image of hBN flakes obtained from LPE deposited on SiO_2/Si

A Raman map of a 48 µm × 58 µm region on hBN film transferred by electrochemical delamination is shown in Fig. 5.6c, the intensity of the Raman peaks, position of the peaks and the full-width and half maximum of the peaks have been shown in order. Selected spectra from the map where fitting was successfully able to be performed on the data have

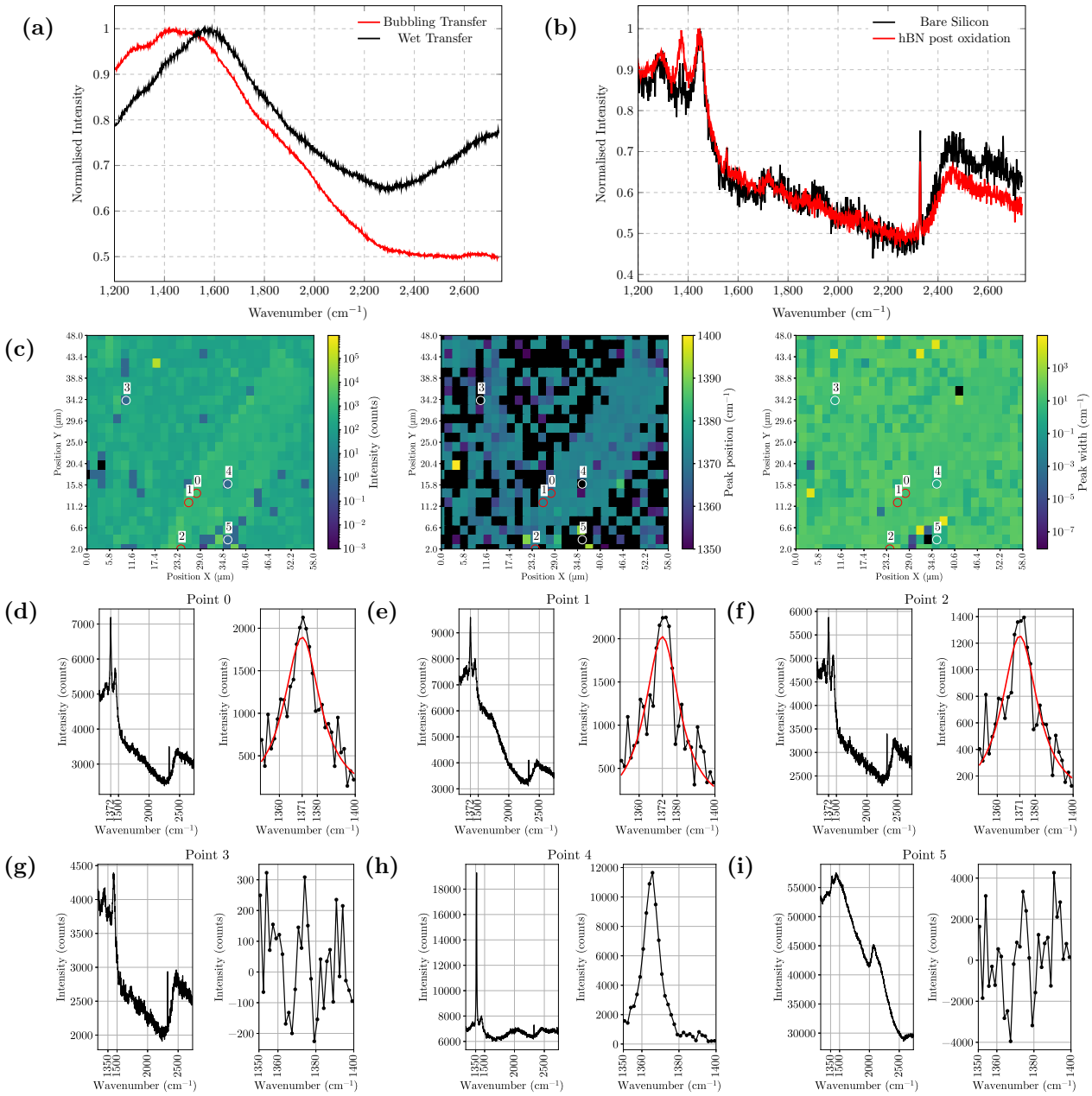

Figure 5.6: **(a)** Raman spectra of CVD hBN transferred using wet transfer (black) and electrochemical delamination (red) before oxidation at 500 °C. **(b)** Raman spectra of CVD hBN after oxidation. **(c)** Raman map of CVD hBN. Starting from the left the images shows the variation of the amplitude, peak position and FWHM of the Lorentzian function fitted to the raw Raman data. Example spectra with successful (red circles) and unsuccessful (white circles) fits are shown. **(d)-(i)** Selected Raman spectra from points on the map, with the point number corresponding to the marked region on the map in **(c)**.

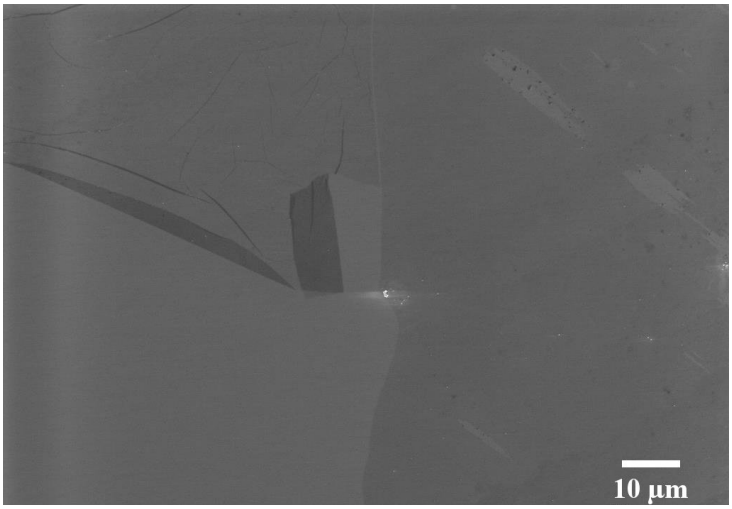

Figure 5.7: SEM image of CVD hBN film transferred using electrochemical delamination.

been shown in Figures 5.6d–5.6f. These were obtained by fitting a Lorentzian function to Raman data at the location of the hBN Raman signal, and the bare SiO_2 spectrum was used to subtract the background signal. Large regions of the film showed a recovery of the peak at $1372\,\mathrm{cm}^{-1}$, which is sufficiently proximate to the bulk hBN Raman peak of $1367\,\mathrm{cm}^{-1}$. The discrepancy can be attributed to the high defect density that is present in atmospheric pressure CVD process used to grow multilayer hBN. The black regions in all the figures show regions where the fitting was not able to be performed. Figures 5.6g–5.6i highlight representative spectra where fitting to a lorentzian was unsuccessful. This could be because, as in Fig. 5.6g, there is no discernable peak in the Raman spectrum at $\sim$$1367\,\mathrm{cm}^{-1}$ although the polymer background has been sufficiently removed. There have been reports in literature where commercial multilayer hBN obtained from Graphene Supermarket has not shown the typical Raman peak attributed to hBN [156]. In Fig. 5.6h, while an intense Raman peak exists, the error can be attributed to the optimisation process conducted by the fitting algorithm not converging to suitable parameters. In Fig. 5.6i, it is revealed that patches of polymer residue survive the oxidation treatment and this results in the broad background that makes the hBN peak sufficiently noisy to not allow successful fitting. Finally, the full-width at half maximum (FWHM) of all points in the map have been shown in the image on the right in Fig. 5.6c. In regions where fitting was successful, the FWHM is uniform, reflecting the uniformity of the quality of the hBN

films in these regions. As in the other panels in Fig. 5.6c, the regions where fitting was unsuccessful have been shown in yellow and black. As in many regions, a discernable hBN peak was not present, but the presence of hBN was confirmed by SEM, Fig. 5.7. An advantage of the wet transfer process over electrochemical delamination is that it does not require the user to handle the PMMA/hBN/Cu structure during the transfer process, which can introduce wrinkles and tears, especially when transferring small areas of films.

hBN flakes were also deposited on substrates by liquid-phase exfoliation as outlined in Sec. 4.1.3. Figure 5.5b shows an SEM image of flakes clustered together after being dropcasted onto a Si wafer. Depending on the duration of sonication, the density of the distributed flakes can be controlled. The images in Fig. 5.8 show how a longer sonication time leads to a reduction in flake density. While it is advantageous to have a high density of flakes, which will correspond to a higher density of SPEs, a short duration of sonication lead to the flakes being concentrated in the central region of the droplet. Therefore, from testing the density and uniformity of flake distribution as a function of sonication time, a 30 min sonication time was found to be a compromise between density and uniformity. A key feature of drop-casted flakes that were in solution is the 'coffee-ring' effect. This corresponds to the effect where the boundaries of the drop-casted region having a larger density of the flakes than the center, leading to a ring being formed.

5.3 Confocal PL Mapping

After transfer, the flakes were annealed in a cold-wall CVD reactor (Black Magic Pro - Aixtron). The hBN was annealed using the standard recipe present in literature i.e. 850 °C with a 1 Torr argon flow for 30 min [2]. Existing studies in literature have shown that annealing is necessary in flakes to increase emitter density [2]. In addition to annealing, a study showed that Ar plasma etching prior to annealing increased emitter density in hBN flakes by 8-fold [157]. As the aim of patterning pillars of different dimensions was to exploit the surface area of the pillar as a means of controlling emitter density, it is necessary to have a high and uniform emitter density.

Fig. 5.9a shows the density of emitters in flakes which have undergone no treatment,

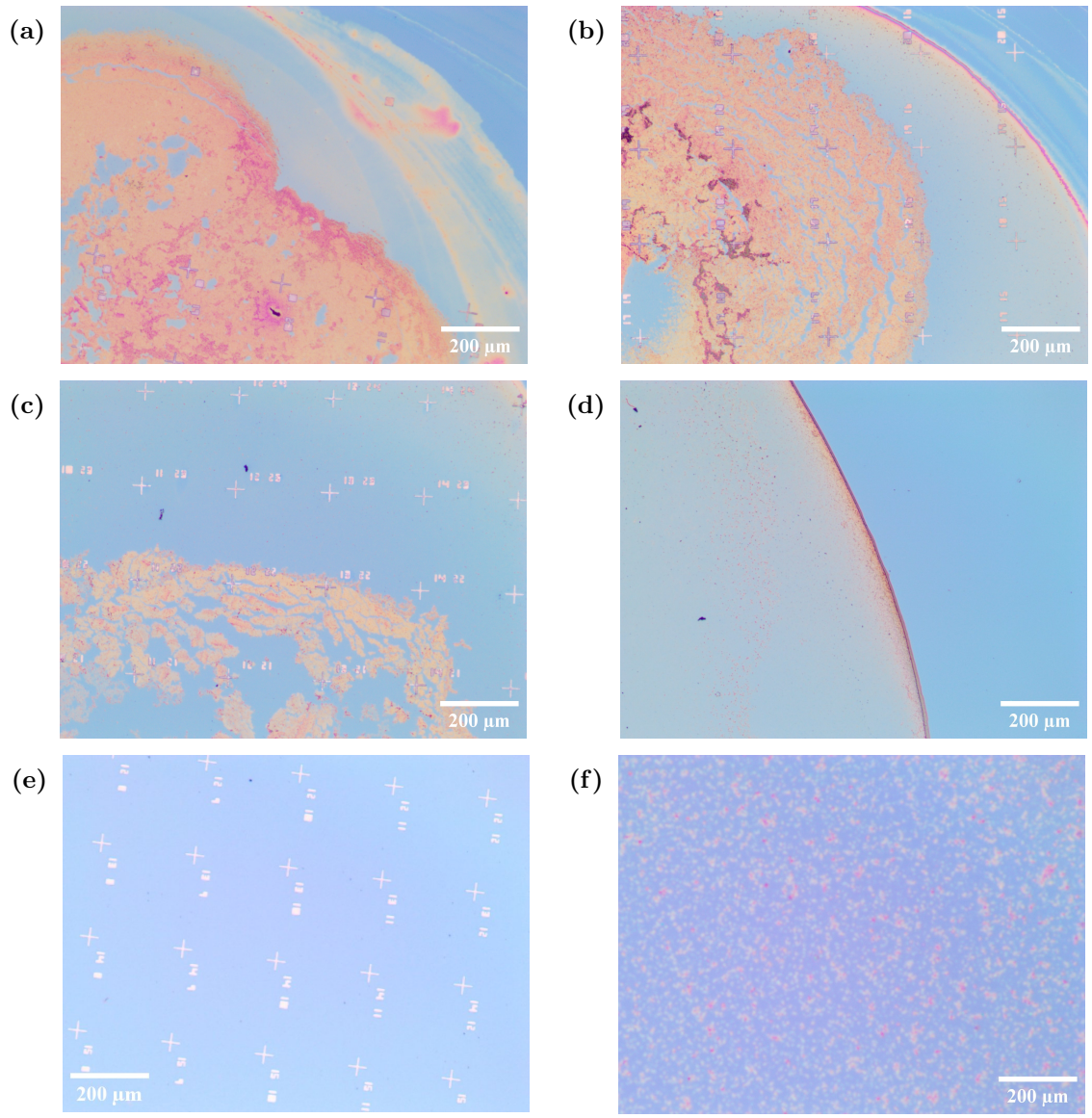

Figure 5.8: **(a) - (e)** are optical images of drop casted hBN taken at 5× magnification. Starting from **(a)** the sonication times were no sonication, 5 mins, 10 mins, 30 mins, 60 mins. **(f)** shows a high magnification (100 ×) image of the dispersed flakes after 30 mins of sonication.

Fig, 5.9b shows flakes that have been subject to argon annealing alone, and Fig. 5.9c shows a confocal map of a sample of hBN LPE flakes that had undergone Ar plasma treatment in an RIE, with a 200 W radio frequency plasma generator, 98 sccm Ar flow for 2 mins at room temperature prior to the standard Ar annealing process. The efficacy of the treatment in increasing emitter density was studied from these images and the most effective treatment process was adopted. Both pure annealing and plasma exposure followed by annealing

lead to a significantly higher density of emitters than when no treatment is performed. Comparing Fig. 5.9b and 5.9c, it can be seen that the emitter density is lower when plasma etching is carried out than when hBN was annealed exclusively. This is contrary to Ref. 157 where plasma etching was found to break B – N bonds and create vacancies, and upon exposure to air were sites for oxygen impurities. A possible explanation for the contradiction could be due to the different thicknesses in the samples studied in Ref. 157 and LPE flakes in this study. The mechanically exfoliated flakes in Ref. 157 were significantly thicker than the LPE flakes used in this study, and as found in the Ref. 157, the Ar etching process lead to the removal of 2 nm of hBN. While in Ref. 157 sufficiently thick hBN remained to host defects, as the LPE flakes can only be a few monolayers thick, complete removal of thin flakes could have occurred. The reduction in flake density would be the cause of reduction in emitter density. Therefore, for the final device fabrication, Ar annealing alone was performed.

PL imaging was also performed on CVD hBN, shown in Fig. 5.9d. While emitter density is significantly higher than in flakes, the emitters were significantly less bright than the LPE hBN samples. Although it was found that annealing was not necessary to induce emitters in CVD hBN due to the natural occurrence of a high number of defects, [47, 48], oxidation to remove polymer residue from the transfer process was not performed on these samples. During this process, defects in hBN are chemically modified and emitters are lost. An Ar annealing process similar to that used for flakes has been found to re-introduce the defects [7]. In many samples, an amorphous carbon layer had formed due to residual PMMA that had not been removed during oxidation and this led to a large background luminescence that prevented the identification of emitters during imaging. It was also difficult to distinguish between luminescence from residual PMMA and defects in hBN from the images as the images did not contain any spectral information.

In each of these samples, in addition to emitters appearing as diffraction-limited spots, they would display temporal properties such as fluorescence intermittency (blinking) and bleaching. Figure 5.10a shows many emitters in the plasma treated sample displaying blinking. Blinking occurs due to electrons being promoted to metastable states during the transition. If a metastable state has a lifetime longer than the pixel dwell time, no

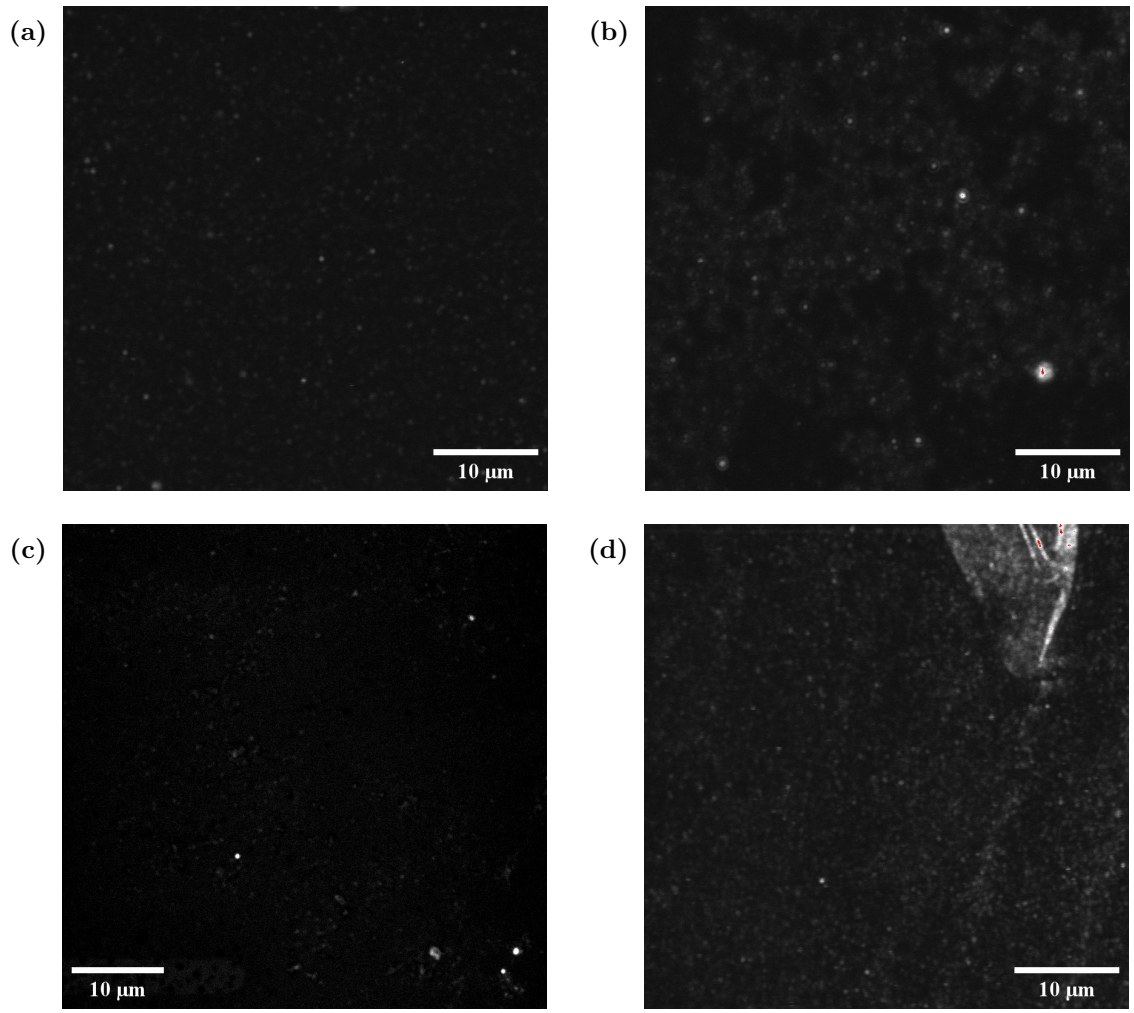

Figure 5.9: Confocal PL intensity map of hBN flakes **(a)** prior to annealing, **(b)** after argon annealing, and **(c)** after argon plasma etching and argon annealing. (d) Emitters in CVD hBN on SiO_2.

signal is obtained in this time, resulting in a dark streak across the emitter. A close up of an emitter showing blinking has been indicated in Fig. 5.10b. This behaviour was not exhibited by all emitters, however was found in all samples irrespective of the method of transfer of hBN to the desired substrate.

5.4 PL spectroscopy

After confirming the presence of emitters in the sample by means of PL imaging, spectroscopy allowed the determination of the nature of the emission. It has been discussed

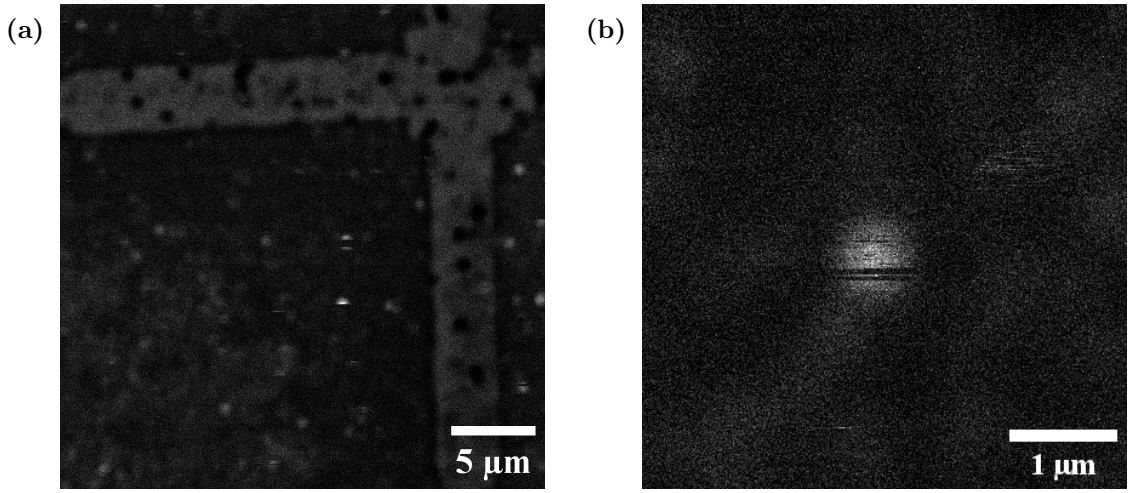

Figure 5.10: **(a)**A PL image of a large region of plasma treated flakes with many emitters showing fluorescence intermittency, **(b)** after argon annealing. **(b)** A close up image of a single emitter exhibiting intermittency in fluorescence.

earlier that hBN is an attractive source of room temperature single-photon emission due to its high Debye-Waller factor, $\sim 80\,\%$, which results in majority of the emission energy being in the ZPL. Hence, a PL signature that would suggest a colour centre in hBN as being the source emission would be a narrow ZPL, and a PSB.

PL spectroscopy was carried out using the methods outlined in Sec. 4.2.2. Figure 5.11a shows a hyperspectral PL map of the sample that had undergone Ar plasma treatment before annealing. PL spectra at selected sites showing bright emission have been shown in Figures 5.11b–5.11e. From these spectra, it can be concluded that the emitters display a wide range of spectral characteristics. In agreement with literature, a large number of emitters have ZPLs close to 580 nm. Spectra, such as that shown in Fig. 5.11e, have been reported in literature studying LPE flakes that have underwent Ar annealing exclusively, [2], and mechanically exfoliated flakes that have been treated with Ar plasma [157]. The multiple lines seen in Fig. 5.11d are indicative of an ensemble of defects [158].

A similar map was performed on LPE samples exclusively annealed in Ar without prior plasma treatment and CVD hBN samples were transferred using electrochemical bubbling, followed by oxidation and Ar annealing. Both samples showed sharp ZPLs in the 580-680 range as expected in literature, [3]. In hBN flakes without pretreatment, a wide range of emission was observed, as with the plasma treated samples. Figs. 5.12a

and 5.12b, display emitters with a ZPL at approximately 615 and 675 nm respectively. In CVD hBN, spectra which was broadband and did not feature a prominent ZPL was considered to be from residual polymer from the transfer process. In Figs. 5.13a and 5.13b PL spectra from emitters which exhibited a sharp ZPL have been shown.

5.5 ALD of Al_2O_3

Using ALD (basic principles outlined in Sec. 4.1.4) an Al_2O_3 layer was deposited on graphene. The purpose of the Al_2O_3 layer was to act as a barrier to quenching between the emitters in hBN and graphene. Compared to ALD on conventional substrates such as SiO_2, ALD on graphene is challenging due to the inertness of the surface. In Fig. 5.14a, the dosage, which is calculated as the product of the width of the pulse in the chamber, t_{dose} and the peak pressure of the precursor in the chamber, P_{dose}, followed standard recipes in literature for the growth of Al_2O_3 on graphene [159, 160]. The pulse time of the precursor/oxidant, t_{pulse}, was set to obtain a dose of 0.5 torr $\cdot$ s.

Fig. 5.14a shows 50 cycles of a standard ALD process on graphene transferred using wet transfer on SiO_2. Al_2O_3 grows preferentially on grain boundaries and wrinkles. This non-uniform growth will lead to a rough oxide layer and different degrees of quenching might be observed throughout the sample.

To avoid the issue of polymer residue initiated nucleation, graphene transferred by polymer free transfer process was purchased from Grolltex. The graphene obtained has uniform coverage and minimal wrinkles. This led to fewer clusters of Al_2O_3 forming on graphene and more uniform coverage. Figure 5.14a shows an SEM image after 50 cycles of ALD on CVD graphene transferred onto SiO_2 using a polymer free transfer technique. The polymer free transfer process was essential as clumps of residual polymer from the transfer process can act as preferential nucleation sites, leading to non-uniform growth of the oxide layer. After the growth process, large regions of graphene remain uncovered by Al_2O_3. This is because of the lack of $-$OH bonds that act as nucleation sites on graphene for TMA.

To encourage non-preferential growth of Al_2O_3 on graphene, the deposition process

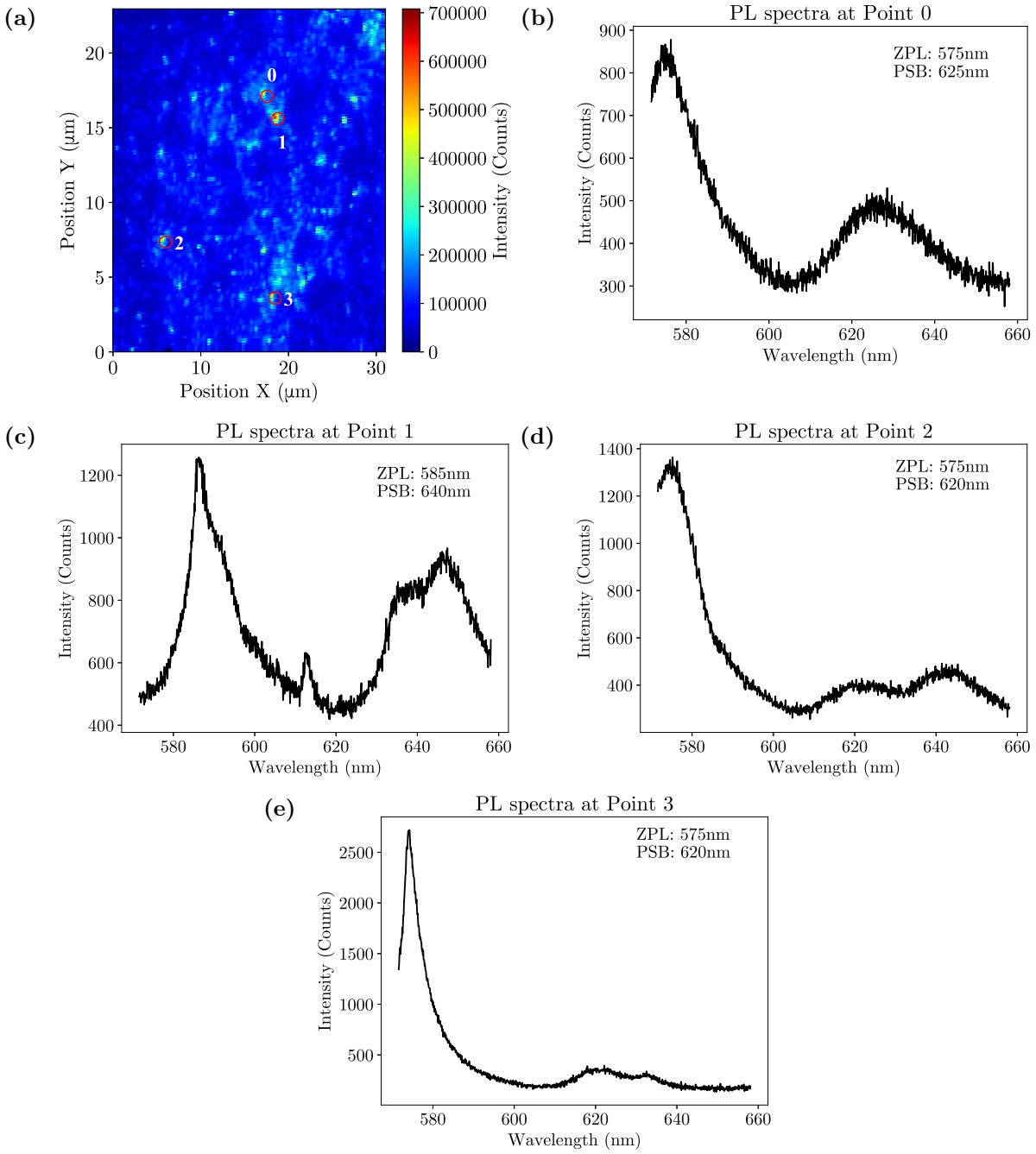

Figure 5.11: **(a)** Intensity map obtained by hyperspectral PL measurement of Ar plasma treated and annealed flakes. **(b)-(e)** are representative spectra of PL obtained from the points in the map marked by red circles. The position of the ZPL and PSB is annotated at the top right of each spectrum. The point number in the title of the spectra correspond to the point number in the label of the red circles in **(a)**.

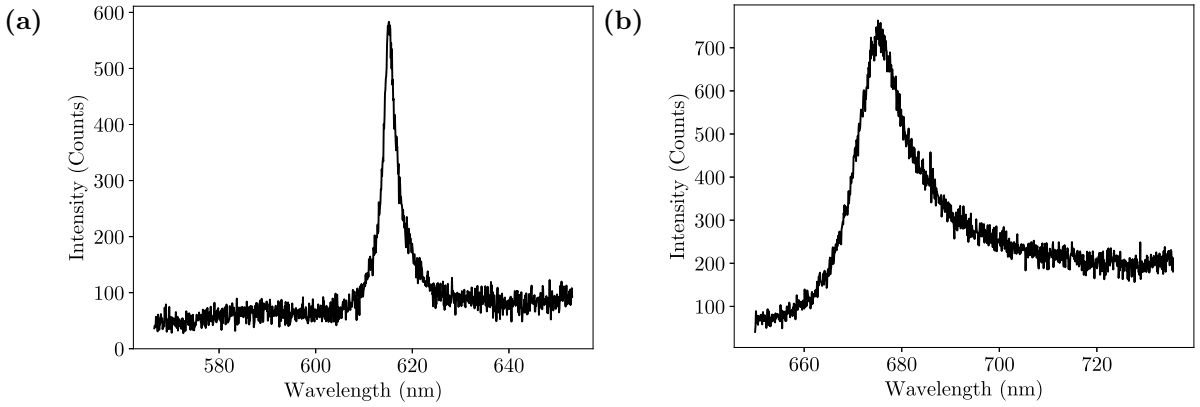

Figure 5.12: PL spectra of emitters in flakes which were only annealed in Ar **(a)** centered around 615 nm and **(b)** 675 nm.

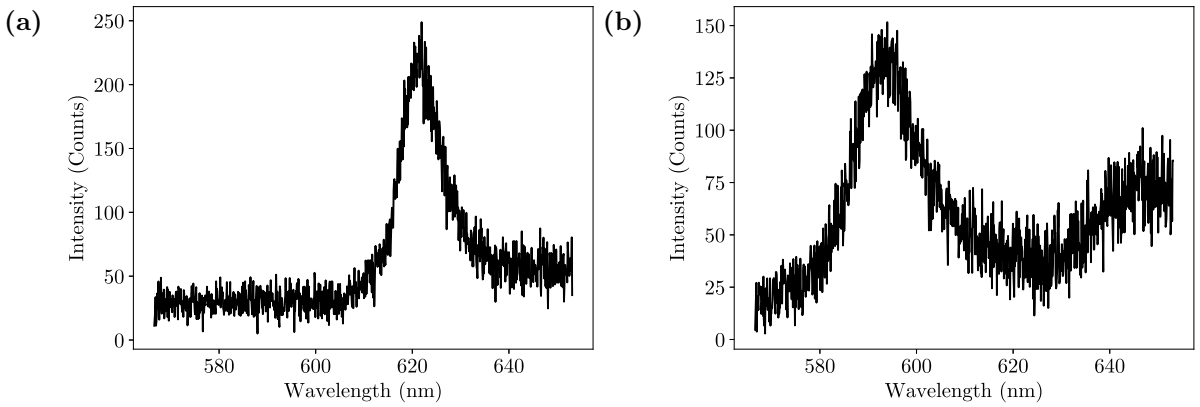

Figure 5.13: PL spectra of emitters in CVD hBN which were transferred by electrochemical delamination **(a)** centered around 620 nm and **(b)** 590 nm.

was modified. In Ref. 159 the parameter space for increasing the nucleation density and uniform growth of Al_2O_3 was studied. Two methods which had the highest success in increasing the coverage of the Al_2O_3 film wer adopted in this project. The first method, which will be known as the pulsed mode, involved pulsing H_2O vapour (PM1) or Ozone (PM2) as an oxidant N number of times, for a fixed t_{dose}, to pretreat the graphene surface prior to the ALD process. The pretreatment process would increase the number of $-OH$ sites for TMA nucleation. The second method, which will be referred to as stopped-flow mode (SM) , involved stopping the flow of the oxidant/precursor in the process chamber for several seconds, t_{hold}, immediately after dosage. Following this, the chamber is purged and the process is continued. The SM mode compensates for the inertness of the graphene

surface and the slow reaction kinetics by increasing the time for nucleation.

PM1 operation was studied first. The advantage of PM1 over SM is the shorter processing time. As t_{pulse} is a fraction of a second at standard deposition temperatures, such as 200 °C, several pretreatment pulses can be performed without an appreciable increase in total growth time. However, in SM mode although the t_{pulse} is the same as in PM1 mode, the additional t_{hold} which is on the order of a few seconds per precursor dose, dramatically increases the process time. This is especially true when a few hundred ALD cycles need to be performed. Hence, PM1 operation is significantly more scalable as it requires less growth time. Fig. 5.14b, shows an SEM image of the coverage of Al_2O_3 on graphene after 10 pretreatment cycles. When compared to Fig. 5.14a, the pretreatment has successfully increased the non-preferential nucleation of Al_2O_3.

Ozone, being a stronger oxidant than H_2O, was also explored as a pretreatment oxidant. The ozone pretreatment had to be performed at a low temperature (80 °C) to avoid damage to the graphene layer. The subsequent growth cycles after pretreatment were performed with H_2O vapor. SEM images after growth, Fig. 5.14d, showed greater uniformity in coverage than when H_2O vapour was used to pretreat the graphene and the pinhole density was also significantly reduced. It is difficult to attribute the increased coverage to the change in oxidant alone as at deposition temperatures below boiling point of water, droplets of H_2O could form on the substrate, which act as nucleation sites. However, such a process would result in a film with a lower density and dielectric constant.

The increased soaking period, $t_{\text{hold}} = 2\,\text{s}$, in SM mode also led to an increased coverage, as shown in the SEM image in Fig. 5.14c. When compared to the other growth techniques, SM operation is the most effective at increasing coverage. After 50 ALD cycles in SM mode, the film is mostly continuous with pinholes on the order of 10 nm width. Whereas in PM1 and standard ALD operation, the nucleation is preferential to graphene grain boundaries and wrinkles. Furthermore, in standard mode, there is no discernable formation of continuous films and in PM1 mode, although the nucleation density was increased, only small islands of continuous films exist. Even in PM2, despite there being non-preferential nucleation of reactants, the pinhole density is greater than in SM operation. Additionally, SM operation has the advantage that it can be performed at

high temperatures, i.e. 200 °C, with negligible damage to graphene. This results in films with a higher dielectric constant [161], and as the quenching efficiency between emitters in hBN and graphene depends on the screening of the Coulomb interaction between the emitter and graphene, Sec. 5.1.2, a film grown using SM would lead to a greater reduction in FRET efficiency than if the Al_2O_3 was grown at a lower temperature. Hence, despite the longer process time, the SM mode was chosen as the growth technique for the Al_2O_3 film.

After choosing the SM process as the preferred growth method, the growth per cycle (GPC) was determined. ALD was performed in the SM technique for 100, 200, 300, 400, and 500 cycles and the film thickness was determined by ellipsometry, Sec. 4.2.4. By fitting a linear function to the data, the GPC was determined to be 0.13 nm/cycle, which is in agreement with standard ALD growth rates of ~ 0.1 nm/cycle. Fig. 5.15 shows the growth rate of Al_2O_3 by the stopped-flow mode [146]. For the final device structure, to achieve 40-50 nm thick Al_2O_3 films, 300-400 cycles of ALD were performed. It is important to note that ellipsometry would have greater inaccuracies at lower thicknesses of the oxide layer as the pinhole density would be greater. Hence, the linear fit was performed to data corresponding to several ALD cycles, where the islands where nucleation had occured would have coalesced to form largely continuous films.

5.6 Patterning of Al_2O_3/Gr

The lithography process was then developed to write the grid of Al_2O_3 pillars. Figure 5.16f, shows a section of the computer-aided design file illustrating the device design. Pillars of Al_2O_3 of different widths were designed with the aim of localising a range of emitters. Larger pillar allow more flakes to be protected from quenching by graphene, leading to a greater number of emitters being active in a defined region. Each array of a given pillar dimension was then labelled with distinct gold registration marks for identification in subsequent imaging. The pillars have a square lateral dimension ranging from 0.5 µm to 4.75 µm in steps of 0.25 µm.

The design was implemented using EBL following the method outlined in Sec. 4.1.5.

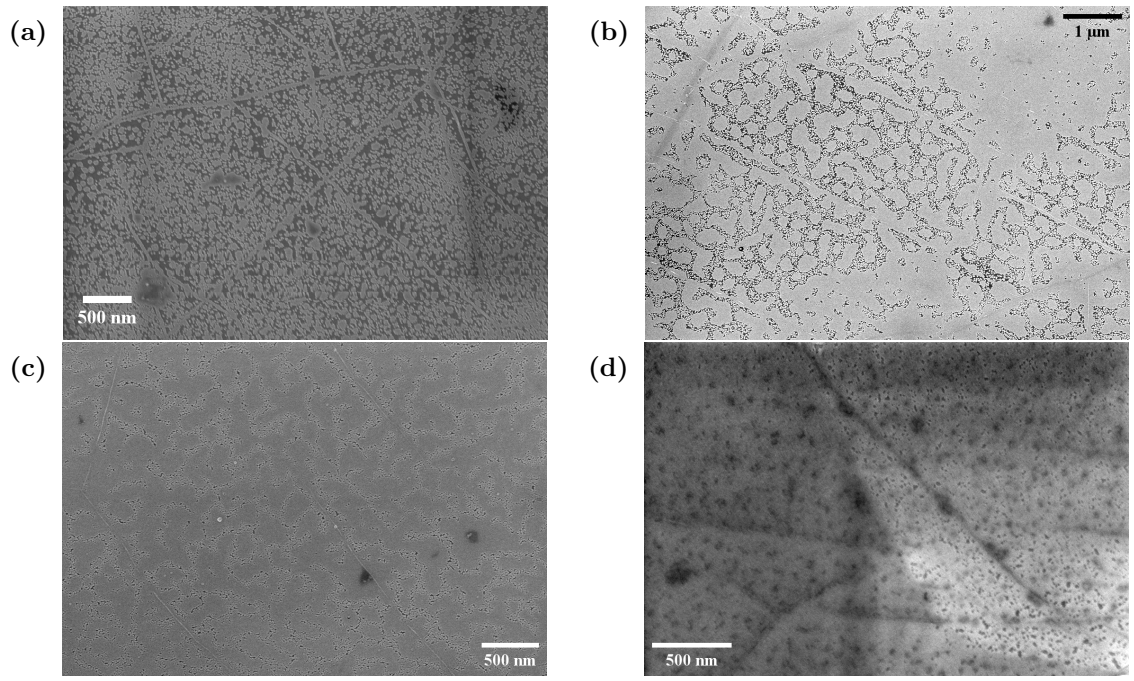

Figure 5.14: **(a)** SEM image of standard Al_2O_3 ALD on graphene. **(b)** Al_2O_3 on graphene after pretreatment by 10 H_2O pulses in the PM process (PM1). **(c)** Al_2O_3 grown using the SM process. **(d)** PM with ozone pretreatment at 80 °C (PM2).

Figures 5.16a and 5.16b, show respectively the bright and dark field image of the result of developing the Ma-N-2410 resist in TMAH, after exposure to the e-beam. The etching times were optimised in accordance with the smallest feature sizes to prevent over-etching. The optical images show that the e-beam exposed regions of the resist still remain on the Al_2O_3 film, allowing the protection of the layer. The dark-field image allows the pattern to be imaged more clearly as the edges of the features scatter light, unlike the film underneath.

The Al_2O_3 film was subsequently developed using phosphoric acid. Figure 5.16c and 5.16d, show high magnification bright and dark-field images of the result of etching of the Al_2O_3 layer. As the undissolved resist caps remain on top of the pillars, it indicates that the underlying Al_2O_3 layer is being protected while the surrounding unprotected film was being removed. Here, the drawbacks of Al_2O_3 growth on graphene is also illuminated. In Sec. 5.5, the non-uniform growth of Al_2O_3 in the ALD process was discussed. The non-uniform growth results in an uneven and polycrystalline oxide layer, which undergoes uniform etching. This leads to islands of Al_2O_3 remaining on graphene after etching.

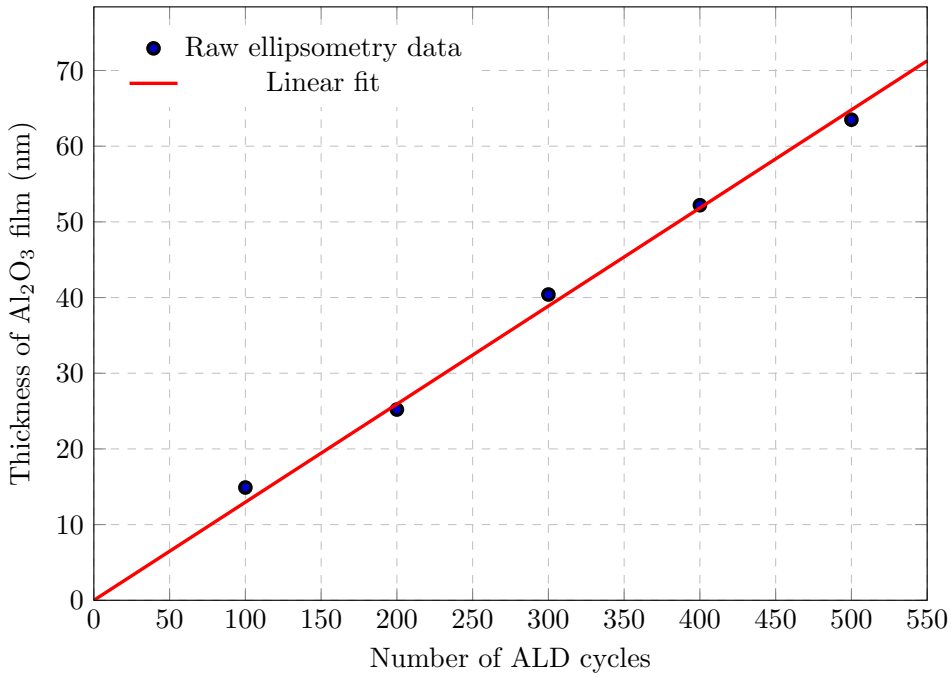

Figure 5.15: Growth per cycle of Al_2O_3 on graphene using SM operation. The black circular markers are raw ellipsometry measurements of thickness and the red solid line is a linear fit to the data. The uncertainty in the fitting of the ellipsometry measurements is of the order ± 0.01 nm. There error bars are therefore less than the markersize and are not indicated.

However, further etching can lead to undercutting of the Al_2O_3 pillars and lift-off of the protective resist layer. As the islands of residual Al_2O_3 are thin, quenching of emitters is still expected to occur.

Following the removal of the unprotected Al_2O_3 film, the remaining resist was removed in an acetone and IPA rinse. Figure 5.16e, shows the pillars of Al_2O_3 after etching. Furthermore, it can be seen that the graphene layer has not been damaged during the etching process. This is evident from the wrinkles and pyramids of multilayer graphene below the Al_2O_3 layer. As many features in the device are below the resolution limit of the optical micrscope and do not scatter light to be visualised in the dark-field (as the resist has been removed), the device was imaged using an SEM. Figure 5.17a shows a low magnification image after etching of Al_2O_3 after 100 ALD cycles. Several multilayer pyramids of graphene can be seen along with wrinkles, confirming the observation in the optical microscope regarding the preservation of the graphene layer. Furthermore, the

features, which are 2.5 µm in lateral dimension have been preserved in all the arrays. A high magnification image of a single pillar obtained using the in-lens detector is shown in Fig. 5.17b. It is apparent in this image that majority of the Al_2O_3 has been removed in the region surrounding the pillar and small islands remain. The boundary of the pillar shows slight over-etching over a width $\sim$ 0.1 µm. As SE2 electrons arise from close to the surface of the features, they allow the imaging of the surface morphology in detail. Figure 5.17c, shows the same pillar in the same region imaged using the ET detector, which detects SE2 electrons. In this image, it is apparent that the etching process has been successful in producing pillars with large areas of uniform surface morphology away from the edges and the residual Al_2O_3 film around the pillar is significantly thinner than the pillar.

To confirm the heights of the pillars as predicted by ellipsometry, AFM measurements were performed. Figure 5.18a shows an AFM image of a 26 µm×26 µm region and Fig. 5.18b, shows the height profile taken along the horizontal line of the crosshair in Fig. 5.18a. No postprocessing was done as the background is negligible. The height obtained from the measurement indicated a step height of 15.37±0.23 nm, which is in agreement with the ellipsometry measurement for 100 ALD cycles of 14.9 nm which was done prior to etching. As the etching process was successful, it was adapted for the final device with 300-400 cycles of ALD and the etch times were appropriately scaled.

5.7 Localisation of emitters

Having developed the methodology for all the steps for device fabrication, from hBN transfer to lithography of Al_2O_3, it was now possible to fabricate the device. For the final device structure, the Al_2O_3 films were grown with 300 and 400 ALD cycles, which would lead to thicknesses of 39 nm and 50 nm respectively, in accordance with the linear fitting to the ellipsometry results in Sec. 5.5.

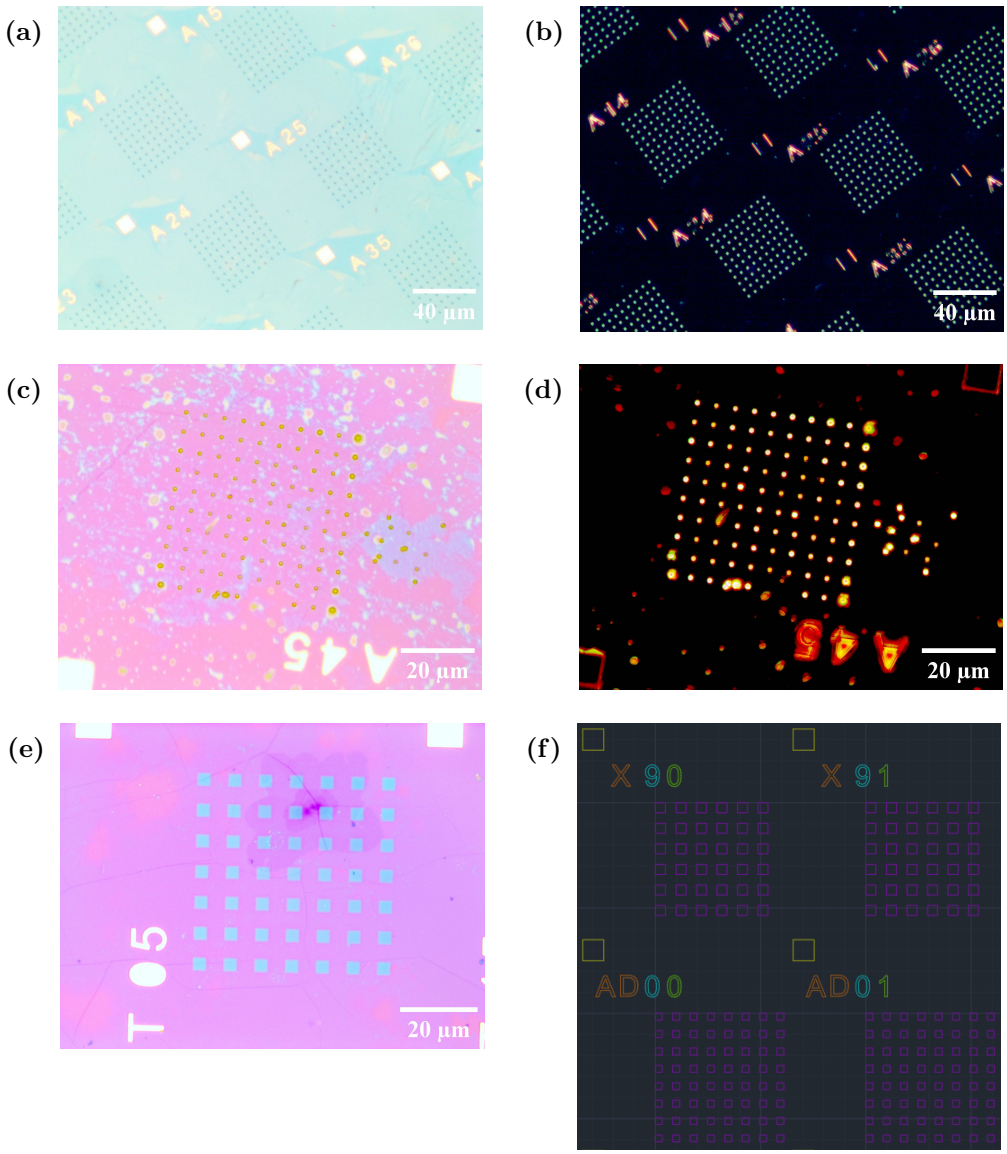

Figure 5.16: **(a)** and **(b)** Show bright and dark-field images of the exposed resist remaining after development using TMAH, respectively. Dark field images allow high contrast imaging of resist remaining in the exposed regions. **c)** and **d)** Show the bright and dark-field images of the exposed resist remaining after the surrounding Al_2O_3 film was removed in phosphoric acid, respectively. **e)** A bright-field image of the Al_2O_3 pillars after the removal of the resist cap by acetone and IPA. This region was specifically chosen to show the preservation of the graphene layer, as can be seen with the multilayer pyramid below the top row of blue Al_2O_3 pillars.

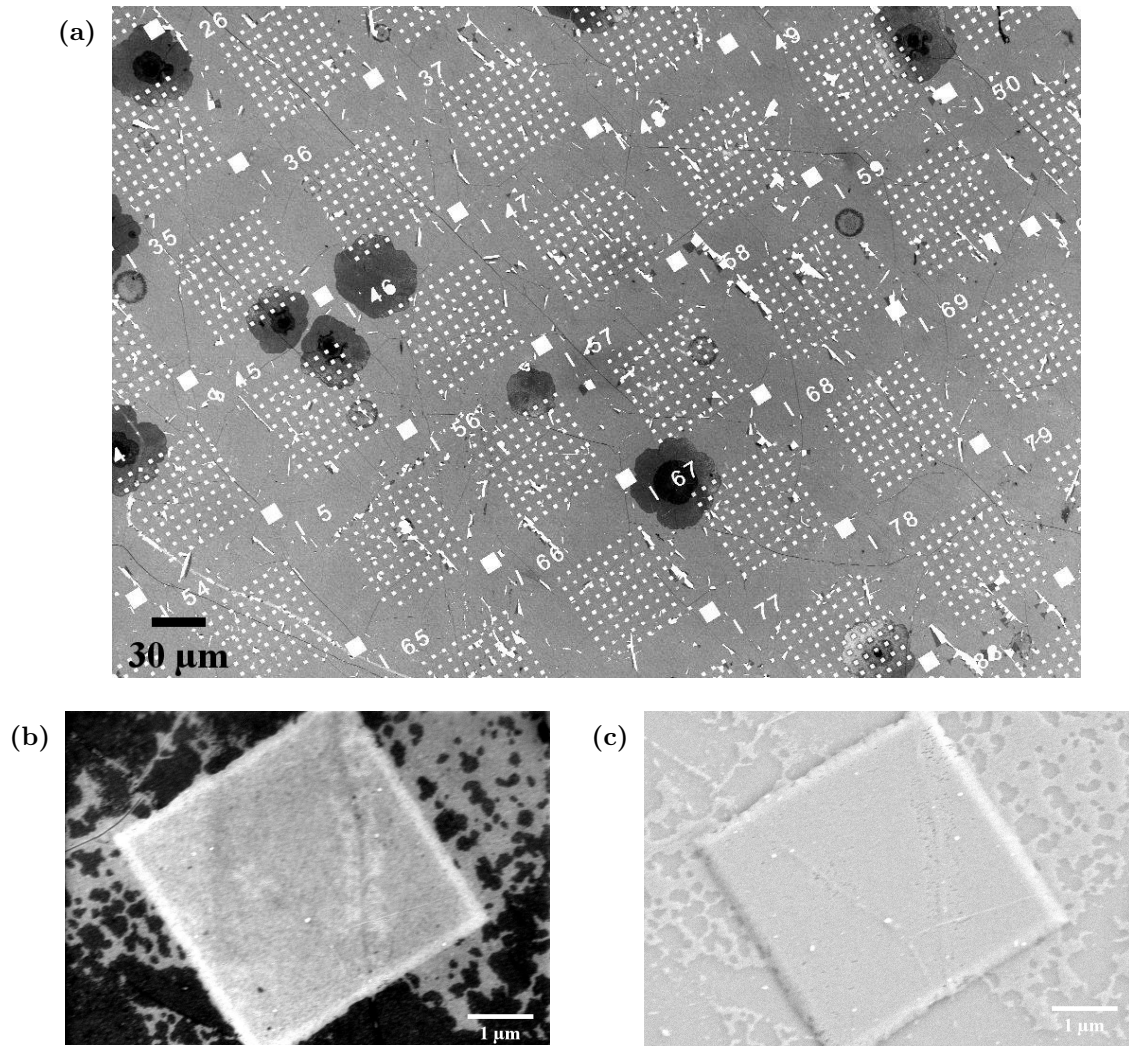

Figure 5.17: SEM images of the etched Al_2O_3 layer, which was grown using 100 ALD cycles. **(a)** A low magnification view of the etched pattern. **(b)** A high magnification image of a single pillar obtained using the in-lens detector for SE1 electrons. **(c)**Image obtained using the Everhart-Thornley detector (SE2). SE2 allows better visualisation of surface morphology.

5.7.1 Quenching in hBN/Graphene heterostructures

The quenching of emitters when on bare graphene was first measured. Both CVD hBN and flakes were transferred onto bare graphene to observe quenching. After CVD hBN was transferred and oxidised to remove the polymer residue, it was observed under PL imaging. Figure 5.19a shows the confocal PL image of a region with graphene covering large parts of the hBN. To obtain this image, the PL setup in Sec 4.2.3, was operated with a 635 nm excitation laser at low laser power and a dichroic mirror to reject majority of the reflected

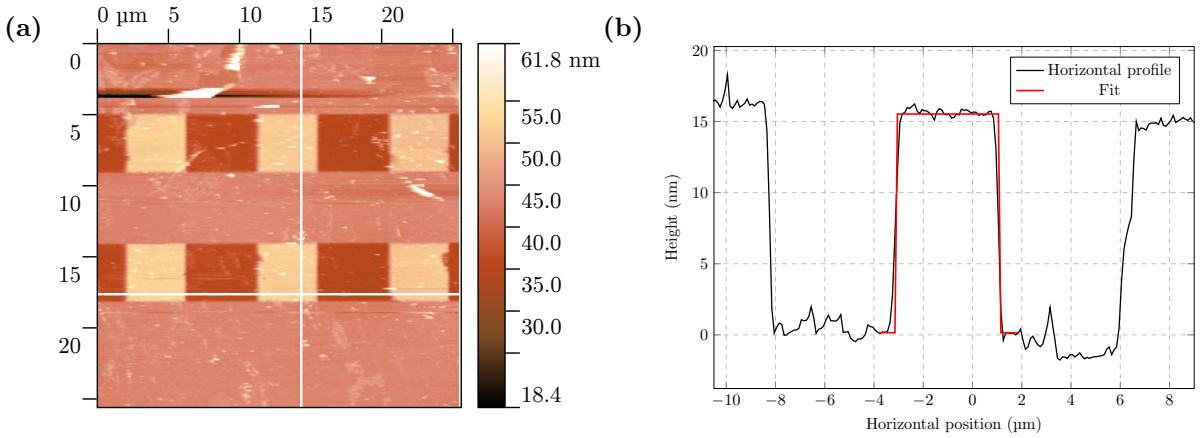

Figure 5.18: a) AFM image of an etched region and b) AFM height profile along horizontal axis of crosshair (black solid line) and step function fit to the middle pillar (red solid line). The fit height is 15.37±0.23 nm.

light, allowing a pseudo bright-field image of the region of interest. A light contrast allows the visualisation of regions with and without a graphene underlayer. Figure 5.19b, shows the PL image of the same region with the setup operating in the normal mode set out in Sec. 4.2.3. It can be observed that no luminescence can be observed where graphene exists and a uniform weak emission is observed where no graphene is present. In the region where luminescence is observed, black ribbons can be observed where quenching has occurred and a circular dark island which corresponds to multilayer graphene can be observed. These are the remnants of the graphene layer, majority of which was removed due to insufficient protection by the hBN layer. Hence patches of quenching is observed in these regions.

hBN flakes were sonicated and drop cast onto the the substrate and left overnight to dry in a fume hood. The device was then annealed to stabilise and increase the density of emitters. Figure 5.20 shows a region where flakes were directly deposited on graphene. In Fig. 5.20a, it can be seen that the graphene layer had scrolled in on itself. However, quenching had still occurred, as shown in Fig. 5.20b, no emission was found in the flakes wrapped by graphene.

The root of the scrolling was found to be due to desorption of residue from the hBN flakes in solution. When a 50:50 mixture of ethanol:DI water solution was dropcasted on graphene , dried and heated to 200 °C, the same effect was found in Fig. 5.21. Such

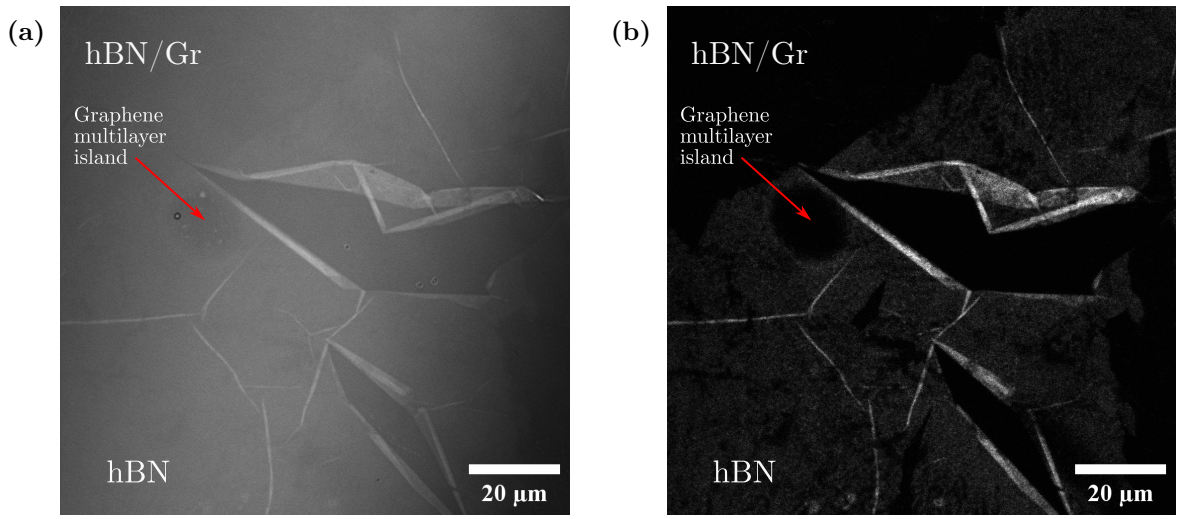

Figure 5.19: **(a)** A pseudo bright-field image of CVD hBN on graphene. **(b)** The same region imaged with 473 nm excitation and a band pass filter as in Sec. 4.2.3. The regions overlapping graphene appear black and weak luminescence is observed in regions without an underlying graphene layer.

scrolling would greatly damage the device and not allow emitter localisation as was observed when hBN flakes dropcasted on Al_2O_3 pillars on graphene, Fig. 5.20c.

Interestingly, multilayer graphene pyramids were not affected by the hBN flakes and did not scroll, suggesting a protective layer deposited on graphene prior to the dropcasting of hBN flakes would prevent scrolling. To achieve this, 50 ALD cycles of Al_2O_3 was deposited using the PM process (described in Sec. 5.5) as a continuous oxide film was not necessary and was a faster process than SM, on the device after the pillars were etched. The hBN flakes were subsequently deposited and annealed. Figure 5.22, shows the successful protection of the graphene underlayer due to the additional ALD process prior to the deposition and annealing of hBN flakes. It can be seen that this is sufficient to prevent scrolling. An area of high density of flakes was imaged, as the residue of the ethanol:hBN solution would be greatest in this region and would most likely result in scrolling.

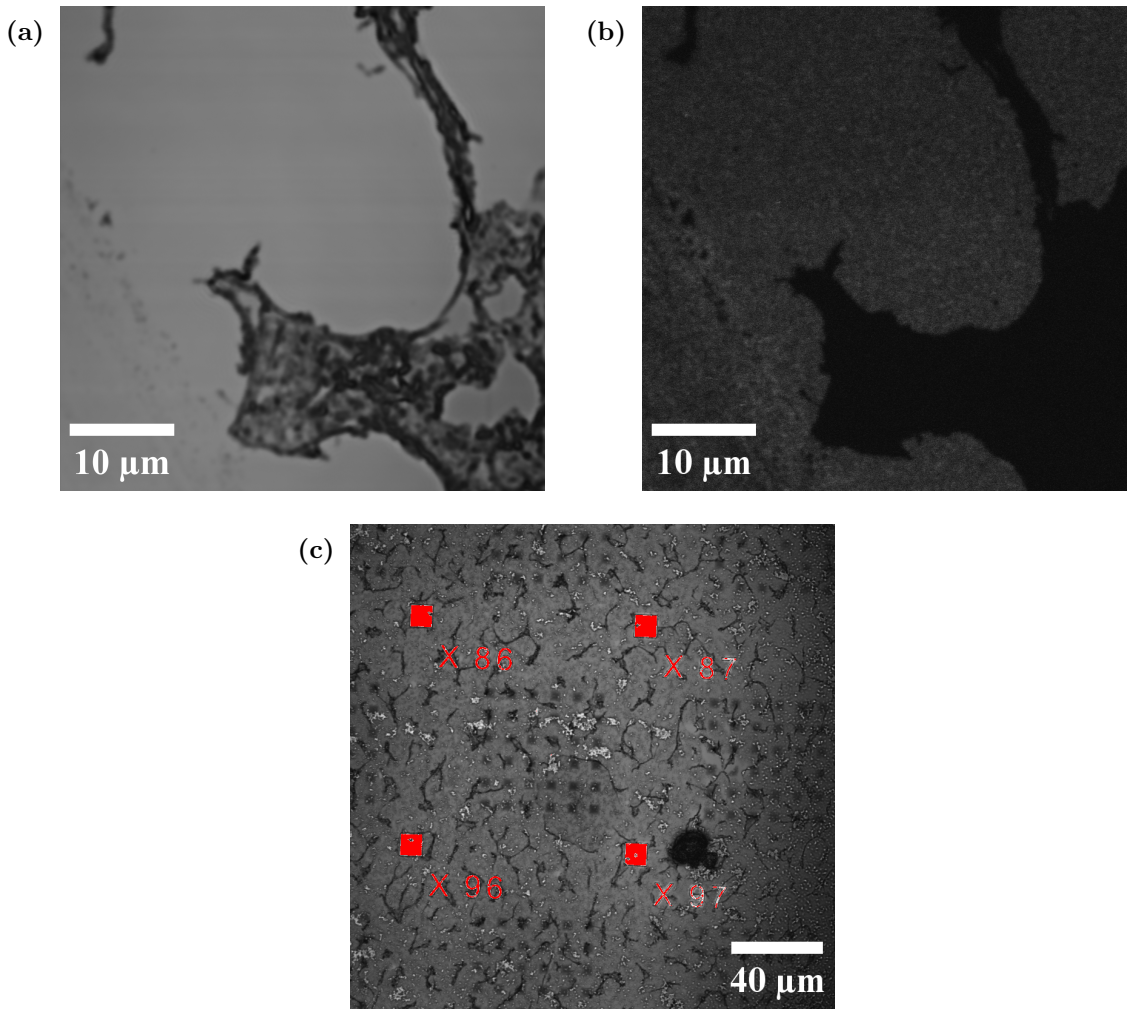

Figure 5.20: **(a)** A pseudo bright-field image of hBN flakes on graphene. **(b)** The same region imaged with 473 nm excitation with a 560-660 nm band pass filter. The PL image shows no active emitters. **(c)** PL image of reflected laser light showing scrolling of graphene due to hBN flakes around Al_2O_3 pillars.

5.7.2 Localisation of emitters in hBN flakes

After the hBN flakes were transferred onto pillars, they were imaged prior to annealing to compare the degree of localisation with the sample post annealing. Figure 5.23b shows a PL map of flakes on the substrate, in a region where the lateral dimensions of the pillars are 4.75 µm × 4.75 µm, before annealing. It can be seen that quenching has occurred in all regions except at the locations of the pillars. Here emission can be found on the edges of the pillars, suggesting that the flakes were predominantly located on the pillar

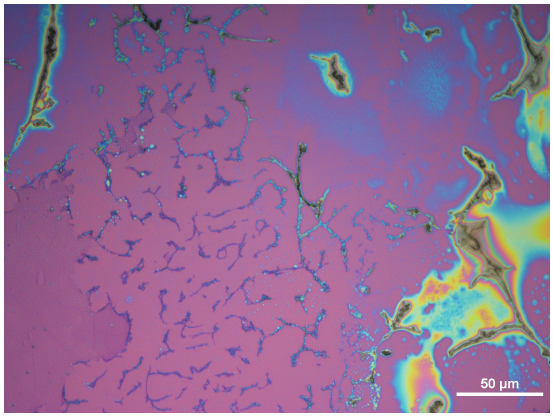

Figure 5.21: Optical image of region of graphene where 50:50 ethanol:DI water solution drop-casted, dried and heated to 200 °C. Scrolling of graphene in regions of Ethanol:Water residue (appear as colourful droplets and films in the image) can be seen.

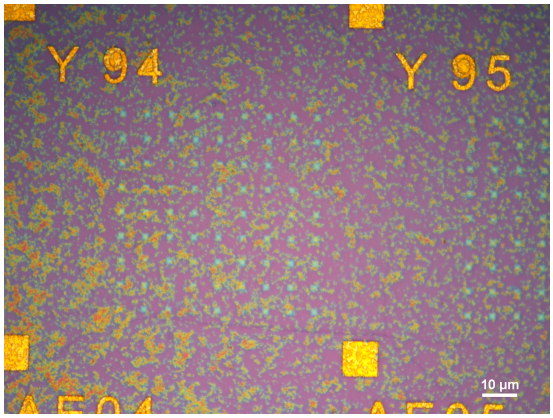

Figure 5.22: Optical image of hBN flakes deposited on Al_2O_3 pillars after an additional 50 ALD cycles in PM operation to grow the passivation film was performed.

edges. To verify this, an SEM image was taken of the region. Figure 5.23c, shows an SEM image of the same pillars. As can be seen, flakes are found throughout the sample, however the lack of a PL signal from areas where bare graphene is present suggests that quenching of these emitters has successfully occurred. Furthermore, it can be seen that the deposited flakes have preferentially agglomerated near the edges of the pillar. This is reminiscent of the "coffee ring" effect mentioned in Sec. 5.2, and supports the observation of emission at the pillar edges. The density of the flakes on the pillar is also significantly lower than on the passivated Al_2O_3/Gr, suggesting that the expected density of emitters on the pillar will also be lower. Additionally, the lack of any distinct PL signal from

regions where no pillars are located provides further evidence for the successful quenching of emitters not protected by Al_2O_3 of sufficient thickness. To further confirm the origin of emission, a hyperspectral map, similar to that performed in Sec. 5.4, was performed. The hyperspectral map has been shown in Fig, 5.23d and the location of emitters have been indicated by red circles. The location of these emitters are almost exclusive to the pillars and no emission is observed where an ultrathin Al_2O_3/Gr exists, conforming the observation in 5.23b. PL spectra from a select few regions circled in red have been shown in Fig, 5.24. These regions clearly show a PL signal, with a large ZPL in comparison to the PSB, and resemble the spectra observed in Sec. 5.4. Particularly, the spectra in Fig. 5.24c and 5.24d show similarities to Fig. 5.12a and 5.11b in terms of spectral shape or ZPL position, providing strong evidence for the source of emission being defects in hBN. It is known that environmental effects, such as strain can cause a shift in the ZPL energy [136, 137]. Hence the same defects can exhibit variation in emission spectra due to a change in substrate as the mismatch in lattice parameter between hBN and the substrate can vary between substrates, leading to different degrees of strain being induced on the defect. Although both Fig. 5.23b and 5.23d show faint luminescence outlining the pillar edges, no remarkable features in the spectra corresponding to this was found. The luminescence can be explained by faint scattering of excitation laser light from the pillar edges or Raman signals from the hBN flakes agglomerated at the pillar boundary. Finally, the sharp features in the spectra at ∼580 nm and ∼620 nm correspond to the G and 2D Raman peaks of the underlying graphene, indicating that the device fabrication process did not damage the graphene substrate.

Although localisation was observed at this stage, it is apparent from Fig. 5.23c that the density of flakes on the pillars is low, which would limit the observation of strong localisation at the pillars as the aim was to observe at least one emitter per pillar, for the pillars with the largest dimension. Hence, to increase the emitter density, a second layer of flakes was dropcasted onto the pillars after the same sonication process and sample was annealed. The aim of annealing was to uniformly increase the emitter density, which would lead to a higher probability of emitters located on top of pillars. As the probability of active emitters being screened by the pillars increases with the surface area of the

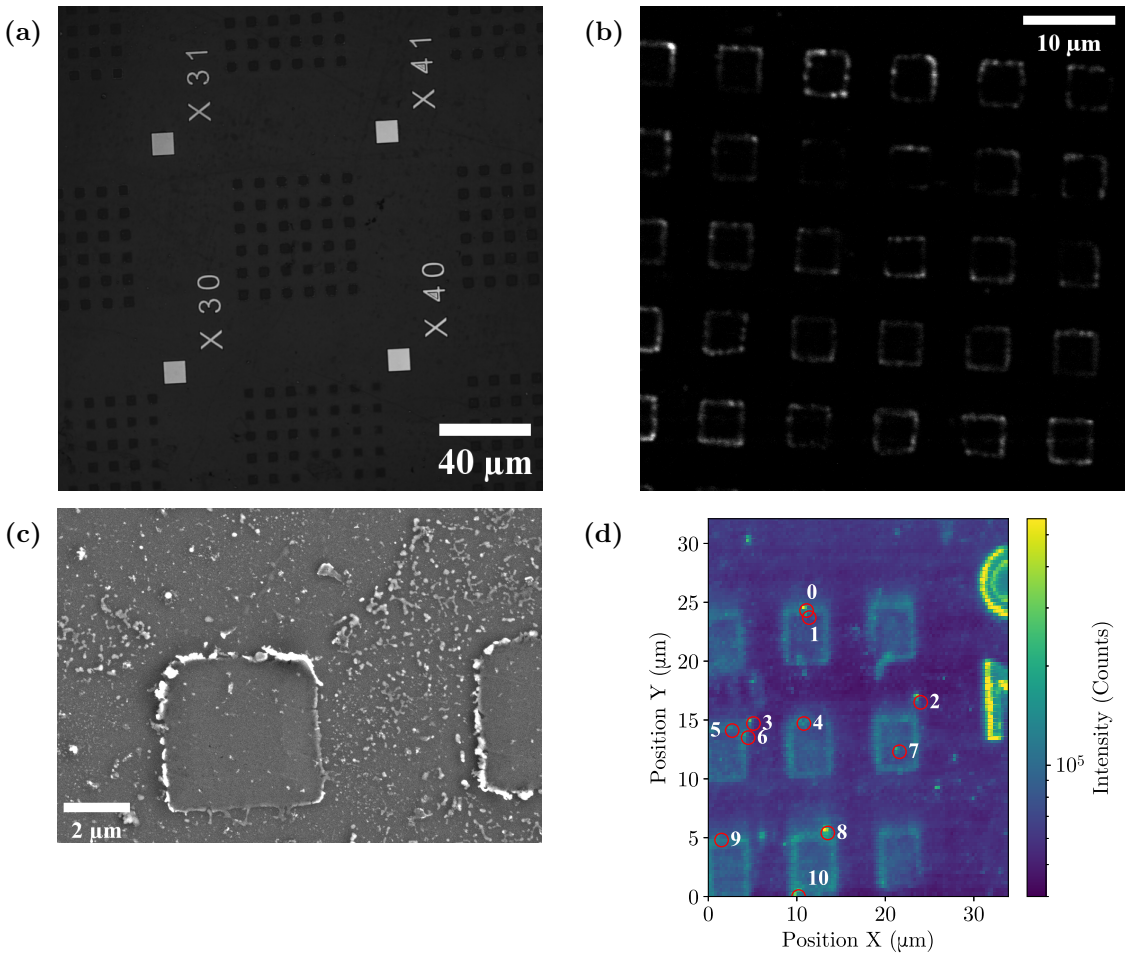

Figure 5.23: (a) Flakes deposited on 300 cycles ($\sim$ 40 nm) of Al_2O_3 grown and patterned into pillars, imaged in the pseudo bright-field mode as in Fig. 5.20a. (b) PL image of the flakes prior to annealing showing luminescence from the edges of the pillars. (c) SEM image of flakes deposited on these pillars. **(d)** A hyperspectral PL map of hBN flakes deposited on pillars formed from 300 ALD cycles performed to grow Al_2O_3. The red circles indicate regions where the spectrums showed a PL signal.

pillar, the pillars with the largest surface area were first explored to observe localisation. Regions close to the coffee-ring boundary of the dropcasted flakes were imaged as well as a region further away from the boundary. This was done to see if the localisation of emitters became more prominent with increasing flake density.

The imaging hereforth was done using Zeiss LSM 880 confocal microscope, using the methodology outlined in Sec. 4.2.3. The spectral scanning capability of this microscope allows immediate verification of the nature of the emission, as emitters would appear in

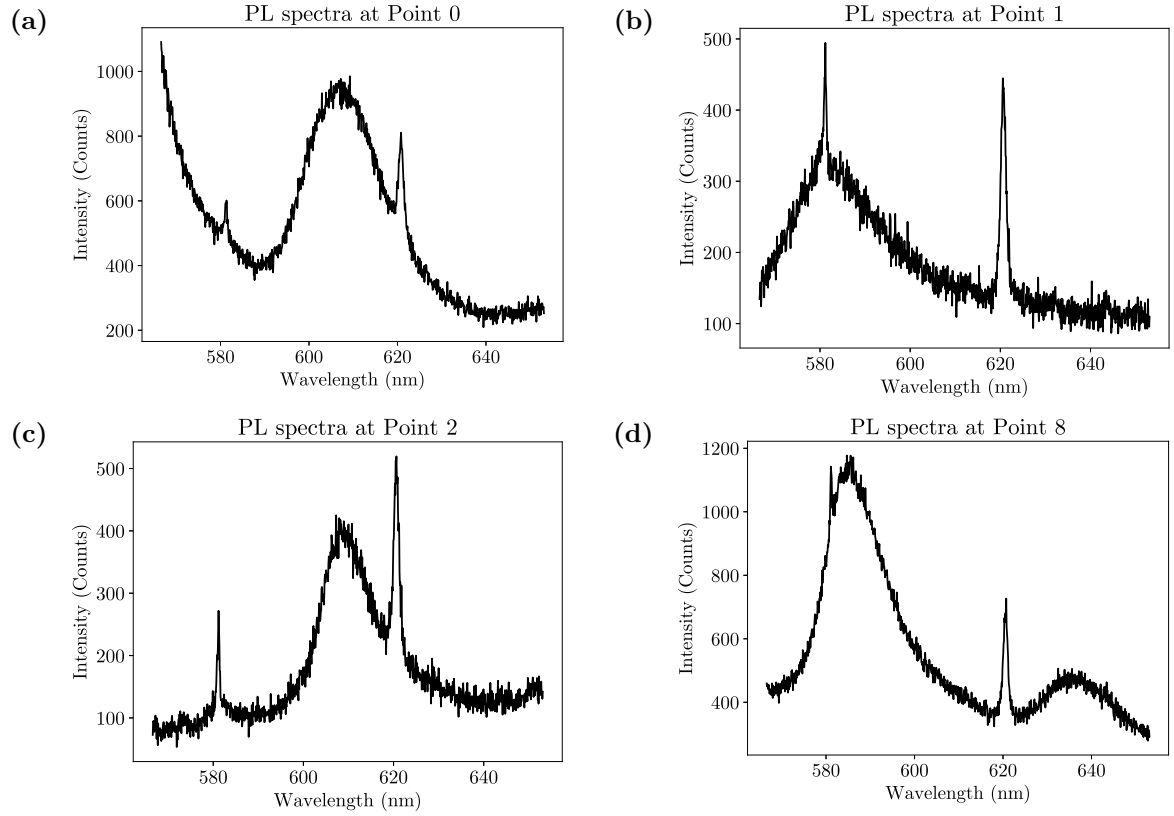

Figure 5.24: PL spectra at selected points, indicated by the title of the spectrum, in the hyperspectral PL map in Fig. 5.23d. **(a)** The ZPL appears to exist outside the measured spectral range. The PSB can be seen at $\sim 610\,\text{nm}$. **(b)** ZPL wavelength at $\sim 580\,\text{nm}$. **(c)** ZPL wavelength at $\sim 610\,\text{nm}$. **(d)** ZPL wavelength at $\sim$590 nm and PSB at $\sim 635\,\text{nm}$. The ubiquitous sharp peaks at 580 nm and 620 nm are the G and $2D$ Raman peaks of the underlying graphene.

a narrow spectral window due to its narrow ZPL. Hence, a feature that appears across several spectral windows, with a bandwidth larger than the typical linewidth of hBN emitters at room temperature $\sim$ 10 - 20 nm, would not be considered a colour centre in hBN. Figure 5.25, shows a pseudo bright-field image of this region. The existence of emitters on regions screened by pillars was verified by PL imaging, with a 561 nm excitation laser and 570 - 695 band pass filter. A spectral scan was performed with 3 nm bandwidth spectral slices, and PL images from each slice was analysed to identify emitters. Figure 5.26a shows the sum of all slices, which is equivalent to taking a single image with a wide band pass filter from 570 - 695 nm. From this image, it can be seen that diffraction limited spots exist at the pillar boundaries. In Figs. 5.26b–5.26f some of the bright spots

appearing in specific windows, circled in red, are seen in the sum of all the slices in Fig. 5.26a.

As emitter localisation was prominent in a region with a high flake density, it was of interest to see if a region away from the "coffee-ring" on the wafer, not to be confused with the "coffee-ring" on each pillar, would also display observable localisation. To observe this, a region of pillars with the same dimensions but uncovered by the second drop of flakes was found. Hence, in this region, the flake density would be comparable to that in Fig. 5.23a and an increase in emitter density could be attributed to annealing process. Fig, 5.27 shows a PL image of this region, with the same pillar dimensions as the region in Fig. 5.26. In comparison to image Fig. 5.23d and 5.23b, it can be seen that there is an increase in the number of emitters per pillar, with multiple difraction limited spots on the edges of nearly each pillar. As the flake density between the two regions is comparable as both regions correspond to the original step of dropcasted flakes, the difference in the number of emitters per pillar can be attributed to the annealing step. However, while emitters are largely restricted to the pillars, some emission can be observed on the Al_2O_3/Gr surrounding. This could be due to islands of residual Al_2O_3 after the etching process, which can be seen surrounding the pillars in Fig. 5.17c, 5.18b and 5.16e, being enhanced in thickness by the additional protective ALD layer, shielding emitters in these regions from quenching. The unwanted screen of emitters from graphene in regions away from the pillars also increase with emitter density and explains the lack of emission away from the pillars in Figures 5.23b and 5.23d.

Additional confirmation of the agglomeration of the flakes on the pillar edges was obtained from AFM measurements of flakes on the pillars, Fig. 5.28. In the image, features with a large height are seen outlining the pillar edges with few tall features on middle of the pillars , Fig. 5.28a. This is inline with the SEM image of the pillars, Fig. 5.23c. A height profile of a region with flakes on both edges of the pillar encountered along the horizontal axis of the crosshair is shown by a solid line in Fig. 5.28b. The dashed lines show the profile at a region on the pillar where flakes are not present at the right edge (dotted line). A fit to the step height on the dotted line is indicated by the red solid line. The step height was measured to be 39.1 ± 2.5 nm, which is the expected pillar height

after 300 ALD cycles with a growth rate of 0.13 nm per cycle. Furthermore, the flakes on the pillar edges agglomerate to clumps that have heights between 20 nm-120 nm. The heights of the flake clumps on the pillar edges are typical of flakes obtained from LPE. This supports the "coffee-ring" ring effect discussed earlier.

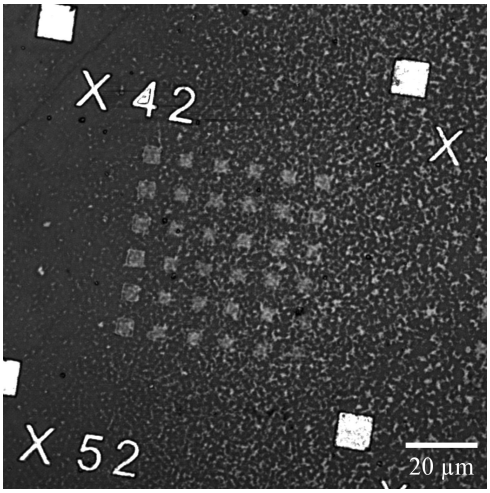

Figure 5.25: A pseudo bright-field image of a region of pillars close to the "coffee-ring" edge of the dropcasted flakes.

5.7.3 Localisation of emitters in CVD hBN

CVD hBN transferred using wet transfer on 40 nm thick Al_2O_3 pillars were imaged by SEM Fig. 5.29. Unlike when flakes were deposited on graphene and annealed, scrolling does not occur with CVD hBN, providing further evidence that the scrolling was due to residue from the flakes. Hence, no protective Al_2O_3 layer was needed to be grown. It can be seen that despite the strong oxidative treatment, the film underlying graphene layer is not damaged. Additionally, the nanometer to micrometer sized dark patches in Fig. 5.29 show that islands of Al_2O_3 remain after the etching process.

PL imaging was performed to determine if the emitters were localised to the pillars. As with flakes, the largest pillars were imaged first as they were most likely to show emission restricted to the pillars. Figure 5.30, show the result of a spectral scan of a subsection of the grid of pillars etched from Al_2O_3 grown from 400 ALD cycles. In Fig. 5.30a, the sum of all the slices is shown in the 570-695 nm spectral range as a single PL image.

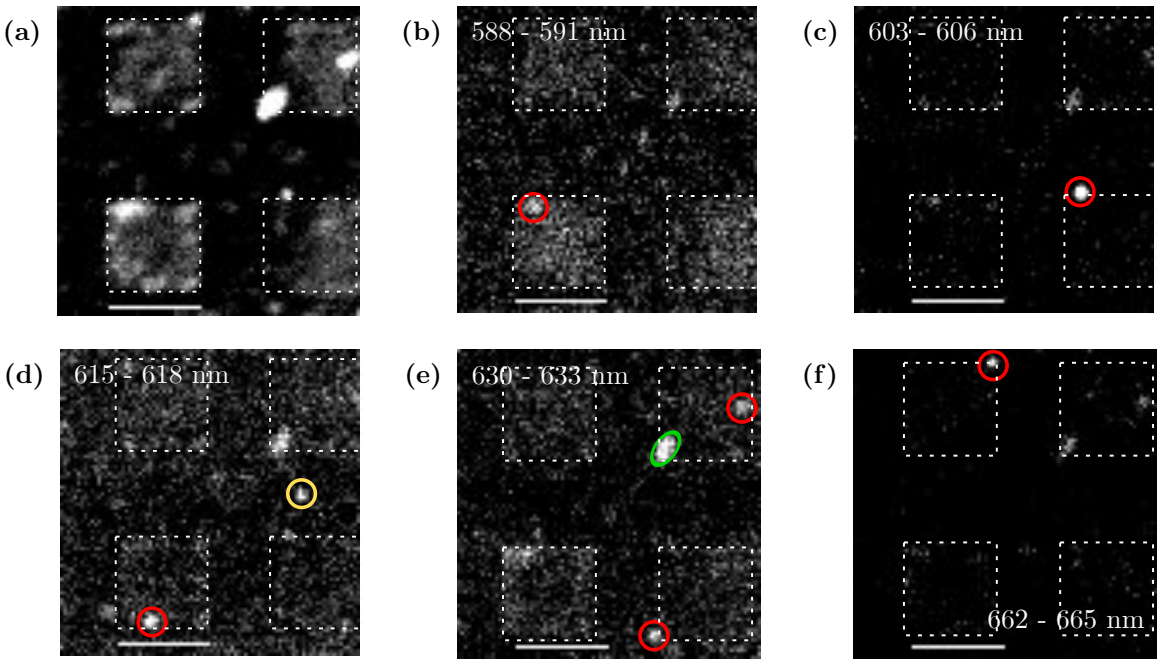

Figure 5.26: **(a)** PL image of the flakes post annealing showing luminescence from the edges of the pillars. This image was obtained by the summation of all the spectral slices over the range of 570-695 nm performed in the spectral scan. **(b)-(f)** Show some of these slices where diffraction limited spots were observed (circled in red). These are representative slices showing the brightest emitters. The yellow circles indicate regions where emission was observed on graphene in a narrow spectral window. The green ellipsoids highlight features that appeared in all windows, indicated a broadband spectrum. The pillars has been outlined by dashed border to aid the identification of their location. The scale bars correspond to 5 µm.

Diffraction limited spots, some of which show fluorescence intermittency, can be seen on the pillar edges and center and the graphene region is mostly dark. The specks which resemble emission are most likely due to the residual Al_2O_3 as seen in Fig. 5.29, which result in a background signal similar to the Al_2O_3 pillars. However, due to the dimensions of the islands being below the diffraction limit of the confocal microscope, they appear as spots that resemble emitters in hBN. To determine if this was indeed true, slices of different spectral windows were analysed to see if the signal from these specks appeared across a broad range of wavelengths. As the signal from these locations were ubiquitous in all spectral slices, they were not assigned as emitters in hBN. Unlike emitters, these islands should not possess well defined wavelengths at which PL signals are detected. In

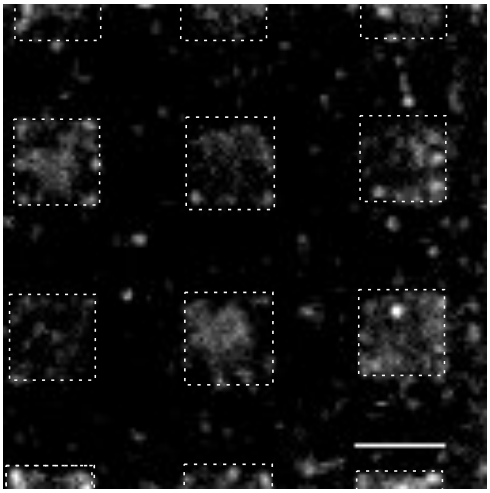

Figure 5.27: A PL image of a subsection of a region with low flake density, away from the coffee ring edge. The scale bar corresponds to 5 µm. The pillars have been outlined by dashed border to aid the identification of their location.

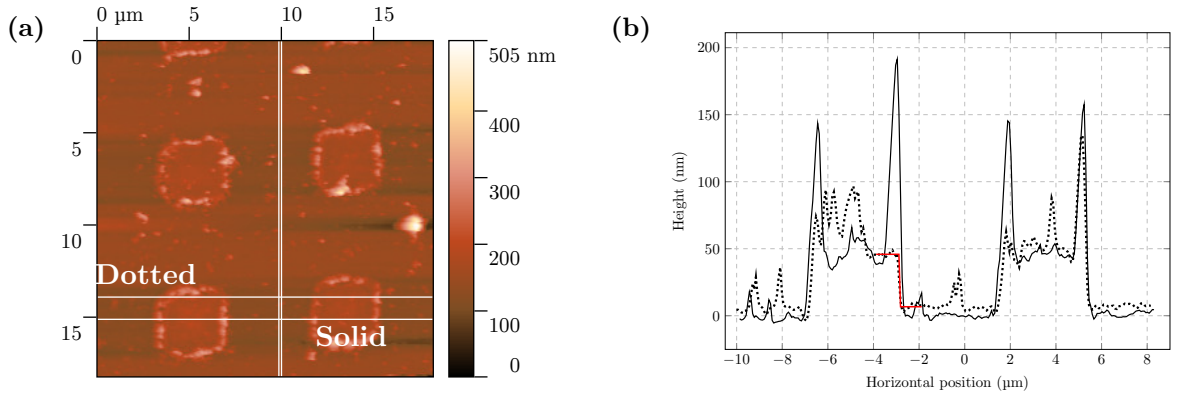

Figure 5.28: **(a)**AFM image of pillars with hBN flakes deposited on top. **(b)** Height profile of the pillars along the horizontal axis of the crosshair showing that the flakes preferentially agglomerate at the pillar edges. The solid line shows a region where the flakes exist on both edges of the pillar. The dotted line is a profile along the same pillar at a region without flakes on the right edge of the left pillar. The fit to the step height of the dotted line is indicated by a red solid line. The measured height is step height 39.1±2.5 nm.

Figures 5.30b–5.30d emission spots that showed a significant drop off in intensity away from the spectral window with peak intensity were accepted to be colour centres in hBN and circled in red. Those spots that did not show a drop off in signal across a wavelength range longer than the typical ZPL linewidth of hBN emitters, ∼20 nm, were determined to

be due to the Al_2O_3 islands or polymer residue on the surface of the multilayer hBN that was not quenched due to the thick (∼13 nm) hBN layer between the emitter and graphene or a combination of these effects. These spots have been circled green. There were also some sources of emission that did display the narrow linewidth character of emitters in hBN but were present in regions where bare graphene was present. These could be emitters in hBN that were screened by a combination of the Al_2O_3 islands and multilayer hBN in regions of bare graphene and have been circled blue. The emitters circled in the images are not an exhaustive list of all the emitters present but a representative selection of the brightest emitters to illustrate the extent to which emitter localisation has been achieved. It can be seen that all pillars in the region host diffraction limited spots at some wavelength range. This is consistent with the large emitter density found in Fig. 5.9d. The same degree of emission from the islands was not found with flakes as the protective ALD layer leads to the Al_2O_3 islands coalescing, leading to a more uniform background.

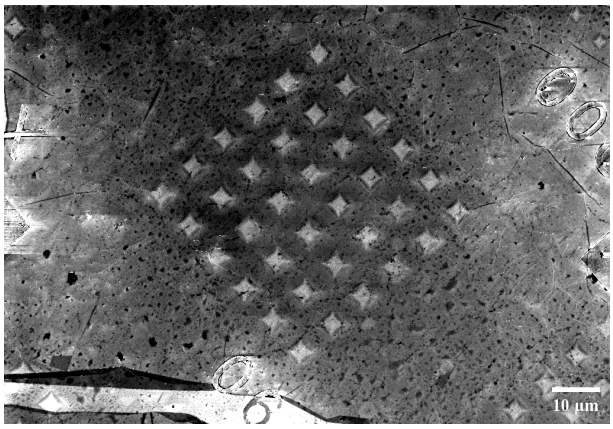

Figure 5.29: An SEM image of 4.75 µm × 4.75 µm pillars with multilayer CVD hBN transferred on top. The pillars were etched from an Al_2O_3 layer grown using 300 ALD cycles.

As the emitter density in CVD hBN was high and multiple emitters were found on all pillars, pillars with lateral dimensions of 3 µm × 3 µm were studied. In Fig. 5.31 a PL image of the subsection of these grids is shown. The sum of all the spectral slices has been shown in Fig. 5.31a, and it can be seen that the brightest spots are found on the pillars and the background spectra on the graphene is negligible. Furthermore, the emitter highlighted in Fig. 5.31c shows fluorescence intermittency, a feature commonly associated with emitters in hBN. The lack of PL signal from the bare graphene could be

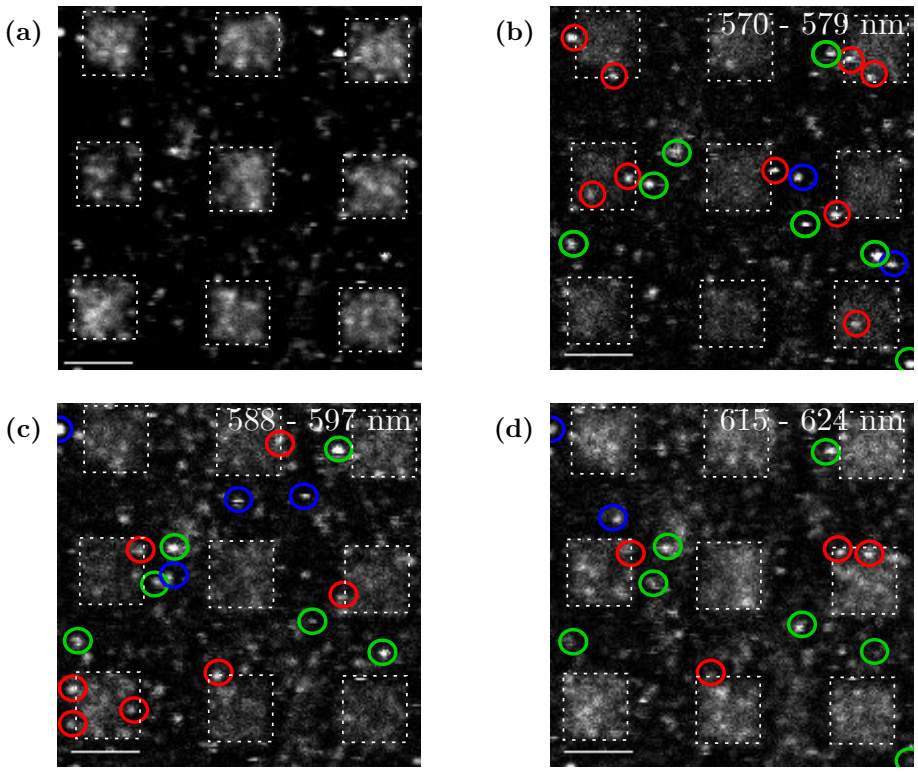

Figure 5.30: **(a)** PL image of the emitters in CVD hBN transferred onto pillars . This image was obtained by the summation of all the spectral slices over the range of 570-695 nm performed in the spectral scan. **(b)-(d)** Show some of these slices where diffraction limited spots which showed spectroscopic character typical to emitters (narrow linewidth emission) observed (circled in red). The blue circles indicate regions where emission was observed on bare graphene in a narrow spectral window. The green oval highlight features that appeared in nearly all windows, indicating a broad spectrum. These are representative slices showing the brightest emitters and are not an exhaustive list. The pillars has been outlined by dashed border to aid the identification of its location. The scale bar in all images corresponds to 5 µm.

due to more complete etching of the Al_2O_3 layer, leaving few islands contributing to the PL signal.

5.8 Discussion

The degree of localisation, challenges and potential solutions are now discussed.

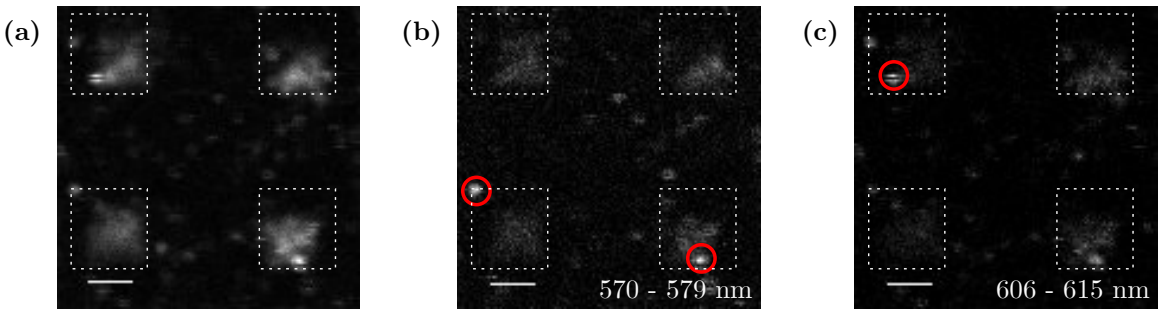

Figure 5.31: **(a)** PL image of the emitters in CVD hBN transferred onto pillars with half the dimension. This image was obtained by the summation of all the spectral slices in the 570-695 nm range performed in the spectral scan. **(b** and **(c)** Show some of these slices where diffraction limited spots which showed spectroscopic character typical to emitters (narrow linewidth emission) observed (circled in red). These are representative slices showing the brightest emitters and are not an exhaustive list. The pillars has been outlined by dashed border to aid the identification of its location. The scale bar in all images corresponds to 2 µm.

5.8.1 Degree of localisation

5.8.1.1 hBN flakes on Al_2O_3/Gr

In Figures 5.26a and 5.23d, it is evident that emitters are present on the pillars. The PL signal from these regions confirm the existence of a sharp ZPL in the 580-610 nm regime, which is the range of wavelengths emitters in hBN are known to most commonly exist [3, 47, 58]. Furthermore, in Fig. 5.24d the phonon sideband is seen $\sim$ 45 nm (180 meV) away from the ZPL. Emitters in hBN are known to possess a PSB that is usually 160-180 meV from the ZPL [3]. The SEM image in Fig. 5.23c and the AFM image in Fig. 5.28a shows that the flakes preferentially cluster at the pillar edges. When compared to Figs. 5.8, a resemblance is seen to the "coffee-ring" edge. The lack of sharp peaks at the center of the pillar in the AFM profile and their general presence at pillar edges further supports this. The SEM image, Fig. 5.23c, also shows a large density of flakes away from the pillars. The lack of emission from these regions despite the presence of a higher density of flakes shows that the Al_2O_3 protective film grown on graphene was sufficient to prevent quenching.

Comparing Fig. 5.27 with Figs. 5.23d and 5.23b, it can be seen that there is an increase

in emitter density. Both regions correspond to pillars with the same dimensions and comparable flake density as both regions were dropcast by flakes once. While multiple (3 or more) diffraction limited spots can be found on most pillars in the sample after annealing, few pillars host more than one emitter when no annealing is performed. Therefore, the observation of a higher density of emitters at pillar edges in Fig. 5.27 can be attributed to the creation and stabilisation of colour centres. This is supported by the observation of an increase in emitter density after annealing in Sec. 5.3. It is not obvious from Fig. 5.26a if the increase in flake density contributed to an increase in emitter density. A larger region needs to be imaged to make a direct comparison with Fig. 5.27. In principle, an increase in flake density should correlate to an increase in colour centre density as there is an increase in host material.

Finally, with the aid of spectral scanning, the emitters in Fig. 5.26 were distinguised from background signal and emission from sources not related to defects in hBN. As the colour centres in hBN have a ZPL transition with a narrow linewidth when compared to the broad background due to Al_2O_3, emission from islands of unetched Al_2O_3 could be ruled out by their presence in a wide spectral window. The bright spots identified as emitters in Fig. 5.26 show spectral characteristics similar to Figs. 5.11 and 5.12a.

5.8.1.2 CVD hBN on Al_2O_3/Gr

For CVD hBN, no protective ALD film had to be grown to prevent the scrolling of graphene. This allows a closer proximity between graphene and colour centres in hBN. However, in Fig. 5.30 it can be seen that there are several bright spots that exist in regions away from the pillars.

With the aid of the spectral scan, many of these bright spots appeared across several spectral windows. The existence of such a broad emission spectrum is consistent with Fig. 5.13, where sharp emission peaks were found where emitters were present. Therefore, these were attributed to islands of residual Al_2O_3 that remained after lithography. The SEM image of CVD hBN shows dark islands away from the Al_2O_3 pillar, Fig. 5.29, confirming the existence of unetched regions of Al_2O_3. These islands are sources of background emission that appear as diffraction limited spots, resembling emitters in hBN.

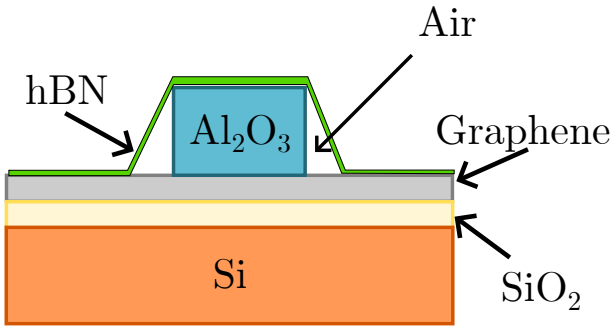

Figure 5.32: An illustration of the draping of the hBN film on an Al_2O_3 pillar

However, these islands can also allow further screening of emitters in hBN. Emitters at the top of the multilayer film experience addition screening from graphene due to the layers below. The combined effect of the islands and pillars can lead to many emitters being present in regions away from the pillars.

Furthermore, from Fig. 5.29, it appears that the hBN film drapes the pillars. This is illustrated in Fig. 5.32. The gap between hBN and the pillar is filled by air. The air acts as a dielectric and can also prevent quenching in the suspended region of hBN.

Finally, it appears that even in CVD hBN, emitters preferentially occur at the pillar edges, as seen in Fig. 5.31. While in the case of flakes it was due to the "coffee-ring" effect, in CVD hBN it is attributed to strain effects. It is well known, that in hBN emitters occur in high concentrations at regions of high strain [6, 137, 144]. At the pillar edges, strain is applied to hBN and emitters preferentially form in this region after annealing. Also, due to the large concentration of emitters in CVD hBN, localisation of emission was found in smaller pillars, with lateral dimensions of 3 µm × 3 µm. In the region imaged in Fig. 5.31a, no observable emission is observed from regions with bare graphene. This could be due to more complete removal of Al_2O_3 in this region compared to Fig. 5.30.

5.8.2 Fabrication challenges and proposed solutions

The two principal challenges are: (1) uniform creation of a high density of emitters and (2) complete etching of Al_2O_3 away from the pillars.

With regards to flakes, a uniform emitter concentration is difficult to achieve due to flakes agglomerating at the pillar edges. A modification of the drop casting process could

offer the solution. This could involve spin coating the flakes onto the substrate. Spin coating uniformly distributes flakes onto the substrate and could eliminate the "coffee ring". Another possible solution is to incorporate treatment techniques that increase emitter density uniformly. If the emitter concentration is higher than the surface area at the top of each pillar, then each pillar could host at least one emitter. These treatments include annealing in methane and oxygen [162, 163]. In CVD hBN, the transfer process leads to polymer residue on the sample that can lead to a broad background contaminating signal from emitters in hBN. The cleaning process involving oxidation in air, while effective in removing the residue, also removes carbon impurities in hBN which are known to be responsible for luminescence in hBN [7, 66]. Subsequent annealing after oxidation is known to recover colour centres [7], however, excessive oxidation may cause damage beyond recovery. Incomplete removal of polymer residue on the other hand can lead to the formation of an amorphous carbon layer, when hBN is annealed in an inert atmosphere. The PL background from the carbon layer can overwhelm the PL signal from the emitters.

A transfer process that leads to less contamination, such as one that uses a support layer that leaves less residue [164], or a polymer removal technique that uses a different environment from oxygen, such as H_2 [49], can improve the device performance. The ideal transfer process would leave no contamination and the films would not need post-transfer treatment.

The challenge with regards to the lithography of the Al_2O_3 pillars is also that of optimisation. In Fig. 5.29, it is clear that the consequence of underetching is the existence of the islands of Al_2O_3. However, the problem cannot be solved by a simple increase in etch times. Figure 5.33a shows pillars etched from Al_2O_3 grown from 500 ALD cycles. The etch times for this sample was significantly longer than that outlined in Sec. 4.1.5. It can be seen from the AFM profile that unlike the flat surface morphology in Fig. 5.33a, the pillars have a pyramidal structure. The height profile, Fig. 5.33b, also shows that the height of the pillar is much lower than the expected 65 nm from the 0.13 nm per cycle growth rate, for most of its volume. The sharp peak at the middle shows a narrow unetched region, with a height similar to the expected height from the ALD growth rate. The pyramidal feature is a consequence of undercutting during wet chemical etching, Fig. 5.33c. This

occurs when the etchant, in this case H_3PO_4, starts to remove the features protected by the e-beam exposed resist. From the AFM image, it can be seen that overetching leaves little Al_2O_3 residue on graphene. The etch times to fully develop the features is also not uniform throughout the sample as the height of the ALD film and its density varies throughout the sample due to the initial stages of non-uniform nucleation. The effect of undercutting is more pronounced in features with a high aspect ratio.

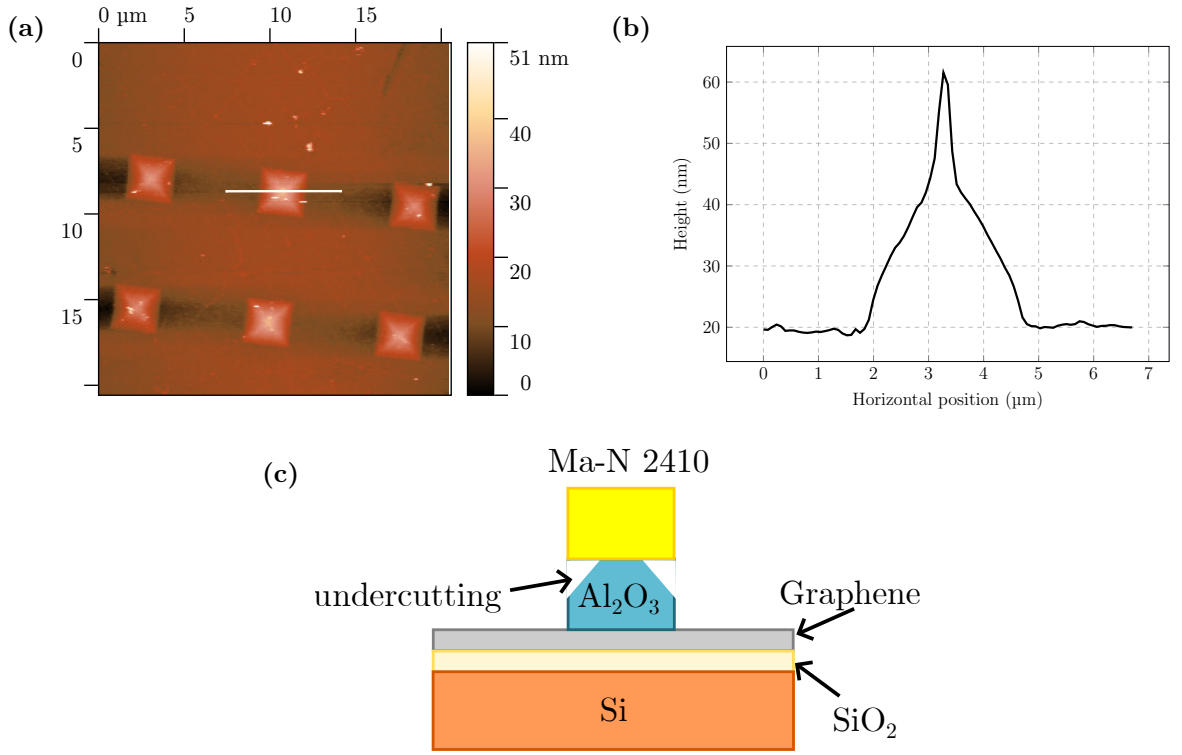

Figure 5.33: **(a)**AFM image of undercut pillars of Al_2O_3 obtained from a film grown using 500 ALD cycles. **(b)** Height profile along white line indicated in **(a)** showing pyramidal shape. **(c)** Shows an illustration of the undercutting process.

To address this problem, a detailed optimisation of the concentration of the etchant, etching temperatures and times need to be made. A more dilute solution will lead to less undercutting, but longer etch times. The process will also be aided by the growth of an ALD film that has uniform density. A mask with greater etch selectivity against Al_2O_3, such as hard masks, can also be used instead of that used in this project.

5.9 Conclusion

In conclusion, it has been shown that colour centres in hBN can be localised to regions with an Al_2O_3 barrier between hBN and graphene. This occurs due to quenching of emission in regions where emitters are in close proximity to graphene. It was found that hBN flakes preferentially agglomerate at the pillar edges due to a "coffee-ring" effect and CVD hBN hosts emitters at the pillar edges due to strain effects. Therefore, simultaneous control of the charge state and strain of the defects can be performed using such a device structure. Finally, it was found that incomplete etching of the ALD film leads to islands of residue that can have the appearance of emitters on graphene. The fabrication of such a device requires careful optimisation of the etch process of ALD films to eliminate residual islands and high and uniform emitter densities. In the future, it will useful to obtain a statistical analysis of emitter density variation with different types of treatment. This will aid in the engineering of pillars that host the desired number of emitters per pillar.

Chapter 6

Overview and Future Outlook

hBN colour centres have significant interest in quantum technologies [33] and defect based LEDs [28]. It is therefore crucial to have on-demand charge control of defects in hBN. In this work, a theoretical framework to understand charge transfer has been developed and the influence of encapsulating hBN and graphene layers on defect thermodynamics has been studied. Experimentally, a device design for the localisation of emitters using charge and energy transfer with a graphene substrate has been shown.

The theoretical explorations showed that at equilibrium, the defects either become charged or remain neutral depending on the position of their donor or acceptor levels with respect to the work function of graphene. For hBN directly interfaced with graphene, particularly when the defects were within a few monolayers from the graphene layer and charge carrier tunnelling was significant (Sec. 5.1), the defects would be in a charged state if thermodynamically feasible, resulting in the absence of photoluminescence. However, as energy transfer occurs over longer length scales (on the order of 10 nm), emitters were quenched via energy transfer for all thicknesses of hBN. Hence, theoretical models of equilibrium charge states and rates of charge transfer via different processes informed the experimental engineering of pillar thickness. The choice of pillar thickness in this thesis was sufficient to suppress energy transfer while still maintaining nanometre thickness. As such, the combined theoretical and experimental approach greatly increases the engineerability of the device for various applications.

This study contributes to the endeavour of achieving electroluminescence in defects in

hBN and electric field control using graphene gates. The advantage of the device design used in this study is in its versatility for use in many applications without significant modifications to fabrication process. To develop this device for charge injection, the barrier thickness can be reduced to allow tunnelling of electrons into defect states. To achieve electric field control on the other hand, the Al_2O_3 layer can be changed to a dielectric with a higher dielectric constant, which allows a larger field to be applied without breakdown. For example, the high wettability of graphene by yttrium allows the growth of continuous Y_2O_3 films via electron beam evaporation of Y on graphene followed by oxidation in air [165]. Y_2O_3 ($k \approx 15$) has a higher dielectric constant than Al_2O_3 ($k \approx 9$) [166], a smaller conduction band offset from graphene (the conduction band edge of Y_2O_3 is nearly 1 eV lower in energy than Al_2O_3) and a 2.8 eV smaller band gap than Al_2O_3 [167]. Thus, the tunnelling barrier height for charge carriers is lower when a Y_2O_3 film is used instead of an Al_2O_3 film, while the higher dielectric constant leads to significantly greater suppression of energy transfer due to greater screening of the Coulomb interaction between the emitter and graphene at smaller film thicknesses. Thus, it is ideal for driving electroluminescence where carrier tunnelling rates need to be enhanced but quenching needs to be suppressed.

In this exploration, the emitter localisation on pillars with a larger surface area have been studied. It is of interest to continue this work and image regions with significantly smaller lateral dimensions to explore the dimensions at which each pillar hosts a single emitter. The nature of such an emitter can be determined by Hanbury Brown and Twiss measurements. Such a device will not only allow site control of emitters in hBN, but also the control of the brightness of LEDs through the deterministic control of the density of emitters in a region.

The theoretical work can be extended to study the impact of spacers of different dielectric constants and band gaps on the degree of charge transfer between defects in hBN and graphene. The additional level of detail in the simulations manifests as a larger system, with significantly more atoms. Hence, future work could greatly benefit from DFT codes that scale linearly with system size, a much faster scaling than the standard DFT used in this thesis that scales as the cube of the system size. This will allow details such as the im-

pact of various types of substrates and grain boundaries on colour centre properties to be simulated. Furthermore, calculations of spectra and radiative lifetimes of different defects for comparison with tunnelling rates across a variety of barriers will aid in the fabrication of devices where not only spatial control over emitters can be achieved via the nanopillars, but control over the types of emitters that remain active can be obtained. Calculations of dynamics usually require schemes beyond standard DFT, such as time-dependent DFT (TD-DFT) [168]. Addtionally, when studying transition paths, such as those in Sec. 3.4, several pathways need to considered and explicitly simulated with full accuracy to find the MEP. Thus, a significant amount of computational resources are consumed on calculations that do not have much significance to the researcher. It is therefore useful to be able to speed up the search over the phase space using techniques such as machine-learning [169]. The future of hBN based quantum technologies relies on the combination of theoretical models with novel fabrication techniques and this thesis contributes to this effort. Such an endeavour will contribute significantly to the advancement of hBN defect based optoelectronics, quantum photonics and metrology.

Bibliography

[1] N. Alem, R. Erni, C. Kisielowski, M. D. Rossell, W. Gannett, and A. Zettl, "Atomically thin hexagonal boron nitride probed by ultrahigh-resolution transmission electron microscopy," *Physical Review B*, vol. 80, no. 15, p. 155425, 2009.

[2] T. T. Tran, K. Bray, M. J. Ford, M. Toth, and I. Aharonovich, "Quantum emission from hexagonal boron nitride monolayers," *Nature Nanotechnology*, vol. 11, pp. 37–41, 1 2016. [Online]. Available: http://www.nature.com/articles/nnano.2015.242

[3] T. T. Tran, C. Elbadawi, D. Totonjian, C. J. Lobo, G. Grosso, H. Moon, D. R. Englund, M. J. Ford, I. Aharonovich, and M. Toth, "Robust multicolor single photon emission from point defects in hexagonal boron nitride," *ACS Nano*, vol. 2017-January, 2016.

[4] M. Kianinia, S. White, J. E. Fröch, C. Bradac, and I. Aharonovich, "Generation of spin defects in hexagonal boron nitride," *ACS Photonics*, vol. 7, 2020.

[5] C. Fournier, A. Plaud, S. Roux, A. Pierret, M. Rosticher, K. Watanabe, T. Taniguchi, S. Buil, X. Quélin, J. Barjon *et al.*, "Position-controlled quantum emitters with reproducible emission wavelength in hexagonal boron nitride," *Nature Communications*, vol. 12, no. 1, p. 3779, 2021.

[6] C. Li, N. Mendelson, R. Ritika, Y. Chen, Z.-Q. Xu, M. Toth, and I. Aharonovich, "Scalable and deterministic fabrication of quantum emitter arrays from hexagonal boron nitride," *Nano Letters*, vol. 21, no. 8, pp. 3626–3632, 2021.

[7] J. C. Stewart, Y. Fan, J. S. Danial, A. Goetz, A. S. Prasad, O. J. Burton, J. A. Alexander-Webber, S. F. Lee, S. M. Skoff, V. Babenko, and S. Hofmann, "Quan-

tum emitter localization in layer-engineered hexagonal boron nitride," *ACS Nano*, vol. 15, 2021.

[8] S. J. U. White, T. Yang, N. Dontschuk, C. Li, Z.-Q. Xu, M. Kianinia, A. Stacey, M. Toth, and I. Aharonovich, "Electrical control of quantum emitters in a van der waals heterostructure (vol 11, 186, 2022)," *Light: Science & Applications*, vol. 11, no. 1, p. 186, JUL 18 2022.

[9] M. C. Payne, M. P. Teter, D. C. Allan, T. Arias, and a. J. Joannopoulos, "Iterative minimization techniques for ab initio total-energy calculations: molecular dynamics and conjugate gradients," *Reviews of Modern Physics*, vol. 64, no. 4, p. 1045, 1992.

[10] S. Grimme, "Density functional theory with london dispersion corrections," *Wiley Interdisciplinary Reviews: Computational Molecular Science*, vol. 1, no. 2, pp. 211–228, 2011.

[11] G. Henkelman, B. P. Uberuaga, and H. Jónsson, "A climbing image nudged elastic band method for finding saddle points and minimum energy paths," *The Journal of Chemical Physics*, vol. 113, no. 22, pp. 9901–9904, 2000.

[12] M. Topsakal, E. Aktürk, and S. Ciraci, "First-principles study of two- and one-dimensional honeycomb structures of boron nitride," *Physical Review B - Condensed Matter and Materials Physics*, vol. 79, 2009.

[13] V. Barone, J. E. Peralta, J. Uddin, and G. E. Scuseria, "Screened exchange hybrid density-functional study of the work function of pristine and doped single-walled carbon nanotubes," *The Journal of Chemical Physics*, vol. 124, no. 2, p. 024709, 2006.

[14] V. Barone, O. Hod, J. E. Peralta, and G. E. Scuseria, "Accurate prediction of the electronic properties of low-dimensional graphene derivatives using a screened hybrid density functional," *Accounts of Chemical Research*, vol. 44, no. 4, pp. 269–279, 2011.

[15] D. Wang and R. Sundararaman, "Layer dependence of defect charge transition levels in two-dimensional materials," *Physical Review B*, vol. 101, 2020.

[16] G. Noh, D. Choi, J. H. Kim, D. G. Im, Y. H. Kim, H. Seo, and J. Lee, "Stark tuning of single-photon emitters in hexagonal boron nitride," *Nano Letters*, vol. 18, 2018.

[17] R. W. Johnson, A. Hultqvist, and S. F. Bent, "A brief review of atomic layer deposition: from fundamentals to applications," *Materials Today*, vol. 17, no. 5, pp. 236–246, 2014.

[18] *PMMA and Copolymer*, Kayaku Advanced Materials, 4 2021, ver 3.

[19] *ma-N 2400 series*, Microresist Technology.

[20] R. V. Gorbachev, I. Riaz, R. R. Nair, R. Jalil, L. Britnell, B. D. Belle, E. W. Hill, K. S. Novoselov, K. Watanabe, T. Taniguchi, A. K. Geim, and P. Blake, "Hunting for monolayer boron nitride: Optical and raman signatures," *Small*, vol. 7, no. 4, pp. 465–468, 2010. [Online]. Available: https://onlinelibrary.wiley.com/doi/abs/10.1002/smll.201001628

[21] W. M. Reilly and C. J. Obara, "Advances in confocal microscopy and selected applications," *Confocal Microscopy: Methods and Protocols*, pp. 1–35, 2021.

[22] S. Bauer, B. Grees, D. Spitzer, M. Beck, R. Bottesch, H.-W. Ortjohann, B. Ostrick, T. Schäfer, H. Telle, A. Wegmann *et al.*, "Ellipsometry with polarisation analysis at cryogenic temperatures inside a vacuum chamber," *Review of Scientific Instruments*, vol. 84, no. 12, 2013.

[23] G. Dehm, J. M. Howe, and J. Zweck, *In-situ electron microscopy: Applications in physics, chemistry and materials science*. John Wiley & Sons, 2012.

[24] O. Salihoglu, N. Kakenov, O. Balci, S. Balci, and C. Kocabas, "Graphene as a reversible and spectrally selective fluorescence quencher," *Scientific Reports*, vol. 6, no. 1, p. 33911, 2016.

[25] R. J. Tilley, *Defects in solids*. John Wiley & Sons, 2008.

[26] N. W. Ashcroft, N. D. Mermin, and S. Rodriguez, "Solid state physics," *American Journal of Physics*, vol. 46, no. 1, pp. 116–117, 1978.

[27] T. Schröder, F. Gädeke, M. J. Banholzer, and O. Benson, "Ultrabright and efficient single-photon generation based on nitrogen-vacancy centres in nanodiamonds on a solid immersion lens," *New Journal of Physics*, vol. 13, no. 5, p. 055017, 2011.

[28] M. Grzeszczyk, K. Vaklinova, K. Watanabe, T. Taniguchi, K. S. Novoselov, and M. Koperski, "Electroluminescence from pure resonant states in hbn-based vertical tunneling junctions," *Light: Science & Applications*, vol. 13, no. 1, p. 155, 2024.

[29] S. H. Lee, H. Jeong, D. Y. Kim, S.-Y. Seo, C. Han, O. F. N. Okello, J.-I. Lo, Y.-C. Peng, C.-H. Oh, G. W. Lee *et al.*, "Electroluminescence from h-bn by using al 2 o 3/h-bn multiple heterostructure," *Optics Express*, vol. 27, no. 14, pp. 19 692–19 701, 2019.

[30] A. Gottscholl, M. Diez, V. Soltamov, C. Kasper, D. Krauße, A. Sperlich, M. Kianinia, C. Bradac, I. Aharonovich, and V. Dyakonov, "Spin defects in hbn as promising temperature, pressure and magnetic field quantum sensors," *Nature Communications*, vol. 12, no. 1, p. 4480, 2021.

[31] I. Aharonovich and E. Neu, "Diamond nanophotonics," *Advanced Optical Materials*, vol. 2, 2014.

[32] F. Fuchs, B. Stender, M. Trupke, D. Simin, J. Pflaum, V. Dyakonov, and G. V. Astakhov, "Engineering near-infrared single-photon emitters with optically active spins in ultrapure silicon carbide," *Nature Communications*, vol. 6, 2015.

[33] I. Aharonovich, D. Englund, and M. Toth, "Solid-state single-photon emitters," *Nature Photonics*, vol. 10, 2016.

[34] D. White, A. Branny, R. J. Chapman, R. Picard, M. Brotons-Gisbert, A. Boes, A. Peruzzo, C. Bonato, and B. D. Gerardot, "Atomically-thin quantum dots integrated with lithium niobate photonic chips [invited]," *Optical Materials Express*, vol. 9, 2019.

[35] Y. M. He, G. Clark, J. R. Schaibley, Y. He, M. C. Chen, Y. J. Wei, X. Ding, Q. Zhang, W. Yao, X. Xu, C. Y. Lu, and J. W. Pan, "Single quantum emitters in monolayer semiconductors," *Nature Nanotechnology*, vol. 10, 2015.

[36] P. Tonndorf, R. Schmidt, R. Schneider, J. Kern, M. Buscema, G. A. Steele, A. Castellanos-Gomez, H. S. J. van der Zant, S. M. de Vasconcellos, and R. Bratschitsch, "Single-photon emission from localized excitons in an atomically thin semiconductor," *Optica*, vol. 2, 2015.

[37] M. Koperski, K. Nogajewski, A. Arora, V. Cherkez, P. Mallet, J. Y. Veuillen, J. Marcus, P. Kossacki, and M. Potemski, "Single photon emitters in exfoliated wse2 structures," *Nature Nanotechnology*, vol. 10, 2015.

[38] C. Palacios-Berraquero, M. Barbone, D. M. Kara, X. Chen, I. Goykhman, D. Yoon, A. K. Ott, J. Beitner, K. Watanabe, T. Taniguchi, A. C. Ferrari, and M. Atatüre, "Atomically thin quantum light-emitting diodes," *Nature Communications*, vol. 7, 2016.

[39] J. Wang, F. Ma, and M. Sun, "Graphene, hexagonal boron nitride, and their heterostructures: properties and applications," *RSC Advances*, vol. 7, 2017.

[40] P. Miró, M. Audiffred, and T. Heine, "An atlas of two-dimensional materials," *Chemical Society Reviews*, vol. 43, 2014.

[41] C. Tan, X. Cao, X. J. Wu, Q. He, J. Yang, X. Zhang, J. Chen, W. Zhao, S. Han, G. H. Nam, M. Sindoro, and H. Zhang, "Recent advances in ultrathin two-dimensional nanomaterials," *Chemical Reviews*, vol. 117, 2017.

[42] Y. Kimura, T. Wakabayashi, K. Okada, T. Wada, and H. Nishikawa, "Boron nitride as a lubricant additive," *Wear*, vol. 232, no. 2, pp. 199–206, 1999.

[43] L. Chen, K. Elibol, H. Cai, C. Jiang, W. Shi, C. Chen, H. S. Wang, X. Wang, X. Mu, C. Li *et al.*, "Direct observation of layer-stacking and oriented wrinkles in multilayer hexagonal boron nitride," *2D Materials*, vol. 8, no. 2, p. 024001, 2021.

[44] Y. Ji, B. Calderon, Y. Han, P. Cueva, N. R. Jungwirth, H. A. Alsalman, J. Hwang, G. D. Fuchs, D. A. Muller, and M. G. Spencer, "Chemical vapor deposition growth of large single-crystal mono-, bi-, tri-layer hexagonal boron nitride and their interlayer stacking," *ACS Nano*, vol. 11, no. 12, pp. 12 057–12 066, 2017.

[45] C. Elias, P. Valvin, T. Pelini, A. Summerfield, C. J. Mellor, T. S. Cheng, L. Eaves, C. T. Foxon, P. H. Beton, S. V. Novikov, B. Gil, and G. Cassabois, "Direct band-gap crossover in epitaxial monolayer boron nitride," *Nature Communications*, vol. 10, 2019.

[46] Z. R. Robinson, S. W. Schmucker, K. M. McCreary, and E. D. Cobas, *Chemical Vapor Deposition of Two-Dimensional Crystals.* Elsevier, 2015, vol. 3.

[47] N. Mendelson, Z. Q. Xu, T. T. Tran, M. Kianinia, J. Scott, C. Bradac, I. Aharonovich, and M. Toth, "Engineering and tuning of quantum emitters in few-layer hexagonal boron nitride," *ACS Nano*, vol. 13, 2019.

[48] H. L. Stern, R. Wang, Y. Fan, R. Mizuta, J. C. Stewart, L.-M. Needham, T. D. Roberts, R. Wai, N. S. Ginsberg, D. Klenerman *et al.*, "Spectrally resolved photodynamics of individual emitters in large-area monolayers of hexagonal boron nitride," *ACS Nano*, vol. 13, no. 4, pp. 4538–4547, 2019.

[49] A. G. Garcia, M. Neumann, F. Amet, J. R. Williams, K. Watanabe, T. Taniguchi, and D. Goldhaber-Gordon, "Effective cleaning of hexagonal boron nitride for graphene devices," *Nano Letters*, vol. 12, no. 9, pp. 4449–4454, 2012.

[50] K. S. Novoselov, D. Jiang, F. Schedin, T. J. Booth, V. V. Khotkevich, S. V. Morozov, and A. K. Geim, "Two-dimensional atomic crystals," *Proceedings of the National Academy of Sciences of the United States of America*, vol. 102, 2005.

[51] G. R. Bhimanapati, N. R. Glavin, and J. A. Robinson, *2D Boron Nitride: Synthesis and Applications.* Elsevier, 2016, vol. 95, pp. 101–147.

[52] A. Hernández-Mínguez, J. Lähnemann, S. Nakhaie, J. M. Lopes, and P. V. Santos,

"Luminescent defects in a few-layer h -bn film grown by molecular beam epitaxy," *Physical Review Applied*, vol. 10, 2018.

[53] M. Koperski, K. Nogajewski, and M. Potemski, "Single photon emitters in boron nitride: More than a supplementary material," *Optics Communications*, vol. 411, 2018.

[54] C. Li, Z. Q. Xu, N. Mendelson, M. Kianinia, M. Toth, and I. Aharonovich, "Purification of single-photon emission from hbn using post-processing treatments," *Nanophotonics*, 2019.

[55] J. D. Caldwell, I. Aharonovich, G. Cassabois, J. H. Edgar, B. Gil, and D. N. Basov, "Photonics with hexagonal boron nitride," *Nature Reviews Materials*, vol. 4, 2019.

[56] L. J. Martínez, T. Pelini, V. Waselowski, J. R. Maze, B. Gil, G. Cassabois, and V. Jacques, "Efficient single photon emission from a high-purity hexagonal boron nitride crystal," *Physical Review B*, vol. 94, 2016.

[57] N. R. Jungwirth, B. Calderon, Y. Ji, M. G. Spencer, M. E. Flatté, and G. D. Fuchs, "Temperature dependence of wavelength selectable zero-phonon emission from single defects in hexagonal boron nitride," *Nano Letters*, vol. 16, no. 10, pp. 6052–6057, 2016.

[58] N. Chejanovsky, M. Rezai, F. Paolucci, Y. Kim, T. Rendler, W. Rouabeh, F. Fávaro de Oliveira, P. Herlinger, A. Denisenko, S. Yang *et al.*, "Structural attributes and photodynamics of visible spectrum quantum emitters in hexagonal boron nitride," *Nano Letters*, vol. 16, no. 11, pp. 7037–7045, 2016.

[59] R. Bourrellier, S. Meuret, A. Tararan, O. Stéphan, M. Kociak, L. H. Tizei, and A. Zobelli, "Bright uv single photon emission at point defects in h-bn," *Nano Letters*, vol. 16, 2016.

[60] S. Choi, T. T. Tran, C. Elbadawi, C. Lobo, X. Wang, S. Juodkazis, G. Seniutinas, M. Toth, and I. Aharonovich, "Engineering and localization of quantum emitters in

large hexagonal boron nitride layers," *ACS Applied Materials & Interfaces*, vol. 8, no. 43, pp. 29 642–29 648, 2016.

[61] Y.-Z. Yang, T.-X. Zhu, Z.-P. Li, X.-D. Zeng, N.-J. Guo, S. Yu, Y. Meng, Z.-A. Wang, L.-K. Xie, Z.-Q. Zhou *et al.*, "Laser direct writing of visible spin defects in hexagonal boron nitride for applications in spin-based technologies," *ACS Applied Nano Materials*, vol. 6, no. 7, pp. 6407–6414, 2023.

[62] A. Gale, C. Li, Y. Chen, K. Watanabe, T. Taniguchi, I. Aharonovich, and M. Toth, "Site-specific fabrication of blue quantum emitters in hexagonal boron nitride," *ACS Photonics*, vol. 9, no. 6, pp. 2170–2177, 2022.

[63] S. Gao, H. Y. Chen, and M. Bernardi, "Radiative properties of quantum emitters in boron nitride from excited state calculations and bayesian analysis," *npj Computational Materials*, vol. 7, 2021.

[64] A. Sajid, M. J. Ford, and J. R. Reimers, "Single-photon emitters in hexagonal boron nitride: a review of progress," *Reports on Progress in Physics*, vol. 83, 2020.

[65] S. A. Tawfik, S. Ali, M. Fronzi, M. Kianinia, T. T. Tran, C. Stampfl, I. Aharonovich, M. Toth, and M. J. Ford, "First-principles investigation of quantum emission from hbn defects," *Nanoscale*, vol. 9, 2017.

[66] N. Mendelson, D. Chugh, J. R. Reimers, T. S. Cheng, A. Gottscholl, H. Long, C. J. Mellor, A. Zettl, V. Dyakonov, P. H. Beton *et al.*, "Identifying carbon as the source of visible single-photon emission from hexagonal boron nitride," *Nature Materials*, vol. 20, no. 3, pp. 321–328, 2021.

[67] Z. Q. Xu, N. Mendelson, J. A. Scott, C. Li, I. H. Abidi, H. Liu, Z. Luo, I. Aharonovich, and M. Toth, "Charge and energy transfer of quantum emitters in 2d heterostructures," *2D Materials*, 2020.

[68] M. Yu, D. Yim, H. Seo, and J. Lee, "Electrical charge control of h-bn single photon sources," *2D Materials*, vol. 9, no. 3, p. 035020, 2022.

[69] G. Grosso, H. Moon, B. Lienhard, S. Ali, D. K. Efetov, M. M. Furchi, P. Jarillo-Herrero, M. J. Ford, I. Aharonovich, and D. Englund, "Tunable and high-purity room temperature single-photon emission from atomic defects in hexagonal boron nitride," *Nature Communications*, vol. 8, 2017.

[70] Y. Xia, Q. Li, J. Kim, W. Bao, C. Gong, S. Yang, Y. Wang, and X. Zhang, "Room-temperature giant stark effect of single photon emitter in van der waals material," *Nano Letters*, vol. 19, 2019.

[71] J. Thijssen, *Computational physics, second edition*. Cambridge University Press, 2007, vol. 9780521833462.

[72] P. W. Atkins, *Molecular quantum mechanics*, 5th ed. Oxford ; New York: Oxford University Press, 2011.

[73] R. O. Jones and O. Gunnarsson, "The density functional formalism, its applications and prospects," *Rev. Mod. Phys.*, vol. 61, pp. 689–746, Jul 1989. [Online]. Available: https://link.aps.org/doi/10.1103/RevModPhys.61.689

[74] M. Bursch, J.-M. Mewes, A. Hansen, and S. Grimme, "Best-practice dft protocols for basic molecular computational chemistry," *Angewandte Chemie International Edition*, vol. 61, no. 42, p. e202205735, 2022.

[75] J. G. Hill, "Gaussian basis sets for molecular applications," *International Journal of Quantum Chemistry*, vol. 113, no. 1, pp. 21–34, 2013.

[76] R. Jones and P. Briddon, *Chapter 6 The Ab Initio Cluster Method and the Dynamics of Defects in Semiconductors*, ser. Semiconductors and Semimetals. Elsevier, 1998, vol. 51, pp. 287–349. [Online]. Available: https://www.sciencedirect.com/science/article/pii/S0080878408630586

[77] D. Hamann, M. Schlüter, and C. Chiang, "Norm-conserving pseudopotentials," *Physical Review Letters*, vol. 43, no. 20, p. 1494, 1979.

[78] G. Kerker, "Non-singular atomic pseudopotentials for solid state applications," *Journal of Physics C: Solid State Physics*, vol. 13, no. 9, p. L189, 1980.

[79] D. Vanderbilt, "Soft self-consistent pseudopotentials in a generalized eigenvalue formalism," *Physical Review B*, vol. 41, no. 11, p. 7892, 1990.

[80] H. J. Monkhorst and J. D. Pack, "Special points for brillouin-zone integrations," *Physical Review B*, vol. 13, 1976.

[81] D. S. Sholl and J. A. Steckel, *Density functional theory: a practical introduction*. John Wiley & Sons, 2022.

[82] P. Pulay, "Convergence acceleration of iterative sequences. the case of scf iteration," *Chemical Physics Letters*, vol. 73, no. 2, pp. 393–398, 1980.

[83] G. Kresse and J. Furthmüller, "Efficient iterative schemes for ab initio total-energy calculations using a plane-wave basis set," *Physical Review B*, vol. 54, no. 16, p. 11169, 1996.

[84] S. Grimme, J. Antony, S. Ehrlich, and H. Krieg, "A consistent and accurate ab initio parametrization of density functional dispersion correction (dft-d) for the 94 elements h-pu," *The Journal of Chemical physics*, vol. 132, no. 15, 2010.

[85] J. P. Perdew, K. Burke, and M. Ernzerhof, "Generalized gradient approximation made simple," *Physical Review Letters*, vol. 77, 1996.

[86] C. Hartwigsen, S. Gœdecker, and J. Hutter, "Relativistic separable dual-space gaussian pseudopotentials from h to rn," *Physical Review B*, vol. 58, no. 7, p. 3641, 1998.

[87] J. G. M. Shaw and P. Briddon, "Marker-method calculations for electrical levels using gaussian-orbital basis sets," *Theory of Defects In Semiconductors*, pp. 69–94, 2007.

[88] K. A. Peterson, D. Feller, and D. A. Dixon, "Chemical accuracy in ab initio thermochemistry and spectroscopy: current strategies and future challenges," *Theoretical Chemistry Accounts*, vol. 131, pp. 1–20, 2012.

[89] L. Cai, X. Fan, H. Su, M. Lv, and B. Xu, "First principles calculation of the lattice constants of hexagonal and cubic boron nitride to 3000 k and 30 gpa," *Ferroelectrics*, vol. 566, 2020.

[90] B. Xu, M. Lv, X. Fan, W. Zhang, Y. Xu, and T. Zhai, "Lattice parameters of hexagonal and cubic boron nitrides at high temperature and high pressure," *Integrated Ferroelectrics*, vol. 162, 2015.

[91] A. Janotti, S. H. Wei, and D. J. Singh, "First-principles study of the stability of bn and c," *Physical Review B - Condensed Matter and Materials Physics*, vol. 64, 2001.

[92] X. Liu, Z. Gao, V. Wang, Z. Luo, B. Lv, Z. Ding, and Z. Zhang, "Extrapolated defect transition level in two-dimensional materials: The case of charged native point defects in monolayer hexagonal boron nitride," *ACS Applied Materials and Interfaces*, vol. 12, 2020.

[93] W. Kohn, A. D. Becke, and R. G. Parr, "Density functional theory of electronic structure," *The journal of physical chemistry*, vol. 100, no. 31, pp. 12 974–12 980, 1996.

[94] R. M. Martin, *Electronic structure: basic theory and practical methods*. Cambridge University Press, 2020.

[95] R. S. Mulliken, "Electronic population analysis on lcao–mo molecular wave functions. i," *The Journal of Chemical physics*, vol. 23, no. 10, pp. 1833–1840, 1955.

[96] F. L. Hirshfeld, "Bonded-atom fragments for describing molecular charge densities," *Theoretica chimica acta*, vol. 44, pp. 129–138, 1977.

[97] G. Henkelman, A. Arnaldsson, and H. Jónsson, "A fast and robust algorithm for bader decomposition of charge density," *Computational Materials Science*, vol. 36, no. 3, pp. 354–360, 2006.

[98] G. Henkelman and H. Jónsson, "Improved tangent estimate in the nudged elastic band method for finding minimum energy paths and saddle points," *The Journal of Chemical Physics*, vol. 113, no. 22, pp. 9978–9985, 2000.

[99] W. Paszkowicz, J. Pelka, M. Knapp, T. Szyszko, and S. Podsiadlo, "Lattice parameters and anisotropic thermal expansion of hexagonal boron nitride in the 10–297.5 k temperature range," *Applied Physics A*, vol. 75, pp. 431–435, 2002.

[100] R. Geick, C. H. Perry, and G. Rupprecht, "Normal modes in hexagonal boron nitride," *Physical Review*, vol. 146, 1966.

[101] J. Serrano, A. Bosak, R. Arenal, M. Krisch, K. Watanabe, T. Taniguchi, H. Kanda, A. Rubio, and L. Wirtz, "Vibrational properties of hexagonal boron nitride: Inelastic x-ray scattering and ab initio calculations," *Physical Review Letters*, vol. 98, 2007.

[102] M. De La Pierre, R. Orlando, L. Maschio, K. Doll, P. Ugliengo, and R. Dovesi, "Performance of six functionals (lda, pbe, pbesol, b3lyp, pbe0, and wc1lyp) in the simulation of vibrational and dielectric properties of crystalline compounds. the case of forsterite mg2sio4," *Journal of Computational Chemistry*, vol. 32, no. 9, pp. 1775–1784, 2011.

[103] R. Demichelis, B. Civalleri, M. Ferrabone, and R. Dovesi, "On the performance of eleven dft functionals in the description of the vibrational properties of aluminosilicates," *International Journal of Quantum Chemistry*, vol. 110, no. 2, pp. 406–415, 2010.

[104] D. Wickramaratne, L. Weston, and C. G. V. D. Walle, "Monolayer to bulk properties of hexagonal boron nitride," *Journal of Physical Chemistry C*, vol. 122, 2018.

[105] H. Henck, D. Pierucci, G. Fugallo, J. Avila, G. Cassabois, Y. J. Dappe, M. G. Silly, C. Chen, B. Gil, M. Gatti, F. Sottile, F. Sirotti, M. C. Asensio, and A. Ouerghi, "Direct observation of the band structure in bulk hexagonal boron nitride," *Physical Review B*, vol. 95, 2017.

[106] A. Catellani, M. Posternak, A. Baldereschi, and A. J. Freeman, "Bulk and surface electronic structure of hexagonal boron nitride," *Physical Review B*, vol. 36, 1987.

[107] N. Ooi, A. Rairkar, L. Lindsley, and J. B. Adams, "Electronic structure and bonding in hexagonal boron nitride," *Journal of Physics Condensed Matter*, vol. 18, 2006.

[108] Y. N. Xu and W. Y. Ching, "Calculation of ground-state and optical properties of boron nitrides in the hexagonal, cubic, and wurtzite structures," *Physical Review B*, vol. 44, 1991.

[109] A. H. C. Neto, F. Guinea, N. M. Peres, K. S. Novoselov, and A. K. Geim, "The electronic properties of graphene," *Reviews of Modern Physics*, vol. 81, 2009.

[110] B. Partoens and F. M. Peeters, "From graphene to graphite: Electronic structure around the k point," *Physical Review B - Condensed Matter and Materials Physics*, vol. 74, 2006.

[111] C. Yelgel and G. P. Srivastava, "Ab initio studies of electronic and optical properties of graphene and graphene-bn interface," vol. 258, 2012.

[112] C. Bena and S. A. Kivelson, "Quasiparticle scattering and local density of states in graphite," *Physical Review B - Condensed Matter and Materials Physics*, vol. 72, 2005.

[113] E. Konstantinova, S. O. Dantas, and P. M. Barone, "Electronic and elastic properties of two-dimensional carbon planes," *Physical Review B - Condensed Matter and Materials Physics*, vol. 74, 2006.

[114] R. M. Torres-Rojas, D. A. Contreras-Solorio, L. Hernández, and A. Enciso, "Band gap variation in bi, tri and few-layered 2d graphene/hbn heterostructures," *Solid State Communications*, vol. 341, p. 114553, 2022.

[115] P. Moon and M. Koshino, "Electronic properties of graphene/hexagonal-boron-nitride moiré superlattice," *Physical Review B - Condensed Matter and Materials Physics*, vol. 90, 2014.

[116] M. K. Prasad, O. A. Al-Ani, J. P. Goss, and J. D. Mar, "Charge transfer due to defects in hexagonal boron nitride/graphene heterostructures: An ab initio study," *Physical Review Materials*, vol. 7, no. 9, p. 094003, 2023.

[117] ——, "Charge transfer and quantum emitters in two-dimensional heterostructures: An ab initio study," in *AIP Conference Proceedings*, vol. 2743, no. 1. AIP Publishing, 2023.

[118] B. Huang and H. Lee, "Defect and impurity properties of hexagonal boron nitride: A first-principles calculation," *Physical Review B - Condensed Matter and Materials Physics*, vol. 86, 2012.

[119] V. Ivády, G. Barcza, G. Thiering, S. Li, H. Hamdi, J.-P. Chou, Ö. Legeza, and A. Gali, "Ab initio theory of the negatively charged boron vacancy qubit in hexagonal boron nitride," *npj Computational Materials*, vol. 6, no. 1, p. 41, 2020.

[120] L. Weston, D. Wickramaratne, M. Mackoit, A. Alkauskas, and C. G. V. D. Walle, "Native point defects and impurities in hexagonal boron nitride," *Physical Review B*, vol. 97, 2018.

[121] J. Strand, L. Larcher, and A. L. Shluger, "Properties of intrinsic point defects and dimers in hexagonal boron nitride," *Journal of Physics Condensed Matter*, vol. 32, 2020.

[122] C. W. Castleton and S. Mirbt, "Finite-size scaling as a cure for supercell approximation errors in calculations of neutral native defects in inp," *Physical Review B - Condensed Matter and Materials Physics*, vol. 70, 2004.

[123] H. P. Komsa, T. T. Rantala, and A. Pasquarello, "Finite-size supercell correction schemes for charged defect calculations," *Physical Review B - Condensed Matter and Materials Physics*, vol. 86, 2012.

[124] H. P. Komsa and A. Pasquarello, "Finite-size supercell correction for charged defects at surfaces and interfaces," *Physical Review Letters*, vol. 110, 2013.

[125] H. P. Komsa, N. Berseneva, A. V. Krasheninnikov, and R. M. Nieminen, "Charged point defects in the flatland: Accurate formation energy calculations in two-dimensional materials," *Physical Review X*, vol. 4, 2014.

[126] ——, "Erratum: Charged point defects in the flatland: accurate formation energy calculations in two-dimensional materials)," *Physical Review X*, vol. 8, 2018.

[127] S. Park, C. Park, and G. Kim, "Interlayer coupling enhancement in graphene/hexagonal boron nitride heterostructures by intercalated defects or vacancies," *The Journal of Chemical physics*, vol. 140, no. 13, p. 134706, 2014.

[128] A. Sajid, J. R. Reimers, and M. J. Ford, "Defect states in hexagonal boron nitride: Assignments of observed properties and prediction of properties relevant to quantum computation," *Physical Review B*, vol. 97, 2018.

[129] F. Wu, A. Galatas, R. Sundararaman, D. Rocca, and Y. Ping, "First-principles engineering of charged defects for two-dimensional quantum technologies," *Physical Review Materials*, vol. 1, 2017.

[130] C. Linderälv, W. Wieczorek, and P. Erhart, "Vibrational signatures for the identification of single-photon emitters in hexagonal boron nitride," *Physical Review B*, vol. 103, no. 11, p. 115421, 2021.

[131] A. Scavuzzo, S. Mangel, J. H. Park, S. Lee, D. L. Duong, C. Strelow, A. Mews, M. Burghard, and K. Kern, "Electrically tunable quantum emitters in an ultrathin graphene-hexagonal boron nitride van der waals heterostructure," *Applied Physics Letters*, vol. 114, 2019.

[132] M. Abdi, J. P. Chou, A. Gali, and M. B. Plenio, "Color centers in hexagonal boron nitride monolayers: A group theory and ab initio analysis," *ACS Photonics*, vol. 5, 2018.

[133] Y. Zhang, G. Cheng, W. Peng, and Z. Tang, "Spintronic and electronic properties of a positively charged nbvn center in hexagonal boron nitride monolayer," *Computational Materials Science*, vol. 95, pp. 316–319, 2014.

[134] P. U. Asshoff, J. L. Sambricio, S. Slizovskiy, A. P. Rooney, T. Taniguchi, K. Watanabe, S. J. Haigh, V. Fal'ko, I. V. Grigorieva, and I. J. Vera-Marun, "Magnetoresis-

tance in co-hbn-nife tunnel junctions enhanced by resonant tunneling through single defects in ultrathin hbn barriers," *Nano Letters*, vol. 18, no. 11, pp. 6954–6960, 2018.

[135] H. Chang, L. Tang, Y. Wang, J. Jiang, and J. Li, "Graphene fluorescence resonance energy transfer aptasensor for the thrombin detection," *Analytical Chemistry*, vol. 82, no. 6, pp. 2341–2346, 2010.

[136] N. Mendelson, M. Doherty, M. Toth, I. Aharonovich, and T. T. Tran, "Strain-induced modification of the optical characteristics of quantum emitters in hexagonal boron nitride," *Advanced Materials*, vol. 32, no. 21, p. 1908316, 2020.

[137] A. B. D.-a. Shaik and P. Palla, "Strain tunable quantum emission from atomic defects in hexagonal boron nitride for telecom-bands," *Scientific Reports*, vol. 12, no. 1, p. 21673, 2022.

[138] S. Lazić, A. Espinha, S. Pinilla Yanguas, C. Gibaja, F. Zamora, P. Ares, M. Chhowalla, W. S. Paz, J. J. P. Burgos, A. Hernández-Mínguez *et al.*, "Dynamically tuned non-classical light emission from atomic defects in hexagonal boron nitride," *Communications Physics*, vol. 2, no. 1, p. 113, 2019.

[139] D. Wang and R. Sundararaman, "Substrate effects on charged defects in two-dimensional materials," *Physical Review Materials*, vol. 3, 2019.

[140] S. Li, A. Pershin, P. Li, and A. Gali, "Exceptionally strong coupling of defect emission in hexagonal boron nitride to stacking sequences," *npj 2D Materials and Applications*, vol. 8, no. 1, p. 16, 2024.

[141] F. Pinilla, W. A. Muriel, J. Cabezas-Escares, I. Chacón, C. Cardenas, and F. Munoz, "Manipulating the stacking in two-dimensional hexagonal boron nitride bilayers: Implications for defect-based single photon emitters," *ACS Applied Nano Materials*, vol. 7, no. 6, pp. 6039–6046, 2024.

[142] D. I. Badrtdinov, C. Rodriguez-Fernandez, M. Grzeszczyk, Z. Qiu, K. Vaklinova, P. Huang, A. Hampel, K. Watanabe, T. Taniguchi, L. Jiong *et al.*, "Dielectric

environment sensitivity of carbon centers in hexagonal boron nitride," *Small*, vol. 19, no. 41, p. 2300144, 2023.

[143] S. K. Narayanan and P. Dev, "Substrate-induced modulation of quantum emitter properties in 2d hexagonal boron nitride: Implications for defect-based single photon sources in 2d layers," *ACS Applied Nano Materials*, vol. 6, no. 5, pp. 3446–3452, 2023.

[144] K. Scheuer, G. Hornig, and R. DeCorby, "Polymer transfer technique for strain-activated emission in hexagonal boron nitride," *Optics Express*, vol. 29, no. 16, pp. 26 103–26 115, 2021.

[145] S. Fukamachi, P. Solís-Fernández, K. Kawahara, D. Tanaka, T. Otake, Y.-C. Lin, K. Suenaga, and H. Ago, "Large-area synthesis and transfer of multilayer hexagonal boron nitride for enhanced graphene device arrays," *Nature Electronics*, vol. 6, no. 2, pp. 126–136, 2023.

[146] S. M. George, "Atomic layer deposition: an overview," *Chemical Reviews*, vol. 110, no. 1, pp. 111–131, 2010.

[147] A. Ott, J. Klaus, J. Johnson, and S. George, "Al3o3 thin film growth on si (100) using binary reaction sequence chemistry," *Thin Solid Films*, vol. 292, no. 1-2, pp. 135–144, 1997.

[148] Z. J. Zhou, "Electron beam lithography," in *Handbook of microscopy for nanotechnology*. Springer, 2005, pp. 287–321.

[149] R. R. Jones, D. C. Hooper, L. Zhang, D. Wolverson, and V. K. Valev, "Raman techniques: fundamentals and frontiers," *Nanoscale research letters*, vol. 14, pp. 1–34, 2019.

[150] H. G. Tompkins and J. N. Hilfiker, *Spectroscopic ellipsometry: practical application to thin film characterization*. Momentum Press, 2015.

[151] N. Jalili and K. Laxminarayana, "A review of atomic force microscopy imaging systems: application to molecular metrology and biological sciences," *Mechatronics*, vol. 14, no. 8, pp. 907–945, 2004.

[152] H. Reittu, "Fermi's golden rule and bardeen's tunneling theory," *American Journal of Physics*, vol. 63, no. 10, pp. 940–944, 1995.

[153] Z. Liu, W. Chim, S. Chiam, J. Pan, and C. Ng, "An interface dipole predictive model for high-k dielectric/semiconductor heterostructures using the concept of the dipole neutrality point," *Journal of Materials Chemistry*, vol. 22, no. 34, pp. 17 887–17 892, 2012.

[154] S. Ichinokura, A. Hemmi, H. Cun, K. Tanaka, R. Shimizu, T. Hitosugi, T. Greber, and T. Hirahara, "Efficiency of electron doping to monolayer hexagonal boron nitride by alkali metals," *Applied Physics Letters*, vol. 122, no. 7, 2023.

[155] H. Sahoo, "Förster resonance energy transfer–a spectroscopic nanoruler: Principle and applications," *Journal of Photochemistry and Photobiology C: Photochemistry Reviews*, vol. 12, no. 1, pp. 20–30, 2011.

[156] C. Li, Z.-Q. Xu, N. Mendelson, M. Kianinia, M. Toth, and I. Aharonovich, "Purification of single-photon emission from hbn using post-processing treatments," *Nanophotonics*, vol. 8, no. 11, pp. 2049–2055, 2019.

[157] Z.-Q. Xu, C. Elbadawi, T. T. Tran, M. Kianinia, X. Li, D. Liu, T. B. Hoffman, M. Nguyen, S. Kim, J. H. Edgar *et al.*, "Single photon emission from plasma treated 2d hexagonal boron nitride," *Nanoscale*, vol. 10, no. 17, pp. 7957–7965, 2018.

[158] A. Bommer and C. Becher, "New insights into nonclassical light emission from defects in multi-layer hexagonal boron nitride," *Nanophotonics*, vol. 8, no. 11, pp. 2041–2048, 2019.

[159] A. I. Aria, K. Nakanishi, L. Xiao, P. Braeuninger-Weimer, A. A. Sagade, J. A. Alexander-Webber, and S. Hofmann, "Parameter space of atomic layer deposition

of ultrathin oxides on graphene," *ACS applied materials & interfaces*, vol. 8, no. 44, pp. 30 564–30 575, 2016.

[160] A. Cabrero-Vilatela, J. Alexander-Webber, A. Sagade, A. I. Aria, P. Braeuninger-Weimer, M.-B. Martin, R. Weatherup, and S. Hofmann, "Atomic layer deposited oxide films as protective interface layers for integrated graphene transfer," *Nanotechnology*, vol. 28, no. 48, p. 485201, 2017.

[161] S. Kim, S.-H. Lee, I. H. Jo, J. Seo, Y.-E. Yoo, and J. H. Kim, "Influence of growth temperature on dielectric strength of al2o3 thin films prepared via atomic layer deposition at low temperature," *Scientific Reports*, vol. 12, no. 1, p. 5124, 2022.

[162] C. Lyu, Y. Zhu, P. Gu, J. Qiao, K. Watanabe, T. Taniguchi, and Y. Ye, "Single-photon emission from two-dimensional hexagonal boron nitride annealed in a carbon-rich environment," *Applied Physics Letters*, vol. 117, no. 24, 2020.

[163] S. S. Mohajerani, S. Chen, A. Alaei, T. Chou, N. Liu, Y. Ma, L. Xiao, S. S. Lee, E.-H. Yang, and S. Strauf, "Narrowband quantum light emission from oxygen-related color centers in hexagonal boron nitride," *ACS Photonics*, 2024.

[164] R. Wang, D. G. Purdie, Y. Fan, F. C.-P. Massabuau, P. Braeuninger-Weimer, O. J. Burton, R. Blume, R. Schloegl, A. Lombardo, R. S. Weatherup *et al.*, "A peeling approach for integrated manufacturing of large monolayer h-bn crystals," *ACS Nano*, vol. 13, no. 2, pp. 2114–2126, 2019.

[165] Z. Wang, H. Xu, Z. Zhang, S. Wang, L. Ding, Q. Zeng, L. Yang, T. Pei, X. Liang, M. Gao *et al.*, "Growth and performance of yttrium oxide as an ideal high-κ gate dielectric for carbon-based electronics," *Nano letters*, vol. 10, no. 6, pp. 2024–2030, 2010.

[166] G. D. Wilk, R. M. Wallace, and J. Anthony, "High-κ gate dielectrics: Current status and materials properties considerations," *Journal of applied physics*, vol. 89, no. 10, pp. 5243–5275, 2001.

[167] J. Robertson, "Band offsets of wide-band-gap oxides and implications for future electronic devices," *Journal of Vacuum Science & Technology B: Microelectronics and Nanometer Structures Processing, Measurement, and Phenomena*, vol. 18, no. 3, pp. 1785–1791, 2000.

[168] M. A. Marques, C. A. Ullrich, F. Nogueira, A. Rubio, K. Burke, and E. K. Gross, *Time-dependent density functional theory*. Springer, 2006, vol. 706.

[169] A. A. Peterson, "Acceleration of saddle-point searches with machine learning," *The Journal of chemical physics*, vol. 145, no. 7, 2016.